Mechanistic Studies of the Effect of Nitrogen-Based Detergents on Gum Adsorption from Gasoline Fuels

Abdulrehman Suhail M Ajina

Submitted in accordance with the requirements for the degree of Doctor of Philosophy

The University of Leeds
School of Chemical and Process Engineering

July, 2019

The candidate confirms that the work submitted is his own, except where work which has formed part of jointly-authored publications has been included. The contribution of the candidate and the other authors to this work has been explicitly indicated below. The candidate confirms that appropriate credit has been given within the thesis where reference has been made to the work of others.

The work in chapter 4.3 was presented as follows:

Abdulrehman S. Ajina and Sven L. M. Schroeder. Gum Formation and Deposition Tendency in Ternary Gasoline Surrogates*. ChemEngDay UK 2016, Bath, United Kingdom.* [Poster]

The work in chapters 4.3, 5.3, and parts of 5.4 was presented and awarded the 'Infineum poster competition prize' as follows:

Abdulrehman S. Ajina, Hu Li, and Sven L. M. Schroeder. Fundamental Studies on the Effects of Nitrogen-based Additives Over Deposit Formation in Ternary Gasoline Surrogates. *EPSRC CDT-cP^3 Research Day, 2018, Leeds, United Kingdom*. [Oral & Poster].

The candidate was responsible for all work in both cases. The role of the other authors was supervisory.

To My Parents,

Suhail & Alawiyyah ..

Acknowledgements

Firstly, I would like to greatly thank my supervisor Professor Sven Schroeder for all his guidance throughout this journey. His support, mentoring, and understanding during difficult times will never be forgotten. Special thanks also go to Dr Hu Li for all his efforts in co-supervising this PhD project. From the versatile X-ray spectroscopy facility at the school of chemical and process engineering, I would like thank Dr Elizabeth Willneff for all the training sessions and great assistance in performing the XPS measurements.

Completing this PhD would not have been possible without the support of my wife, Dina Tayeb. I will never be able to thank her enough for all her support, encouragement, and compassion during the course of this challenging adventure of our life. In addition, the amount of moral support I received from my family and family-in-law will always be commendable. I would also like to apologise to my children, Celine and Yusuf, for all the times I have been away, both physically and mentally.

Next, I would like to specially thank my dear friend Mohammed Jeraal. His support during tough times was of a great help to me to get through this PhD. Our “Nero sessions” and late office nights will always be remembered. Special thanks also go to my office mate Jessica Shiels for all her ‘Positive Mental Attitude’ posts and encouragements. Finally, I am very grateful to have my friends who have been truly my ‘family in Leeds’, namely Hussam Fallatah, Adham Ibrahim, Majed Khair Allah, Almoataz Hassan, and Abdullah Iskandrani.

Finally, I would like to acknowledge Dr David Morgan and the group from the EPSRC National Facility for XPS (‘HarwellXPS’) at Cardiff University, for collecting part of the XPS data presented in this thesis (under contract number: PR16195). Special thanks also go to the Research and Development Centre at the Saudi Arabian Oil Company (Saudi Aramco) for funding this research. Thanks are also due to the Engineering and Physical Sciences Research Council (EPSRC) Centre for Doctoral Training in Complex Particulate Products and Processes (CDT-cP^3) for their support through academic development programs and access to national facilities (under EPSRC Grant number: EP/L015285/1).

Abstract

Deposition of carbonaceous materials on internal surfaces of spark ignition engines is a long-standing problem that can seriously impact engine performance. For gasoline fuel, deposit control additives (‘detergents’) comprising nitrogen-based detergents are commonly used to inhibit deposition and minimise its effects. However, the molecular basis of their detergency is still poorly understood. The most commonly quoted mechanistic hypothesis assumes that gasoline detergents inhibit deposit formation via surface passivation. i.e. by forming an adsorbed 2D thin film phase that protects the metal surface. The present work constitutes a first step towards establishing a systematic protocol for analysing the molecular mechanisms leading to the macroscopically observable detergency effect. This was done by synthesising a model fuel system that contained carbonaceous material (‘gum’) that can deposit on steel surfaces. First, a method for the synthesis of gum by a radical oxidation of mono- and diolefin components with air was developed. This established a reproducible method for oxidising gasoline surrogate to create gum. FTIR spectroscopy along with other analytical characterisation techniques were employed to validate the formulation and oxidation methods, the resulting oxidation product, and their deposits on steel surfaces. Then, the influence of a model detergent, 1-octadecylamine (ODA), on the oxidised fuel was studied. In solution, it interacts strongly with polar groups of the gum, likely solubilising it and thereby shifting any interfacial adsorption equilibrium towards the solution state. Gum deposition and detergency were then examined by using 316 stainless steel substrates. The ODA concentration was found to not only influence the adsorption equilibrium, but also the morphology of deposits on the surfaces, minimising the surface area covered by them. A systematic experimental design was developed to investigate the solid-liquid interactions at the stainless steel/solution interface in more detail. X-ray photoelectron spectroscopy was extensively used as the main surface sensitive technique to gain insight into the molecular basis of adsorption and detergency in this system. The results revealed that the detergency process was related mainly to solubilisation of gum in the solution phase, rather than surface passivation by formation of an adsorbed ODA layer. Adsorbed ODA was only evident when unrealistically high ODA concentrations were used.

Table of Contents

List of Tables

List of Figures

List of Abbreviations

AI	Active ingredient
AISI	American iron and steel institute
ASTM	American society for testing and materials
ATR-FTIR	Attenuated total reflectance – Fourier transform infrared
a.u.	Arbitrary unit
B.E	Binding energy
CC	Combustion chamber
CHC	Critical hemimicelle concentration
CMC	Critical micelle concentration
CPS	Counts per second
DCAs	Deposit control additives
DISI	Direct injection spark ignition
DLS	Dynamic light scattering
DTG	Differential thermogravimetric
EDX	Energy Dispersive X-ray
GC-MS	Gas chromatography coupled with mass spectroscopy
IR	Infrared radiation
IV	Intake valve
IVDA	Intake valve deposits apparatus
K.E	Kinetic energy
LbV	Linear by volume
MLbV	Modified linear by volume
MON	Motor octane number
MW	Molecular weight
NAP-XPS	Near ambient pressure X-ray photoelectron spectroscopy
NMR	Nuclear magnetic resonance
ODA	Octadecylamine
OM	Optical microscopy

PFI	Port fuel injector
PIBA	Polyisobutylene amine
PRF	Primary reference fuel
R&D	Research and development
RON	Research octane number
S	Sensitivity
SEM	Scanning electron microscope
SI	Spark ignition
SS	Stainless steel
TAM	Toluene, acetone, methanol
tBHP	Tertiary butyl hydroperoxide
TGA	Thermogravimetric analysis
TRF	Toluene reference fuel
UHV	Ultrahigh vacuum
UV-Vis	Ultraviolet and visible
XPS	X-ray photoelectron spectroscopy

Chapter 1 Introduction

1.1 Background

Fossil fuel has been used by mankind as a resource for lighting and energy for millennia. Advancements in science and technology in the 19th and 20th centuries have opened up numerous other applications of fossil fuels, making them one of the main pillars of the world economy. Petroleum derived fuels are complex mixtures of hydrocarbon compounds that are capable of generating power and energy. Gasoline fuel in particular is dominant in the automotive industry. However, markets around the world differ in their gasoline product specification in a number of aspects including, but not limited to, hydrocarbon composition, sulphur content, and octane number. Specifications and fuel composition contribute significantly to fuel quality and hence engine performance. (1) During gasoline fuel refining processes, functionalised chemical additives are blended with the fuel, fulfilling functions such as tackling combustion complications, enhancing gasoline performance and stability, and controlling sulphur levels. (2-4) Gasoline combustion is a complex process in spark ignition (SI) engines. By-products formed in the combustion cycle have received extensive attention from engines manufacturers and researchers. Their impact on ignition, fuel economy, and hydrocarbon emissions is well established. For instance, materials deposition on engine internal parts (e.g. combustion chamber (CC), intake valves (IV), and port fuel injectors (PFI)) has the potential to severely impact on the combustion cycle and lead to practical complications (Figure 1). (5-8) This is because the accumulation of deposits can drastically increase engine temperature causing uncontrolled ignition, knocking, and higher CO exhaust emissions. (9)

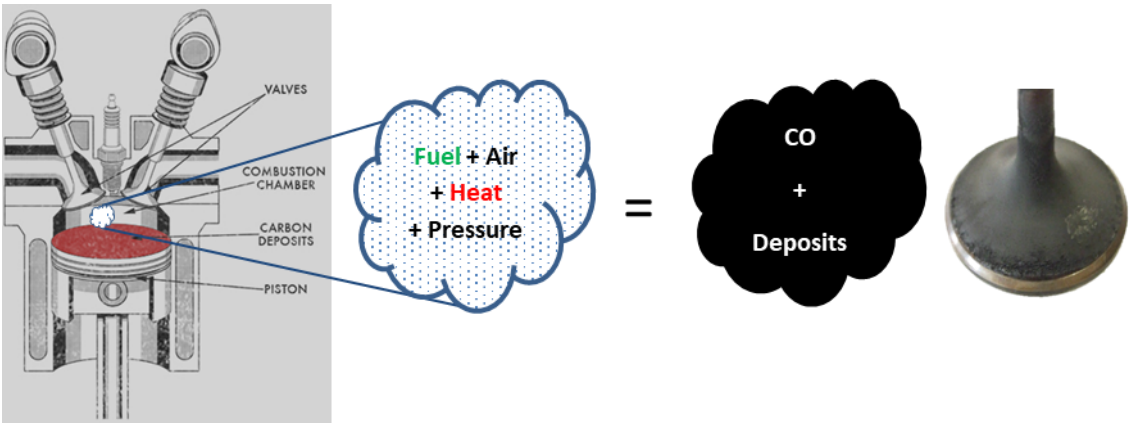

Figure 1 Cross sectional image of a typical SI engine (10), showing engine conditions leading to deposits accumulation on IV surfaces (far right).

Deposit control additives (DCAs) are therefore widely applied to treat post-combustion materials and control their deposition, which promotes fuel economy. (11) Within the chemical additives industry, DCAs hold a market share of approximately 40% – 50%. In most modern applications, engine internal parts are treated in two consecutive stages. Stage one, clean up, involves removing accumulated deposits with a high concentrated DCAs dosage. Stage two, keep clean, ensures continuous treatment to engine internal parts with lower concentration dosages. (12)

1.2 Motivation

DCAs utilised with gasoline fuel contain three main ingredients, namely detergent as active ingredient (AI), solvents, and a carrier fluid, with a typical formulation containing 30%, 30%, and 40% v/v of these components. The functional groups within the AI possess the utmost influence over the deposited materials. Several studies have discussed the positive effects of amine functional groups ($-NH_2$) in gasoline detergents. Furthermore, nitrogen-based detergents have been tested in several commercial products and showed promising results. However, the relationship between nitrogen concentration in the additive and the function of detergency remains an area of considerable research. (13-16) The interactions of gasoline detergents with engine metal surfaces and gum deposits in fuel require further extensive studies at microscopic and molecular levels. (17) Hence, the research question underlined by this study is: **How do nitrogen-based DCAs inhibit (or minimise) gum adsorption from gasoline fuels?** A deep understanding of the attachment mechanism as well as of the detergent and deposit chemical structures is vital to achieve successful and reliable results in this field. The association mechanism of amines in complex hydrocarbon systems was studied and characterised by various analytical techniques to better understand the influence of such compounds on engine deposits. (18, 19) Infrared spectroscopy has been particularly utilised in the characterisation of fuel and fuel additives. (15, 20) Various hypotheses have been developed over the years to explain the action mechanism of amine-based detergents. Current understanding (and the most extensively used hypothesis) focuses on passivation or ‘stick and eliminate’ scenario (Figure 2), in which active ingredients within the additive (i.e. the amine functional polymer) forms a thin adsorbed layer on the metal surface to prevent deposit accumulation. (5) However, competing with their adsorption is the surfactant nature of the AI in DCAs, which stabilises them colloidally in solution.

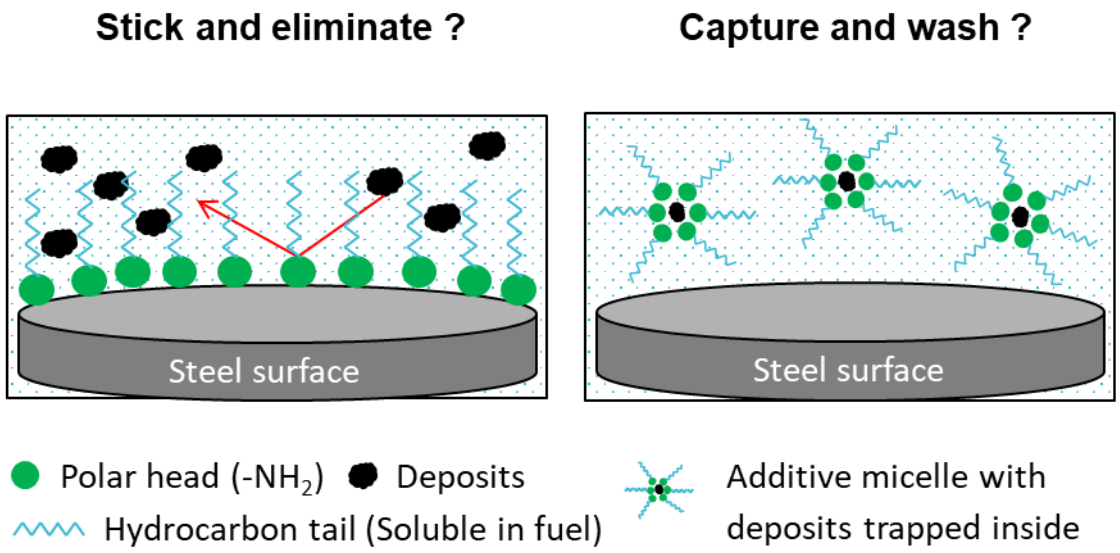

Figure 2 Schematic representations of the hypotheses developed to explain DCAs behaviour in eliminating deposit and gum formation in gasoline fuels.

The AI molecules (i.e. R-NH_2) can form micelles and solubilise gum and deposit particles in the gasoline (Figure 2), prohibiting precipitation on the metal surfaces. (21) This mechanism will be referred to as 'capture and wash' in this thesis. The well-known 'hump-effect' phenomenon observed for DCAs in gasoline fuels (Figure 3) is the observation that fuels treated with very low concentrations of DCA can create more deposits than entirely untreated fuels. This suggests that the AI additive only starts to solubilise gum when it is present in concentrations sufficient for colloidal action. At lower concentrations it may even promote more gum deposition by binding both to gum (through its non-polar groups) and the metal surface through its polar headgroups, acting as an 'anchor' for gum at the metal surface. (22, 23)

To provide a brief overview of the hump-effect phenomenon, performance of commercial detergents was evaluated at Saudi Aramco Research and Development Centre (R&DC) using intake valve deposits apparatus (IVDA) developed by Southwest Research Institute (SwRI®). (24) Experiments were conducted at various DCA concentrations using the same gasoline product to understand the impact of concentration over IV deposits (Figure 3). Test runs were repeated three times for each concentration and all low, medium, and high results were recorded. The test, in principle, calculates IV deposits gravimetrically based on the ASTM D-6201 standard test method for dynamometer evaluation of unleaded spark-ignition engine fuel for intake valve deposit formation. (25) It was clearly evident that at lower concentrations, higher amount of deposits have

accumulated on the outer surface (tulip) of the intake valves. Once the DCA concentration has exceeded 200 ppm (w/v), a clear reduction in deposition was observed, indicating good and reliable 'keep clean' detergency effects. (26)

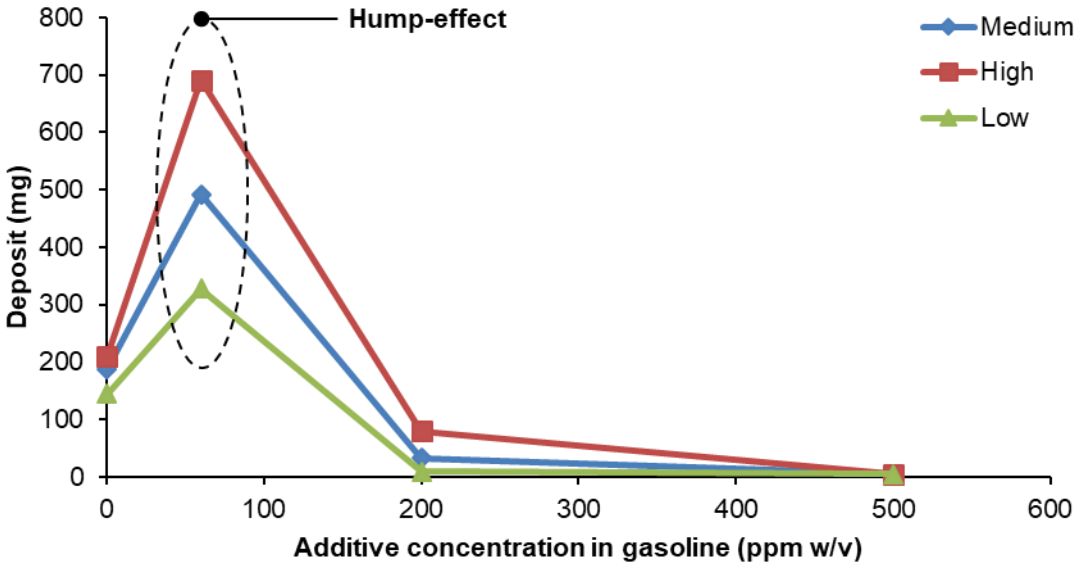

Figure 3 IVDA experimental results showing a hump-effect at lower concentrations (< 100 ppm w/v).

Based on the above discussions, both mechanisms depicted in Figure 2 are plausible scenarios. In fact, one may well envision their concurrent action. However, no fundamental studies have been conducted at the molecular level to investigate and pinpoint whether, or when, one or the other predominates, and what the balance between these two mechanistic pathways may be. (13-19) Therefore, this research focused on devising a systematic approach to fundamentally answer the research question stated above. Due to the complexity of the reactions involved in gum and deposits formation from gasoline fuels, it was decided that a model system needed to be developed to facilitate a fundamental study at the molecular level. The model system was primarily designed to mimic the components and interactions depicted in Figure 2. Thus, it was comprised of four components, namely a fuel model, synthesised deposits (gum), a model nitrogen-based detergent, and a metal substrate. Solid-liquid interactions at the substrate interfaces were then investigated using X-ray photoelectron spectroscopy (XPS) as a main surface sensitive technique. Probing the uppermost layers of the substrates at the nanometer scale was expected to allow a deeper molecular-level understanding of the attachment and detergency mechanisms of the nitrogen-based additive. The resulting study would thus be at the interface of applied research and fundamental surface science.

1.3 Research objectives

The overall aim of this research was to fundamentally investigate the effect of gasoline detergents on gum adsorption on metallic surfaces. The passivation hypothesis and the ‘stick and eliminate’ mechanism (Figure 2) are widely supported in the previous literature. (5, 21, 27) It therefore appears sensible to orient the studies towards testing and evaluating this hypothesis. A systematic programme of work comprising a series of mechanistic studies was set out to mimic and investigate gum adsorption/inhibition behaviour. The specific objectives were as follows:

- To establish a method for reproducibly formulating a simple gasoline fuel surrogate.
- To establish a reproducible method for synthesising model deposits (gum) from the formulated surrogate.
- To characterise the physical and chemical properties of the synthesised gum, as well as of the formulated surrogate fuel.
- To establish reproducible methods to prepare metallic surfaces for gum adsorption studies and surface sensitive analyses.
- To establish a laboratory scale method for gum adsorption on metallic surfaces.
- To introduce a nitrogen-based model detergent capable of inhibiting (or minimising) gum adsorption.
- To investigate the ability of the model detergent to adsorb onto metallic surfaces and consequently eliminate gum adsorption.
- To investigate the ability of the model detergent to remove adsorbed gum from the surface.
- To investigate the effects of the liquid-liquid interactions between the synthesised gum and the detergent on the adsorption behaviour.

1.4 Thesis structure

The body of this thesis is divided into five main chapters as briefly outlined in below.

Chapter 2 Literature review: Provides insight into the theoretical concepts and background knowledge relevant to the methods, materials, principles, and techniques applied throughout the course of this research.

Chapter 3 Experimental materials and methods: Describes the experimental methods, frameworks, and reproducibility studies designed for each phase of the project.

Chapter 4 Oxidative formation of gum in model surrogate fuel: Presents and discusses the results obtained pertaining the formulation and characterisation of the surrogate fuel and the synthesised gum.

Chapter 5 Addition of ODA into oxidised surrogate fuel: Presents and discusses the results obtained following the addition of the model detergent into the gum-containing surrogate fuels. This chapter serves as a proof of concept to the interactions between the model detergent, surrogate fuel, and gum.

Chapter 6 Systematic studies of interfacial behaviour by XPS: Presents and discusses the results obtained pertaining the systematic studies designed to extensively investigate the adsorption, detergency, and interactions behaviours within the model system.

Chapter 2 Literature review

Gasoline fuel is a complex mixture of hydrocarbons in the range of C_4 – C_{20} (boiling points of 30 – 220°C), which is used primarily in SI engines. Chemical composition of a typical gasoline product would include olefinic, paraffinic, and aromatic compounds as well as small contents of oxygenates to enhance fuel performance (e.g. ethanol as octane number booster). As a result of the refining of gasoline fuel, it contains traces of metals, sulphur, and nitrogen which in large concentrations can adversely affect fuel quality and provoke harmful exhaust emissions such as NO_x and SO_x.(17, 28-32) Therefore, legislation and monitoring programs have been developed to minimise environmental impact and regulate gasoline products specifications. (1) Following the combustion reaction in SI engines, certain products accumulate on engine metal surfaces such as intake valves and port fuel injectors affecting engine performance, combustion cycle, and fuel economy. Such products are commonly described in the literature as engine deposits and they have been widely investigated. (5, 7, 17, 33-36) One of the most common and effective solutions to tackle engine deposits is the use of gasoline detergents. (1, 5, 6, 37, 38) In the following, the four components of the model system designed to investigate the mechanism of nitrogen-based detergents in inhibiting deposits formation will be reviewed, followed by a review of the relevant literature on surface interactions.

2.1 Surrogate fuel model

Several surrogate fuels have been developed to study gasoline behaviour before and after the combustion cycle. Among formulated gasoline surrogates, toluene reference fuel (TRF) has been widely used in combustion and simulation studies. TRF is a hydrocarbon mixture based on primary reference fuel (PRF: n-heptane and iso-octane) with the addition of toluene to enhance the research octane number (RON) and the motor octane number (MON) of the blend and hence fuel's sensitivity (S = RON – MON). The RON value is determined at low engine speed and intake temperature of 600 rpm and 52°C, respectively, whereas the MON value is determined at 900 rpm and 149°C to represent motorway driving modes. (39-41) The following table illustrates the octane numbers for each component (42).

Table 1 Knock resistance values for TRF blend components.

Component	RON	MON
Toluene (tol)	120	109
n-Heptane (nH)	0	0
Iso-octane (io)	100	100

Alternative methods for creating gasoline surrogates have considered different blending components and ratios. For instance, Vanhove et al. suggested formulating ternary gasoline surrogates using toluene, iso-octane, and 1-hexene. (43) Moreover, additional compounds may be added to gasoline surrogate blends to mimic certain properties. Numerous studies have discussed the addition of olefin compounds as well as other classes of chemicals and functional groups to formulate more complex surrogates. (44-50) When compared to a basic TRF surrogate, complex TRF blends would allow for more advanced studies and investigations to be conducted. Matching surrogate properties to that of gasoline product is a key parameter when formulating alternative fuels. The RON and MON are essential values when it comes to TRF blends performance. Morgan et al. have developed a mathematical model to calculate volume fractions needed to formulate any TRF blend with targeted RON and MON, and hence predict the blend's sensitivity. (42) The work was based on a series of engine experiments using several TRF blends to identify knock resistance values (i.e. RON and MON). (51-54) Three models were developed to determine blends sensitivity, namely linear by volume (LbV), second order, and modified linear by volume (MLbV). The LbV model proposes linear addition of components to achieve targeted RON and MON values. However, it has been observed that such a model lacks the ability to adequately take interactions between the blend components into account, and while RON and MON values are reasonably well predicted, their difference (i.e. their sensitivity) might deviate significantly from the experimentally observed values. The following equation describes the proposed LbV model.

Equation 1

$$RON = a_{tol}.x_{tol} + a_{io}.x_{io} + a_{nH}.x_{nH}$$

Where '*a*' represents the RON value for the components listed in Table 1 and '*x*' is the corresponding volume fraction. Figure 4 illustrates how the proposed model predicts RON and MON values based on toluene volume fraction in the blend.

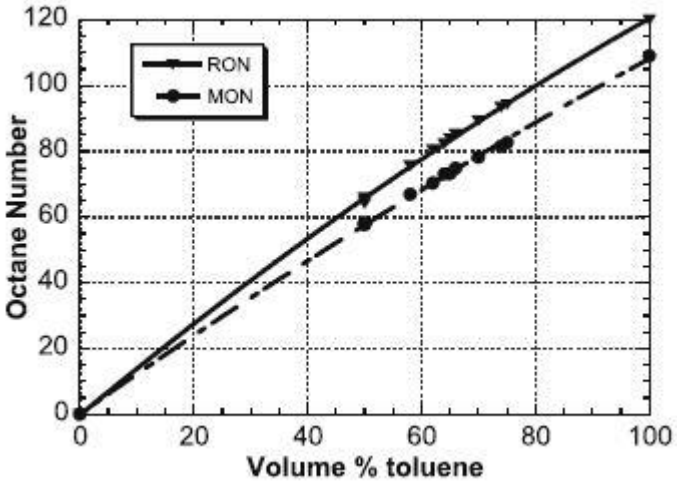

Figure 4 Prediction of octane number as a function of toluene volume percentage in TRF blends using LbV model. Data points are experimental, lines are calculated LbV values (42)

A second order model was developed to provide a more precise account to the influence of components on sensitivity. The model includes an interaction parameter to describe the interaction between toluene and PRF. (42) Due to the complexity of this model, a third model was proposed to address all interactions parameters and provide a more accurate definition for fuel system sensitivity prediction. The MLbV model uses a parameter '*p*' which introduces a normalised PRF volume fraction into the model according to

Equation 2

$$p = \frac{x_{io}}{x_{io} + x_{nH}}$$

and hence,

Equation 3

$$RON = a_p.p + a_{tol}.x_{tol} + a_{tol2}.x_{tol}^2 + a_{tol,p}.x_{tol}.p$$

Where all the coefficients can be defined as per the following table (42).

Table 2 Coefficients of the MLbV model using response surface model for RON, MON, and Sensitivity.

Coefficient	a_p	a_{tol}	a_{tol2}	$a_{tol,p}$
RON	100	142.79	-22.651	-111.95
MON	100	128.00	-19.207	-119.24
Sensitivity	0	14.79	-3.444	7.29

Further validation of the MLbV method led to a method that allows to predict the exact composition of any TRF blend to achieve a targeted RON value. A validation equation was developed to ensure precise matching between TRF blend properties and that of gasoline fuel. Figures 5-7 illustrate how TRF components affect a blend's RON, MON, and sensitivity values (42).

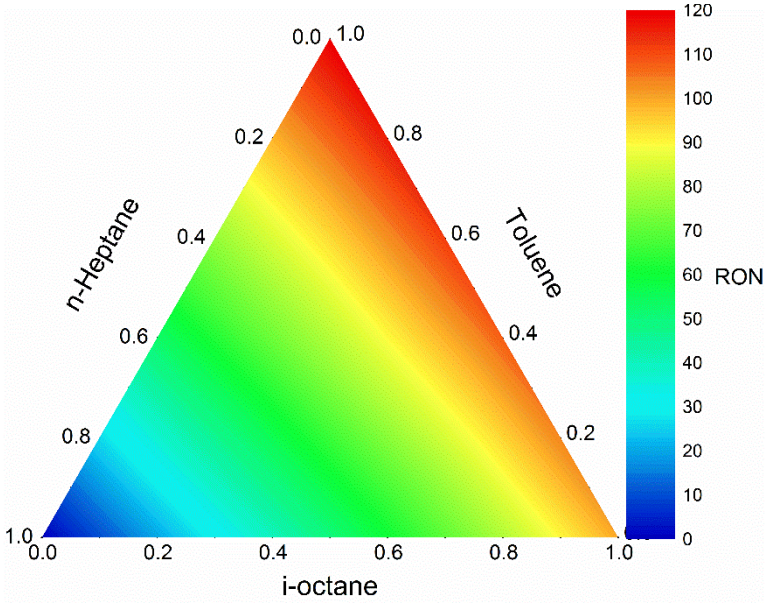

Figure 5 RON contour plot in ternary gasoline surrogate (TRF), reconstructed using MLbV model. (42)

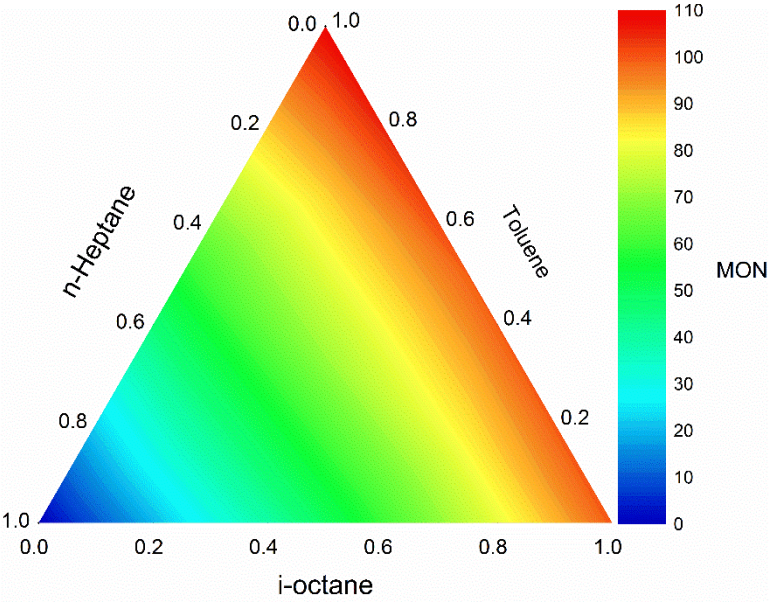

Figure 6 MON contour plot in ternary gasoline surrogate (TRF), reconstructed using MLbV model. (42)

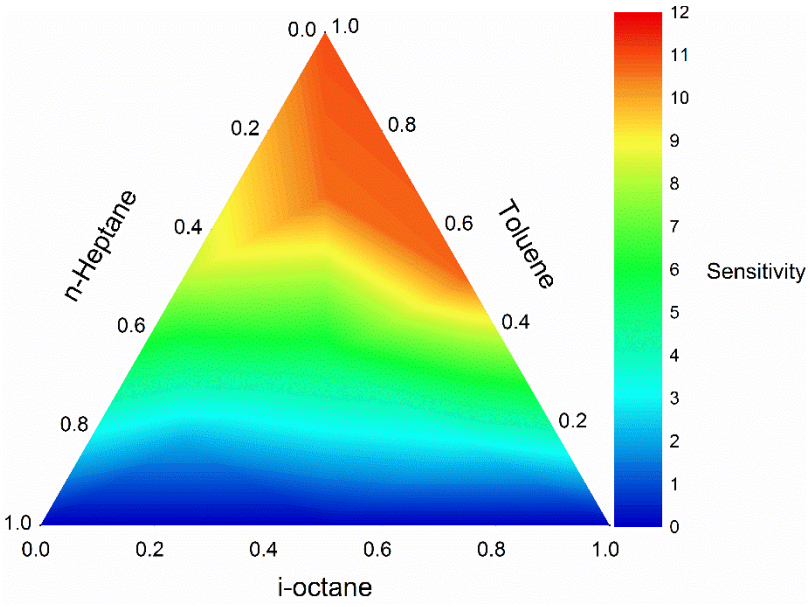

Figure 7 Sensitivity contour plot in ternary gasoline surrogate (TRF), reconstructed using MLbV model. (42)

The following equations describe the final model.

Equation 4

$$p = \frac{RON - (a_{tol}.x_{tol} + a_{tol2}.x_{tol}^2)}{100 + a_{tol,p}.x_{tol}}$$

and

Equation 5

$$S = a_{s,tol}.x_{tol} + a_{s,tol2}.x_{tol}^2 + \frac{a_{s,tol,p}.x_{tol}\,(RON - a_{R,tol}.x_{tol} - a_{R,tol2}.x_{tol}^2)}{100 + a_{R,tol,p}.x_{tol}^2}$$

Where subscripted '*S*' and '*R*' denote sensitivity and RON values, respectively, which were defined in Table 2.

By implementing the MLbV model, it was possible to produce a TRF blend in accordance with the British and European standards of unleaded petrol (EN-228) (55). Similar TRF surrogate fuels were used as the gasoline models for this PhD.

Table 3 TRF blends compositions in volume percentage with 95 RON and 85 MON using the MLbV model.

Blend no.	Toluene	n-Heptane	Iso-octane
1	60.54	18.82	20.65
2	71.37	22.04	22.04

2.2 Gum and deposit formation in SI engines

2.2.1 Definition

In the gasoline fuel industry, the term ‘gum’ is used to describe the insoluble, polymeric, and non-volatile products resulting primarily from oxidation of hydrocarbons in the fuel by oxygen absorbed from the atmosphere. It occurs due to the undesired changes in fuel stability either during storage or when exposed to high temperatures. Fuel (or storage) stability can be controlled by introducing sufficient inert gas into fuels storage tanks (e.g. nitrogen blanket) or via the use of oxidation inhibitors. Moreover, exposing light hydrocarbon fuels such as gasoline to high temperatures affects the fuel ability to resist changes in physical and chemical properties. (17) Table 4 defines the common terms used in literature to describe gum formation in fuel.

Table 4 Vocabulary used to identify different types of gum in testing practice.

Expressions	Definition
Soluble gum	Non-volatile product left following fuel and toluene/acetone washing and evaporation. (56)
Insoluble gum	Product deposited to the sample flask after removing fuel, soluble gum, and any precipitates (calculated gravimetrically). (56)
Potential gum	Sum of the soluble and insoluble gum. (56)
Existent gum	Residue following aviation fuel evaporation, without any further treatment. (57)
Residual gum	Product collected after evaporation, distillation, filtration, or extraction. (58)
Washed gum	Heptane-insoluble, residue of gasoline fuel evaporation. (57)
Unwashed gum	Residue of motor gasoline and non-volatile additives evaporation. (57)

2.2.2 Nature and composition

Gum is believed to be one of the main precursors of post-combustion deposits on SI engines. During the combustion cycle, gum can react within the complex or combust to form solid carbonaceous materials, which in turn precipitate as deposits on engine metal surfaces. (36, 59) Several studies have discussed the

nature, composition, and adverse effects of gum and deposit formation on engine performance. (5, 17, 41, 60) Gum formation is a complex process and is affected by numerous factors. Temperature variations at engine surfaces and the actual surface chemistry play a major role in determining the nature and composition of the formed gum. For example, surface temperatures at the fuel injectors' tips are just over 100°C, whereas in the combustion chamber they may vary from 250°C to over 600°C at the exhaust valves. (5, 6, 8, 61, 62) Gasoline composition is also a key factor in gum formation. Certain compounds are notorious for increasing the tendency of gum formation in fuel. In increasing order, the following chemical families trigger the formation reaction: paraffins, naphthenes, iso-paraffins, aromatics, olefins, aromatic olefins, and diolefins. The presence of such compounds within the complex induce the oxidation reaction to occur, forming oxygenated products which in turn produce the undesired resinous gum either via thermal condensation or polymerisation reactions caused by free radicals in the system. (60) Other elements such as sulphur, nitrogen, and traces of metals can also act as a catalyst to the oxidation reaction. (5, 60) Details of the formation mechanism will be discussed in section 2.2.3. The oxidation reaction is also governed by the surface interactions between the metal surfaces and the produced particles. In a study conducted by Tseregounis, more particles were deposited on clean steel surfaces when compared to surfaces covered by thick oxide films. (36) The surface interactions are very poorly understood and thus remain an area requiring considerable research, especially to generate molecular level mechanistic insight. (5, 17)

The chemical composition of gum varies depending on fuel composition, formation process, and location inside the engine. IR spectroscopy and NMR have revealed that gum in gasoline fuel are highly aromatic compounds with a molecular weight in the range of 200 – 500 $g.mol^{-1}$. (17, 63) Moreover, elemental analysis confirmed the presence of oxygen, sulphur, nitrogen, carbon, and hydrogen in different concentrations. In a comparable study conducted on cracked naphtha, Kawahara illustrated that sulphur compounds present in the gum are mainly in the form of thioethers. Other components include dialkyl peroxides, hydroperoxides, ether and ester groups, acids, carbonyl, and hydroxyl groups. (64) However, it is important to mention that gum composition has changed drastically due to the strict legislations in controlling sulphur content in gasoline fuel. Current regulation states that sulphur content in unleaded gasoline and diesel fuels should not exceed 10 ppm. (65)

2.2.3 Formation and reaction mechanism

Gum in gasoline fuel is a product of the oxidation reaction occurring within the system. Unsaturated species such as olefins exhibit higher rate of oxidation among other constituents. (66) Several experimental studies have replicated the process of gum formation on metal surfaces to understand the reaction and attachment mechanisms. (35, 36, 60) In 1988, Tseregounis developed an oxidation rig to study thin deposit films from oxidised gasoline on steel surfaces. (36) The gasoline used was specially blended for deposition studies. (61) Full specification can be found in Table 5.

Table 5 Unleaded gasoline specifications for PFI testing. (61)

Property	Value
Octane number, (RON+MON) / 2	87 (min.)
Existent gum	5 mg/100 ml (max.)
Sulphur content	0.09 – 0.11 mass %
Olefins	20 – 25 vol %
Aromatics	30 – 40 vol %
Reid Vapour Pressure (RVP)	11.5 psi (max.)
Distillation	**10%** (60°C max.) **50%** (77 - 116°C) **90%** (185°C max), **100%** (205 - 225°C)

440C chromium steel coupons were used as a metal substrate. Prior to the experiment, coupons were polished with 6µm diamond paste on nylon cloth, using lapping oil as a lubricant. The oxidation rig setup and the experimental parameters are illustrated in Figure 8 and Table 6, respectively. The experimental setup consisted of a round bottom flask with a stirring rod, air inlet, condenser, and a thermometer. The stirring rod was attached to a coupon holder and rotated using an overhead stirrer. Prior to the experiment, the blend was heated to 100°C to remove lighter components and coupons were heated in air to 200°C. (36)

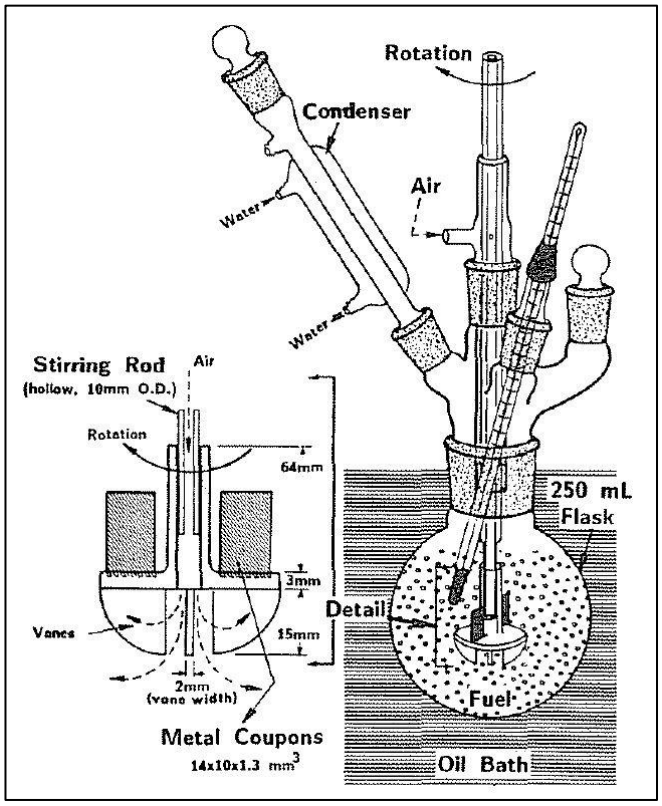

Figure 8 Experimental setup of the gum formation rig. (36)

Table 6 Experimental parameters of gum formation from oxidised gasoline fuel.

Condition	Value
Fuel temperature	100°C
Air flow rate	30 ml/min
Condenser fluid temperature	22 – 24°C (Water)
Experiment duration	24 h
Rotation speed	150 rpm
Fuel quantity	200 ml

Deposition of thin brown layers was observed on the metal substrates. The coupons were then placed in a desiccator for further analysis. Figure 9 shows the scanning electron microscope (SEM) image of the formed deposits.

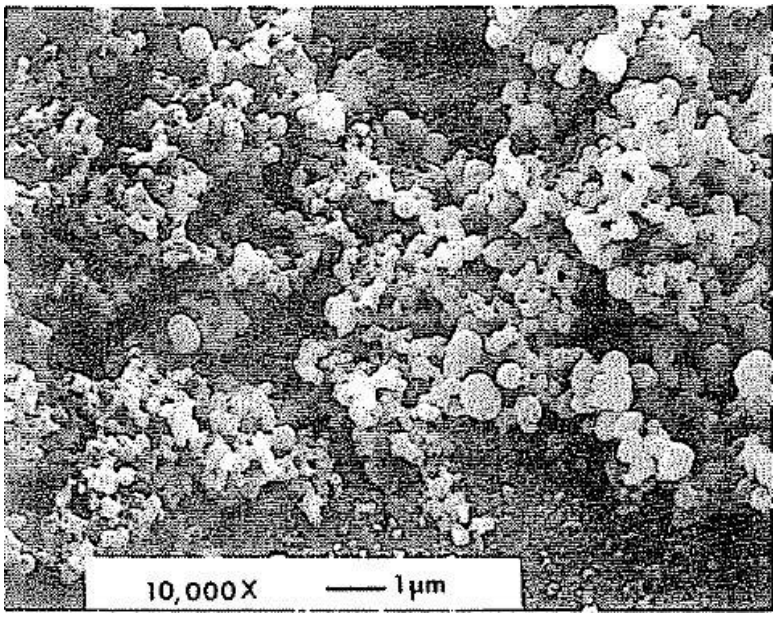

Figure 9 SEM image of deposits formed on a polished 440C steel surface. (36)

The outcome of this study confirmed the possibility of inducing gasoline fuel to undergo controlled oxidation reaction and to deposit resulted products onto steel surfaces.

Researchers have proposed different mechanisms of gum formation in hydrocarbon fuels. The general and current understanding is that the reaction undergoes several free radical chain processes, where the olefins react through the addition of peroxide radicals to the double bonds. (66, 67) Impurities such as moisture and metal ions in the fuel can catalyse the decomposition of the peroxides into radical species. (17) It was observed that the hydroperoxide formation reaction is extremely slow. However, once there is sufficient hydroperoxide within the system, the consequent formation of oxygenated products can be fairly fast; as alkyl radicals can also be an additional source to the hydroperoxide and peroxy decomposition. (68, 69) The overall mechanism of the reaction is usually described as follows:

Initiation: $RH \rightarrow R\bullet + H\bullet$ (1)

Propagation: $R\bullet + O_2 \rightarrow ROO\bullet$ (2)

$ROO\bullet + RH \rightarrow ROOH + R\bullet$ (3)

Termination: $R\bullet + R\bullet \rightarrow R - R$ (4)

$ROO\bullet + R\bullet \rightarrow ROOR$ (5)

$ROO\bullet + ROO\bullet \rightarrow$ Products (6)

Where ‘RH’ is unsaturated hydrocarbon (e.g. olefins), ‘R•’ is a free radical, ‘ROO•’ is the peroxy radical, and ‘ROOH’ is the hydroperoxide. Free radicals are formed from the unsaturated hydrocarbon, during the initiation reaction (step 1). During the propagation stage (steps 2 and 3), the free radicals react with oxygen to form a peroxy radical, which consequently reacts with another hydrocarbon molecule yielding additional free radicals into the system (chain process). The chain oxidation process continues until it is completed by one of the termination reactions (steps 4, 5, or 6). (17) A more detailed mechanism was proposed by Pereira et al. (70) where they showed a complete oxidation reaction for 2,4-hexadiene, a diolefin capable of forming allylic radicals ($H_2C=CH-CH_2R•$), which contributes significantly to gum formation in gasoline fuels. It was emphasised that the reaction force is governed by the stability of the allylic radicals. In other words, the longer the radical exists, the higher the potential of gum formation. (17, 70) The suggested mechanism was described as follows.

Initiation: $RH + ROO• \rightarrow ROOH + R•$ (7)

Propagation: $R• + O_2 \rightarrow ROO•$ (8)

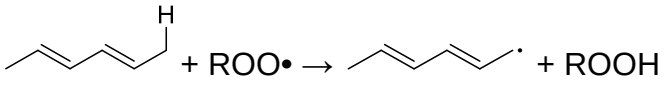

(9)

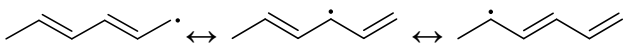
(10)

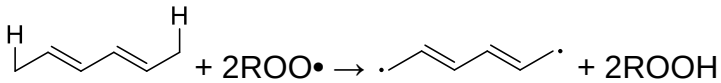

(11)

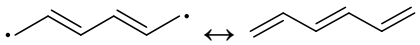
(12)

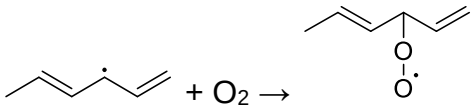

(13)

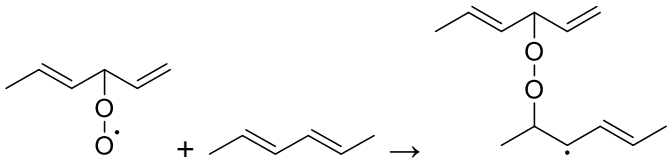

(14)

Termination: $ROO• + R• \rightarrow ROOR$ (15)

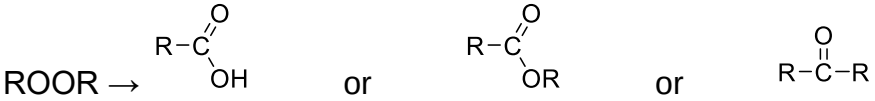

Although researchers have proposed several oxidation mechanisms for different species in gasoline fuel, the exact and overall gum formation mechanism is still an area of research.

2.2.4 Effects on emissions and engine performance

The adverse effects of gum formation and engine deposits are well established. Deposits at different locations within the engine result in various complications, which increase the difficulty to pinpoint problems and prime causes. Moreover, quantitative engine deposition tests (e.g. IVDA) are notorious for poor repeatability and reproducibility. However, significant efforts have been made to qualitatively explain the deposition effects. (41) There are three main locations where deposition mostly occurs: port fuel injectors, intake valves, and most critically the combustion chamber. The following table shows the most common effects noted in literature.

Table 7 Effects of deposit formation on engine performance and emissions.

Location	Effects on engine performance	Effects on emissions
Port fuel injectors (PFI)	Restricts fuel flow, causing major power disruption. (6, 8, 61, 71)	Disruption of fuel spray leads to an increase in CO levels as well as particulates and fuel consumption. (72, 73)
Intake valves (IV)	Reduces air flow to engine causing power loss. (8, 71)	Increase in combustion rates leading to an increase in NO_X emissions. (8, 74)
Combustion chamber (CC)	Deposits form hot spots due to heat stored during the combustion cycle. (41) Deposits occupy volume, which increases compression ratio. (41)	Deposits are estimated to increase bulk gas temperature by 50°C (heat transfer modelling), increasing NO_X by approximately 44%. (75)

2.3 Metal substrates

Surface interactions between fuel, deposits, and engine metals affect the deposition mechanism and, hence, deposition rate. Numerous studies have demonstrated how different metal substrates can interact with deposit particles within oxidised fuels. (35, 36) However, the detailed mechanism of surface interactions at the molecular level is still largely unexplored. (17) In most gum

formation studies, martensitic carbon/chromium stainless steel (AISI 440C) is used as a metal substrate due to its heat resistance and durability. (76) Elemental analysis showed the following chemical composition (36).

Table 8 Chemical composition of 440C steel coupons used in gum formation studies. (36)

Element	Mass %	Element	Mass %
Chromium, Cr	16.0 – 18.0	Phosphorous, P	0.040
Carbon, C	0.95 – 1.20	Sulphur, S	0.030
Silicon, Si	1.0	Molybdenum, Mo	0.75
Manganese, Mn	1.0	Iron, Fe	Max.77.98 (balance to 100)
Nickel, Ni	0.0		

Another metal grade used for similar applications is the AISI C1010, which has a lower carbon content in the range of 0.08 - 0.13 mass% and a high iron content (max. 98.86 mass%); as this grade does not contain chromium. (77) Metal coupons used for fouling and deposition studies usually come with a mounting hole at one end, pre weighed, blast finished, and stencilled with part number to facilitate robust workflows and recording of data. The following picture shows an example of C1010 coupons.

Figure 10 Back and front of AISI C1010 coupons. Dimensions: L: 14 mm, W: 9 mm. Mounting hole diameter: 3 mm, and thickness: 1 mm.

Since the fuel surrogate described in chapter 2.1 is a simple blend formulated primarily for systematic simulation studies, it was reasonable to use a basic metal substrate for this project. A common stainless steel (SS) grade used in hydrocarbon processes and applications (e.g. corrosion monitoring) is SS316. Elemental analysis of SS316 showed similar elements to that of 440C, but with

different composition (mass%). The following table illustrates the composition of a typical SS316 substrate (78). Figure 11 shows an example of the SS316 coupons used in this study.

Table 9 Typical chemical composition of a 316 SS coupon used in corrosion monitoring. (78)

Element	Mass %	Element	Mass %
Chromium, Cr	16.0 – 18.0	Phosphorous, P	0.045 max.
Carbon, C	0.08 max.	Sulphur, S	0.030 max.
Silicon, Si	0.75 max.	Molybdenum, Mo	2.0 – 3.0
Manganese, Mn	2.0 max.	Nitrogen, N	0.10 max.
Nickel, Ni	10.0 – 14.0	Iron, Fe	Max.62.00 (balance to 100)

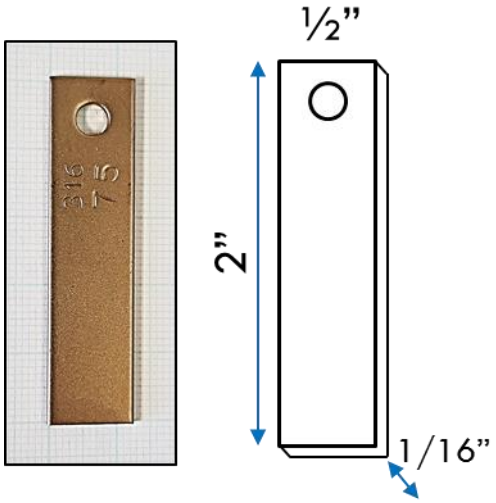

Figure 11 Unpolished 316 SS coupon used throughout this project, showing stencilled side (left) and dimensions (right).

2.4 Gasoline fuel additives

Gasoline fuel additives have been utilised since the 1920’s to improve fuel quality and engine performance. Examples of common commercial additives include corrosion inhibitors, anti-oxidants, deposit control additives, and octane boosters. (37) Other additives may be blended with fuels for legal purposes. For example, dyes and fuel markers are being added to distinguish and track fuels in an attempt to minimise fuel smuggling. (79) This section is devoted to discussing the fuel

additives utilised to control and minimise deposits and gum formation in gasoline fuels.

2.4.1 Deposit control additives

As stated previously, deposit formation on engine internal parts can harm engine performance, decrease fuel economy, and seriously affect the environment. Thus, control measures have to be in place. Engine deposits can be controlled by different methods, and the engine design can be a key factor in minimising material deposition. For instance, direct injection spark ignition (DISI) engines used to exhibit high levels of intake valves deposits. This issue was resolved by re-designing the exhaust gas recirculation system and oil flow down the valve stem. Another method of controlling engine deposits is to manipulate the fuel composition. For example, an increase in olefin and sulphur content generally leads to higher deposit formation rates. (60) However, it is often economically difficult to improve fuel quality by manipulating the composition. (41) As a result, the use of DCAs is the most practical solution to minimise deposit formation in SI engines, especially PFI and IV systems. (8, 71)

DCAs are usually applied in two modes, ‘clean up’ and ‘keep clean’. The former is used at higher concentrations to remove existing deposits accumulated in engines. It is believed that in this mode the additive associates with the deposits and eventually dissolves the soluble parts. A considerable fraction of additive is spent this way reactively and removed from the engine, and consequently, a higher concentration of the additive is needed to compensate for the lost amount. (27, 41) Once the ‘clean up’ mode has been applied for a sufficient period of time, typically 3 – 6 months, the DCA dosage is reduced to moderate ‘keep clean’ levels (< 200 ppm). (12, 41)

Several mechanisms were developed to explain the behaviour of DCAs in controlling deposition in SI engines. As illustrated in Figure 2, the general consensus is that the polar head groups are either attached towards the engine metal surfaces (i.e. forming a thin film) or to the gum molecules (i.e. forming a micelle), whereas the hydrocarbon tails are projected towards the fuel. (21, 27) Molecular weight (MW) of the additive is mainly dependent on the length of the hydrocarbon tail. It was reported that high MW additives (~ 1000 MW) exhibit better detergency in gasoline; as the long hydrocarbon tail allows for easier dissolution. On the other hand, additives of < 500 MW showed better adsorption on metal surfaces. (27)

The chemical composition of a typical DCA is consisted of a detergent as active ingredient, a carrier fluid, and a solvent. The active ingredients are in the form of a polymeric material consisting a polar head group and a hydrocarbon-soluble

tail. Common compounds used in DCA formulations include amino amides, polyether, polybutene amines (e.g. polyisobutylene amine, PIBA), and polybutene succinimides. Figure 12 shows the chemical structures for two of the most widely used active ingredients in DCA formulations. (80)

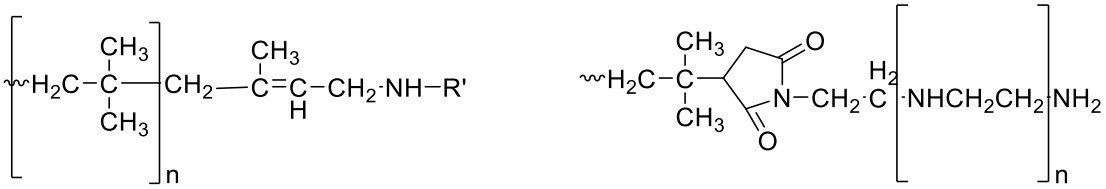

Figure 12 Chemical structures of PIBA (left) and polyisobutylene succinimide (right). (80)

Long chain alkylamines and di-amines (C_8 – C_{22}) are also widely used in the oil and fuel industry. Depending on their chain length, polar head, and degree of saturation, they can be applied as surfactants, corrosion inhibitors, gasoline and fuel oil additives, or even as asphalt emulsifiers. (81, 82) In gasoline fuels, primary amines with chain length of C_{18} such as octadecylamine (ODA, $C_{18}H_{39}N$) and 9-octadecenylamine (Oleylamine, $C_{18}H_{37}N$) are used as DCAs active ingredients or detergent precursors. (82, 83) Due to the simple composition of the gasoline surrogate formulated for this PhD project, it was preferable to use a primary amine as a detergent model rather than a polymeric surfactant such as PIBA. Moreover, upon reviewing the physical and chemical properties of ODA and oleylamine, it was found that ODA is more stable than oleylamine at ambient conditions (melting points = 53°C vs 21°C, respectively). (82) Therefore, ODA was chosen as a model detergent throughout this study.

2.4.2 Oxidation inhibitors

Gasoline refining processes such as thermal and catalytic cracking can result in high volume of olefinic components in the final product. The stability of olefins, and especially diolefins, is considered very low, as they can easily undergo aerobic or radical oxidation reactions, forming undesired oxidation products (gum). (66) Therefore, oxidation inhibitors are blended into gasoline fuels to compete with the gum formation kinetics, especially by neutralising free radicals in the system. Conventional active ingredients used as oxidation inhibitors are aromatic amines (e.g. phenylenediamine) and hindered phenols. (37) Anti-oxidants and DCAs can both be used to target gum and deposits precursors and consequently minimise engine deposits. (84) However, anti-oxidants do not act

as detergents to clean accumulated deposits on engine surfaces. Thus, anti-oxidants are mainly used to enhance storage stability of hydrocarbon fuels. (85)

2.5 Surface interactions

Several studies have discussed the adsorption behaviour and surface interactions of long chain alkylamines on various metallic and non-metallic substrates. (86-93) ODA (Figure 13) is a saturated, hydrophobic mono-amine capable of forming superhydrophobic layers that can act as corrosion inhibitors in oil pipelines and water desalination units. (82, 94, 95) To establish a complete understanding of known alkylamine adsorption behaviour and surface interactions, this section will now be divided into two main categories, namely structural orientation of adsorbed alkylamines (fundamental research) and adsorption behaviour on metal surfaces (applied research).

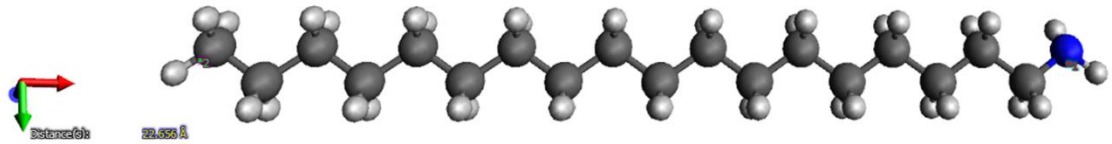

Figure 13 Geometry-optimised chemical structure of octadecylamine (ODA, $C_{18}H_{39}N$) showing a head-to-tail molecule length of approximately 22.7 Å. Carbon, hydrogen, and nitrogen are shown in black, white, and blue respectively.

2.5.1 Structural orientation of adsorbed alkylamines

The adsorption mechanism, including packing information, of long chain alkylamines on minerals was of a great interest to industrialists back in the period from 1960 into the 1980s. Particularly, mono-alkylammonium salts were widely used during the treatment process of silicates. (96, 97) Several techniques have been employed to investigate the surface interactions of alkylamines, including surface force, contact angle, and flotation recovery. It was found that at neutral and slightly acidic conditions, alkylamine molecules became ionised, whereas the surface became negatively charged, increasing adsorption potential. (98-100) However, the amine concentration plays a major role in surface adsorption. For instance, at low amine concentrations the surface is characterised by a low contact angle (i.e. low hydrophobicity) due to the poor structural packing of the amine ions at the surface. The area taken up by adsorbed amine on the surface was found to be greater than 134 $Å^2$/molecule, whereas the theoretical area needed for a close-packed monolayer is approximately 25 $Å^2$/molecule. (101-103) At such low concentrations, amine ions adsorb far apart from each other

and thus cannot maintain a hydrophobic state of the surface. Moreover, even at higher amine concentrations, where the electrostatic interaction between the amine cations and the negatively charged surface steeply increases, the surface is still poorly hydrophobic. (102-105) The poor hydrophobicity in such instances is attributed to the disordered packing of the amine molecules on the surface, which can be caused by steric hindrance between the hydrocarbon chains (tails) and the repulsion between the charged amino groups (polar heads). (96, 106) Only when the amine concentration at the interface surpasses the critical micelle concentration (CMC), molecules begin to orderly pack themselves and form a mono-layer at the surface; in which the head groups are attached to the surface and the hydrocarbon tails are oriented towards the liquid phase. (107, 108)

Structural orientation and adsorption behaviour of dodecylamine (C_{12}) and hexadecylamine (C_{16}) on silicate quartz (SiO_2) were evaluated in (96) using XPS and FTIR spectroscopy. The quartz substrates were treated with dodecylamine-acetate (DAAc) and hexadecylamine-acetate (HAAc) solutions for 5 min. It was found that at low amine concentrations, surface silanol groups (SiOH) interacted with the amine head groups via hydrogen bonding ($R\text{-}NH_3^+$- - -OHSi), at concentrations insufficient to form a densely packed mono-layer of ordered material on the surface (Figure 14, region II). The point at which a dense, ordered mono-layer is formed on the surface was referred to as the critical hemimicelle concentration (CHC). At the CHC point, molecular as well as protonated amines were adsorbed onto the surface, with the hydrophobic hydrocarbon tails oriented outward and upright at an angle of ~30°, which increases surface hydrophobicity. At concentrations greater than the CHC point, amine precipitation beyond a mono-layer occurs and bulk molecular amine starts to pack on the surface (Figure 14, region III). The surface elemental composition on the quartz substrates was quantified using XPS analysis. Substrates treated with DAAc (C_{12}) solution showed higher carbon and nitrogen content in comparison to those treated with HAAc (C_{16}) solution, despite containing the same amine concentration of 0.2 mM. Table 10 lists the XPS data obtained for the adsorbed amines on the studied substrates. (96)

Table 10 XPS binding energy (B.E) and concentration of carbon and nitrogen on the quartz surfaces as a function of amine solutions. (96)

Element	DAAc (at%)	B.E (eV)	HAAc (at%)	B.E (eV)
Carbon (C 1s)	43.08	285.0	33.1	285.0
Nitrogen (N 1s)	1.23	400.1	0.64	399.5
			0.54	401.4

The observed carbon (C 1s) emission at a binding energy around 285.0 eV in XP spectra (Table 10) stems from aliphatic C-C in the hydrocarbon chains. (109, 110) The nitrogen (N 1s) peak at 400.1 eV observed on the surface treated with DAAc arises from amine head groups (NH_2). (86, 111) A shift in N 1s binding energy to about 401.4 eV indicated protonation on the surface (NH_3^+). (86, 90, 93, 112, 113) Such chemical speciation has indicated that at equal concentration of amine solutions (0.2 mM), C_{16} molecules have adsorbed via hydrogen bonding and formed a hydrophobic mono-layer on the surface. The presence of molecular amine groups (NH_2 at 400.1 eV) as well as the higher carbon content on the surface treated with DAAc solution was indicative of admicelles formation on the surface. Other studies have postulated that further molecular amine precipitation could lead to the formation of other admicelles (bilayers) or even full micelles on the surface, especially in the case of shorter chain lengths (C_{10} – C_{14}). In such cases, polar, hydrophilic head groups could be oriented towards the solution and thus the surface would revert to and/or stay in a hydrophilic state. (102, 114, 115)

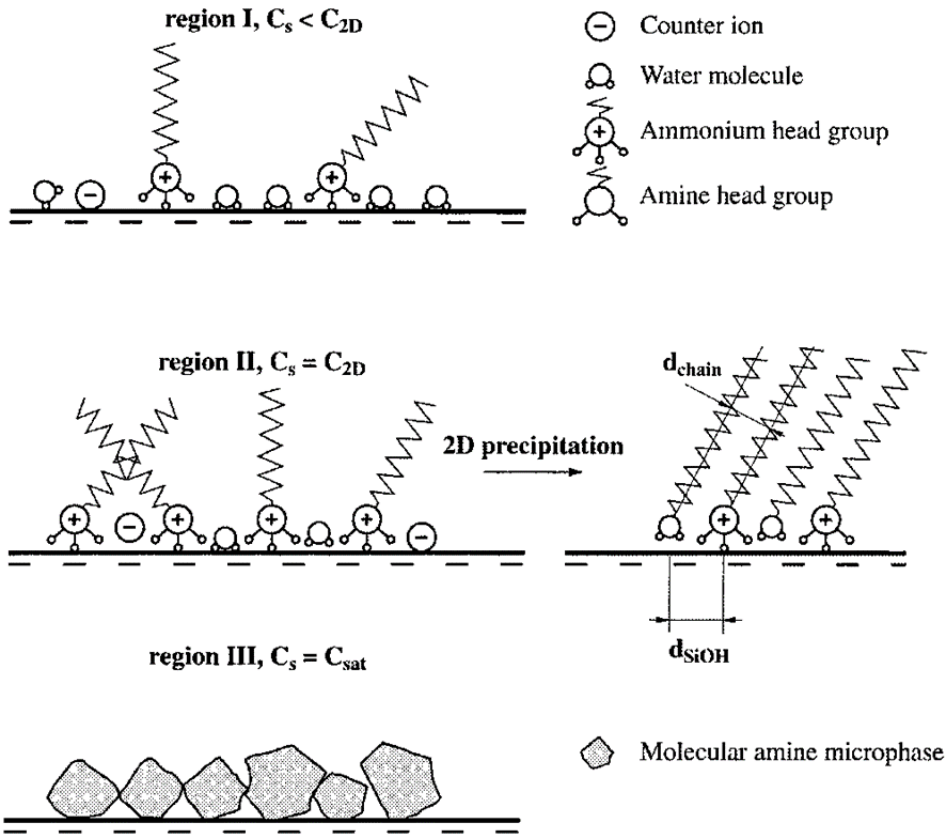

Figure 14 Schematic representation of long chain alkylamines adsorption on silicate quartz as depicted in (96). Regions I, II, and III represent amine concentrations below, at, and above the CHC point respectively.

Similar, but more recent, work was conducted on ODA (C_{18}) to investigate its packing information and adsorption behaviour on mica surfaces, using XPS and ATR-FTIR spectroscopy. (86) Nitrogen-free, double cleaved mica substrates were immersed in a 15 mM ODA/chloroform solution for 1 minute. Once removed, they were allowed to dry under dry N_2 for 2 – 3 min and then to ripen in contact with air from few hours to 7 days. (86, 116) Structural packing information retrieved from IR spectroscopy was complemented by molecular dynamic (MD) simulations. Analysis revealed that self-assembled ODA mono-layers were orderly packed with a tilt angle (θ) of 15 – 20° (Figure 15). Adsorption mechanism and findings from this study were in agreement with the observations discussed above for C_{16} molecules. In particular, XPS analysis confirmed the presence of protonated amine species ($-NH_3^+$ at 401.7 eV) on the surface of all samples, regardless of amine concentration or ripening time. Authors, however, postulated adsorption via acid-base reaction with adsorbed water layer on the surface. (86)

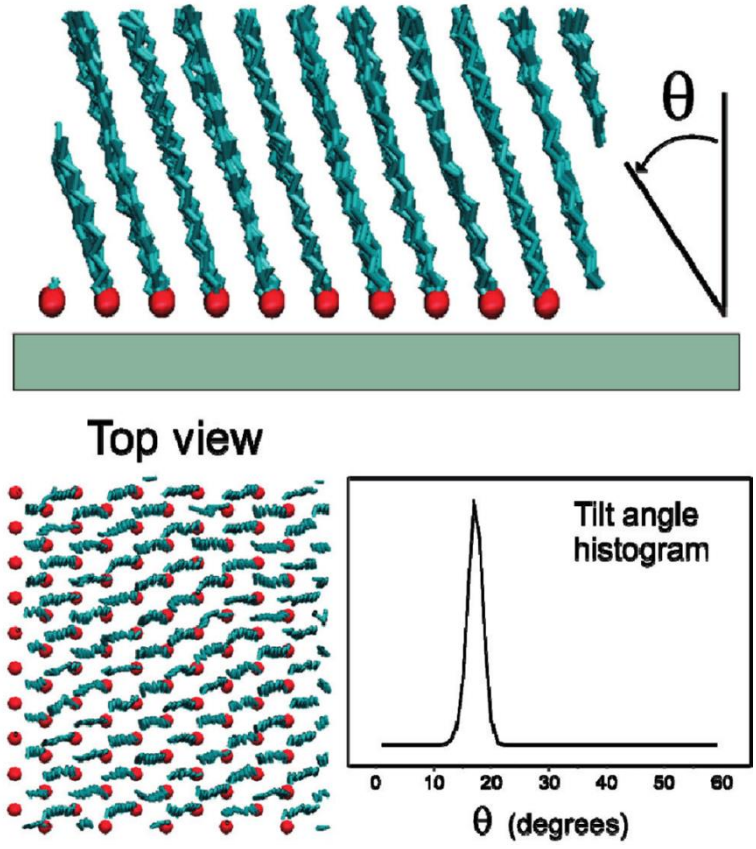

Figure 15 MD simulations output showing ordered arrangement of ODA molecules on a flat surface with intermolecular distance of 4.7 Å. (86) Polar head (NH_2) and CH_n groups are represented as red spheres and green bonds, respectively.

Fundamental studies on long chain alkylamines (≥ C_{12}) have shown a positive affinity towards adsorption and formation of ordered structures on mineral-based surfaces. In industrial and chemical processing applications, formation of such hydrophobic layers via grafting of film-forming amines can provide robust surface protection in corrosive environments. (117, 118) Thus, it was of great interest to review the mechanistic effects of film-forming amines from a more applied perspective to the oil and gas industry.

2.5.2 Adsorption on metallic surfaces

Several studies have employed surface and near-surface characterisation by XPS, ATR-FTIR, and SEM to investigate the adsorption behaviour of alkylamine self-assembled mono-layers on stainless steel and other iron-based surfaces. (119-121) In a study conducted on 316L stainless steel, long chain alkylamines (C_{10}, C_{12}, C_{16}, and C_{18}) were dissolved in various polar and non-polar solvents including isopropanol, toluene, ethanol, and hexane. (119) Mechanically polished substrates (average surface roughness ca. 0.03 µm) were then immersed in solutions for times ranging from 30 min – 3 h, at room temperature. All coating processes were conducted under a nitrogen blanket. FTIR characterisation of the coated surfaces showed stronger -CH_2- and -CH_3 (2800 – 3000 cm^{-1}) absorption bands as a function of amine chain length (Figure 16), which indicates effective coating. XPS analyses were performed on the coated surfaces to gain a better understanding of the adsorption behaviour at atomistic levels. The substrate coated with ODA (C_{18}) was compared to a blank substrate and found to exhibit different features, especially in the nitrogen (N 1s) region (Figure 17). Immersion in ODA-containing solution resulted in an increase in intensity of the -NH_2 peak at 400.5 eV and a distinctive shoulder at 397 eV, which was assigned to nitrogen bound to the metals (i.e. Cr-N and Fe-N) at the substrate. (122) Other studies have attributed the observed shoulder to chemisorption of nitrogen-containing compounds to Cr and Fe. (111, 123, 124) The build-up in nitrogen intensity was accompanied by an increase in carbon (C 1s) content and an attenuation in substrate elements (Cr and Fe). Contact angles of deionised water were measured on the polished reference substrate and compared to those coated with C_{10}, C_{12}, C_{16}, and C_{18} alkylamines. Indications of a hydrophobic effect of the coatings were observed. Advancing contact angles on the bare reference were 45° ± 2°, whereas values measured for the coated coupons were 90° ± 2°, 92° ± 2°, 104° ± 2°, and 109° ± 1° for C_{10}, C_{12}, C_{16}, and C_{18} molecules (in hexane), respectively. (119) Although quoted measurements agree in principle with literature values reported elsewhere (111, 118, 125), the alkylamine

concentration in solution was believed to be extremely high (50 mM), which may have resulted in physical precipitation of bulk amines, rather than chemisorption on the surface. Nevertheless, the obtained FTIR and XPS data presented evidence that supports substrate immersion as a viable 'surface coating' technique. Other studies have also adopted this method (113, 126) and thus it was considered throughout this PhD.

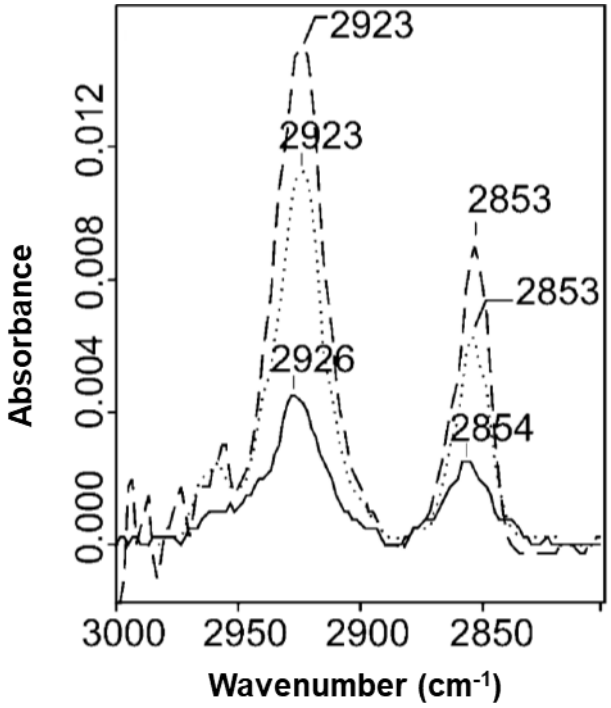

Figure 16 ATR-FTIR spectra of stainless substrates coated with alkylamine films of different chain lengths. Spectral lines represent $C_{10}NH_2$ (solid), $C_{12}NH_2$ (dotted), and $C_{16}NH_2$ (dashed). (119)

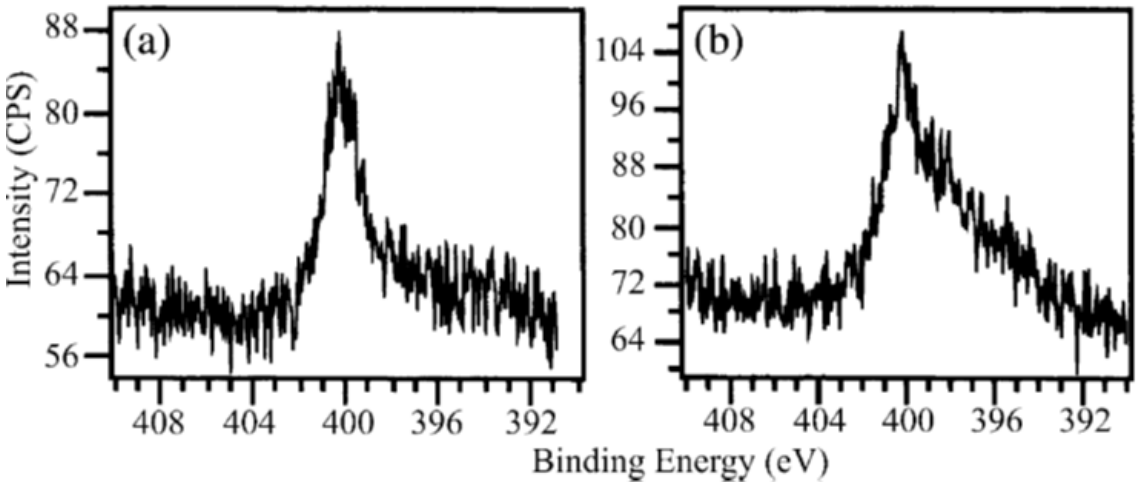

Figure 17 N 1s XPS spectra of **a)** the reference stainless steel substrate compared to **b)** the ODA coated surface, showing appearance of an Fe-N shoulder around 397 eV. (119)

Superior coating methods such as magnetron sputtering (90) or plasma polymerisation using monomeric organic molecules (127, 128) have been employed in other adsorption studies. In a study conducted to investigate the adsorption behaviour of hexadecylamine (C_{16}) at the iron oxide-oil interface (90), the use of reactive magnetron sputtering allowed for the iron oxide layer to be uniformly sputtered on a silicon substrate to a thickness of 20 nm. Such level of precision in surface sensitive applications is extremely valuable; as it allows for accurate quantification and better understanding of the studied systems. In the hexadecylamine study, a combination of a solution-depletion isotherm and XPS measurements was performed to explore the solid-liquid interactions and adsorption behaviour as a function of concentration. (90) The adsorption isotherm of deuterated hexadecylamine was found to be steeply increasing with concentration until it reached a plateau at approximately 1×10^{-3} M. The adsorbed layer thickness was determined to be 16 ± 3 Å at lower amine concentrations (1.03×10^{-4} and 4.18×10^{-4} M) and 20 ± 3 Å in the steady state ($[amine]_c \approx 1 \times 10^{-3}$ – 2.5×10^{-3} M), at maximum surface coverage (adsorbed area $\approx 3 \times 10^{-6}$ $mol.m^{-2}$). Adsorption via protonation was also evident upon investigating the surface by XPS. The nitrogen (N 1s) spectrum revealed the distinctive peak of protonated amine species ($-NH_3^+$) at a binding energy of about 401.1 eV. Geometric calculation based on the surface thickness at the plateau and a chain length of 21.5 Å revealed a tilt angle for the hydrocarbon chain of approximately 22° (90), which can be compared to the tilt angle range of 15 – 20° measured for ODA in (86).

One limitation to adsorption on metallic surfaces is the instant formation of oxide layers upon exposure to atmosphere. (129) Researchers have dealt with such limitations in various ways. For instance, an attempt was made to electrochemically reduce the substrates used in (119) to minimise the oxide levels on the surface. Walczak et al. designed an oxygen-free system and attached it to the XPS instrument to prepare and analyse the samples in the least oxidised state. (129) Argon-ion etching under vacuum (XPS) is another effective method to obtain oxide-free surfaces. (130) On the other hand, other studies have demonstrated that the formed oxide layers are of distinctive and characteristic features of the real-world systems, which in turn allowed for accurate determination and quantification of features arising from other adsorbed layers. (131, 132) Although minimising post-immersion oxidation was demonstrated to be feasible in XPS applications (129, 130), it was impractical to adopt such methods throughout this PhD.

Chapter 3 Experimental materials and methods

3.1 Materials

Tables 11-12 list all chemicals and materials used throughout the research reported in this dissertation.

Table 11 Description of the chemicals used for TRF formulation and oxidation.

Chemical	Supplier	Description (Purity%)
Toluene	Sigma Aldrich	Certified AR for analysis (99.8%)
n-heptane	Fisher Scientific	B.P. 98°C (99%)
Iso-octane	Fisher Scientific	B.P. 98-99°C (99%)
1-pentene	Fisher Scientific	Acroseal (97%)
1-octene	Sigma Aldrich	100 ml. (98%)
2,4-hexadiene	Fluorochem	25 ml mixture of isomers (95%)
Tertiary butyl hydroperoxide (tBHP)	VWR Int.	70% solution in water
Octadecylamine	Sigma Aldrich	25 g (99% GC)
Thermal fluid (H335)	Julabo	Range = +40°C to +335°C

Table 12 Description of the materials used in preparing and polishing the SS substrates used in the gum adsorption experiments.

Material	Supplier	Description (Dimensions)
Stainless steel (SS) coupons	Rose Corrosion Services Limited (RCSL)	Strip weight loss coupons in 316 SS (L=2" x W=0.5" x H=0.0625"). Pre weighed, pre numbered, blast finished. Each packed in a VCI envelope with 1x (Ø=0.1875" clearance) mounting hole at one end, centred at 0.25" from end.
Silicon carbide grinding papers	MetPrep	Adhesive backed discs (Ø=8"). Grit size P120, P320, P600, and P1200.

Material	Supplier	Description (Dimensions)
Polishing cloths	Buehler	Magnetic backed discs (Ø=8"). MicroFloc.
Aquapol-P diamond suspension	Kemet	Water-based polycrystalline (3 µ).
Polishing and finishing cloths	Arco	Automax rolled sheets (L=36 cm, W=26 cm, weight=60 gsm).

3.2 Experimental

3.2.1 TRF oxidation setup

The TRF oxidation rig (Figure 18) consisted of a 3-neck round bottom flask, a thermometer, an adjustable Drechsel bottle head, a double surface condenser, an air pump (max. flow rate 120 l/hr), an oil bath, a heating and stirring plate, and a chiller (Thermal Exchange CS20).

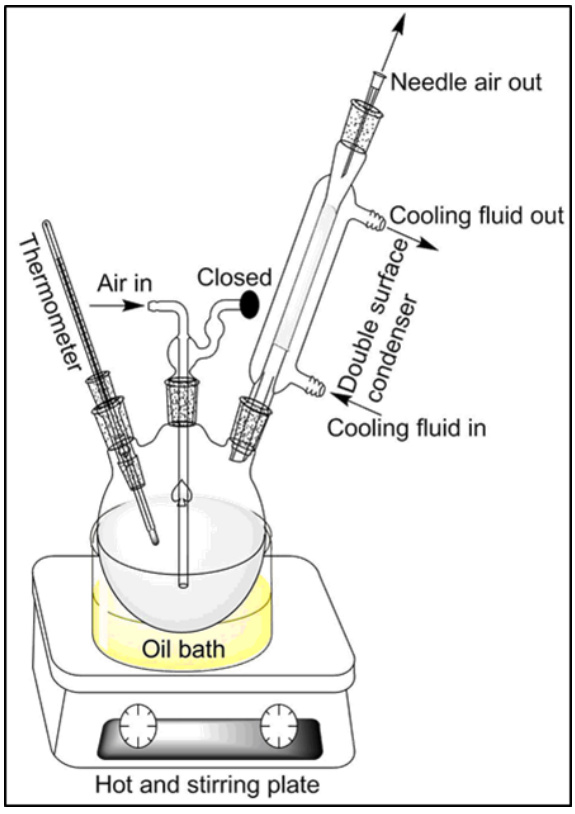

Figure 18 Single-batch TRF oxidation rig which connects to an air pump to bubble air through at a rate of 60 ml/min, via the air inlet at the top of the Drechsel bottle head.

Experimental conditions during the single-batch TRF oxidation process were as follows.

Table 13 Conditions chosen for the TRF oxidation process

Condition	Value
Oil bath temperature	85°C (mono-olefins) 75°C (diolefins)
Air flow rate	60 ml/min
Condenser fluid temperature	10°C (95:5 Water:Ethylene glycol)
Experiment duration	48 h
Blend quantity	100 ml

The process was optimised by using a Radley Carousel 6 Plus Reaction Station™ (Figure 19) to perform six parallel oxidation reactions. The instrument was manually fitted with 1/16" PTFE Teflon tubes to allow for uniform air-bubbling in all flasks. It was also fitted with needle outlets to ensure pressure equilibrium throughout the reaction time. The station was placed in a fume hood to ensure no off-gases were released into the laboratory.

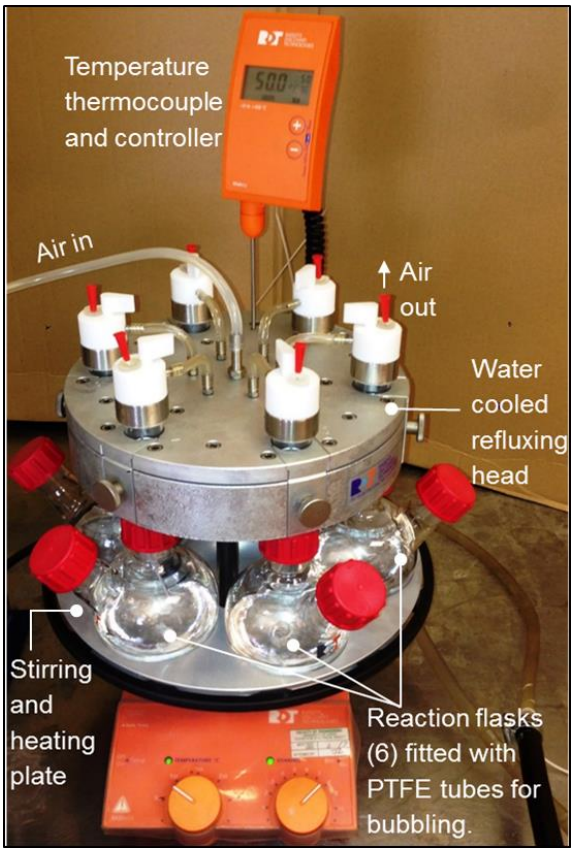

Figure 19 Radley multi-batch reaction system.

3.2.2 Gum content tests

Quantification measurements of the oxidation products (gum) were done using a modified lab-scale ASTM D381 (Standard Test Method for Gum Content in Fuels by Jet Evaporation). (57) Once the TRF oxidation experiment was terminated, 50 ml of the oxidised TRF was collected in a beaker and placed in an oil bath at 120°C for approximately 30 – 45 min (Figure 20). The beaker was weighed before and after the experiment to determine the gum content. All calculations were done as per the equations stated in the ASTM D381 standard method.

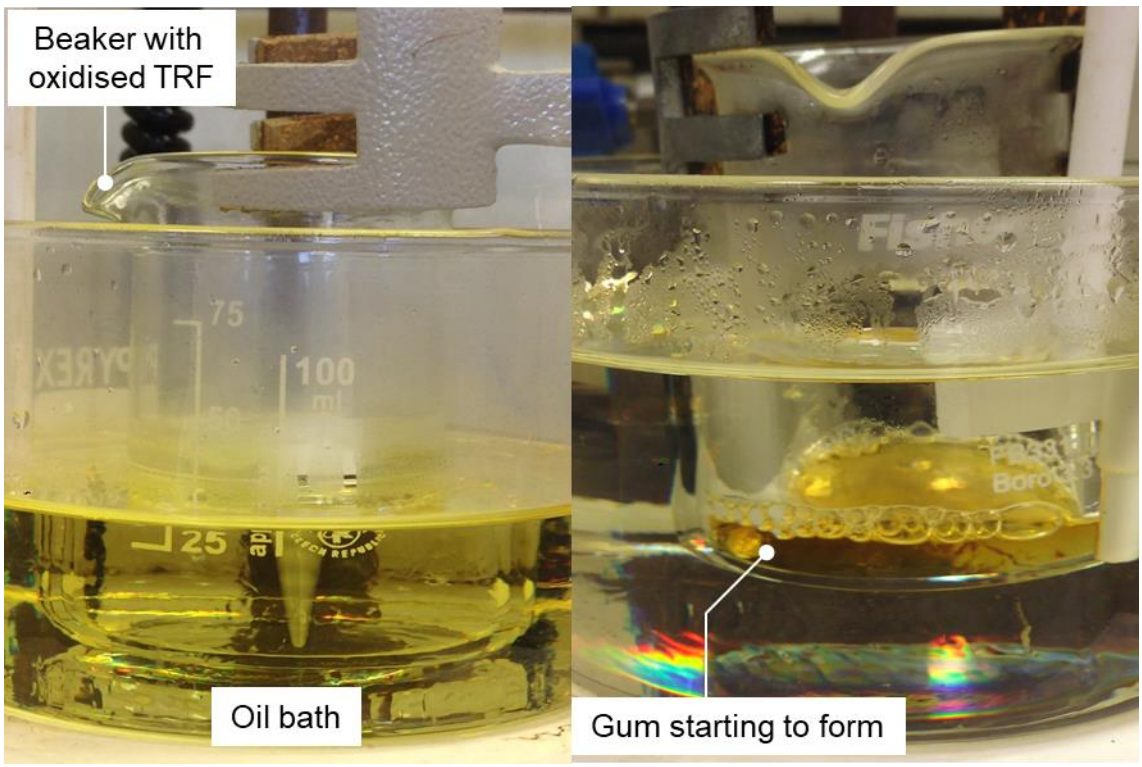

Figure 20 Gum content evaluation setup showing oxidised TRF at different stages during the evaporation process. Gum appeared at the bottom of the beaker as a brown resinous material.

3.2.3 Gum adsorption experiments

3.2.3.1 Preparation for SEM/EDX and XPS measurements

Gum adsorption experiments conducted for the short studies described in sections 5.4.3 and 5.4.4, later in this thesis, were performed by immersing five stainless steel substrates in oxidised TRF blends containing various ODA concentrations (zero, 50, 500, 1000, and 2000 ppm w/v). Immersion was performed in a fume hood at room temperature for 10 s. Once a coupon was taken out, it was left to dry in the fume hood prior to analysis. No further treatments were performed.

3.2.3.2 Preparation for XPS studies

Adsorption experiments conducted and described in sections 6.3.1, 6.3.2, and 6.3.3 were performed by immersing 1 x 1 cm^2 stainless steel substrates in TRF blends for 24 h, at room temperature. Composition and components concentrations varied depending on the objectives of the experiment. Full details are described in the relevant sections. Once taken out, substrates were soaked a few times in neat TRF to remove any heavy polar hydrocarbon residue on the surface. Finally, substrates were rinsed with heptane to remove any nonpolar residues. Such treatment allowed for better analysis to the chemisorbed species.

3.3 Analytical and characterisation techniques

3.3.1 Attenuated total reflectance – Fourier transform infrared (ATR-FTIR) spectroscopy

Reference materials and TRF blends, both neat and oxidised, were analysed using a Thermo Scientific Nicolet iS10 FTIR Spectrometer equipped with a Diamond/Zinc Selenide (ZnSe) ATR sampling accessory. Briefly, the IR source provides a light beam, focused via several mirrors, which illuminates the sample. The amount of absorbed light is determined as shown in Figure 21. Knowledge of absorbed and incident beam intensity determines the absorbance (A) or percentage transmittance (%T) as a function of the light wavelength (400 – 4000 cm^{-1}). Characteristic peaks correspond to specific molecular vibration frequencies. FTIR spectroscopy was a primary technique throughout this PhD; as it is capable of fast turnaround and providing quick analysis of the influence of experimental variations on samples.

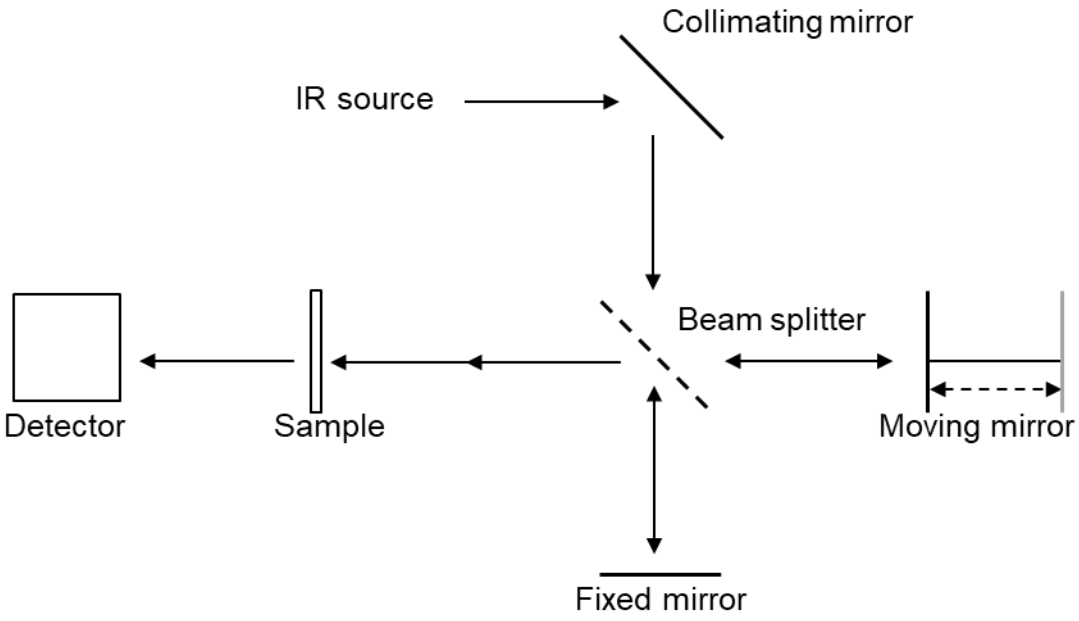

Figure 21 Schematic diagram of the basic principle of FTIR spectroscopy. (133)

The absorbance (A) is calculated using the following equation. (133)

Equation 6

$$\mathrm{A} = \log_{10}\left(\frac{I_0}{I}\right) = log_{10}(I_0) - log_{10}(I)$$

Where 'I_0' is the incident light intensity and 'I' is the transmitted light intensity.

Spectra can also be plotted as percentage transmittance (%T).

Equation 7

$$\%\mathrm{T} = 100 \text{ x } (\frac{\mathrm{I}}{\mathrm{I_0}})$$

In ATR-FTIR applications, the IR beam travels through a crystal of high refractive index (n_c) into the sample which has a lower refractive index (n_s) (Figure 22). The difference in refractive indices results in light internal reflectance depending on the incidence angle (θ_i). If the incidence angle is small, the light will partially reflect internally creating an angle of reflectance (θ_r) as well as a refracted beam, which travels through the sample. The angle the refracted beam travels against the surface normal is called the angle of refraction (θ_R). The relationship between θ_i and θ_R is proportional. (134) However, at certain θ_i angles, θ_R becomes 90° which results in no refracted beam to travel through the sample. Hence, the term total internal reflectance was introduced. The minimum θ_i which allows for internal

reflectance is called critical angle (θ_c). In other words, internal reflectance occurs whenever $\theta_i \geq \theta_c$. The critical angle (θ_c) correlates to the refractive indices of the crystal (n_c) and sample analysed (n_s) in accordance to the following equation. (133)

Equation 8

$$\theta_c = \sin^{-1}\left(\frac{n_s}{n_c}\right)$$

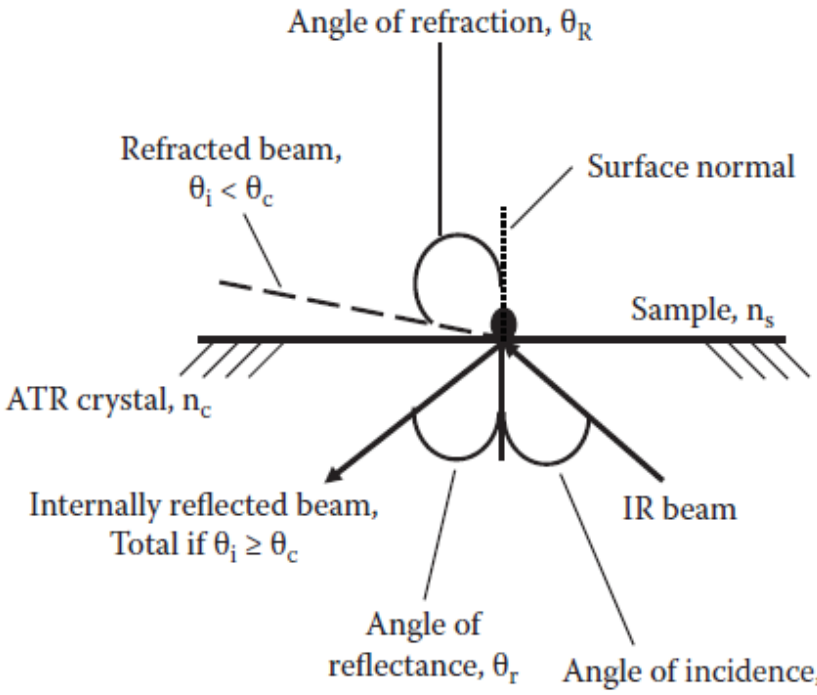

Figure 22 Schematic diagram representing the basic principle of ATR internal reflectance. (133)

3.3.2 Gas chromatography coupled with mass spectroscopy (GC-MS)

3.3.2.1 Validation of the TRF formulation method

TRF blending was verified via GC-MS analysis using a PE Clarus 500 GC and PE Clarus 560S MS, with a 30 m long column (PE Elite 5 ms, 250 µm I.D). GC-MS is a technique used to separate components using a temperature-controlled column and detect the fragmented species using a mass spectrometer. The resulted chromatogram quantifies components within the sample (i.e. area under the curve) against the time taken for each component to travel through the

separation column and reach the detector (i.e. retention time). For accurate quantification, parameters in Table 14 were applied to the method detailed in Table 15 in order to calibrate the instrument and analyse the studied systems. All calibration standards were prepared by adding 10 µl of sample to 1 ml of n-pentane followed by 5 µl of n-decane as an internal standard.

Table 14 Parameters of GC-MS method developed to characterise the TRF blends.

Carrier Gas	Flowrate	Split ratio	Injection temperature	Temperature
Helium (He)	1 ml/min	50:1	200°C	40°C, 6min, 100°C at 20°C/min, 3min

Table 15 GC-MS calibration standards composition in volume percentage.

Blend no.	Toluene	Iso-octane	n-Heptane	Sample type
1	10	45	45	Reference
2	50	25	25	Reference
3	90	5	5	Reference
4	45	10	45	Reference
5	25	50	25	Reference
6	5	90	5	Reference
7	45	45	10	Reference
8	25	25	50	Reference
9	5	5	90	Reference
10	62	19	19	Check sample

Based on this method, the composition of the prepared TRF blends was validated, indicating a composition of 61.02, 19.30, and 18.95 vol% for toluene, iso-octane, and n-heptane, respectively. This shows excellent correlation between actual and calculated compositions. The calibration curves for the reference materials can be found in the appendices (Figure A 1, Figure A 2, and Figure A 3).

3.3.2.2 Characterisation of oxidation products (gum)

1 mg of gum was dissolved in 1 ml of acetone and analysed using a HP 6890/5973 GC-MS with the method summarised in Table 16.

Table 16 Parameters of the GC-MS method developed to characterise the gum product.

Carrier Gas	Flowrate	Split ratio	Injection temperature	Temperature profile
Helium (He)	2.6 ml/min	100:1	250°C	40°C, 5min, 200°C at 12.5°C/min, 17min

3.3.3 Ultraviolet and visible (UV-Vis) spectroscopy

UV-Vis spectroscopy is an analytical technique used to characterise materials based on their ability to absorb light waves. In simple terms, a light source is used to radiate electromagnetic waves in the visible region of the electromagnetic spectrum (390 – 780 nm). A monochromator is then used to separate the lights into different wavelengths, which transfer through the sample. Depending on the sample material, an aliquot of light gets absorbed and/or scattered. Spectrophotometer detectors then measure the intensity of the transmitted light (I) and compare it to the original intensity (I_0). A reference material can be used to remove background absorption (e.g. by air) from the sample spectrum. (135)

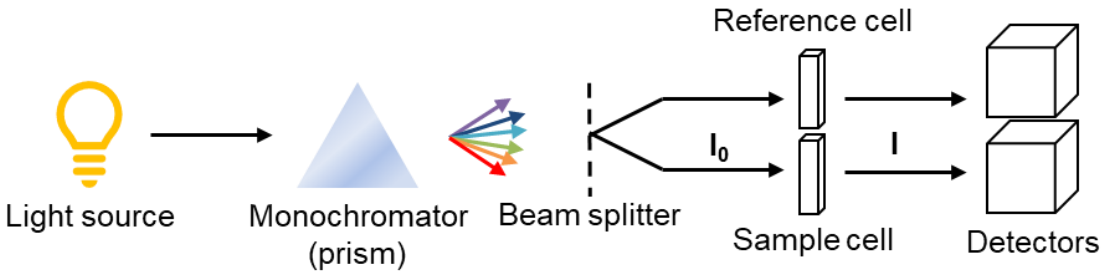

Figure 23 Schematic representation of the basic principle of a UV-Vis spectrometer. (136)

The ratio between the light intensities before and after the analysed sample (I/I_0) can be calculated as a percentage transmittance (T). However, UV-Vis spectra are conventionally plotted as absorbance (A) over wavelength. Absorbance, which is a dimensionless quantity, can be calculated as per the following equation. (135)

Equation 9

$$A = -\log(T)$$

In all UV-Vis measurements conducted in this study, approximately 2 ml of sample was placed in a rectangular 3.5 ml quartz cuvette (Agilent Technologies 5061-3387), using glass Pasteur pipettes. The cuvette was rinsed with toluene three times between runs to ensure no cross contamination between samples.

3.3.4 Thermogravimetric analysis (TGA)

TGA is an analytical technique in which the mass of a sample is monitored via a very sensitive balance as a function of sample's temperature or heating time. Temperature profile can be recorded as a function of constant heat rate introduced to the sample (dynamic measurement) or as a function of a specific temperature the sample is held at (isotherm measurement). TGA results are conventionally plotted as mass percentage against time or temperature. The first derivative of the TGA curve with respect to time (or temperature) usually complements the TGA data by showing the mass change rate. The resulting curve is denoted as differential thermogravimetric (DTG) curve. Sample mass changes as it interacts with the surroundings in the presence of temperature and processing gas. This change leads to steps in the TGA curve and events (or peaks) in the DTG curve. (137) Methods and details of processing gases used in this study are described in chapter 4.3.4.2.

3.3.5 Dynamic light scattering (DLS)

In colloidal and suspension systems, DLS is a powerful technique used to determine the size, size distribution, and shape of the studied particles. The technique uses a monochromatic laser beam to hit the particles and create scattered light. The change in wavelength between the scattered and unscattered light provides information about size, distribution, structure, and shape of the particles. (138) In all DLS measurements conducted in this study, approximately 2 ml of sample was placed in a rectangular 3.5 ml quartz cuvette (Agilent Technologies 5061-3387), using glass Pasteur pipettes. The cuvette was rinsed with toluene three times between runs to ensure no cross contamination between samples.

3.3.6 Contact angle

Contact angle (θ) and diameter (d) of deionised water droplets on polished 316 stainless substrates were measured using a pendant drop camera (KSV Modular CAM200 Optical Angle) and a Surface Tension meter with a Sensirion sensor and a Firewire camera. A single water droplet was placed on the substrate using Hamilton 10 µl syringe with cemented needle of 22s gauge. Images were taken at a fast rate of 1 frame/second. Analysis was performed using Biolin Scientific software (Attension® Theta).

3.4 Surface analysis techniques

3.4.1 Scanning electron microscopy (SEM) with energy-dispersive analysis of X-rays (EDX)

SEM is a microscopic imaging technique capable of providing information on the morphology, topography, and sometimes also crystallographic properties of the sample. In comparison to optical microscopy (OM), magnification in SEM applications can be orders of magnitude higher ($2x10^6$x vs 500 – 1500x) with a resolution down to 0.4 nm, compared to 0.3 µm in OM. SEM utilises a focused electron beam to scan samples and interact with electrons. Following this interaction, beam electrons undergo elastic and inelastic scattering. Electrons exhibiting elastic scattering change their direction, but they do not lose energy, whereas inelastically scattered electrons do lose part of their energy. Other effects of the interaction between the electron beam and the sample include emission of secondary electrons, backscattered electrons, and X-ray emissions. Emission of secondary electrons is the most reoccurring effect and thus contribute the most to the SEM imaging signal. As the name suggests, backscattered electrons are being reflected as a result of the elastic collision between the electron beam and the atom. Intensity of the generated signal is then displayed as a black and white image, depending on the atomic weight of the detected element. The heavier the element, the brighter the region. (139)

In EDX spectroscopy, the incident energetic electrons excite electrons in atomic core levels. The decay of these excited states generates characteristic fluorescent photons in the X-ray range. The wavelength of the emitted X-rays is characteristic for the chemical element and thus can be used for elemental microanalysis. The resolution of the output spectrum depends on the energy of the emitted X-rays as well as the atomic weight of the detected element. Generally, elements with higher atomic number generate stronger EDX signals

due to higher probabilities of core hole decay under emission of fluorescent photons. (140-142)

The instrument used for SEM/EDX analysis in chapter 5.4.3 was a Carl Zeiss EVO MA15 (Tungsten gun) coupled with Oxford Instruments AZtecEnergy EDX system with 80 mm X-Max silicon drift detectors (SDD) for secondary and backscattered imaging and EDX elemental mapping. Samples were mounted on standard specimen stubs using double sided carbon tape and analysed at accelerating voltage of 5 kV.

3.4.2 X-ray photoelectron spectroscopy (XPS)

XPS is a surface sensitive technique based on the photoemission principle, with X-ray photons exciting electrons from the valence and core levels of atoms (Figure 24). Due to the high cross section for inelastic losses and re-absorption in condensed matter, only photoelectrons generated near the surface (i.e. 20 – 50 Å) are capable of escaping without energy loss. (143) The binding energy of each atomic core level is characteristic for each element, permitting elemental analysis through quantitative analysis of the intensities of the characteristic photoemission lines. For a given photon energy, the binding energy (B.E, E_B) can be, in a first approximation, calculated as the difference between the photon energy and the measured kinetic energy (K.E., E_K) of the detected photoelectrons. The electron spectrometer is designed to provide a high resolution spectrum of the photoemission line intensities (plotted as absolute counts or counts per seconds, CPS) as a function of the kinetic energy. Conventionally, the photoelectron spectra are therefore plotted as intensity as a function of electron energy (either the measured kinetic energy or, more commonly, the derived binding energy), calculated via (144)

Equation 10

$$\mathrm{B.E} = \mathrm{h}\nu - \mathrm{KE} - \mathrm{W}$$

‘W’ is the spectrometer work function, which represents the difference between the Fermi level and the vacuum level. It can be determined spectroscopically by measuring the difference between the Fermi level and the cut-off at the low kinetic energy scale. (145) Subtracting the work function from the photon excitation energy should, by definition, corresponds to a binding energy of 0 eV, with reference to the Fermi edge. Thus, the work function can be used in calibrating the B.E scale. (146) B.E is usually expressed in electron volt (eV) units. Final state effects, e.g. due to core hole relaxation during the emission, influence the measured value of the B.E as well, but this is a secondary effect.

Photoelectron spectra produced in terms of binding energy can give insight into the electronic structure of the studied element. Excited or ejected electrons which escape from the core level contribute to characteristic peaks at specific binding energy values. Once a photoelectron has been ejected, the atom undergoes a relaxation process via fluorescent emission of X-ray photons, or radiationless decay through Auger electron emission. (144)

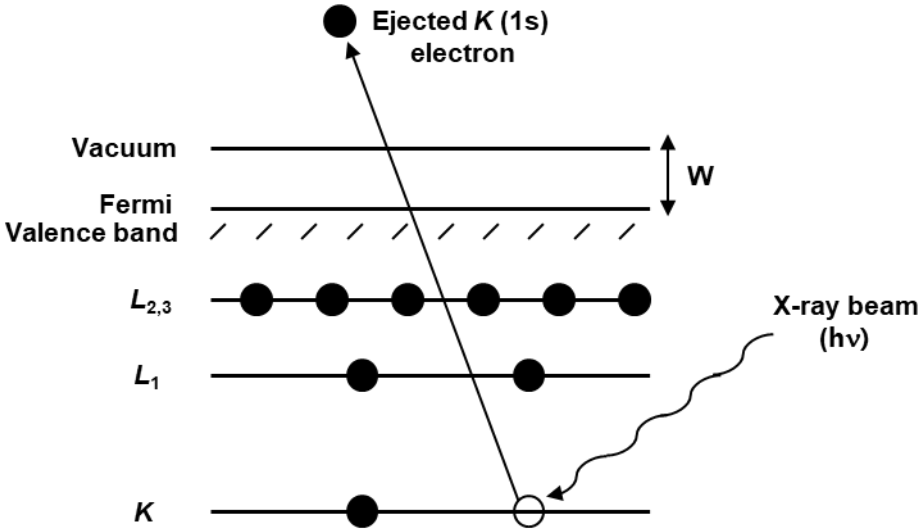

Figure 24 Schematic diagram of the XPS principle illustrating photoemission process of an atom by the incident X-ray beam, resulting in an ejected core-level electron. (144)

XPS allows for quantification of elemental and chemical state composition. The photoemission intensity is the area under the curve of the produced photoelectron emission peak. Once a set of peak areas has been calculated, intensity can be interpreted as atomic percentage (at%) of the studied elements. However, several factors have to be taken into consideration to ensure accurate quantification. Of these factors, the relative sensitivity factor (F) which is element dependent and includes the photoelectron cross-section, instrumental factors, and electron attenuation depth (λ), typically up to 5 nm. Once all these parameters have been determined, surface composition in terms of at% can be calculated by dividing the peak area (I_A) by the sensitivity factor (F_A) and expressing it as a fraction of the summation of all normalised intensities (Σ I/F). (144)

Equation 11

$$\text{at\%} = \left\{ \frac{\left(\frac{I_A}{F_A}\right)}{\sum\left(\frac{I}{F}\right)} \right\} \text{x } 100\%$$

It is important to mention that the above equation assumes that the area analysed by XPS is homogeneous and representative of the whole sample. Therefore, a systematic study was applied to the analysed stainless steel substrates to verify and confirm surface homogeneity (section 3.5.3).

The spectral lineshapes resulting from the core level photoemission process are Lorentzian, with an asymmetric tail towards high binding energy, as described by Doniach-Sunjic theory. However, the natural lineshape is influenced by several factors. The Kα X-ray source, for example, contributes towards a Lorentzian line-shape, while spectrometer broadening gives rise to Gaussian broadening. Moreover, variations in intermolecular relaxation processes can account for an increase in linewidth (FWHM). (109, 110) In other words, lower-energy emission lines typically lead to narrower FWHMs. The FWHM of the peak can also be artificially affected (i.e. broadened and with asymmetrical features) as a result of surface charging. (110)

The notation followed in XPS applications is conventionally in the formula of 'nl_j', where n is the principal quantum number (e.g. 1, 2, 3, etc.), l is the angular momentum number of the electron (e.g. 0 = s, 1 = p, 2 = d, and 3 = f), and $j = |l + s|$ (where s is the spin angular momentum number, which can be either +1/2 or -1/2). Therefore, XPS spectral peaks derived from orbitals with angular momentum (l) > 0 (i.e. p, d, or f) typically split into two peaks (i.e. spin orbit splitting). For instance, an electron from orbital p would have a j value of 3/2 (l + s) or 1/2 (l – s) (e.g. in the case of iron, Fe $2p_{3/2}$ and Fe $2p_{1/2}$). An electron from a d orbital, on the other hand, would result in j values of 5/2 and 3/2. (144)

The angle at which the sample is analysed at is also of great importance in XPS applications. Although conventional XPS is considered as advanced surface sensitive technique, analysis depth may be varied based on the angle of measurement. Thin surfaces of up to 3 nm can be accurately probed by tilting the surface to increase the surface area exposed to the X-ray beam. (144) This method is called surface angle measurements and allows for more sensitive analysis of the surface (Figure 25). The angle between the surface normal and the direction in which the photoelectrons leave the surface towards the analyser is called the electron take-off angle (θ). At $\theta = 0°$, the X-ray beam can penetrate the surface to deeper levels and partially probe the bulk material as well. This method is called bulk angle measurements.

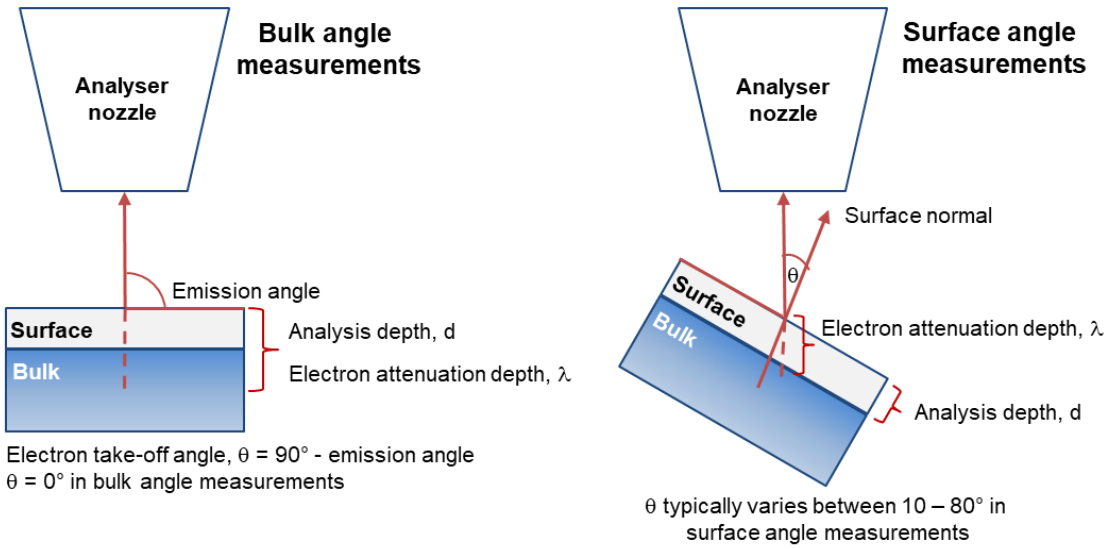

Figure 25 Schematic representation of bulk vs surface angle measurements in XPS applications showing deeper λ at θ = 0°.

Intensity of emitted electrons (I) from all depths can be then calculated as per the following equation. (144)

Equation 12

$$I = I_0 \exp\left(-\frac{d}{l.\cos\theta}\right)$$

Where 'I_0' is the electron intensity in the bulk, 'd' is the analysis depth, 'λ' is the attenuation depth, and 'θ' is the electron take-off angle.

Since the objective of this PhD was to study the attachment of ODA and gum on stainless steel, bulk angle was used in all XPS measurements to understand, both, bulk and surface properties within the studied systems.

3.4.2.1 Ultrahigh vacuum (UHV) XPS

UHV-XPS measurements were performed on FlexMod (SPECS™) UHV-XPS system using Aluminium (Al) K_α unfocused twin anode (XR 50) and monochromatic (FOCUS 500) X-ray sources (400 W, 14.99 kV) within a rectangular area of approximately 3.5 x 1 mm^2 (Figure 26). Standard lens iris diameter of 60 mm was applied in conjunction with the hemispherical analyser (PHOIBOS). Samples were mounted on the instrument's standard sample plates with an electron take-off angle (θ) of 0° using high purity double sided carbon tape (Figure 27). Measurements were conducted at analysis chamber pressure of $7x10^{-10}$ mbar. Charge neutralisation was done using ions flood gun (FG 15/40) at 2 eV energy, 25 μA electron emission, and 2.1 A filament current.

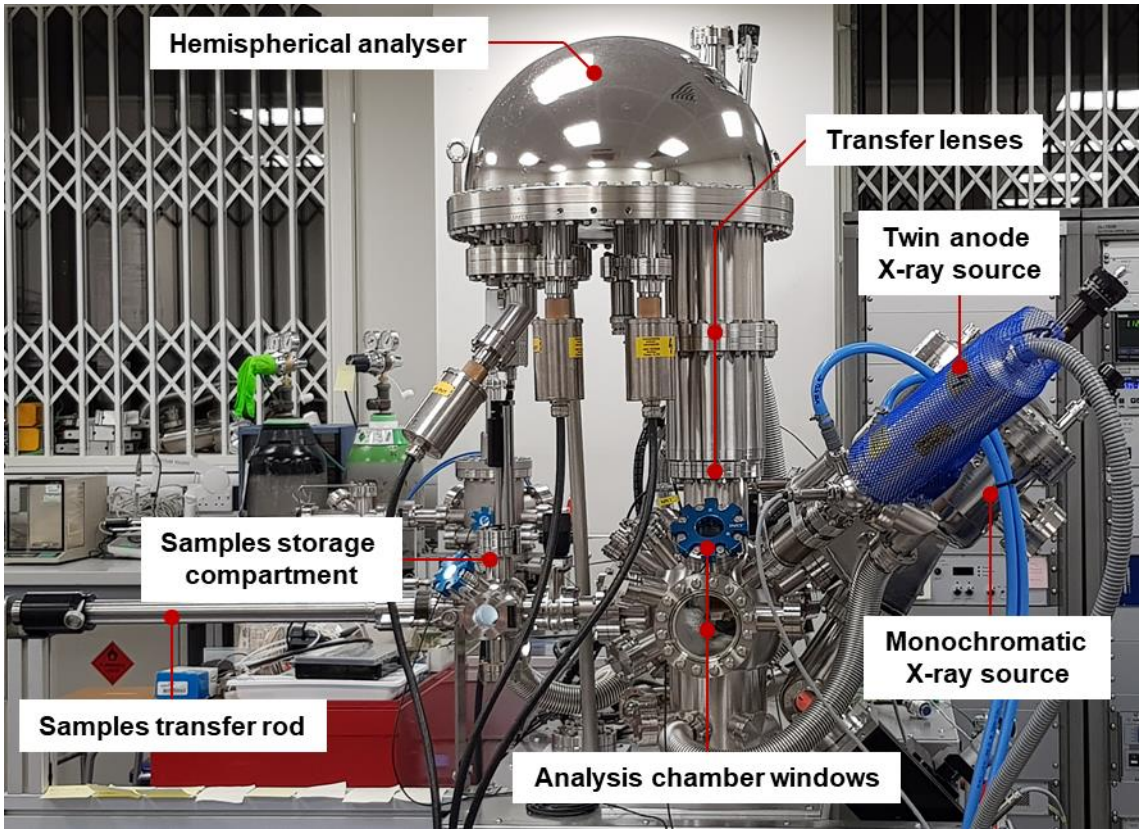

Figure 26 Actual image of the UHV-XPS system used, showing key instrumental components.

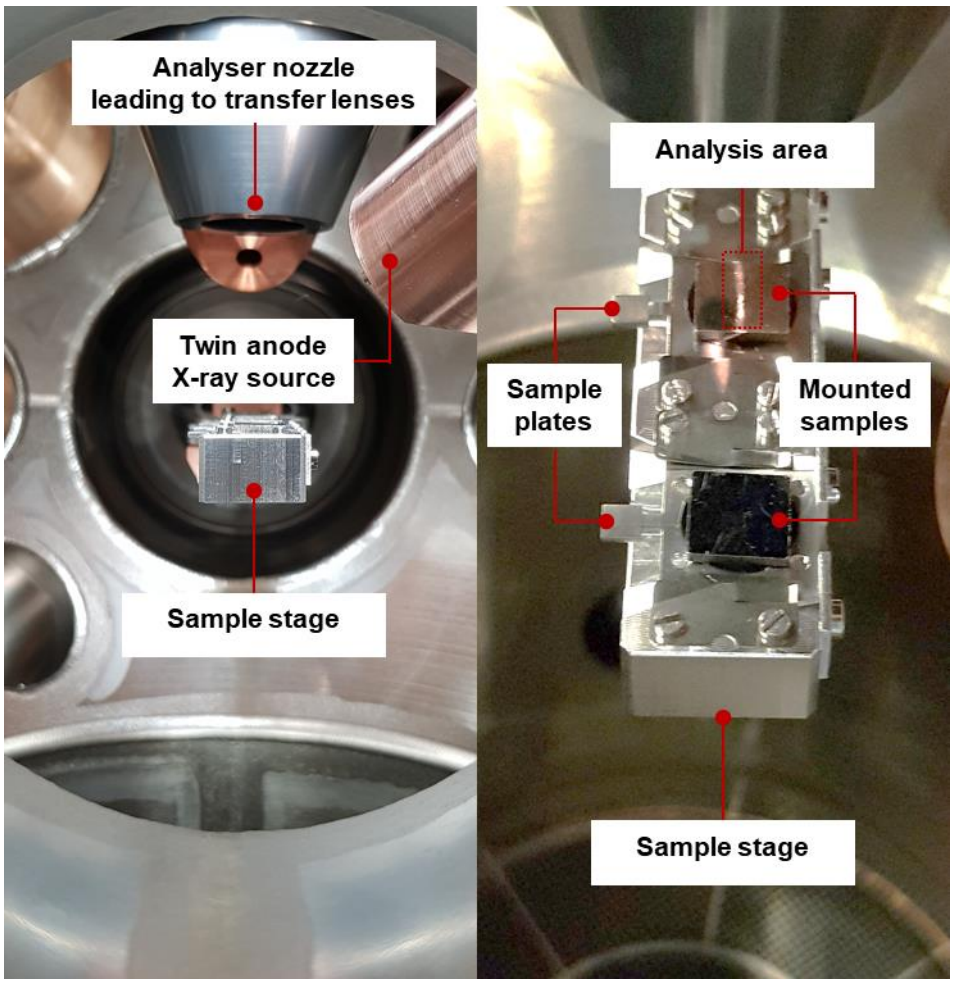

Figure 27 Samples layout as seen from the analysis chamber windows.

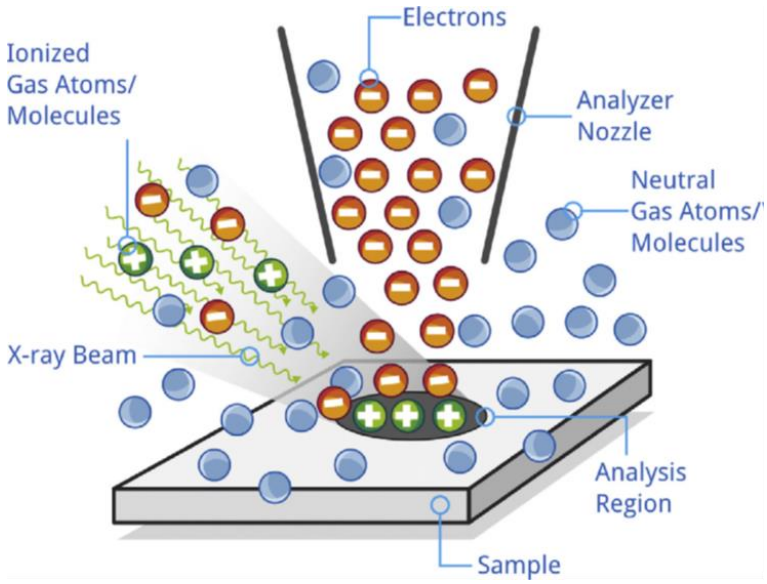

Figure 28 Illustration of the charge correction process in near-ambient XPS applications. (147)

3.4.2.2 Near ambient pressure XPS (NAP-XPS)

Analysis was performed on EnviroESCA™ electron spectrometer (SPECS™ Surface Nano Analysis GmbH) using Aluminium (Al) K_α micro-focused monochromator ($h\nu$ = 1486.7 eV) over a circular area of approximately 300 µm. Samples were mounted on standard specimen stub using high purity double sided carbon tape and placed in the instrument's designated sample plate in an electron take-off angle (θ) of 0°. Measurements were conducted at analysis chamber pressure of $9x10^{-7}$ mbar. Sample charge is neutralised by generation of electron/ion pairs in the gas phase as shown in Figure 28.

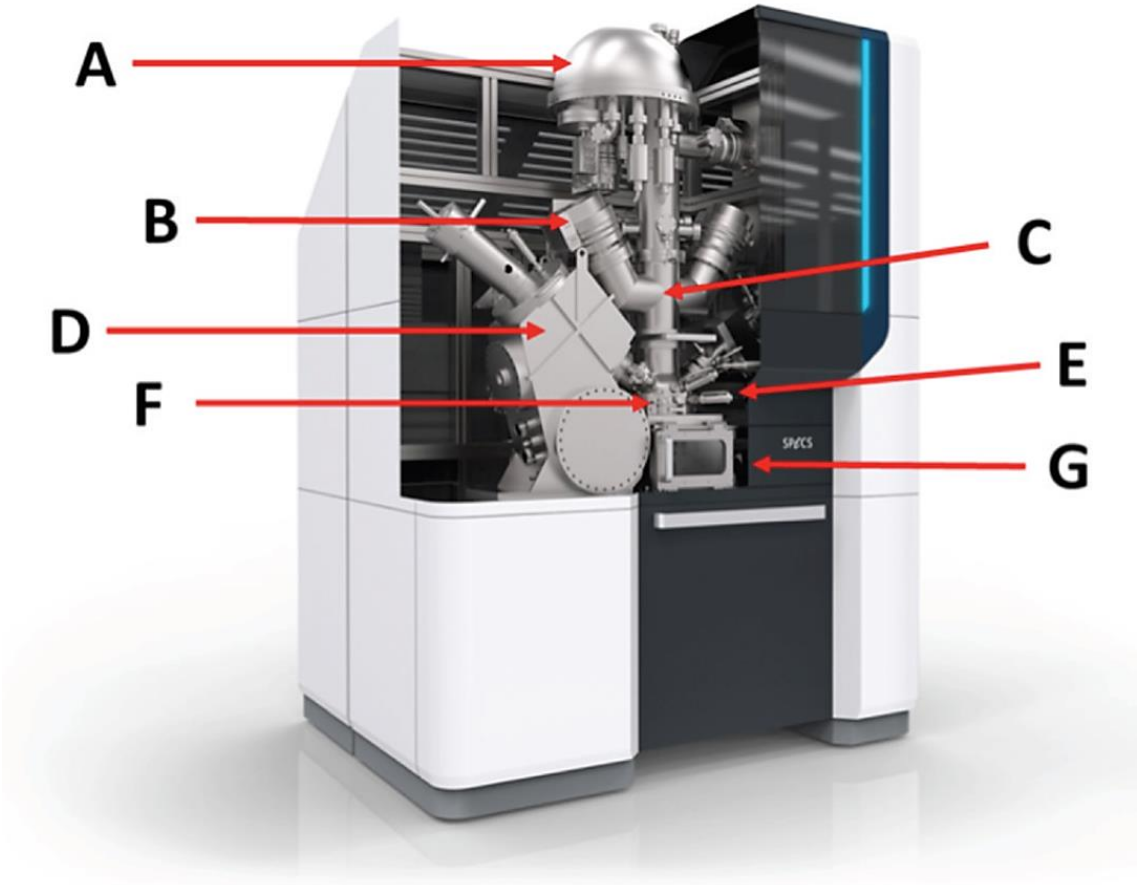

Figure 29 Cross-section view of the EnvrioESCA™ system showing **A)** hemispherical analyser, **B)** differential stage pump, **C)** analysis column with pumping stages and transfer lenses, **D)** X-ray generating system, **E)** digital microscopes, **F)** analysis chamber, and **G)** sample transfer environment. (148)

3.4.2.3 Harwell XPS

XPS measurements presented in chapter 5.4.4 were performed on a Thermo Fisher Scientific K-alpha+ spectrometer. Samples were analysed using a micro-focused monochromatic Al X-ray source (72 W) over an area of approximately 400 microns. Data was recorded at pass energies of 150 eV for survey scans and 40 eV for high-resolution scans with 1 eV and 0.1 eV step sizes respectively. Charge neutralisation of the sample was achieved using a combination of both low energy electrons and Ar+ ions. Data analysis was performed in CasaXPS using a Shirley background and Scofield cross sections, with an energy dependence of -0.6.

3.5 Methodology

The experimental framework set up for the methods established to formulate the TRF surrogate fuels used in chapter 4 will be summarised in section 3.5.1. Sections 3.5.2 and 3.5.3 will discuss in detail the reproducible polishing and cleaning methods established to prepare the substrates for the adsorption experiments and concurrently the surface sensitive analyses conducted throughout this PhD. The applied methods allowed for quantitative measures to ensure roughness uniformity and cleanliness across all substrates.

Any further optimisations to the methods detailed in this chapter will be discussed and justified in the relevant chapters.

3.5.1 Fuel model formulation

A gasoline surrogate was formulated based on the TRF fuel model described in chapter 2.1. Equation 4 was rearranged to a quadratic equation to generate a general formula that give the exact volume percentages needed to make any TRF blend at a certain RON value (R) and a normalised PRF volume ratio (*P*). Mathematical computing software (Maple™ 18) was used for all calculations. (149) The new equation can be described as follows:

Equation 13

$$0 = (P * a1 * \chi) + (a3 * \chi) + (a2 * \chi) + (100 * P) - R$$

Where a1, a2, and a3 are constants a_{tolp}, a_{tol}, and a_{tol2} respectively, as described in Table 2 (chapter 2.1). χ = total volume.

Equation 5 was used to validate the sensitivity of the generated blends. Acceptable blends would typically have a sensitivity (S) in the range of 8 – 10. (42) The following TRF blend was formulated based on the generated equations.

Table 17 TRF blend compositions in volume percentage with 95 RON and 1:1 normalised PRF ratio (*P* = 0.5) using the rearranged equation of MLbV model.

Toluene	n-Heptane	Iso-octane	Sensitivity
61.8	19.1	19.1	9.04

TRF composition was first based on engine performance calculations to meet RON values of > 95. However, meeting such RON values required very high aromatic contents, which resulted in unrealistic gasoline surrogates. Composition was adjusted to meet the maximum aromatic and olefin content values as per the EN-228 specifications for unleaded gasoline.

Table 18 TRF surrogate fuel composition based on engine performance calculations compared to EN-228 gasoline specifications.

Component	Initial composition (vol%) (Engine performance)	Optimised composition (vol%) (EN-228 specification)
Toluene	54.5	35.0
n-heptane	15.0	22.6
Iso-octane	25.0	22.6
tBHP	0.5	1.8
1-octene	--	13.0
2,4-hexadiene	5.0	5.0

Full TRF blend calculations retrieved from Maple software can be found in Appendix 1. Furthermore, Equation 6 can be rearranged to calculate the RON value of any generated TRF blend by manipulating toluene and PRF composition. The sensitivity equation can be also applied for validation. An example of a calculation can be found in Appendix 2.

3.5.2 Substrates preparation methods

16 x grade 316 SS coupons were wet-polished using Buehler BETA Grinder-Polisher (Figure 30). Consecutive courses of silicon carbide papers were used to polish the coupons (Grit P120, P320, P600, and P1200). 3µ water-based polycrystalline diamond suspension (Aquapool 3-WP) was used in combination with a MicroFloc polishing cloth to achieve the final mirror-finish of the surface. All coupons were polished manually by holding the coupons perpendicularly onto the desk at 3 o'clock position, with slight alternation between 1 and 5 o'clock positions to ensure polishing uniformity. This method was repeatedly performed across all coupons.

Figure 30 Generic image of the Buehler B.ETA polisher used for coupons preparation. (150)

3.5.2.1 Polishing and finishing effects

Coupons were weighed pre- (as received) and post-polishing using a micro-gram scale as a mean to aid in recording all physical changes on the prepared substrates. Average masses of neat and polished coupons were 7.1768 g and 6.9915 g respectively, with an average mass loss of 185.35 mg (2.58%). 12 out of the 16 polished coupons fell within ± 1 standard deviation (St. Dev., σ) of mass loss, which indicated a reproducible polishing procedure. The following table lists the raw values for all polished coupons.

Table 19 Measured and calculated mass values of all polished coupons.

Coupon number	Mass before (g)	Mass after (g)	Mass loss (mg)	Percentage loss (%)
Reference polished	7.2136	6.9803	233.30	3.23
1	7.1964	7.0770	119.40	1.66
2	7.2056	6.9150	290.60	4.03
3	7.2017	6.9924	209.30	2.91
4	7.1979	7.0579	140.00	1.95
5	7.1984	7.0324	166.00	2.31
6	7.1960	7.0267	169.30	2.35
7	6.9565	6.7818	174.70	2.51
8	7.2043	7.0605	143.80	2.00
9	7.1678	6.9977	170.10	2.37
10	7.1938	6.8196	374.20	5.20
11	7.1705	7.0452	125.30	1.75
12	7.1844	6.9192	265.20	3.69
13	7.1766	7.0606	116.00	1.62
14	7.1716	7.0318	139.80	1.95
15	7.1943	7.0657	128.60	1.79
Average	**7.1768**	**6.9915**	**185.35**	**2.58**
St. Dev.	**0.0584**	**0.0862**	**70.89**	**0.97**

The following figure compares the unpolished side in one of the SS coupons to the polished side.

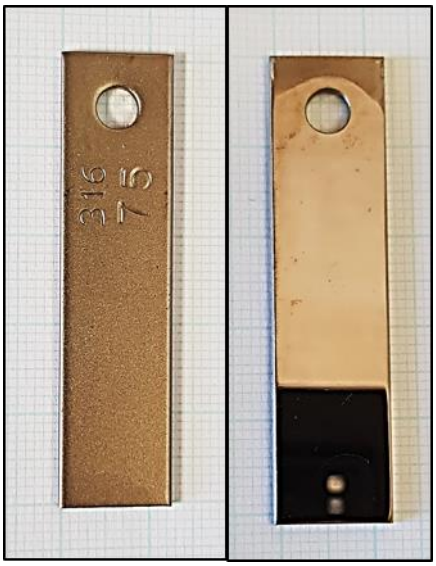

Figure 31 Left: Unpolished, rough surface on the back side of the coupon compared to (right) mirror-polished front side, reflecting surroundings as the photo was taken.

SEM images were taken to visualise the difference in coupons' surface roughness at a micrometer scale.

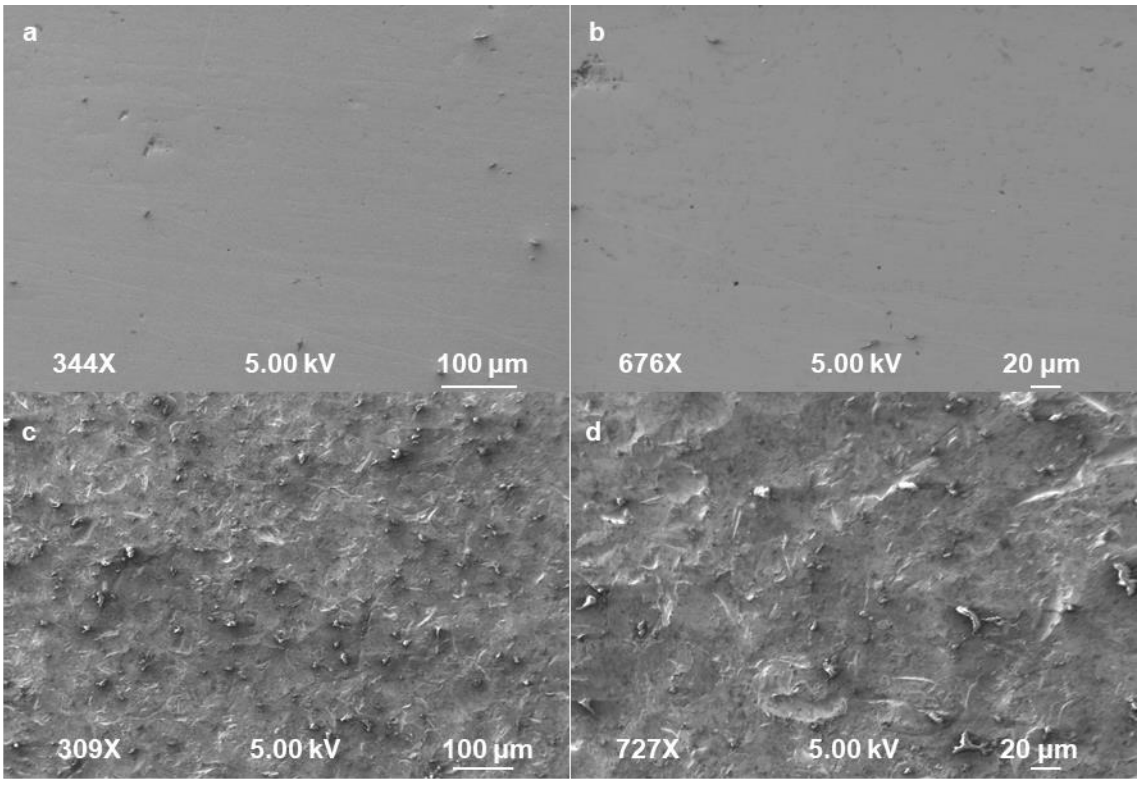

Figure 32 SEM images of polished (a and b) compared to unpolished (c and d) stainless steel coupons at 100 and 20 µm scales.

3.5.2.2 Surface roughness measurements

Due to the restricted availability of the surface profilometer and the high repeatability of the established polishing method, it was decided to randomly select three samples for surface roughness analysis. Therefore, average surface roughness (R_a) measurements were determined for coupons number 4, 8, and 13 using a Taylor-Hobson Talysurf I20-L Profilometer (Figure 33).

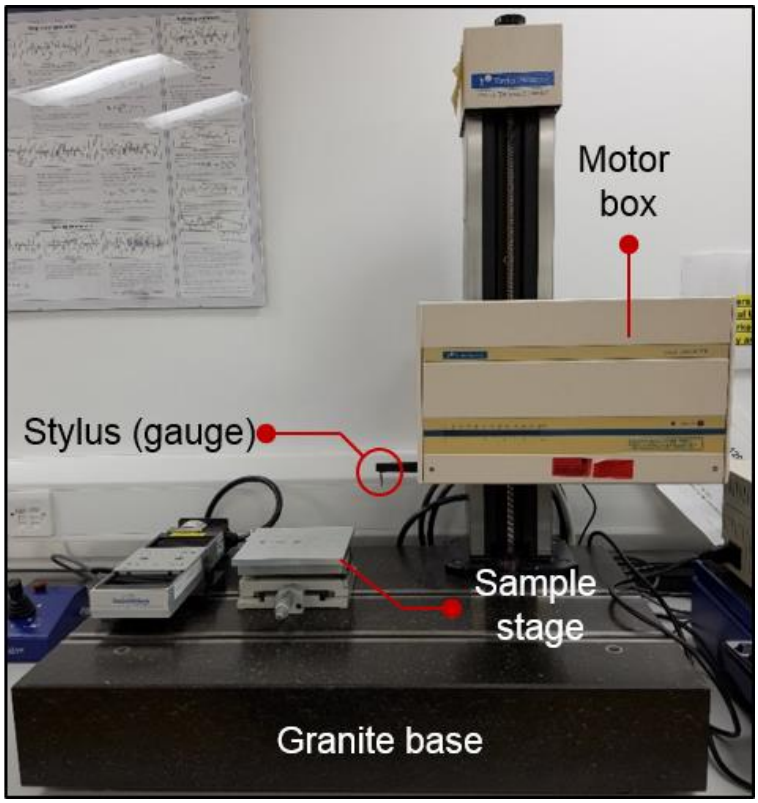

Figure 33 Actual image of the Talysurf profilometer used for roughness measurements, detailing key parts of the instrument.

X-Y directional surface roughness was measured at six different sites on each coupon, three sites on each direction (Figure 34). Analysis length was 8 mm with a cut-off value at 0.8 mm and a measurement angle of 0°. Average X and Y axes R_a value calculated for the three coupons, and reported to two significant digits, was 0.01 µm. Surface roughness for the unpolished (as received) reference coupon (denoted as Ref.U in Table 20) was also determined and found to be 1.15 µm. This demonstrates the efficacy of the polishing procedure. The following schematics illustrate the sites and directions where each measurement was taken, followed by tabulated roughness values of the profiled coupons.

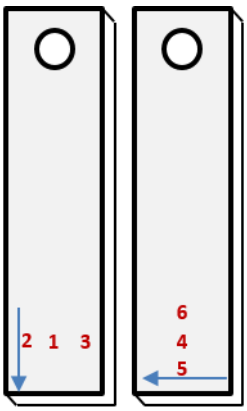

Figure 34 Schematic diagram of a stainless steel coupon indicating an approximation of the three measured sites (in red) at Y and X axes, left and right respectively. Blue arrow indicates the direction of profiling.

The following table lists the raw surface values measured for each coupon, where R_a = Arithmetic average height, R_{sk} = Skewness, R_p = Maximum peak height, R_q = Root mean square roughness, R_v = Maximum valley depth, and R_t = Maximum height of the profile. (151)

Table 20 Values of surface roughness parameters measured for each coupon.

Coupon number (site)	R_a (µm)	R_{sk}	R_p (µm)	R_q (µm)	R_v (µm)	R_t (µm)	Axis
Ref.U (1)	1.01	0.10	3.60	1.30	3.17	9.56	Y
Ref.U (2)	1.17	0.15	3.82	1.46	3.73	9.63	Y
Ref.U (3)	1.21	0.30	4.27	1.53	3.50	10.24	Y
Average	**1.13**	**0.18**	**3.90**	**1.43**	**3.46**	**9.81**	
Ref.U (4)	1.14	-0.04	3.63	1.43	3.62	9.72	X
Ref.U (5)	1.17	0.09	4.08	1.45	3.35	9.41	X
Ref.U (6)	1.18	-0.03	3.72	1.47	3.74	10.14	X
Average	**1.16**	**0.01**	**3.81**	**1.45**	**3.57**	**9.76**	
13 (1)	0.02	-0.05	0.05	0.02	0.04	0.12	Y
13 (2)	0.02	-0.84	0.05	0.03	0.07	0.22	Y
13 (3)	0.02	-1.33	0.05	0.02	0.08	0.35	Y
Average	**0.02**	**-0.74**	**0.05**	**0.02**	**0.06**	**0.23**	
13 (4)	0.01	-0.07	0.02	0.01	0.03	0.09	X

Coupon number (site)	R_a (µm)	R_{sk}	R_p (µm)	R_q (µm)	R_v (µm)	R_t (µm)	Axis
13 (5)	0.01	0.11	0.02	0.01	0.03	0.07	X
13 (6)	0.01	0.20	0.02	0.01	0.02	0.07	X
Average	**0.01**	**0.08**	**0.02**	**0.01**	**0.03**	**0.08**	
4 (1)	0.02	0.11	0.04	0.02	0.06	0.19	Y
4 (2)	0.02	-0.22	0.04	0.02	0.07	0.19	Y
4 (3)	0.01	-0.36	0.04	0.02	0.04	0.14	Y
Average	**0.02**	**-0.15**	**0.04**	**0.02**	**0.06**	**0.17**	
4 (4)	0.01	0.04	0.02	0.01	0.03	0.08	X
4 (5)	0.01	-1.63	0.03	0.02	0.05	0.19	X
4 (6)	0.01	0.13	0.02	0.01	0.03	0.10	X
Average	**0.01**	**-0.49**	**0.03**	**0.02**	**0.04**	**0.12**	
8 (1)	0.01	0.13	0.03	0.01	0.03	0.08	Y
8 (2)	0.01	0.03	0.04	0.02	0.04	0.10	Y
8 (3)	0.01	-0.02	0.03	0.01	0.03	0.08	Y
Average	**0.01**	**0.05**	**0.03**	**0.01**	**0.03**	**0.09**	
8 (4)	0.01	-0.12	0.02	0.01	0.02	0.06	X
8 (5)	0.01	0.20	0.02	0.01	0.02	0.06	X
8 (6)	0.01	-0.05	0.02	0.01	0.02	0.06	X
Average	**0.01**	**0.01**	**0.02**	**0.01**	**0.02**	**0.06**	

Figure 35 compares the average R_a values of the polished coupons to the reference point.

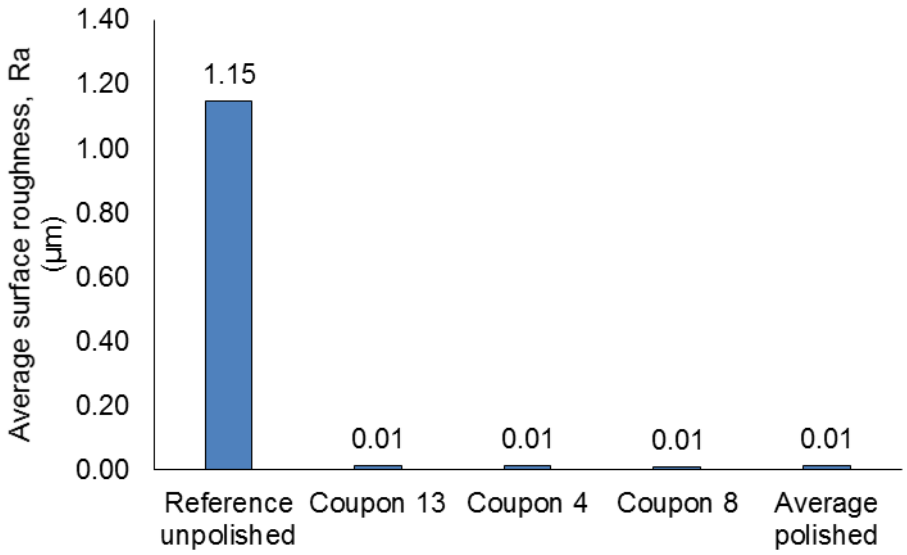

Figure 35 Average surface roughness (Ra) of unpolished vs. 3 polished coupons, showing ca. 99% reduction in roughness (Reference vs. average).

Due to the relatively large size of the coupons, it was decided at a later stage of the project to laser-cut each coupon into three smaller substrates (Figure 36). Reducing coupons size allowed for better optimisation for the adsorption experiments as well as all the consequent surface sensitive analyses.

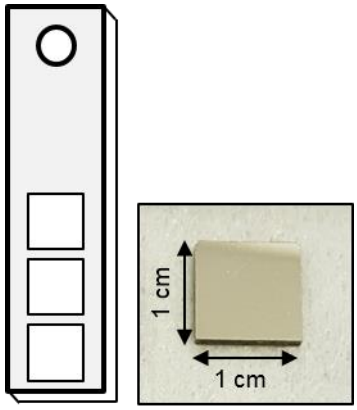

Figure 36 Schematic drawing of a stainless steel coupon (left) showing locations where the laser cutting was performed. Right: 1x1 cm laser-cut coupon.

3.5.2.3 Substrate cleaning method

It is vital in surface analysis to establish a rigorous, reproducible cleaning method to achieve reliable results. (152-154) Surface elemental composition is a key factor contributing to chemical interactions at the interface. (155, 156) In this study, a cleaning method utilising a solution of polar and non-polar solvents was

established to ensure removal of both polar and non-polar contaminants. The solution was consisted of toluene, acetone, and methanol (TAM) in 1:1:1 ratio. Five substrates at a time were immersed in a Duran bottle containing the TAM solution and placed in a water-filled ultrasonic bath for 15 min, at room temperature. Coupons were the taken out of solution, rinsed individually with acetone, and wiped thoroughly with a finishing cloth. This cleaning cycle was repeated for three times with the TAM solution being changed and the Duran bottle cleaned in between each run. Following the last cycle, coupons were allowed to dry in an oven for 3 h at 65°C to ensure removal of any residual acetone. The following figure shows the effectiveness of the established method in cleaning the stainless steel substrates.

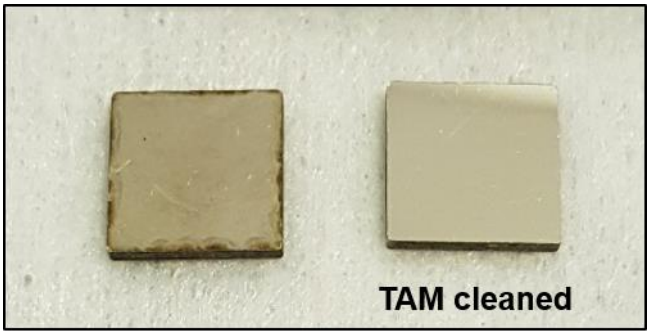

Figure 37 Uncleaned (left) compared to a TAM-cleaned (right) substrate showing noticeable improvements, especially around the edges.

XPS was utilised to compare the cleaning efficiency of TAM solution against that of acetone, on two SS substrates. Data were collected as per the following parameters.

Table 21 XPS scanning parameters used to probe the surfaces of the acetone and TAM cleaned coupons

Scan range	Pass energy (eV)	Dwell time (s)	Step size (eV)	Number of scans
Survey	100	0.1	1	1
High-resolution (C, N, O, Fe)	10	0.4	0.1	4, except for N 1s (8)

Binding energy (B.E) scale was calibrated to aliphatic C-C emission at 285.0 eV. (109, 110) Data analysis was performed in CasaXPS using Scofield cross sections, Shirley background, and Gaussian-Lorentzian line shape, GL(30), unless otherwise stated. Wide range survey scans resulted in the same major

elements (i.e. C, N, O, Cr, and Fe), except where 1.55 atomic percentage (at%) of fluorine (F1s) was found on the surface of the TAM cleaned coupon. It was believed that this was due to the use of a fluorinated solvent bottle to contain the TAM solution. Figure 38 compares the elemental composition of both coupons.

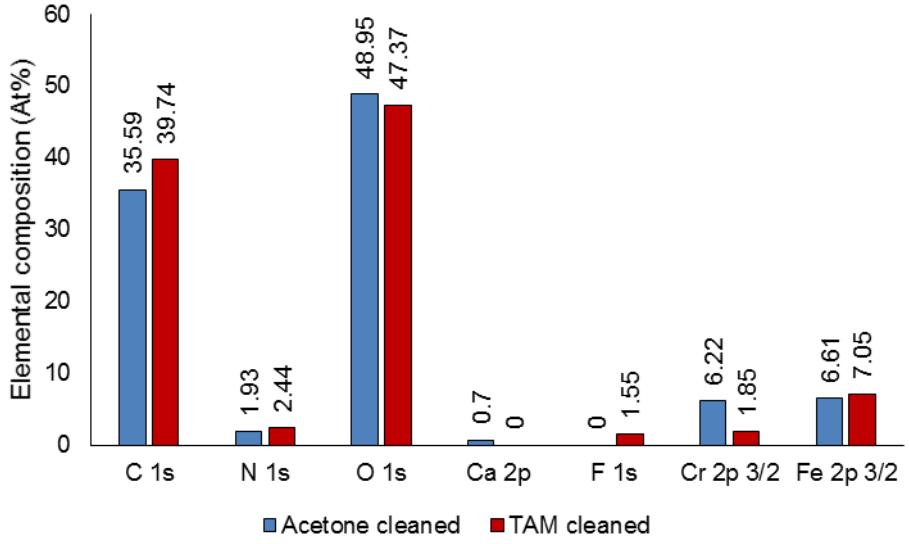

Figure 38 Elemental composition obtained from survey scans for the acetone and TAM-cleaned coupons.

It can be seen from Figure 38 that iron (Fe $2p_{3/2}$) and nitrogen (N 1s), which are integral to the substrate, (123, 156, 157) showed 6.66% and 26.42% increase respectively, in favour of the TAM cleaning method. However, it was imperative to investigate the adventitious layer elements, especially carbon (C 1s) and oxygen (O 1s), in more details to gain a wider understanding of chemical species behaviour on the surface.

Upon deconvoluting the high-resolution C 1s spectra (Figure 39), three main peaks were assigned for the adventitious carbon layer, namely aliphatic C-C at 285.0 eV, C-O at 286.2 – 286.5 eV, and C=O at 288.4 – 288.6 eV. (156) Carbonyl species on the surface showed an attenuation of 5.15 at% in the favour of TAM cleaning. On the other hand, O 1s high-resolution spectra (Figure 40) was fitted to a Lorentzian function line shape, LF(1,1,25,280), and deconvoluted into three main peaks, metal oxides at 529.9 eV, C-O at 531.3 – 531.4 eV, and C=O at 532.7 – 532.9 eV. (146) Adventitious C-O and C=O showed an attenuation of 3.21 and 4.97 at% respectively, in the favour of TAM cleaning. Moreover, the metal oxide peak increased by 8.19 at% with TAM cleaning, which indicated more exposure of the surface. Table 22 lists the C 1s and O 1s core level binding energies (B.E), full width at half maximum (FWHM), peak area, and atomic percentage (at%) for each component.

Table 22 Carbon (C 1s) and oxygen (O 1s) XPS core level binding energy, FWHM, and peak intensities as a function of cleaning method.

	Acetone cleaned				TAM cleaned			
Species	**B.E (eV)**	**FWHM**	**Peak area**	**at%**	**B.E (eV)**	**FWHM**	**Peak area**	**at%**
C 1s								
C-C	285.0	1.2	144.07	61.57	285.0	1.1	180.05	66.53
C-O	286.2	2.7	36.52	15.61	286.5	1.3	42.75	15.80
C=O	288.4	1.5	53.40	22.82	288.7	2.0	47.81	17.67
O 1s								
Metal oxides	529.9	1.1	116.01	41.54	529.9	1.1	141.60	49.73
C-O	531.3	1.9	126.40	45.26	531.4	1.9	119.73	42.05
C=O	532.7	1.8	36.86	13.20	532.9	1.8	23.42	8.23

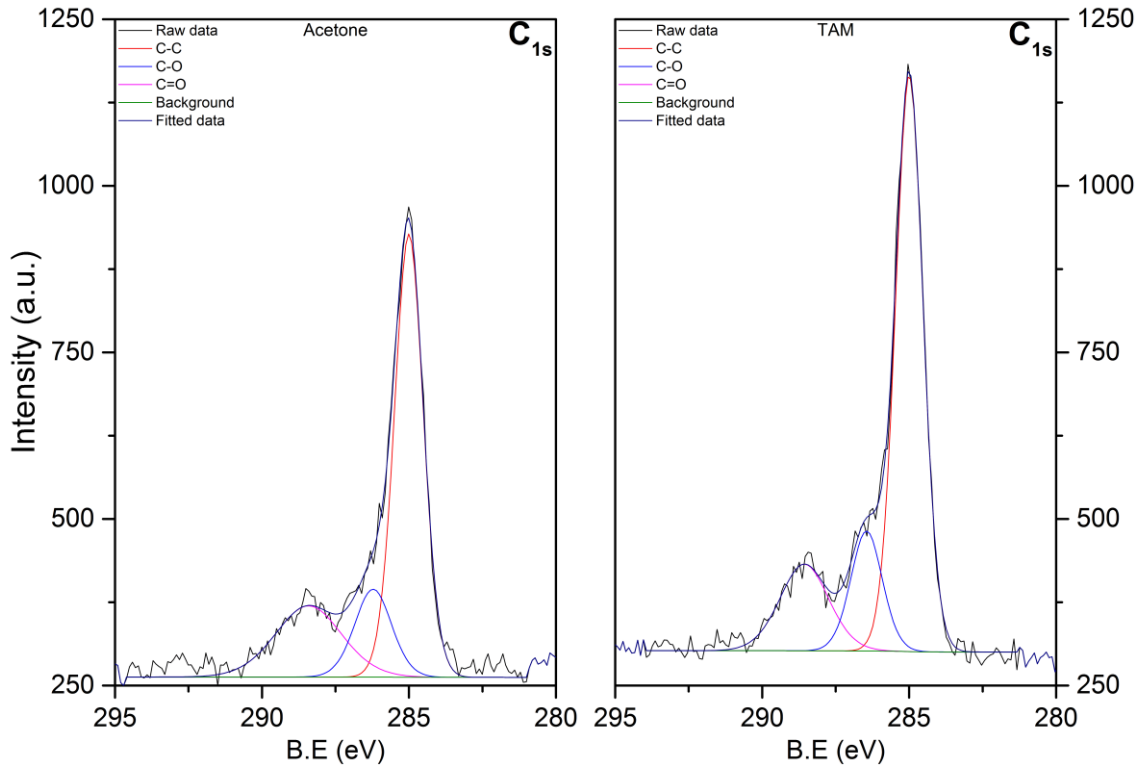

Figure 39 Carbon (C 1s) high-resolution spectra of acetone vs. TAM cleaned coupons.

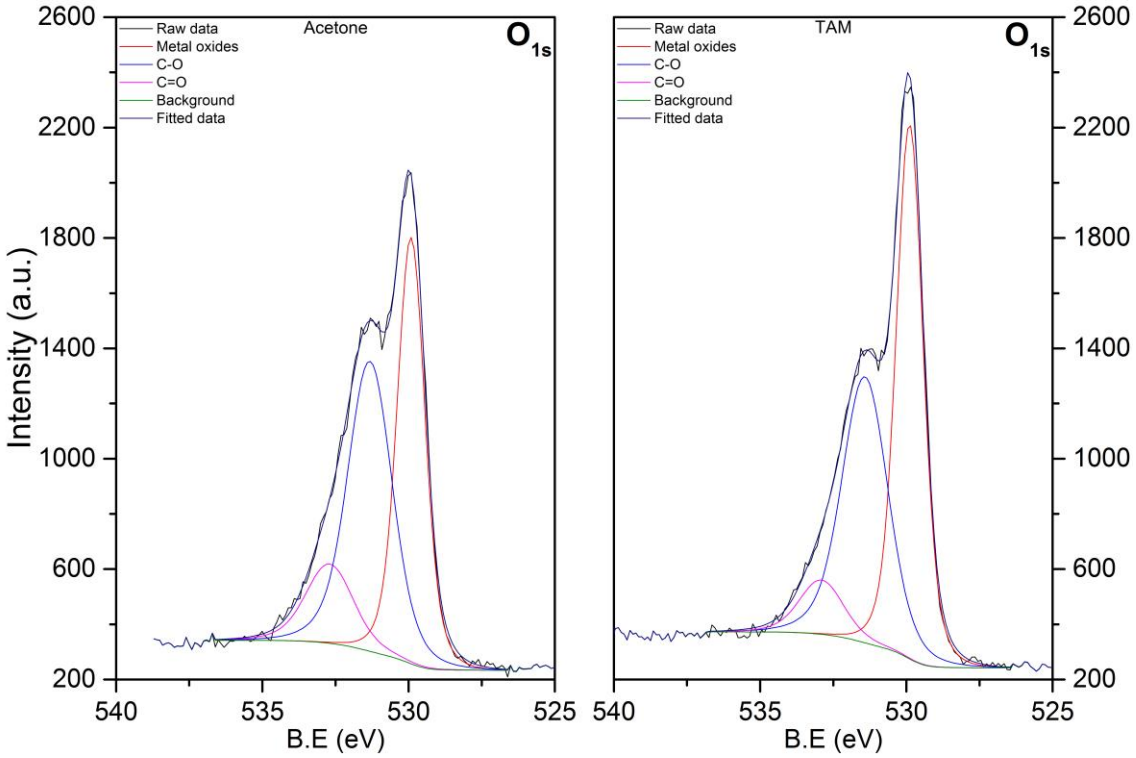

Figure 40 Oxygen (O 1s) high-resolution spectra of acetone vs. TAM cleaned coupons.

Following establishing the above discussed cleaning method, it was crucial to statistically evaluate the consistency of producing clean substrates with comparable elemental composition. Section 3.5.3 discusses the reproducibility of post-cleaning surface composition.

3.5.3 Reproducibility of surface elemental composition

Due to the nature of this PhD in using XPS as the main technique to probe the solid-liquid interactions at the interface and the large number of substrates used, it was time consuming and costly to scan three sites at each coupon. Thus, a systematic study was conducted to evaluate the compositional uniformity within each coupon (i.e. Intra-surface composition) and across various coupons (i.e. Inter-surface composition). Outcomes of this study allowed for better optimisation to the scanning time, by reducing number of sites to one or two, while maintaining high levels of confidence and reliability of the collected data.

3.5.3.1 Intra-surface composition study

A single TAM-cleaned coupon was survey scanned at six different positions using an EnviroESCA™ electron spectrometer and as per the parameters in Table 21, denoted as P1 – P6 throughout this section, to quantify the elemental composition on the surface. Average composition was calculated for each element, with an error margin of ± 1 standard deviation (Figure 43). Elemental composition from central position (i.e. P1) was compared to the average of position 2 – position 6 (P2 – P6). Analysis showed good correlation between P1 and average P2 – P6 on the surface (Figure 44), which suggested that P1 was representative of the surface and hence was chosen as an optimum scanning site.

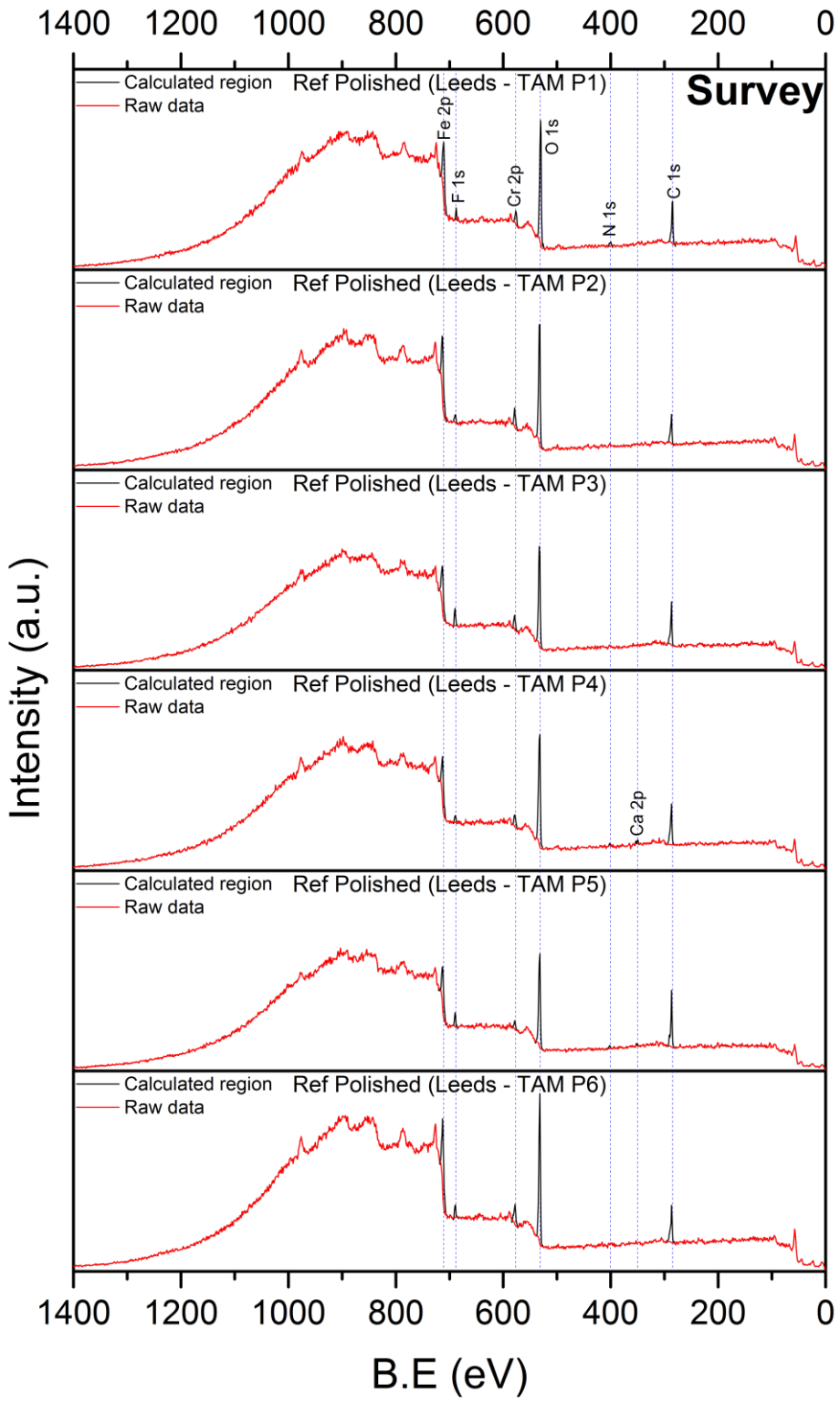

Figure 41 Survey spectra collected at six different positions on a single TAM-cleaned coupon. Positions are denoted P1 – P6.

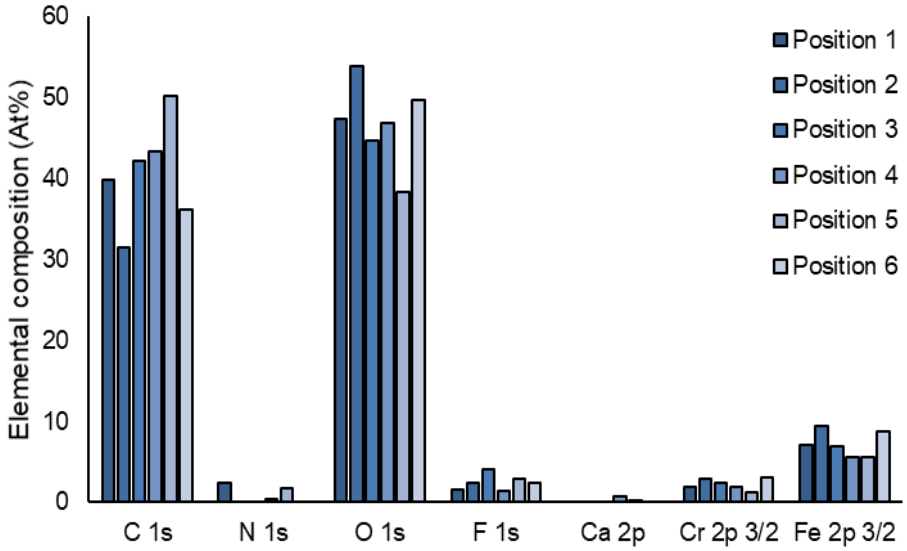

Figure 42 Intra-surface elemental composition, showing clear variation within the same coupon.

Table 23 lists the elemental composition plotted in Figure 42 as a function of scanning position. By examining the calculated regions, it can be seen that nitrogen (N 1s) and calcium (Ca 2p) were not detectable in all positions, which indicated that those two elements were not uniformly distributed across the surface. Moreover, high levels of iron (e.g. P2 and P6) were associated with high levels of oxygen at the same positions, which suggested that metal oxides were the main constituent of oxygen (O 1s) on the surface. Such observation validates the postulation proposed in section 3.5.2.3 to consider contents of metal oxides on the substrate as a mean to evaluate surface exposure to the X-ray beam, in addition to iron content.

Table 23 Composition of surface elements in atomic percentage calculated from survey scans (Figure 41). Green cells fall within an error margin of ± 1 σ (St. Dev.)

Position	C 1s	N 1s	O 1s	F1s	Ca 2p	Cr $2p_{3/2}$	Fe $2p_{3/2}$
P1	39.74	2.44	47.37	1.55	0.00	1.85	7.05
P2	31.47	0.00	53.84	2.35	0.00	2.87	9.47
P3	42.10	0.00	44.60	4.10	0.00	2.35	6.84
P4	43.22	0.43	46.79	1.41	0.69	1.94	5.53
P5	50.23	1.70	38.24	2.89	0.15	1.20	5.59
P6	36.09	0.00	49.66	2.41	0.00	3.06	8.78
Average	**40.48**	**0.76**	**46.75**	**2.45**	**0.14**	**2.21**	**7.21**
St. Dev.	**5.86**	**0.96**	**4.76**	**0.90**	**0.25**	**0.63**	**1.48**

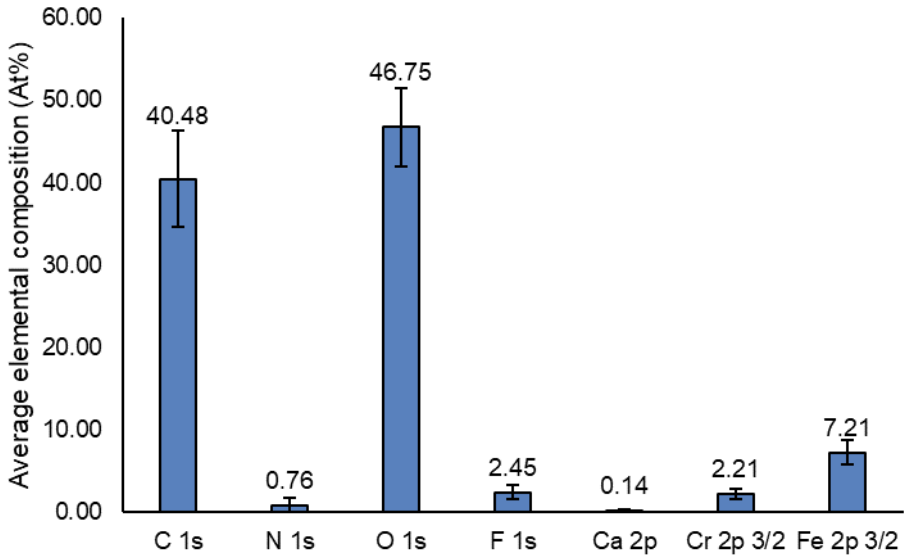

Figure 43 Average intra-surface elemental composition for all positions, showing acceptable error margin (± 1 σ).

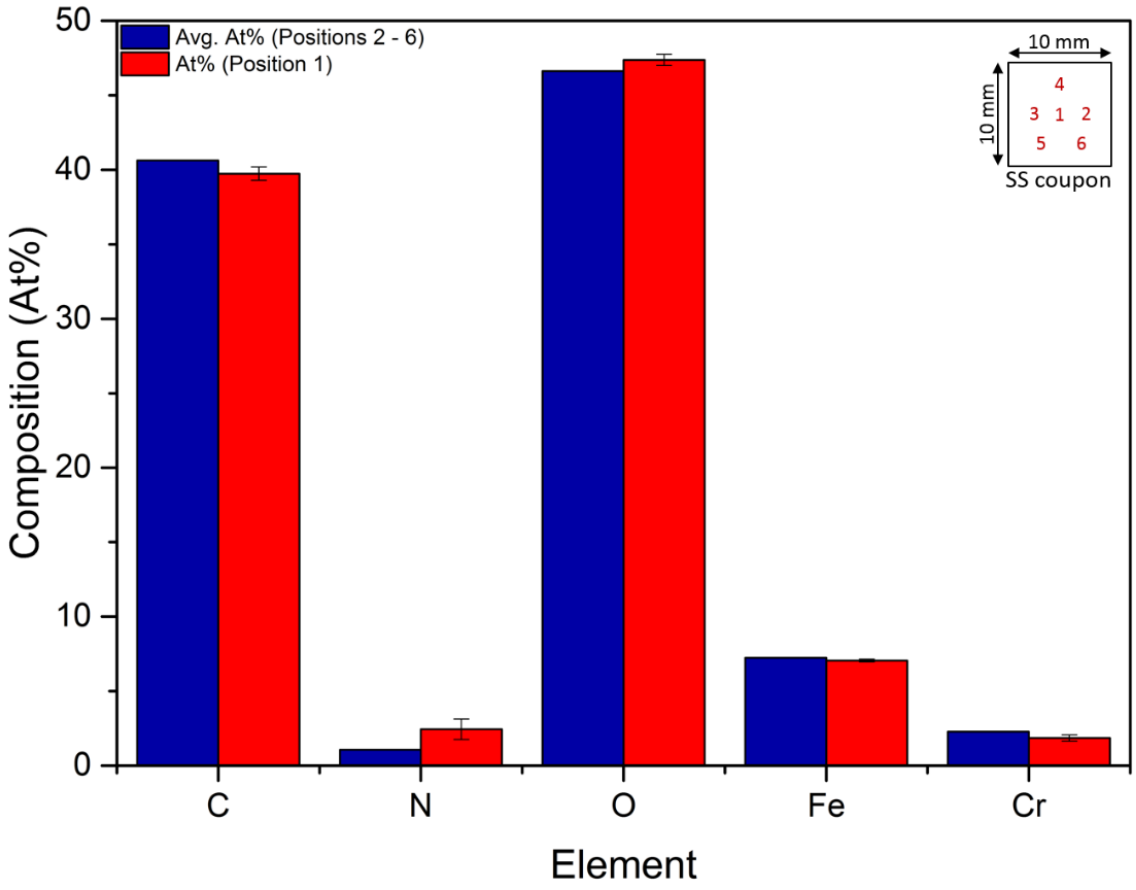

Figure 44 Bar chart comparing composition of major surface elements at P1 against average of positions P2 – P6. Error margin (± 1 σ) shown on the graph signifies how P1 composition varies in comparison to the surrounding positions (P2 – P6). Schematic representation of positions is illustrated on the top right corner.

3.5.3.2 Inter-surface composition study

Based on the outcomes from the intra-surface composition study, it was sensible to implement a comparable approach to study the cleaning method's reproducibility across various coupons. Thus, six blank, polished coupons were treated using the TAM cleaning method described in chapter 3.5.2.3. Wide range XPS survey scans were taken at two central sites within each coupon to quantify elemental compositions on the surface. Average elemental composition was calculated for each coupon (Figure 45) and an error margin of ± 1 σ was applied to better understand elemental composition variation across the coupons (Figure 46). Full spectra and table of raw values can be found in the appendices (Figure A 4, Figure A 5, and Table A 1).

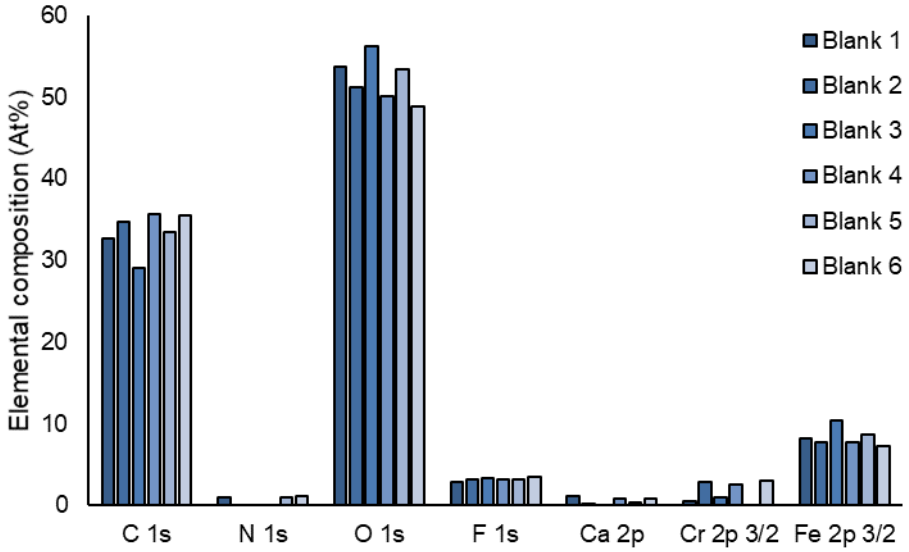

Figure 45 Average inter-surface elemental composition calculated from survey scans at two sites on each coupon.

Table 24 lists the average elemental compositions plotted in Figure 45, for all measured coupons. Similar observations found to those in section 3.5.3.1 were also valid and evident in this study. For instance, in coupons 2, 3, and 4 no nitrogen (N 1s) content was detected by XPS, which agrees with the previous findings to suggest that nitrogen is not uniformly distributed on the surface. Correlation between iron and oxygen levels were also in agreement with the postulations proposed in sections 3.5.2.3 and 3.5.3.1. In such instances, high levels of iron found on the surface of coupon 3 contributed towards the high levels of oxygen on the same coupon; as metal oxides were believed to be the main constituent of the oxygen peak in the spectra.

Table 24 Average elemental composition per coupon in atomic percentage calculated from survey measurements of two sites on each coupon. Green cells fall within an error margin of ± 1 σ (St. Dev.).

Coupon	C 1s	N 1s	O 1s	F1s	Ca 2p	Cr $2p_{3/2}$	Fe $2p_{3/2}$
1	32.66	0.95	53.75	2.80	1.16	0.49	8.20
2	34.76	0.00	51.15	3.25	0.26	2.81	7.78
3	29.11	0.00	56.27	3.27	0.00	0.92	10.44
4	35.66	0.00	50.07	3.11	0.85	2.52	7.81
5	33.44	0.97	53.34	3.11	0.43	0.00	8.73
6	35.51	1.14	48.81	3.47	0.83	2.96	7.30
Average	**33.52**	**0.51**	**52.23**	**3.17**	**0.59**	**1.62**	**8.38**
St. Dev.	**2.24**	**0.51**	**2.50**	**0.20**	**0.39**	**1.18**	**1.02**

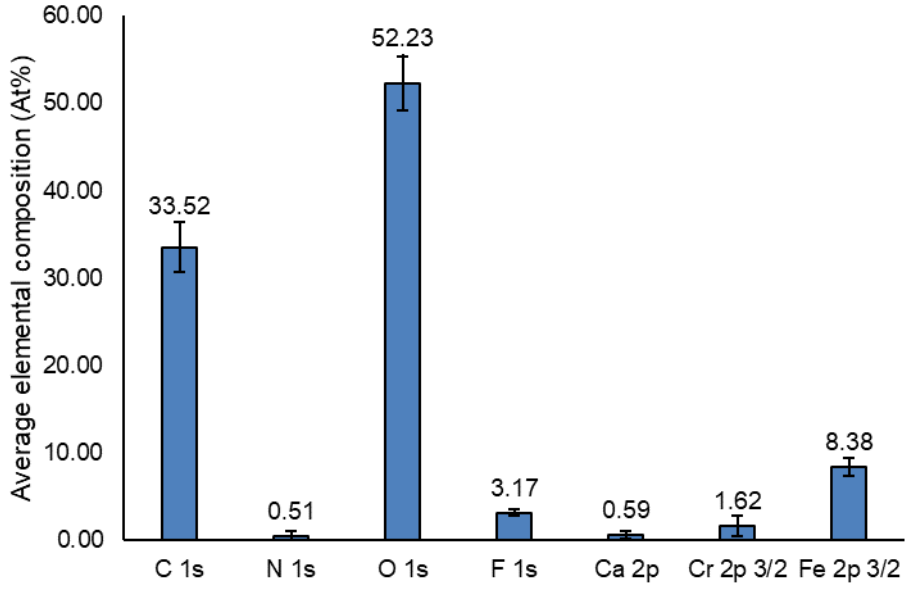

Figure 46 Average inter-surface elemental composition of coupons 1 – 6, showing acceptable error margin (± 1 σ).

Average elemental composition of coupon 1 was then compared to the average of coupons 2 – 6. Results revealed acceptable correlation across various coupons, which validates the TAM cleaning method to produce comparable surfaces with regard to elemental composition.

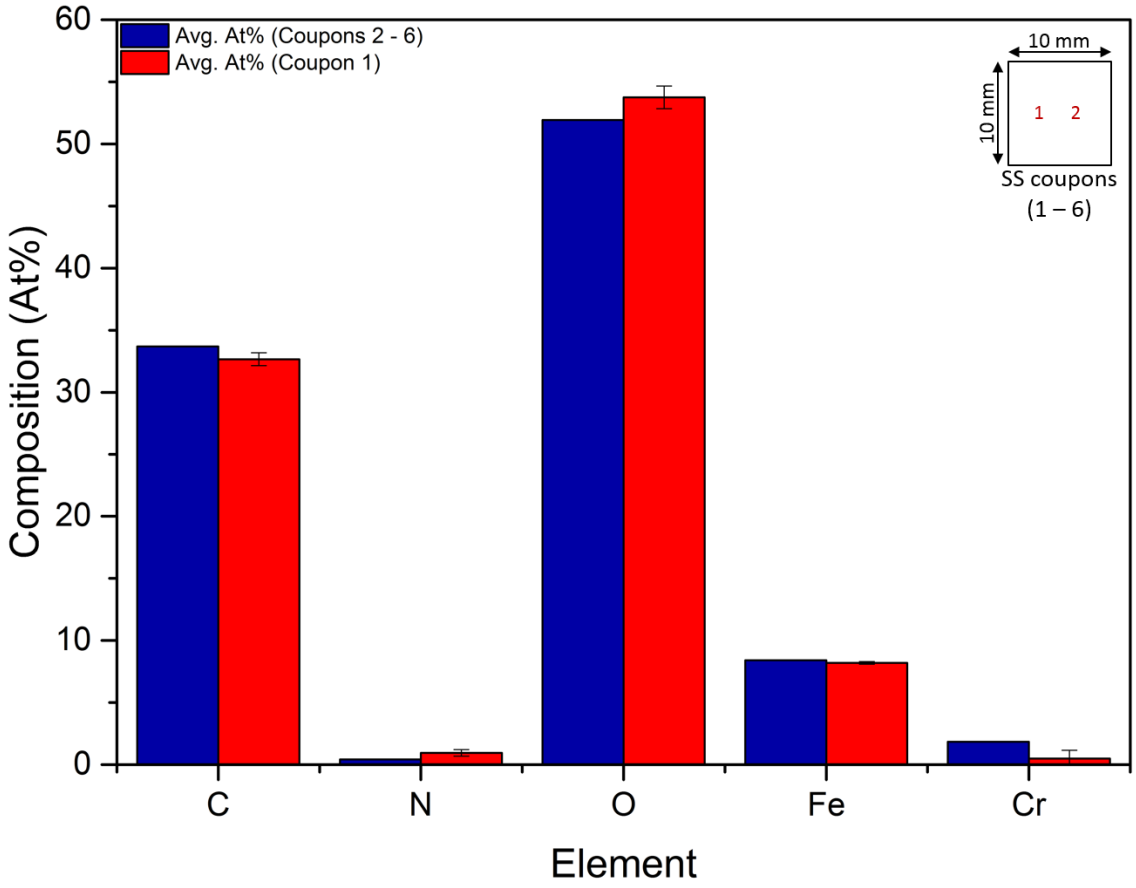

Figure 47 Bar chart comparing average composition of major surface elements at coupon 1 against average of coupons 2 – 6. Error margin (± 1 σ) shown on the graph signifies how the average composition of coupon 1 varies in comparison to coupons 2 – 6. Schematic representation of the two measured sites on each coupon is illustrated on the top right corner.

Overall, section 3.5.2 discussed the surface preparation methodology with respect to polishing, finishing, and cleaning. R_a values measured for the three polished coupons showed significant reduction in surface roughness when compared to the unpolished reference, 1.15 vs. 0.01 µm.

XPS was employed to compare the cleaning effects of the TAM solution against acetone. Results showed reduction in adventitious carbonyl species (C=O) in both C 1s and O 1s XP spectra, in favour of the TAM cleaning method. In addition, higher levels of iron content (Fe $2p_{3/2}$) and metal oxides were found on the surface of the TAM cleaned coupon, which indicated more exposure of the surface to the X-ray beam, or in other words a cleaner surface.

The reproducibility of the TAM cleaning method was then evaluated throughout a comprehensive set of inter- and intra-surface composition studies (section 3.5.3). Analysis from the intra-surface composition study revealed that central

position (i.e. P1) is representative of the surface and can be confidently chosen as an optimum scanning site. The inter-surface study, on the other hand, showed acceptable correlation of elemental composition across various coupons treated using the TAM cleaning method. More importantly, both studies have indicated that nitrogen was not uniformly distributed across the surface of the coupons.

Chapter 4 Oxidative formation of gum in model surrogate fuel

4.1 Introduction

In this chapter, TRF surrogate formulation and oxidation methods as well as analytical characterisation of the oxidation products (gum) are described and discussed. The TRF formulation method was based on the surface response model discussed in chapter 2.1. The development of the oxidation process was based on the gum formation mechanism described in chapter 2.2.3. ATR-FTIR spectroscopy was used as a main analytical technique to investigate changes in chemical composition by detecting characteristic functional groups on the oxidised TRF as well as the formed gum. GC-MS, SEM and TGA were used to characterise the synthesised gum.

4.2 Surrogate fuel components

As already discussed in Chapter 2 and Chapter 3, surrogate fuels are typically used in engine performance predictions and combustion simulations. (39, 42) Conventionally, iso-octane and dodecane are used as single-compound surrogates to represent gasoline and diesel fuels, respectively. However, such single component surrogates cannot realistically represent real fuel systems that are much more complex, especially for combustion studies. (158, 159) In this study, as a compromise, blends of toluene, n-heptane, and iso-octane were chosen to represent the typical mixture of aromatics and saturated alkanes in gasoline fuels. Blending volumes were initially calculated to be compatible with reasonable engine performance (i.e. RON and MON values), as per the fuel design principles reviewed in chapter 2.1. (42) For the envisaged studies of gum deposition and detergency, the TRF blend composition had to be extended to include gum. It is well established that reactions of olefins are associated with aerobic oxidation of gasoline fuels. (17, 60, 70) Consequently, 1-octene and 2,4-hexadiene, representing mono- and diolefins, respectively, were added to the blend to facilitate a simulated fuel oxidation process to form the model gum. Final blending composition were optimised and adjusted as per the British and European standards of unleaded petrol (EN-228). (55)

4.3 Formulation and oxidation of TRF blends

4.3.1 FTIR signatures of the TRF formulation and its components

The TRF blend was initially prepared as per the composition detailed in Table 17. Figure 48 illustrates the FTIR spectra of the TRF blend and the reference materials, followed by a discussion explaining the observed characteristic IR absorption bands.

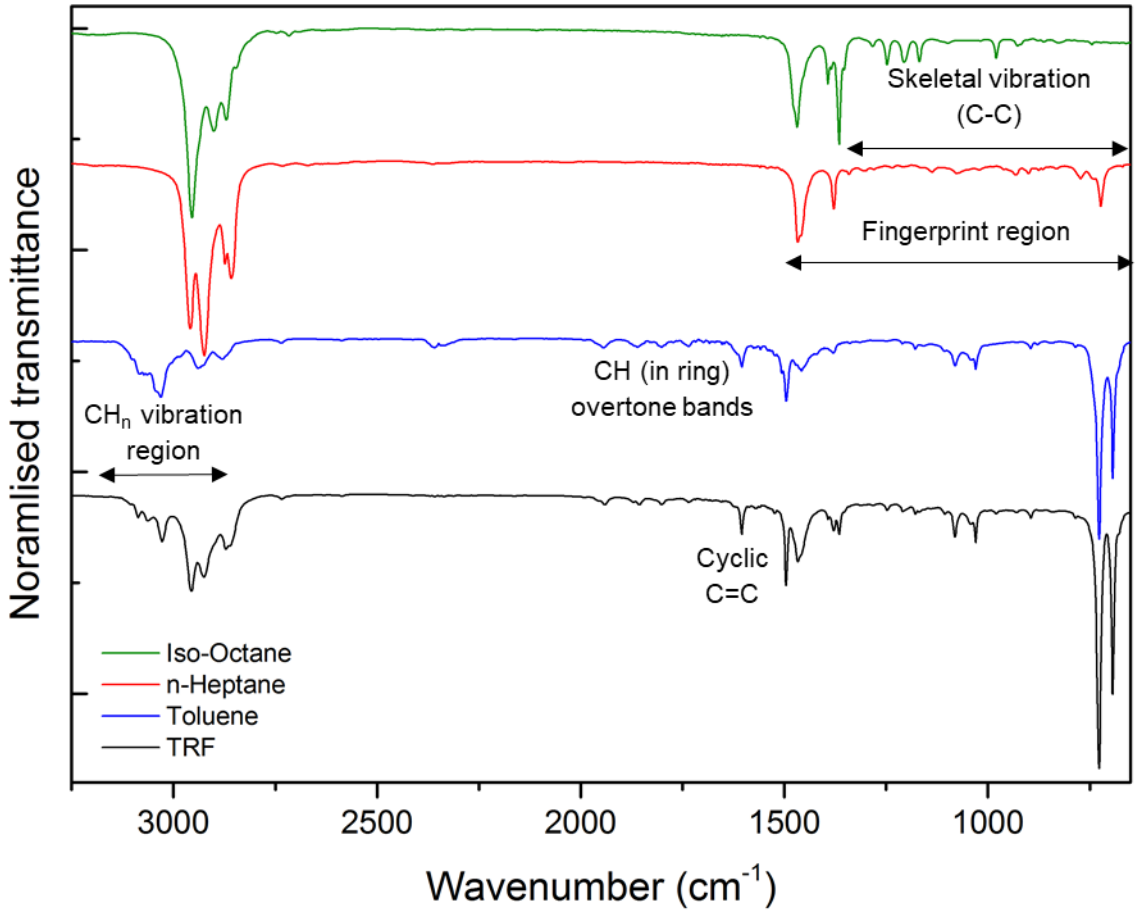

Figure 48 Y-axis offset stacked FTIR spectra comparing reference materials against formulated TRF blend.

The FTIR spectrum of the TRF blend exhibited the characteristic strong absorption bands of aromatic mono-substituted benzene rings at 693 and 727 cm^{-1}. The two intense peaks at the lower end of the spectrum are characteristic of the adjacent =CH out of plane bonds deformation (i.e. change in bond angle) vibration in toluene rings. (160) In-plane deformation vibration of the same molecules appeared as two weak peaks at 1030 and 1081 cm^{-1}.

Unique branched methyl ($–CH_3$) groups at the 2,2 position in the iso-octane (2,2,4 tri methyl pentane) vibrated symmetrically at 1365 and 1393 cm^{-1}. The bend deformation at 1365 cm^{-1} is stronger, which explains the intensities at these

wavenumbers in the TRF blend spectrum. Moreover, due to the third aliphatic methyl group attached to the carbon atom at position 2 in the iso-octane molecule, a third weak peak was found at 1379 cm^{-1}. (160) Similar vibration response within the same region was expected to be arisen from the two aliphatic methyl groups in the n-heptane molecule. CH_3 bend vibration of the methyl groups in iso-octane and n-heptane appeared in the TRF blend spectrum at 1466 cm^{-1}.

C=C in electron donor mono-substituted benzene rings (e.g. toluene) have a very unique deformation mode at ~1500 cm^{-1}. (160) A relatively strong peak at 1496 cm^{-1} was observed in the spectrum. Characteristic C=C stretch in the toluene ring also appeared at 1604 cm^{-1}. Furthermore, it is typical for mono-substituted benzene rings to show combination bands and overtone vibration (four small consecutive peaks) in IR spectroscopy at 1660 – 2000 cm^{-1} due to the =CH out of plane deformation. Toluene overtone peaks appeared in the TRF blend spectrum at 1735, 1800, 1856, and 1940 cm^{-1}. It is important to mention that C=C bonds in olefins and C=O in carbonyl groups may interfere with these bands around the 1600-1650 and 1700-1750 cm^{-1}, respectively.

The aliphatic methyl groups stretch vibration resulted from the $–CH_3$ in iso-octane and n-heptane was observed at 2871 and 2956 cm^{-1}. An iso-octane molecule has more aliphatic CH_3 groups than a n-heptane molecule (5 vs 2), which explains the higher intensity found at 2956 cm^{-1}. Similarly, the stretch vibration at 2925 cm^{-1} corresponds primarily to the acyclic $–CH_2–$ groups in the n-heptane rather than that of iso-octane (5 vs 1), which explains the comparable intensity to that of CH_3 vibrations around 2956 cm^{-1}. The relatively small peaks at the far end of the spectrum (> 3000 cm^{-1}) correspond mainly to the =CH stretch in toluene ring. All three peaks are due to the mono-substitution in the benzene ring. According to literature, the number of peaks decrease with the increase in substitution. (160)

Finally, formation of undesired products during blending can affect consequent oxidation reactions. FTIR characteristic absorption bands of the reference materials appeared unchanged in the formulated TRF blend spectrum (Table 25), confirming that no reactions have took place during blending. Therefore, the formulated TRF blend can be used in all consequent experimental stages.

Table 25 Details of characteristic IR absorption bands of the formulated TRF blend. Reference IR regions retrieved from (160).

Sample	Region (cm^{-1})	Frequency (cm^{-1})	Assignment
	670-710	693	=CH in **toluene**
	720-820	727	=CH in **toluene**
	1000-1040	1030	=CH in **toluene**
	1050-1085	1081	=CH in **toluene**
	1350-1395	1365	2,2, CH_3 bend in **i-octane**
	1370-1390	1379	–CH_3 rock in **i-oct & n-hep**
TRF	1350-1395	1393	2,2, CH_3 bend in **i-octane**
blend	1435-1475	1466	CH_3 bend in **i-oct & n-hep**
	1470-1525	1496	–C=C– in **toluene**
	1590-1625	1604	–C=C– in **toluene**
	2865-2875	2871	CH_3 stretch in **i-oct & n-hep**
	2915-2940	2925	–CH_2 stretch in **n-heptane**
	2950-2975	2956	CH_3 stretch in **i-oct & n-hep**
	3000-3105	3028	=CH stretch in **toluene**

Full details of the ATR-FTIR spectra of iso-octane, n-heptane, and toluene can be found in the appendices (Table A 2, Table A 3, and Table A 4, respectively).

4.3.2 Experimental development of TRF oxidation method: Overview

Following the formulation of the neat TRF blend, several methods were carried out to induce oxidation of the mono- and diolefin components added to the blend. Previous research had demonstrated that such olefins components can be oxidised and hence trigger gum formation in gasoline fuel (5, 17, 60). A diagrammatic overview of the TRF oxidation development process is given in Figure 49.

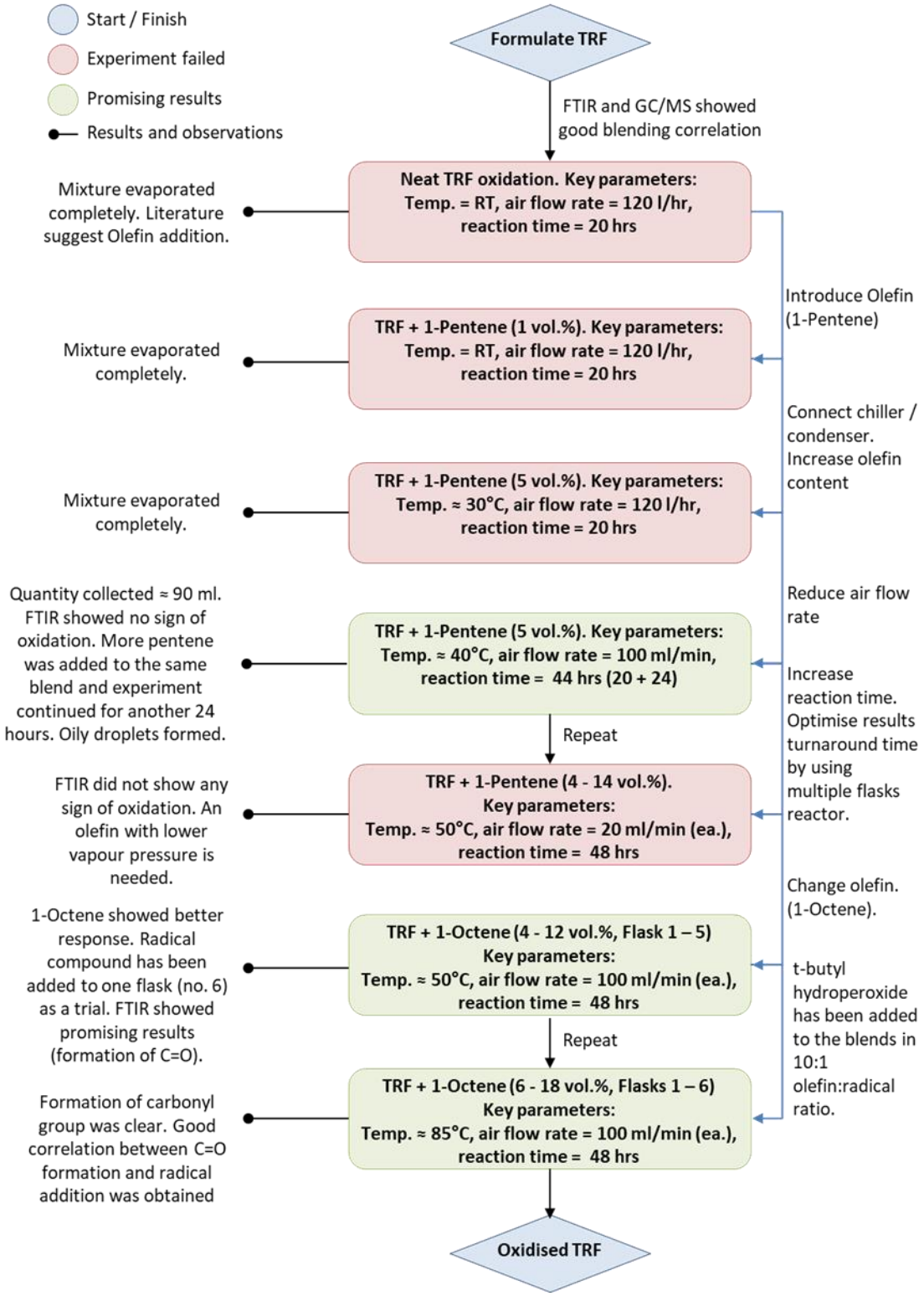

Figure 49 Colour-coded flow chart of the preliminary work conducted to oxidise the TRF surrogate.

Initially, the TRF oxidation rig shown in Figure 18 was used for this work. Its construction was informed by gum formation research reported in the literature. (35, 36) Preliminary work with this rig started by bubbling air at 120 l/h through the neat formulated TRF mixture in an open system, using an INTERPET AP1 aqua air pump at room temperature for 20 h to evaluate the possibility of oxidising the system without the aid of olefins. However, evaporative losses from the open system were too substantial to allow this approach. For example, direct oxidation with air was attempted with 1 vol% of 1-pentene, a typical olefin susceptible to oxidation in gasoline fuel. (161) Once the experiment was completed, residual materials on the flask were dissolved in acetone and analysed using FTIR. Spectra showed typical TRF absorbance with no signs of oxidation products. Moreover, no sign of olefin composition was found which indicates a complete loss of pentene during the reaction, mainly due to the considerably high vapour pressure of 1-pentene (0.82 bar at 24°C). (162)

For subsequent experiments, a quasi-closed system approach was taken, using a double surface condenser to capture and re-feed evaporated components. A water-based cooling fluid was circulated throughout the system at 10°C using a Thermal Exchange CS20 circulation chiller. Olefin content was increased to 5 vol%, but the mixture had still evaporated completely from the reaction flask with no sign of oxidation products in the IR spectra of the residual materials (not shown).

To reduced evaporative losses further, the air flow rate was controlled and adjusted to 100 ml/min to prevent excessive evaporation. A sintered Drechsel bottle head was used to enhance bubbling uniformity. 90% of the blend was thereby retained after 44 h. However, IR spectra showed no sign of oxidation products (data not shown).

4.3.3 Results

4.3.3.1 Mono-olefin oxidation in TRF

As an initial study, different TRF blends were investigated in flasks 1 – 6 of the multi-reaction system (Figure 19), with compositions summarised in Table 26. It was found that 1-octene (vapour pressure 0.02 bar at 24°C) (163) showed better response compared to that of 1-pentene. The reduction on the FTIR band at 1365 cm^{-1} indicated that the concentration of branched CH_3 functional groups from iso-octane had been reduced as a result of the reaction (Figure 50). Moreover, the extent of the peak intensity reduction was found to scale with the olefin and radical addition. More precisely, CH_3 bands were present in flask 1

(4 vol% olefin) spectra whereas flasks 5 (12 vol% olefin) and 6 (0.5 vol% tBHP) did not show any absorbance at the same IR region. This pattern suggests that an oxidation reaction has occurred. Further analysis in the carbonyl vibration region can validate these observations and help to identify any oxidation products.

Table 26 Initial TRF blend compositions by volume percentage (vol%), as utilised in the Radley carousel reaction system.

Flask no.	Toluene	Iso-octane	n-heptane	1-octene
1	62	17	17	4
2	62	16	16	6
3	62	15	15	8
4	62	14	14	10
5	62	13	13	12
6	62	12	12	5 + 0.5 tBHP

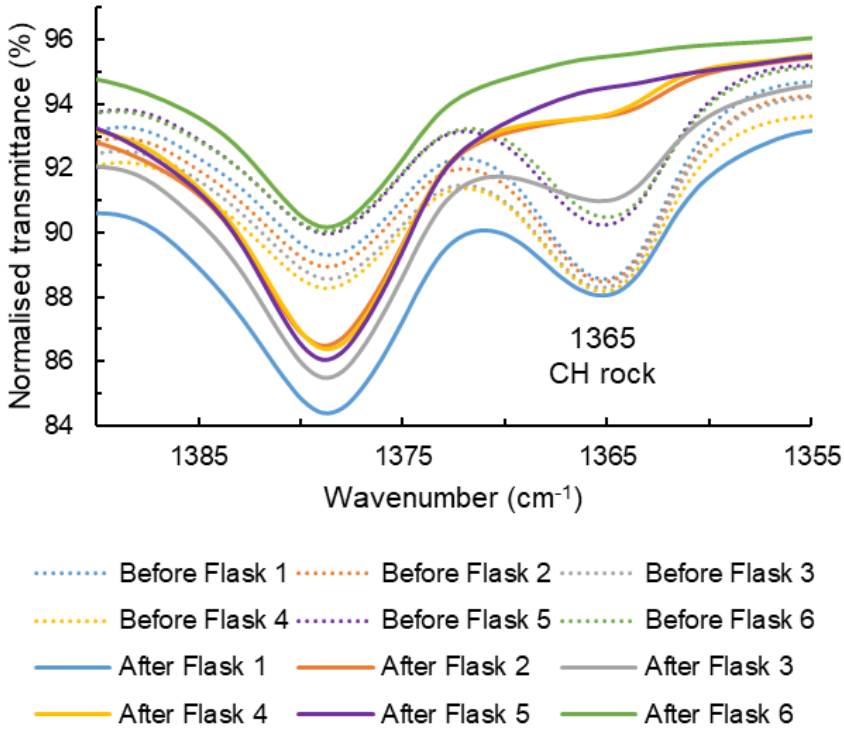

Figure 50 Pre and post-reaction FTIR absorption bands of in the symmetrical deformation region of the CH_3 group (1365 cm^{-1}).

Indeed, the spectra revealed that addition of tBHP resulted in the formation of a product with a carbonyl group (C=O) (Figure 51 and Figure 52), as one would expect as a result of oxidation (chapter 2.2.3). It appeared that some other blends showed a response similar to that observed for flask 6, around the same carbonyl vibration region (e.g. flask 5). Therefore, further analysis of the spectra was needed. Pre-reaction absorption bands were subtracted to analyse bands which will only appear as a result of the reaction. The generated spectra confirmed that the C=O band only appeared in flask 6 post-reaction spectrum.

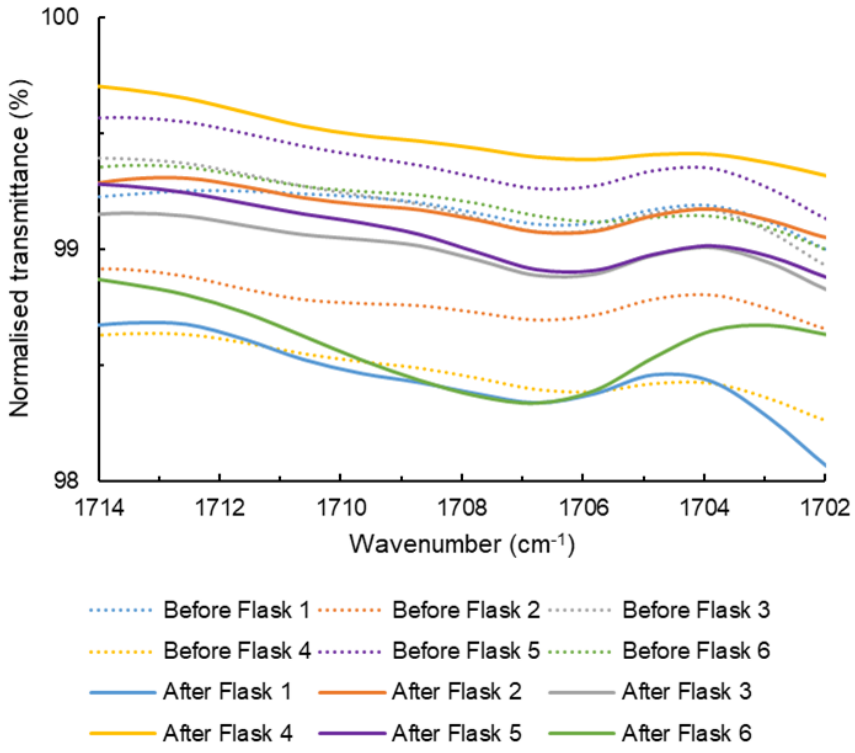

Figure 51 Pre and post-reaction FTIR absorption bands at the beginning of the C=O stretching region of carbonyl groups (1700 – 1750 cm^{-1}).

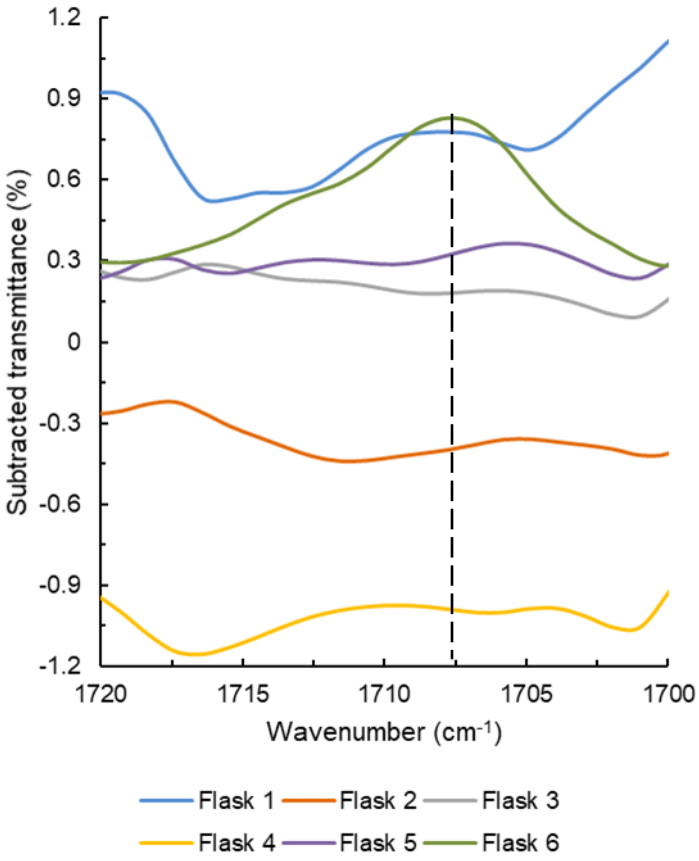

Figure 52 TRF blends difference FTIR spectra showing the positive response following the addition of tBHP and 1-octene.

According to the mechanism illustrated in chapter 2.2.3 and the reagents used in this reaction, it was believed that the oxidation product will be in the form of a ketone ($R-\overset{O}{\overset{\|}{C}}-R$). The carbonyl stretching vibrations in unsaturated ketones generally occur in the 1660 – 1700 cm^{-1} region. (160) In Figure 51, the C=O band was observed at 1707 cm^{-1}. According to the literature, the methyl vinyl ketone (Butenone) carbonyl stretching vibration appears at 1707 cm^{-1}. (164) However, additional analytical techniques are needed to confirm the chemical structure of the oxidation product.

Following the promising results achieved by adding tBHP to the composition of flask 6 (Figure 52), TRF blends were further optimised as per the composition detailed in Table 27.

Table 27 Optimised TRF blend compositions by volume percentage (vol%), as utilised in the Radley carousel reaction system.

Flask no.	Toluene	Iso-octane	n-heptane	1-octene	tBHP
1	62	17.35	17.35	3	0.3
2	62	15.70	15.70	6	0.6
3	62	14.05	14.05	9	0.9
4	62	12.40	12.40	12	1.2
5	62	10.75	10.75	15	1.5
6	62	9.10	9.10	18	1.8

Moreover, the influence of temperature was examined to ensure sufficient heat is provided to initiate the radical reaction. Several experimental studies have previously discussed the oxidation reaction of 1-octene using molecular oxygen or other oxidants such as tBHP. Temperatures quoted in literature varied between 80, 90, and 120°C depending on reaction conditions (e.g. pressure and catalyst used). (165, 166) Consequently, the reaction temperature was adjusted to match that of literature. The main constraint was the boiling point of tBHP (96°C) (167), and thus the reaction temperature was set to 85°C to avoid evaporation of the reactant during the reaction. After 48 h reaction, the appearance of blends containing higher olefin and tBHP concentrations has changed. A yellowish-brown colour was clearly apparent in the samples collected from flasks 5 and 6 (Figure 53), when compared to the clear colourless liquids in flasks 1 and 2.

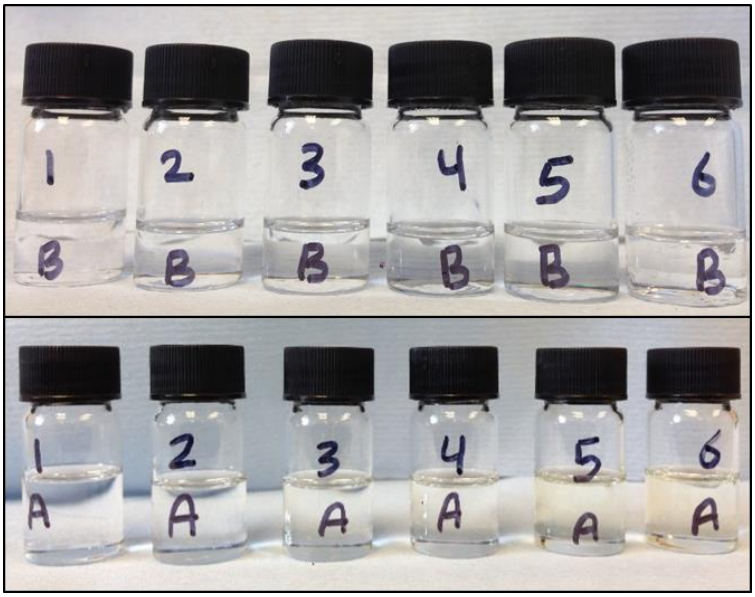

Figure 53 Top: TRF blends prior to oxidation reaction. Bottom: TRF blends following oxidation reaction.

FTIR absorption bands measured for the blends showed a similar response to that of previous experiment. Branched methyl groups at 1365 cm^{-1} have disappeared for flasks 2 – 6 following the free radical reaction. Figure 54 illustrates the resulting spectra.

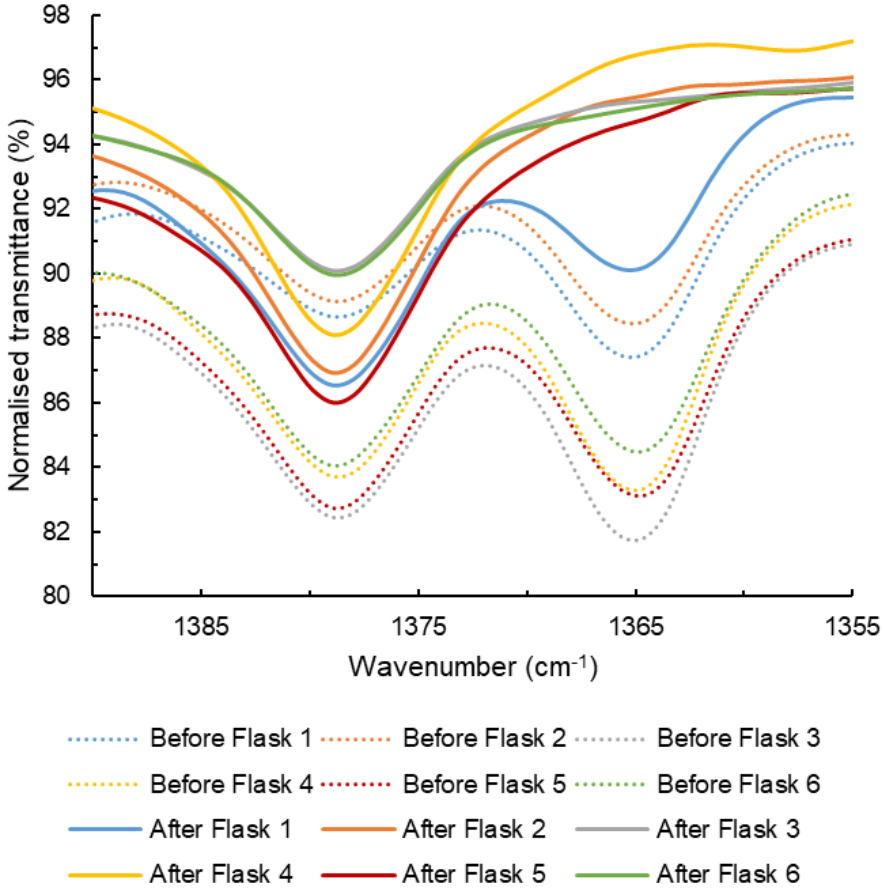

Figure 54 FTIR absorption bands of TRF blends with 1-octene and tBHP showing clear difference between the branched CH_3 bands at 1365 cm^{-1}.

This behaviour is expected due to the higher reactivity of tertiary alkyl groups ($–C(CH_3)_3$) compared to the other alkyl groups within the system. Bond energies provide a predictive indication of reactivity, as molecules with low bond energies are easier to transform into radicals. (168) Their radical forms are then more stable compared to radicals from molecules with higher bond energy. Table 28 lists the dissociation energies which are generally associated with alkyl groups.

Table 28 Absolute bond dissociation energies (kJ/mol) for branched alkyl groups. (168)

Methyl	**Primary**	**Secondary**	**Tertiary**
$–CH_3$	**$–C(CH_3)$**	**$–C(CH_3)_2$**	**$–C(CH_3)_3$**
439	423	410	397

Another region of interest is the region of C=C vibrations. It has been established that the radical reaction in olefin oxidation is governed by the stability of the allylic radicals. (17, 70) Therefore, allylic absorbance, near the 1640 cm^{-1} region, following the reaction should indicate the magnitude of the radical transformation (i.e. oxidation reaction). Figure 55 shows the FTIR transmittance of the C=C region.

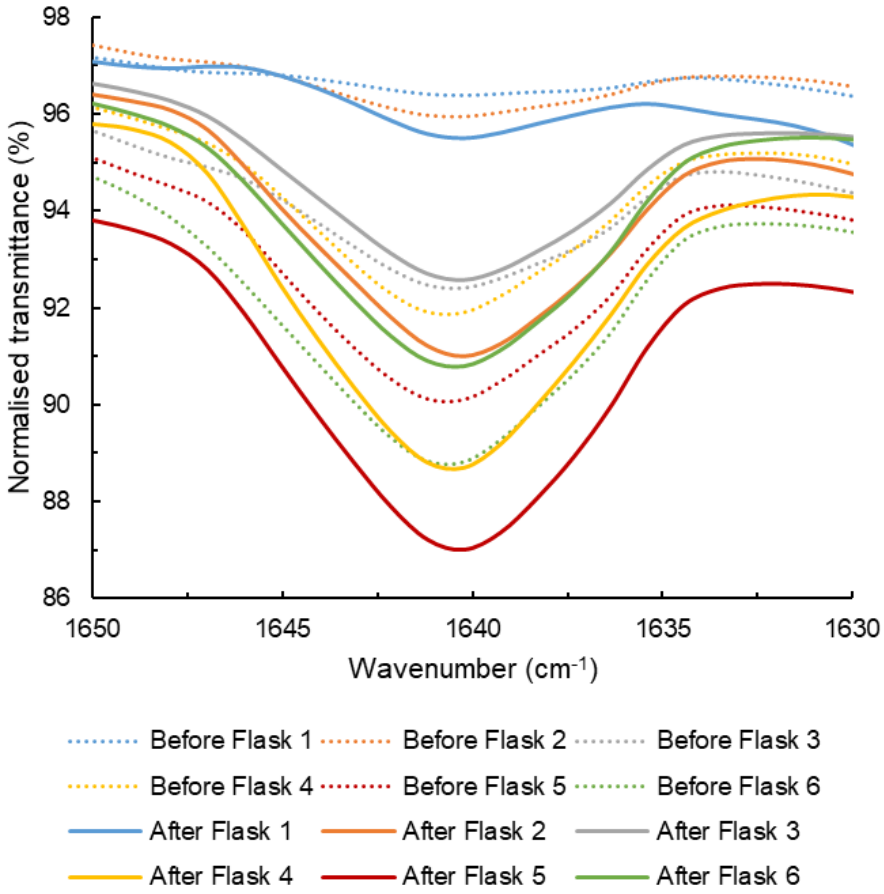

Figure 55 Pre and post-reaction FTIR spectra showing the vibrational response at the isolated alkenes stretching region (1640 cm^{-1}).

It can be seen that prior to the reaction, the C=C vibrational band intensity increases with olefin concentration in each blend, as one would expect. However, the spectrum has slightly changed following the reaction. It can still be seen that flask 1 has lower C=C intensity compared to flask 5 (3 vol% vs. 15 vol%), but a relatively stronger decrease for flask 5 indicated that the reaction had resulted in more radical transformation. Consequently, there should also be more oxidation product in flask 5, and this is indeed borne out by higher intensity, compared to other flasks in the carbonyl vibration region (Figure 56).

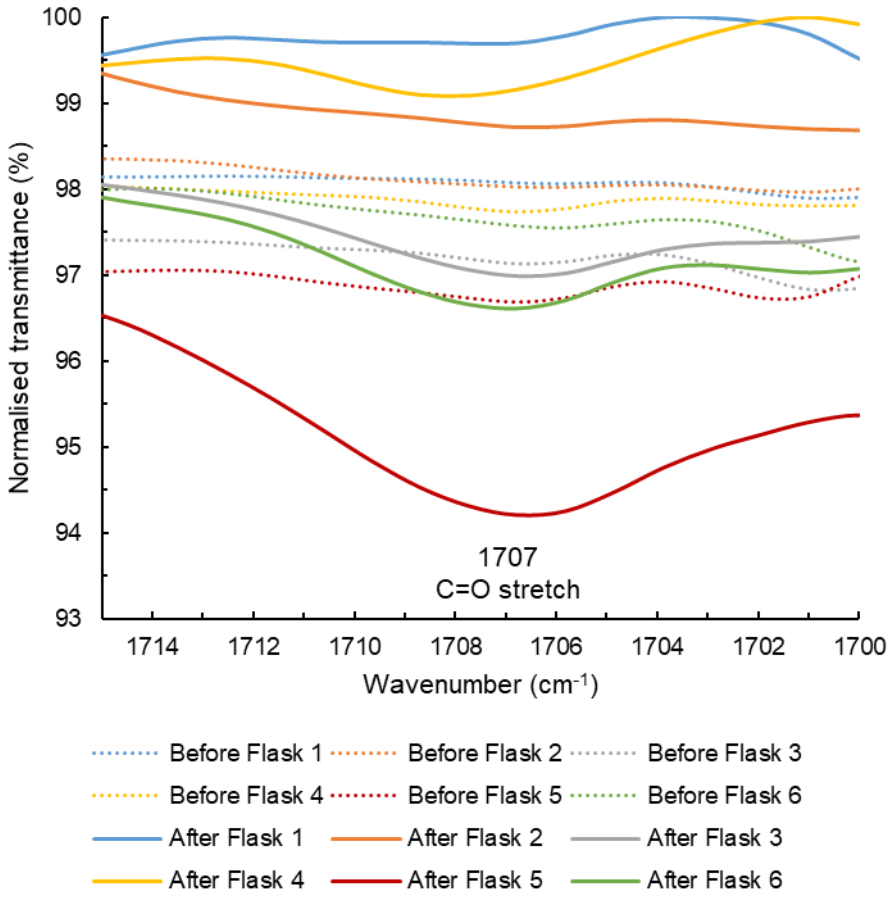

Figure 56 Pre and post-reaction FTIR spectra comparing the intensities of the carbonyl groups resulted from the oxidation reaction.

The post-reaction FTIR analysis similarly indicated that no oxidation products were observed in blends with low concentrations of olefins and tBHP (e.g. flasks 1 and 2). Although it was expected that flask 6 will have the highest intensity, calibration curve of the bands at 1707 cm^{-1} showed that reactions in flasks 4 and 6 did not follow the expected pattern. Periera et al. argued that the oxidation reaction force is governed by the stability of the allylic radicals. In other words, the longer the radical exists, the higher the potential of gum formation. (17, 70) Further analysis of the carbonyl (C=O) region (1700 – 1750 cm^{-1}) was used to examine the oxidation reaction. Figure 57 and Figure 58 illustrate the FTIR transmittance patterns of the TRF blends oxidised using 1-octene at the C=C (1640 cm^{-1}) and C=O (1707 cm^{-1}) IR regions.

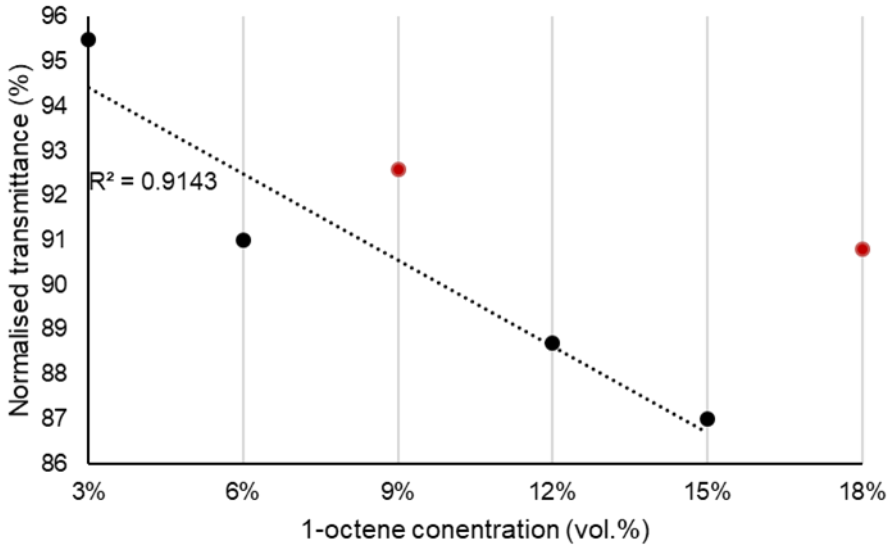

Figure 57 Intensity of the isolated alkenes C=C stretching band absorptions of the reaction product as a function of initial 1-octene concentration. Data derived from Figure 55.

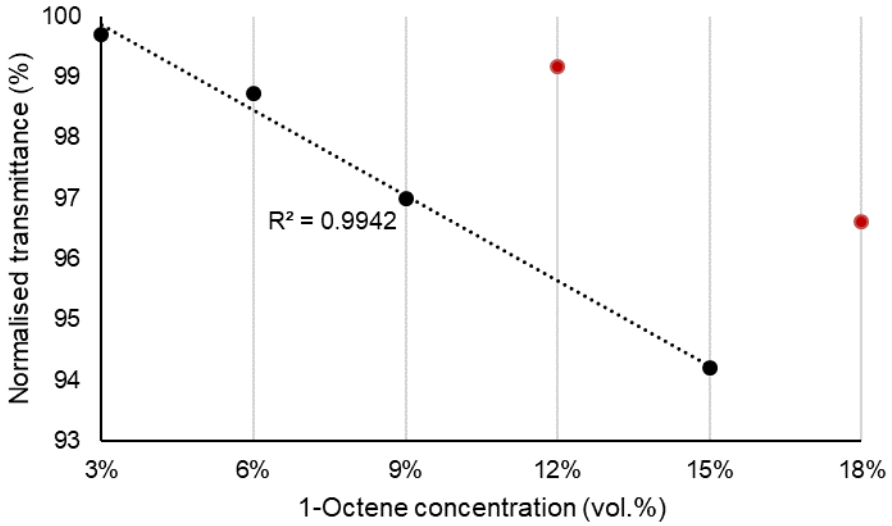

Figure 58 Intensity of the carbonyl group C=O stretching band absorptions of the reaction product as a function of initial 1-octene concentration. Data derived from Figure 56.

Overall, it can be concluded that the employed TRF blend oxidation method led to the formation of oxygenated compounds, including carbonyl species, but no evidence for high molecular weight compounds resembling gum was observed. The formation of 2-octenal has previously been reported for the oxidation of 1-octene in the presence of tBHP, (169) and this would be compatible with the observations made here.

The following mechanistic model could explain the anticipated radical transformation (where I: Initiation, P: Propagation, and T: Termination) leading to 1-octenal and ketones. However, there was no indication that the reaction proceeded beyond the formation of light oxygenated products, which is perhaps not too surprising given the monofunctional nature of 1-octene.

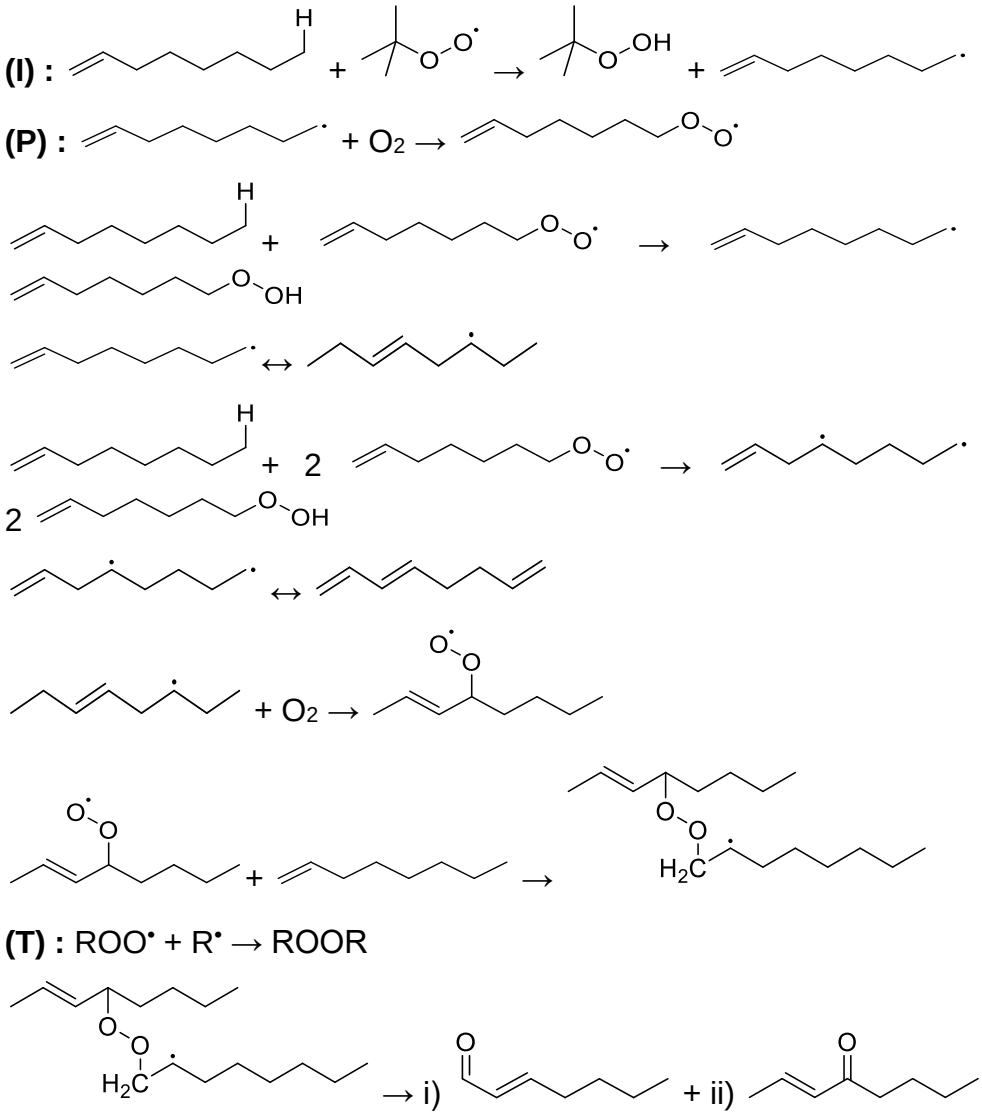

4.3.3.2 Diolefin oxidation in TRF

Only a small amount of gum was observed with 1-octene (see section 4.3.3.3), presumably due to its monofunctional nature that does not allow for extensive condensation and cross-linking of several hydrocarbon components. 2,4-hexadiene was therefore added to the formulation to allow the gum formation process. The addition of diolefins resulted in a noticeable response with respect to C=O group formation due to the formation of allylic radicals. FTIR spectra were collected for the neat and oxidized TRF blends to emphasise on the formed

chemical groups. The following spectrum shows the subtracted transmittance near the carbonyl region.

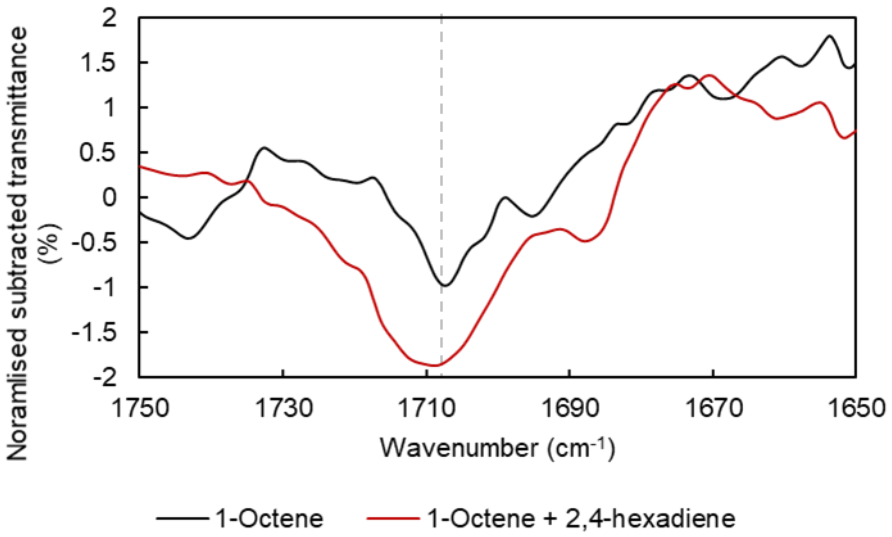

Figure 59 Subtracted FTIR spectra showing C=O bond formation at 1709 cm^{-1}. Negative y-axis values indicate less transmittance from the oxidised TRF blend.

In a similar previous study, base gasoline samples were spiked with different mono- and diolefins namely 1-octene, 1-hexene, cyclohexene, 1,5-hexadiene, and 2,4-hexadiene to evaluate the effect of each component on gum formation. It was found that cyclic and conjugated olefins forming secondary allylic radicals (i.e. cyclohexene and 2,4-hexadiene) contributed the most towards gum formation. Mono- and non-conjugated olefins did not exhibit similar effects (70), as observed in the 1-octene experiment in this study (flask 6 in Figure 57 and Figure 58).

4.3.3.3 Gum content evaluation

It is well established that mono- and diolefins tend to increase the tendency of gum and deposit formation in gasoline fuels. Several studies have illustrated that olefinic molecules have higher susceptibility towards oxidation and consequently formation of gum precursors, typically in the form of polymerised ketones, aldehydes, carboxylic acids, or esters. (17, 35, 60, 170) For gum quantification, a sample beaker was weighed before and after the modified lab-scale gum content method explained in chapter 3.2.2. Calculation as per the ASTM D-381 (57) revealed formation of 110 mg / 100 ml of oxidation products (gum). Figure 60 show the resinous formed products.

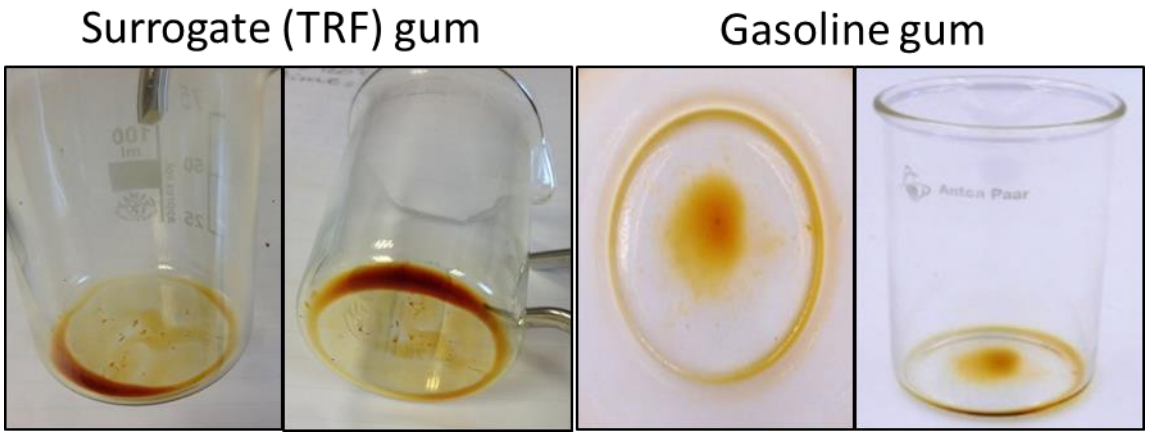

Figure 60 Oxidation products collected using the lab-scale gum content method (left) compared to actual gasoline gum obtained using standard ASTM D-381 method (right). Actual gasoline's gum images retrieved from Anton Paar (171).

Further systematic experimental repeats were conducted to ensure the method's reproducibility. Quantified gum increased to an average of 452.9 mg / 100 ml (σ = 12.7 mg / 100 ml) within three consecutive repeats. It is important to mention that the 110 mg / 100 ml sample was produced from a TRF blend oxidised using mono-olefins. Once diolefins were introduced into the blends, gum content has increased significantly (Figure 61).

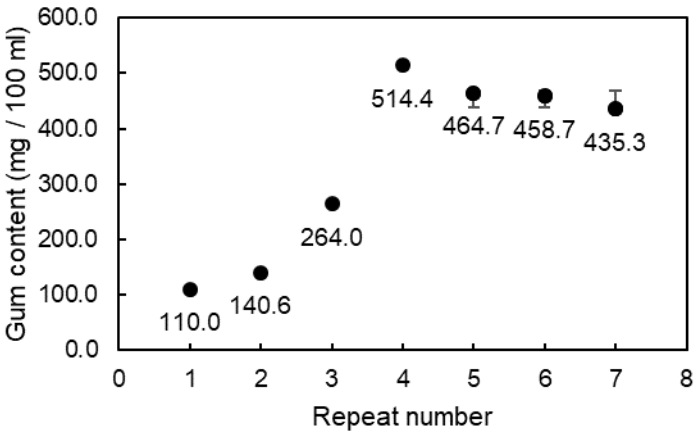

Figure 61 Repeats of gum formulation and quantification methods showing acceptable reproducibility within the last three consecutive tests (± 1 σ).

4.3.4 Physical and chemical characterisation of oxidation products (gum)

4.3.4.1 ATR-FTIR analysis

Formulated gum was analysed using FTIR spectroscopy to pinpoint the chemical functional groups of the oxidation products and eventually enable chemical structure prediction. It was suspected that the mono- and diolefin compounds will combine to form tri-olefin species within the oxidation products. The fingerprint region of the spectrum showed C=C vibration bands at 968 and 1621 cm^{-1}, which correlate with tri-olefins IR bands from literature (987 and 1621 cm^{-1}). (172) It can also be deduced that the transmittance spectrum does not follow that of a carboxylic acid, where the OH vibration band is usually observed within the same region of the CH stretching (~3000 cm^{-1}). (160) The following table lists the characteristic IR peaks observed for the fingerprinting chemical functional groups.

Table 29 Characteristic ATR-FTIR band assignments of oxidation products.

Chemical group	Wavenumber	Assignment
C=C *w*	1605-1640	Olefinic C=C stretch
C=O *s*	1707	Carbonyl stretch
CH *m*	2858-2957	CH_n stretch region
OH *b*	3379-4446	Hydroxyl stretch

Legend: (*w*) weak, (*s*) strong, (*m*) medium, and (*b*) broad.

FTIR spectra were collected for the oxidised TRF blend and the gum product throughout different stages of the gum content experiment to observe the changes in functional groups as a function of time. The first sample was taken prior to the gum content experiment (i.e. for the oxidised TRF blend at zero minute). The second sample was a gum-concentrated TRF, which was collected after 20 min from the start of the experiment. The same sample was further concentrated by adding gum product, which was collected at the end of the experiment, to verify that the observed C=O (Figure 62) and OH (Figure 63) absorption bands increase as a function of gum content. Full spectra can be found in the appendices (Figure A 6).

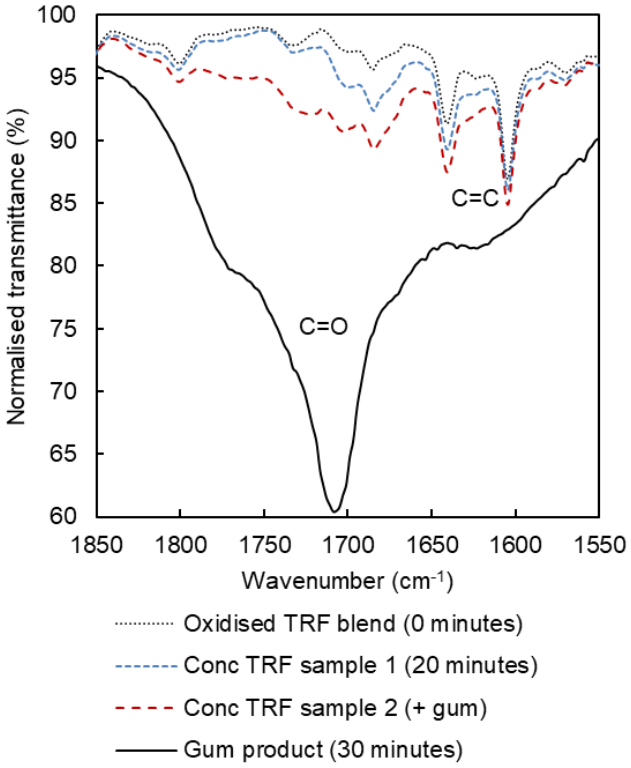

Figure 62 Alkenes (C=C) and carbonyl (C=O) FTIR absorption bands from the oxidised TRF blends and oxidation products (gum) collected at different times.

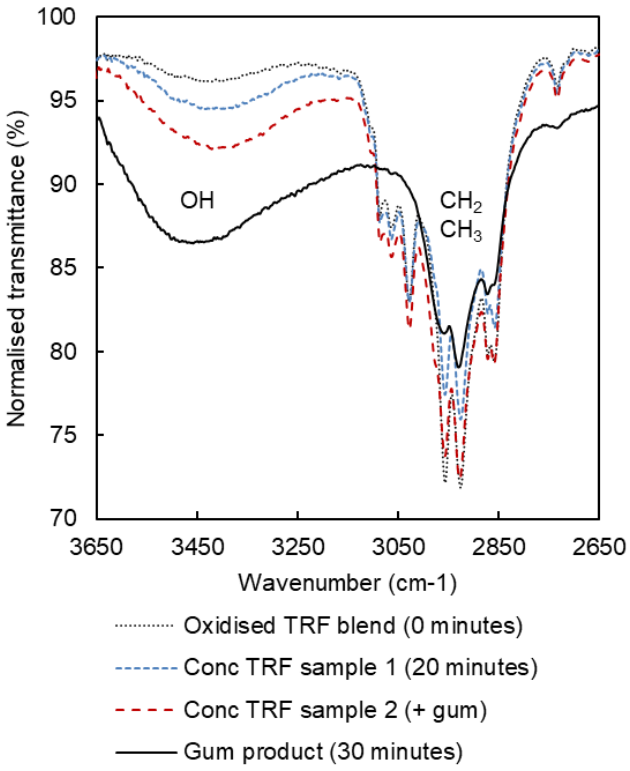

Figure 63 Aliphatic (CH_n) and hydroxyl (OH) FTIR absorption bands from the oxidised TRF blends and oxidation products (gum) collected at different times.

4.3.4.2 Thermogravimetric analysis (TGA)

Thermal degradation of the oxidation products was also taken into consideration when analysing the formed gum. The decomposition profiles is crucial to understand the structural integrity of the formed products. Analysis was conducted using Mettler Toledo TGA/DSC 1 thermogravimetric analyser. Two samples of oxidation product (gum) were heated under nitrogen (35 – 400°C) and nitrogen/air (35 – 200°C / 200 – 400°C) respectively. The first sample (N_2) was subjected to 10 min isotherm at 200°C, whereas the N_2/air sample was subjected to 3 min isotherm at 200°C followed by 20 min isotherm once air was introduced. Data analysis was performed using Mettler Toledo STARe Evaluation Software. The following figures illustrate the decomposition behaviour of the oxidation products (TGA) in addition to the differential thermogravimetric (DTG) curve as a time derivative (dx/dt).

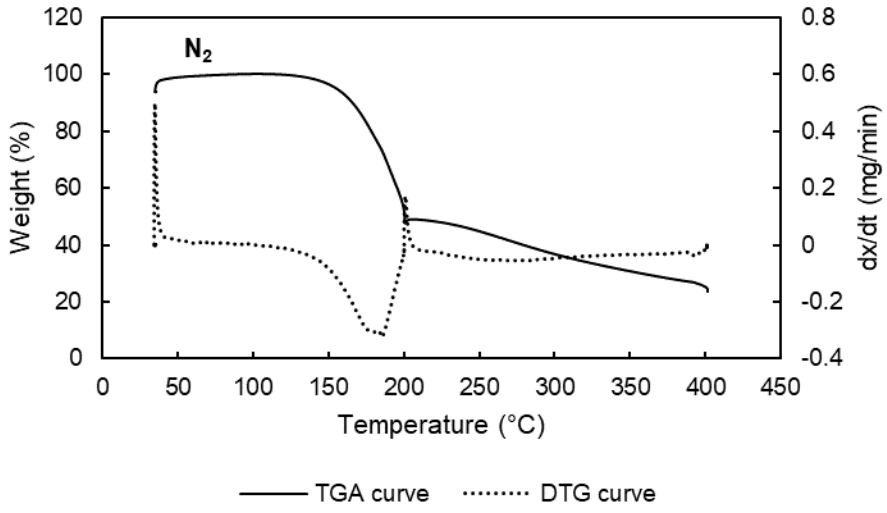

Figure 64 Thermal degradation profile of the oxidation products heated under nitrogen, showing gum decomposition of ≈ 75% (35 - 400°C) with a sharp mass loss (48%) between 150-200°C.

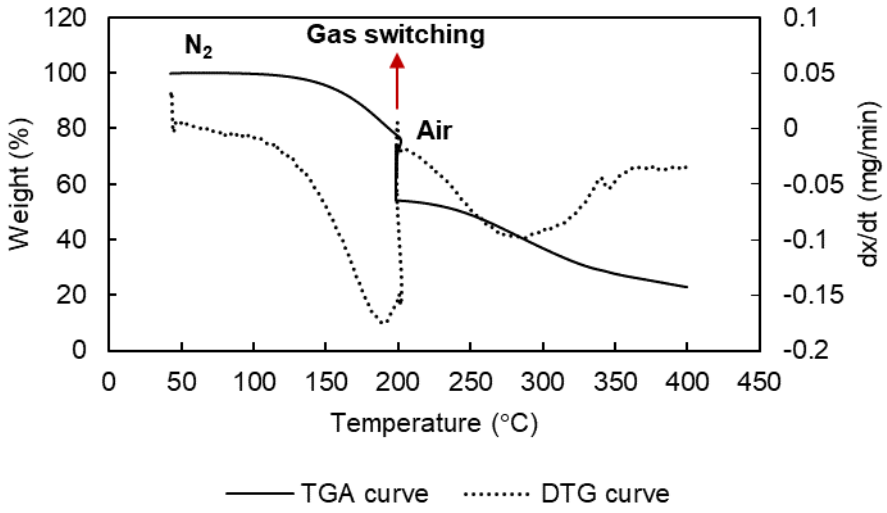

Figure 65 Thermal degradation profile of the oxidation products heated under nitrogen/air, showing gum decomposition of ≈ 74% (35 - 400°C), with a sharp mass loss (43%) between 150-200°C.

TGA and DTG curves of both samples exhibited a thermal event between approximately 150 – 200°C. Another event was only observed in the N_2/air sample (~ 250°C). A similar number of events were observed for actual gasoline gum samples heated under nitrogen and air. (31) However, onset and endset temperatures were slightly higher due to the complex composition of gasoline in comparison to the formulated/oxidised TRF. Table 30 lists the thermal events and decomposition values.

Table 30 TGA results calculated for the gum samples processed under nitrogen and nitrogen/air.

Gas	Event	Onset T (°C)	Endset T (°C)	Mass loss (%)	Residual mass (%)
N_2	1	159	195	48	25
N_2/Air	1	153	200	43	26
	2	241	328	20	

In comparison, onset and endset temperatures for actual gasoline gum heated under nitrogen were 208 and 268°C respectively. Samples heated under air recorded two thermal events with onset and endset temperatures of 207 – 278°C and 512 – 578°C respectively. (31) In SI engines, surface temperatures at fuel injectors' tips would typically reach just over 100°C, whereas at the combustion chamber may vary between 250°C to over 600°C at the exhaust valves. (5, 6, 8, 61, 62) Thus, the observed mass losses between 150 – 200°C indicate that gum or gum precursors would decompose and form hard deposits on the injectors' tips and intake valves tulips (outer surface). Since the aim of this work was to study gum behaviour prior to combustion, it was decided to evaluate the decomposition profile to a maximum temperature of 400°C

4.3.4.3 Gas chromatography coupled with mass spectroscopy (GC-MS)

Following the results obtained from TGA, it was of a great benefit to identify the components which constitute most of the oxidation products. The obtained mass spectrum revealed that the most abundant molecule within the oxidation products has a molecular weight (MW) of 208.1 $g.mol^{-1}$ with a retention time of 13.14 min. Typical MW values of gum in gasoline fuel varies in the range of 200 – 500 $g.mol^{-1}$. (63) Since the oxidation products were formed from relatively low MW components, representing the light fraction of gasoline fuel, it was expected to be at the lower end of the typical range. Actual m/z values (208.1: 100%, 209.1: 15.8%) retrieved from OpenChrom (173) following the analysis of the mass spectrum showed good correlation with that of theoretical values calculated by ChemDraw. Moreover, the MW of the fragmentation shown in Figure 66 (i.e. 71, 97, 123, and 165 $g.mol^{-1}$) match that of the calculated fragment ions for the anticipated chemical structure ($C_{13}H_{20}O_2$), shown in Figure 67. The following figure illustrates the fragment ions of the subject molecule, including the parent peak (M+).

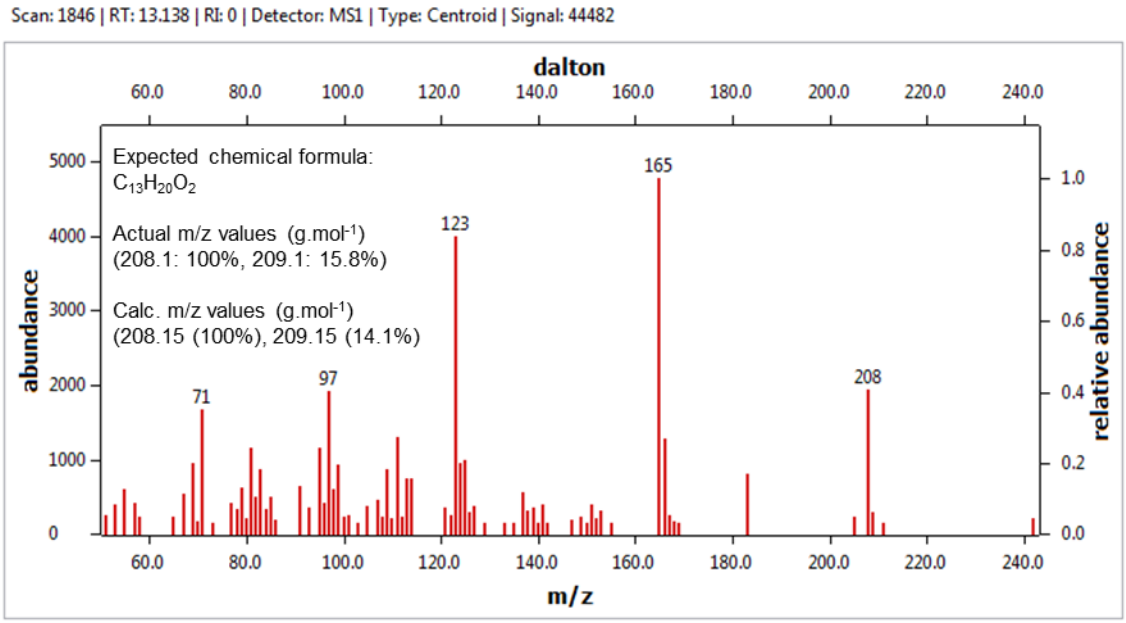

Figure 66 Fragment-ion mass spectrum of the abundant molecule in the gum product.

It was expected from the radical chain reaction with 1-octene and 2,4-hexadiene to produce a tri-olefin molecule, which was also suggested by the obtained FTIR spectroscopy. C=O and OH functional groups were also confirmed to be present. Hence, based on the above described analyses, the following chemical structure was expected to be most relevant to the synthesised gum (or gum precursor).

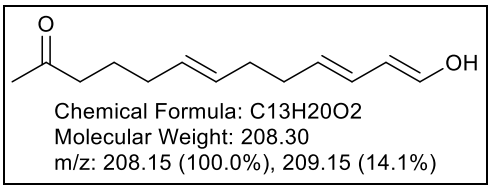

Figure 67 Predicted chemical structure of the most abundant molecule found within the oxidation product.

The observed molecular masses also correlate to the fragment ions of the predicted molecule.

Table 31 Fragment ions and molecular weights as calculated from the predicted molecule.

Fragment ion	MW (g.mol^{-1})	Fragment ion	MW (g.mol^{-1})
$C_4H_7O^{\bullet}$	71	$C_{11}H_{17}O^{\bullet}$	165
$C_6H_9O^{\bullet}$	97	$C_{13}H_{20}O_2$ (M^+)	208
$C_8H_{11}O^{\bullet}$	123		

4.3.4.4 IR frequency prediction

In support of the predicted structure, Density Functional Theory (DFT) calculations were performed to predict the IR frequency of the proposed gum structure shown in Figure 67. Geometry of the predicted molecule was initially optimised using molecular modelling and visualisation package (Avogadro 1.1.1). (174) The force field chosen for the molecule was MMFF94 with a steepest descent algorithm. (175) Cartesian coordinates were then used for tighter geometry optimisation and IR frequency calculation using quantum chemistry software (ORCA 3.0.3). (176) Optimisation was converged using B3LYP functional and def2-TZVP basis set with a maximum SCF iterations of 125. (177) A RIJCOSX approximation with def2-TZVP/J auxiliary basis set was applied to the calculations to speed up the Hartree-Fock step. (178) ORCA_mapspc function was then called to extract the IR frequency and plot the spectrum as per the following values (-w = 25, -x0 = 650 cm^{-1}, -x1 = 4000 cm^{-1}, and -n = 3476). Where -w is Gaussian width, -x0 and -x1 are wavenumbers representing the start and end of the spectrum, and -n is number of points. Scale factor of 0.965 was applied. (179) The predicted IR frequency was found to be in good correlation with the actual spectrum of gum.

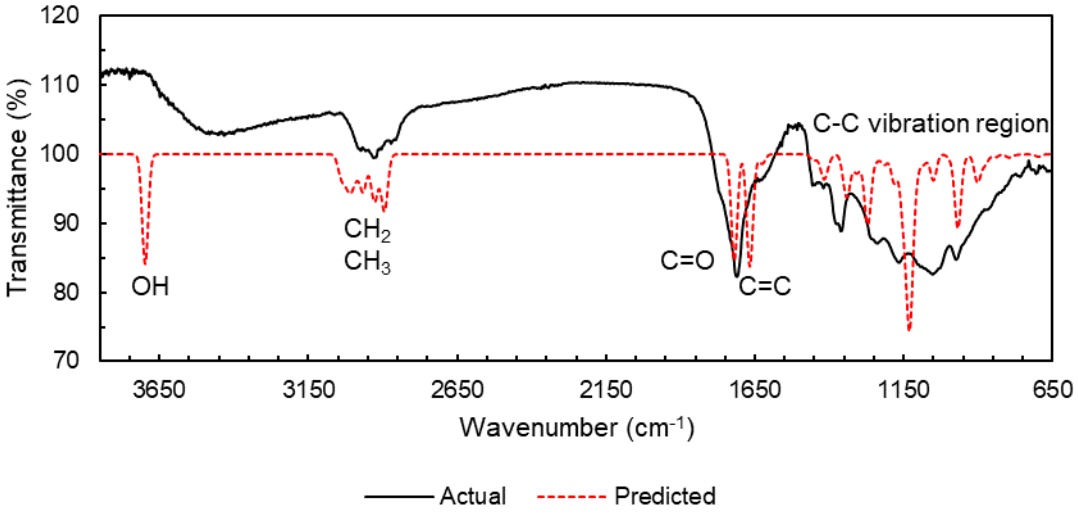

Figure 68 Actual vs predicted IR frequencies of gum sample and predicted molecule respectively.

4.3.4.5 Scanning electron microscope (SEM)

Microscopic images of the oxidation products were taken using Carl Zeiss EVO MA15 SEM instrument. Mirror-polished 316 stainless steel (SS) coupon (surface roughness, Ra = 0.01 µm) was immersed into oxidised TRF blend for 10 seconds at room temperature. Once taken out, the coupon was allowed to dry in fume hood prior to scanning. Images revealed circular islands of gum distributed over the metal substrate. Gum deposits exhibited 'coffee-stain' effect which resulted in the observed ring shape (Figure 69, b). The rings inner diameter was approximately 90 – 100 µm. In a comparable study conducted on gasoline fuel, gum deposits were also found to form clusters on the steel surface (Figure 9). (36) However, unlike the TRF gum, gasoline gum deposits were in the form of fused spherical particles.

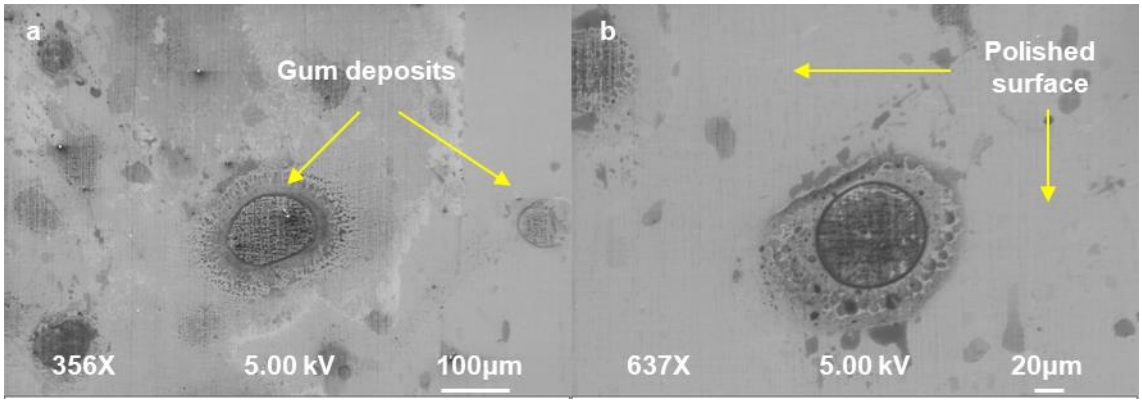

Figure 69 SEM images of residual gum on top of a 316 SS coupon at 100 and 20 µm scale, a and b respectively.

4.4 Conclusion

In summary, a TRF surrogate fuel has been formulated using toluene, n-heptane and iso-octane as primary components. Mono-olefinic component (1-octene) was added to the blend to trigger the oxidation reaction. Tertiary butyl hydroperoxide was used as a radical initiator in a 1:10 radical to olefin ratio. Oxidation process was then further optimised by the addition of 2,4-hexadiene; as diolefins are more susceptible towards oxidation. All volumes were optimised and adjusted as per the EN-228 gasoline specification.

Presence of oxidation products containing carbonyl (C=O) functional group was confirmed by ATR-FTIR spectroscopy. Analysis of TRF blends oxidised using diolefins showed better response with regard to the C=O peak (1709 cm^{-1}), compared to 1-octene. Gum content evaluation also showed significant increase, in favour of 2,4-hexadiene (110 vs 453 mg / 100 ml).

FTIR analysis of the oxidation products showed sharp intense C=O peak at 1707 cm^{-1} as well as a characteristic OH peak at ~ 3440 cm^{-1}. The thermal decomposition profile of gum showed significant mass loss of 48% and 43% between 150 – 200°C for samples heated under nitrogen and nitrogen/air respectively. GC-MS analysis suggested that the molecular weight of the most abundant molecule was approximately 208 $g.mol^{-1}$ with an expected chemical formula of $C_{13}H_{20}O_2$. Computed IR frequency was in agreement with the obtained FTIR spectra for the oxidation products. SEM images of deposits on stainless steel substrates showed ‘rings’ of gum randomly distributed over the surface.

4.5 Recap

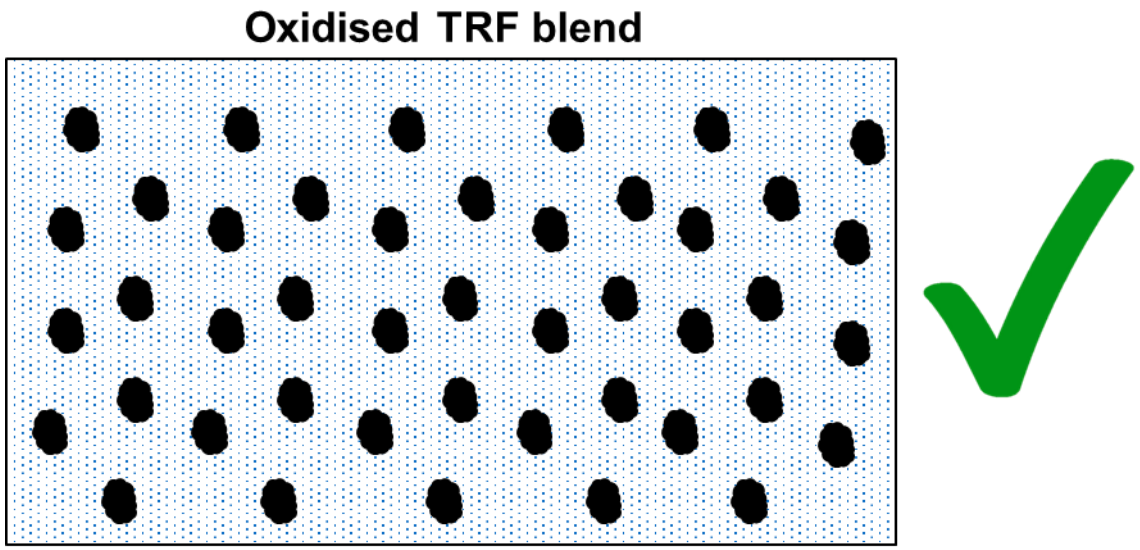

Next chapter . . .

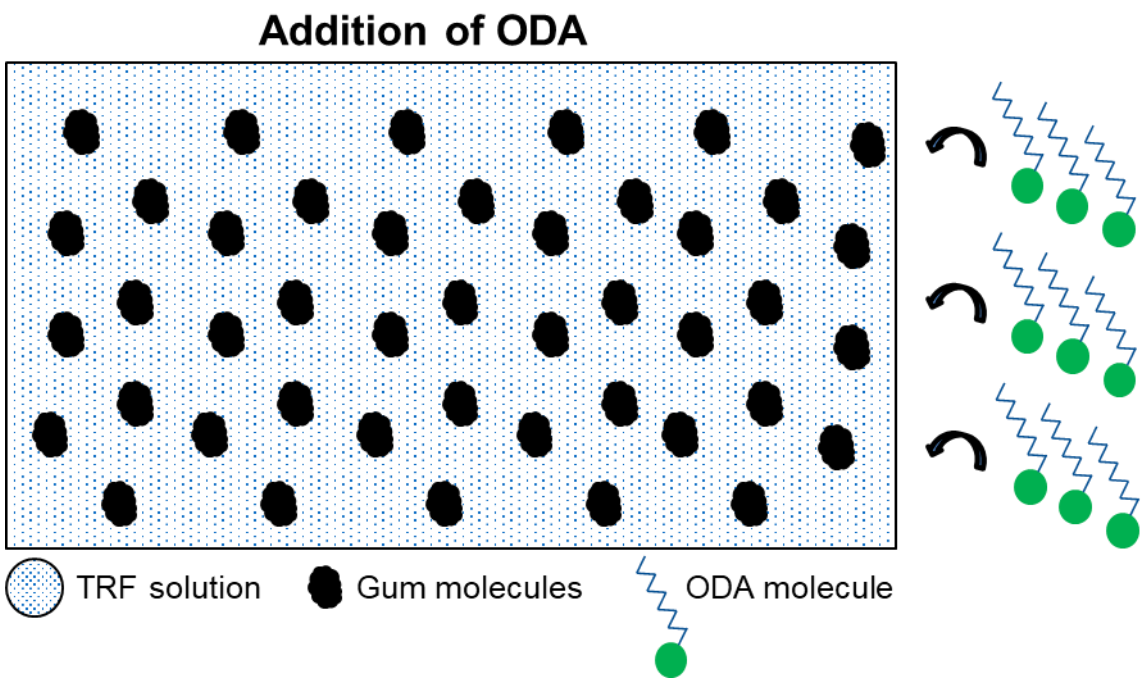

Chapter 5 Addition of ODA into oxidised surrogate fuel

5.1 Introduction

After having established a reproducible method to formulate TRF surrogate fuels with and without gum, introduction of the third component of the model system, the model detergent, was examined. As discussed in chapter 2.4.1, octadecylamine is a primary amine with a long aliphatic hydrocarbon tail (C_{18}) which resembles the characteristic chemical structure of gasoline detergents (i.e. fuel-soluble tail with a polar amine head). In this chapter, the effect of ODA introduction into the oxidised TRF blends at various concentrations is described to examine the effects of ODA on gum and gum adsorption. The resulting system will provide the basis for examining the effect of ODA on gum and the metallic substrates.

5.2 Characterisation of ODA

5.2.1 ATR-FTIR spectroscopy

Figure 70 displays the ATR-FTIR spectra of solid ODA. Characteristic peaks are assigned on the spectra and detailed in Table 32. The CH_2 splitting observed at 1462 – 1473 cm^{-1} is characteristic of ordered packing in crystalline molecules. (86) The split is typically of the order of 8 – 12 cm^{-1} depending on chain length. (180) In the present case, it was found to be 11 cm^{-1} which was very close to the 10 cm^{-1} split observed in (180) for C_{18} molecules. The weak NH_2 peak at 1607 cm^{-1} arises from -NH_2 groups in primary amines. (160, 181) The broad peaks near 3165 – 3252 cm^{-1} as well as the strong narrow peak at 3330 cm^{-1} likewise arise from NH_2 and NH stretching vibrations in primary amines. (160, 182) The CH_n region (2848 – 2964 cm^{-1}) exhibited characteristic CH_2 and CH_3 vibrations. The two strong peaks at 2848 and 2916 cm^{-1} correspond to symmetric and asymmetric CH_2 stretching vibrations, respectively. Significantly weaker CH_3 peaks were observed at 2955 and 2964 cm^{-1}. The difference in intensity was due to the large number of CH_2 groups in comparison to the end alkyl group (17 vs 1 in each ODA molecule).

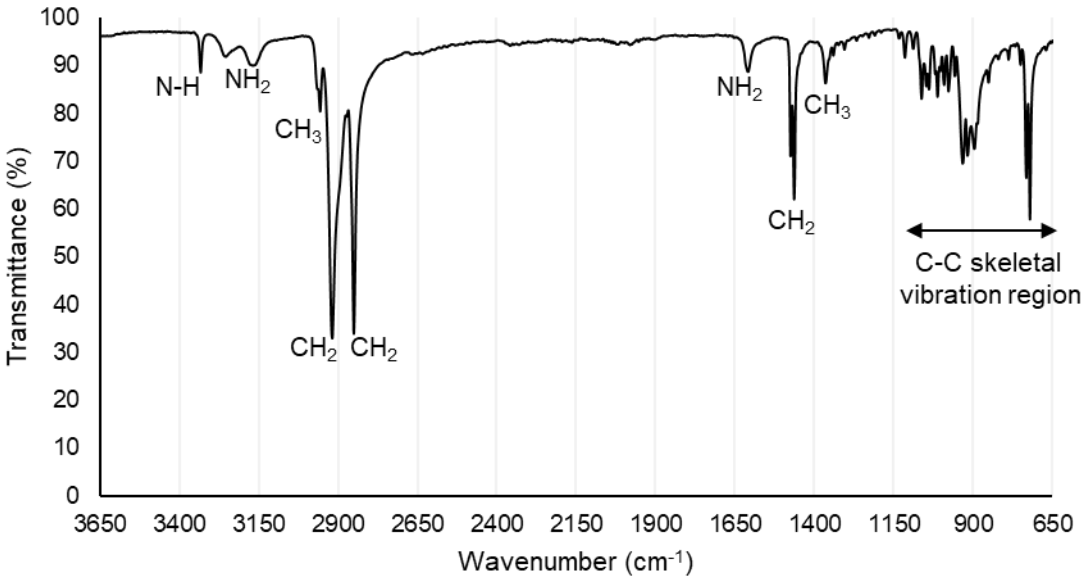

Figure 70 ATR-FTIR spectrum of solid octadecylamine.

Table 32 ATR-FTIR band assignments of solid octadecylamine.

Wavenumber (cm^{-1})	**Reference (cm^{-1})** (86)	**Assignment**
1363	1363	CH_3 *w*
1462 - 1473	1462 - 1472	CH_2 *s*
1607	1607	NH_2 *w*
2848	2848	CH_2 *s*
2896	2897	CH_2 *w*, *sh*
2916	2916	CH_2 *s*
2955 – 2964	2953 - 2960	CH_3 *w*
3165 – 3252	3170 – 3254	NH_2 *w*, *b*
3330	3330	NH *s*

Legend: (*w*): weak, (*s*): strong, (*sh*): shoulder, (*m*): medium, and (*b*): broad

5.2.2 Critical micelle concentration (CMC) by dynamic light scattering (DLS)

Water is conventionally used as a solvent to determine CMC point of surfactants. (183-185). An attempt was made to determine the CMC point of ODA in TRF, by DLS, to better understand the effects of concentrations over ODA interactions with gum. Average particle diameter was measured as a function of ODA concentration. The inflection point at approximately 0.38 mM and 1500 nm was believed to be the CMC value of ODA in TRF (Figure 71). A theoretical CMC value of ODA found in literature was 0.4 mM. (186) Although it was expected for the average diameter to increase as a function of concentration, it has been reported that surfactants (e.g. dodecyltrimethyl ammonium bromide) may exhibit a decrease in size due to repulsion forces between micelles. (187) Since ODA forms reverse micelles in hydrocarbon solutions, a similar effect may be applicable.

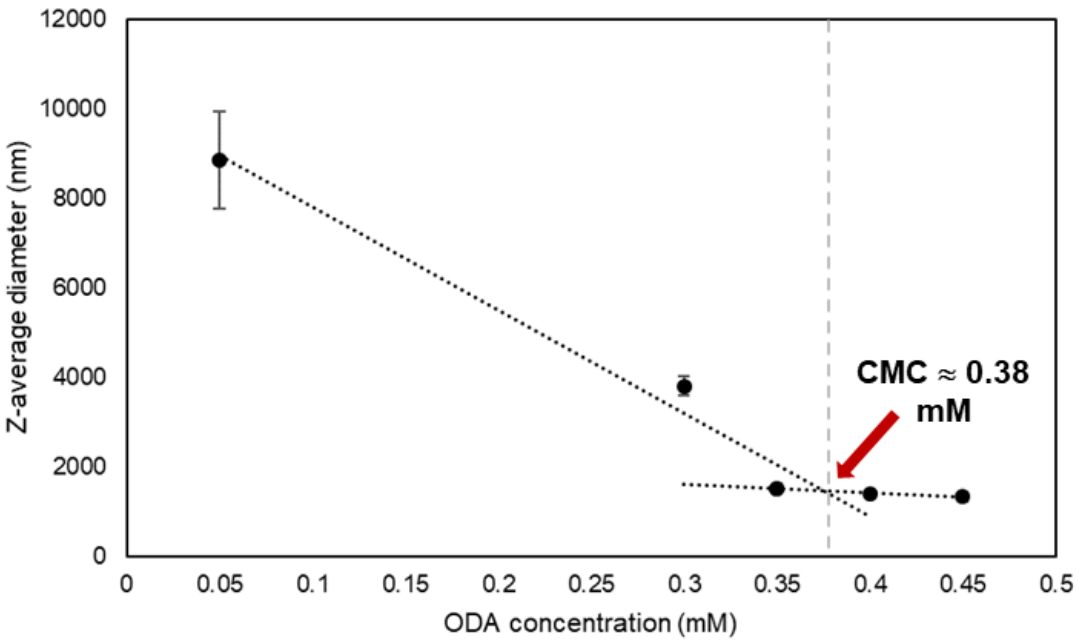

Figure 71 Average particle diameter as a function of ODA concentration. Inflection point represents the CMC of ODA in TRF.

To be consistent with the concentration format used throughout this study, the CMC value was converted into ppm (w/v) using the molecular weight of ODA (269.51 $g.mol^{-1}$), resulting in a value of 102.33 ppm.

5.3 ODA-Gum interactions

Five TRF blends were oxidised as per the parameters detailed in Table 13. Four out of five blends were spiked with 50, 500, 1000, and 2000 ppm of ODA (w/v), while keeping the fifth blend as a reference point. UV-Vis analysis was conducted to examine changes in chemical and functional groups as a function of ODA concentration.

5.3.1 Ultraviolet-Visible spectroscopy (UV-Vis)

Immediate and apparent changes in colour were observed following the addition of ODA into the oxidised blends (Figure 72). UV-Vis spectroscopy was performed to quantify the observed effect. Unsaturated molecules found in gasoline fuels typically undergo $\pi \rightarrow \pi^*$ (C=C) and n $\rightarrow \pi^*$ (C=O) transitions near the 200 – 350 nm region. (188, 189) Due to the presence of large numbers of unsaturated molecules resulting from the TRF radical oxidation reaction, it was difficult to interpret the spectra. An increase in absorbance at $\lambda_{max} \approx 350$ nm as a function of ODA concentration was observed, but this peak intensity turned out to be undistinguishable from samples with zero and 50 ppm ODA concentration. Thus, it was decided to consider the zero ppm ODA sample as a reference spectrum for obtaining difference spectra that allow to interpret changes in absorbance as a function of ODA concentration with a view to its effect on gum in solution.

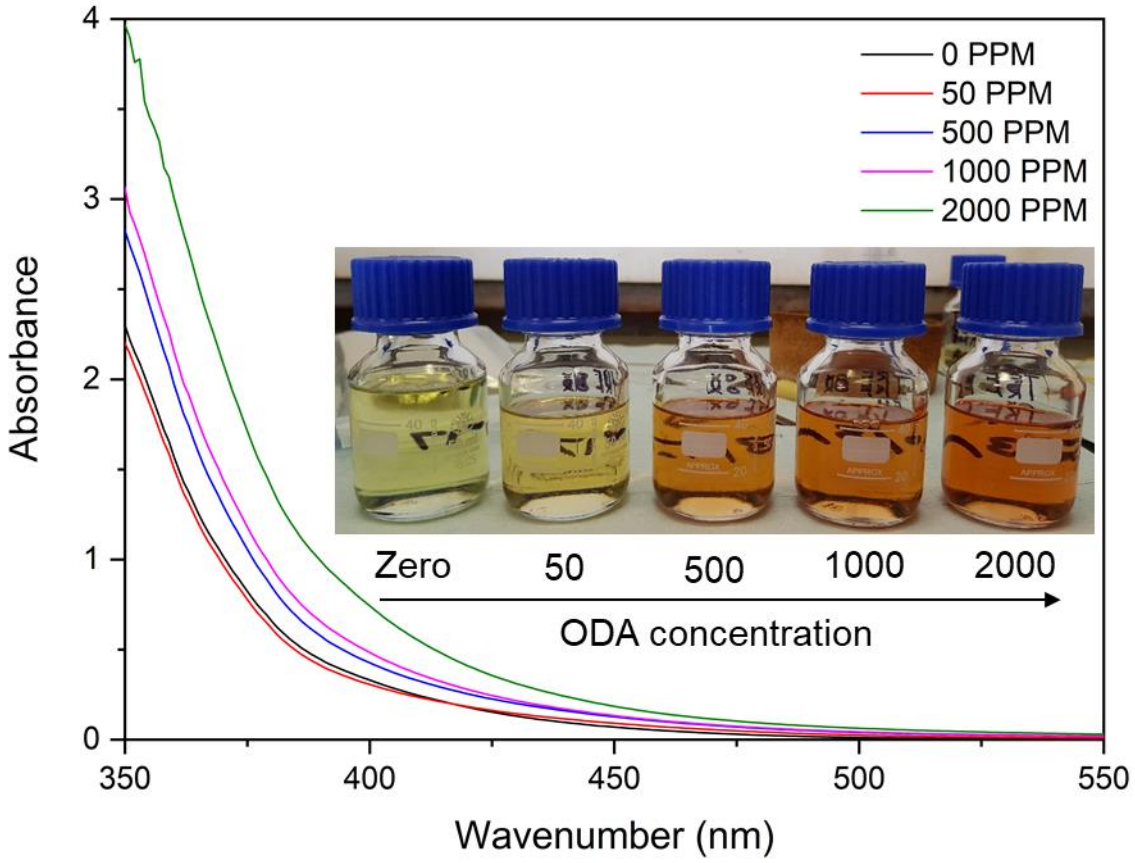

Figure 72 UV-Vis spectra of the TRF oxidised blends (shown on figure) as a function of ODA concentration.

The resulting difference absorbance profiles in Figure 73 showed a pattern of increasing absorption as a function of concentration. The 50 ppm ODA solution exhibited what appears to be a weak decrease in overall absorption, but this is likely within the experimental reproducibility limits, i.e. an undetectable change (see also the similarity of the spectra in Figure 72). With the 500, 1000, and 2000 ppm samples, a significant increase of the absorption in the wavelength range up to about 500 nm was observed. Absorption at these wavelengths corresponds to the removal of blue and violet light components, explaining the yellow/orange/red colour of the solutions. Since ODA is not UV-Vis active in the absence of gum, this increase in light absorption at the lower end of the visible spectrum must be associated with the interaction of gum with ODA. The UV-Vis data thus confirm, that a significant interaction between ODA and gum takes place in solution, which leads to additional functional groups absorbing in the near-UV region, thereby influencing the visible light absorption at low wavelengths in the visible region. Note that for the ODA concentration range investigated here, the difference spectra indicate a linear relationship between the intensity of the additional light absorption and the ODA concentration (Figure 74). This suggests that even at 2000 ppm there is no free ODA in the solutions – all ODA appears to be interacting with gum.

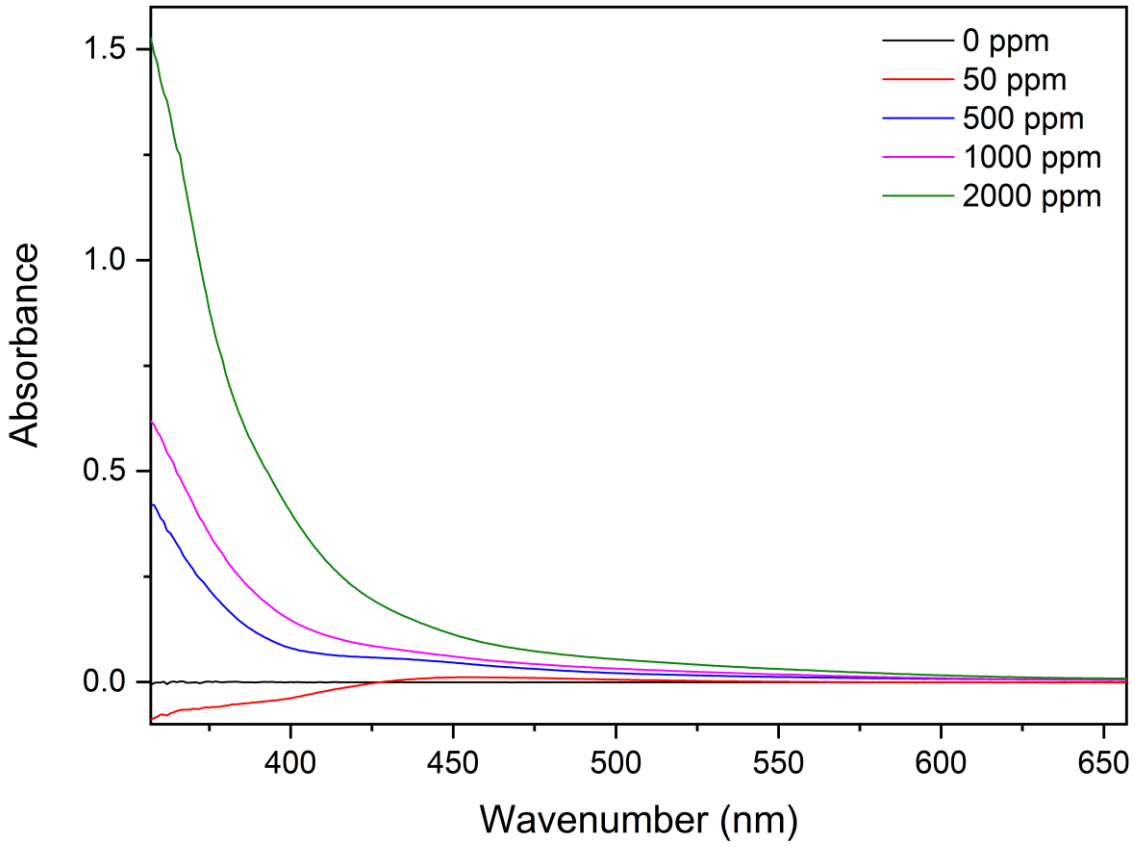

Figure 73 Difference UV-Vis spectra of oxidised TRF blends mixed with increasing ODA concentration.

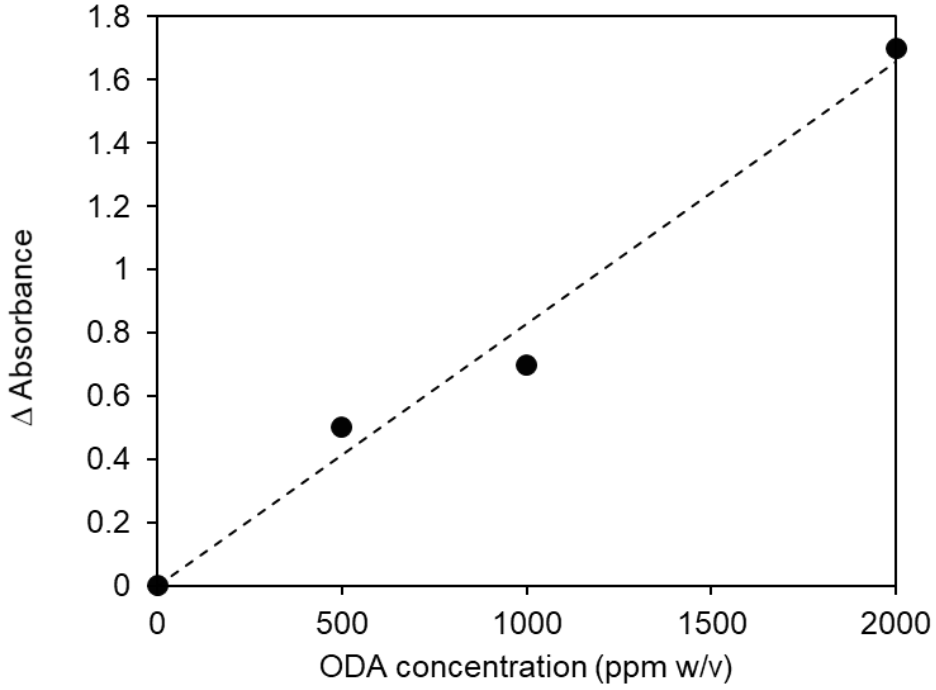

Figure 74 Increase in UV-Vis absorption as a function of ODA concentration. Data derived from Figure 72.

5.4 Deposition of gum and ODA on steel surfaces

5.4.1 ODA adsorption on 316 SS: Contact angles

Attachment of long chain alkylamines onto metallic substrates have been studied extensively. (90, 91, 93, 118) Contact angles are commonly used to characterise the hydrophobicity of metallic surfaces. (190) ODA adsorption is known to lead to hydrophobic surfaces, and even superhydrophobic surfaces with contact angle $\theta > 145°$. (191) To study the adsorption of ODA on steel surfaces, steel substrates were immersed in neat (i.e. not oxidised, gum-free) TRF solutions containing 400, 800, and 1600 ppm of ODA for 24 h. They were then carefully removed from solution and contact angles of deionised water (10 µl) were measured. The results showed the expected pattern of increasing contact angle as a function of ODA concentration. These findings confirm that ODA adsorbs from TRF onto metallic substrates in the concentration range examined in this thesis (Figure 75). At ODA concentrations lower than 400 ppm, the contact angle variations could not be determined reliably.

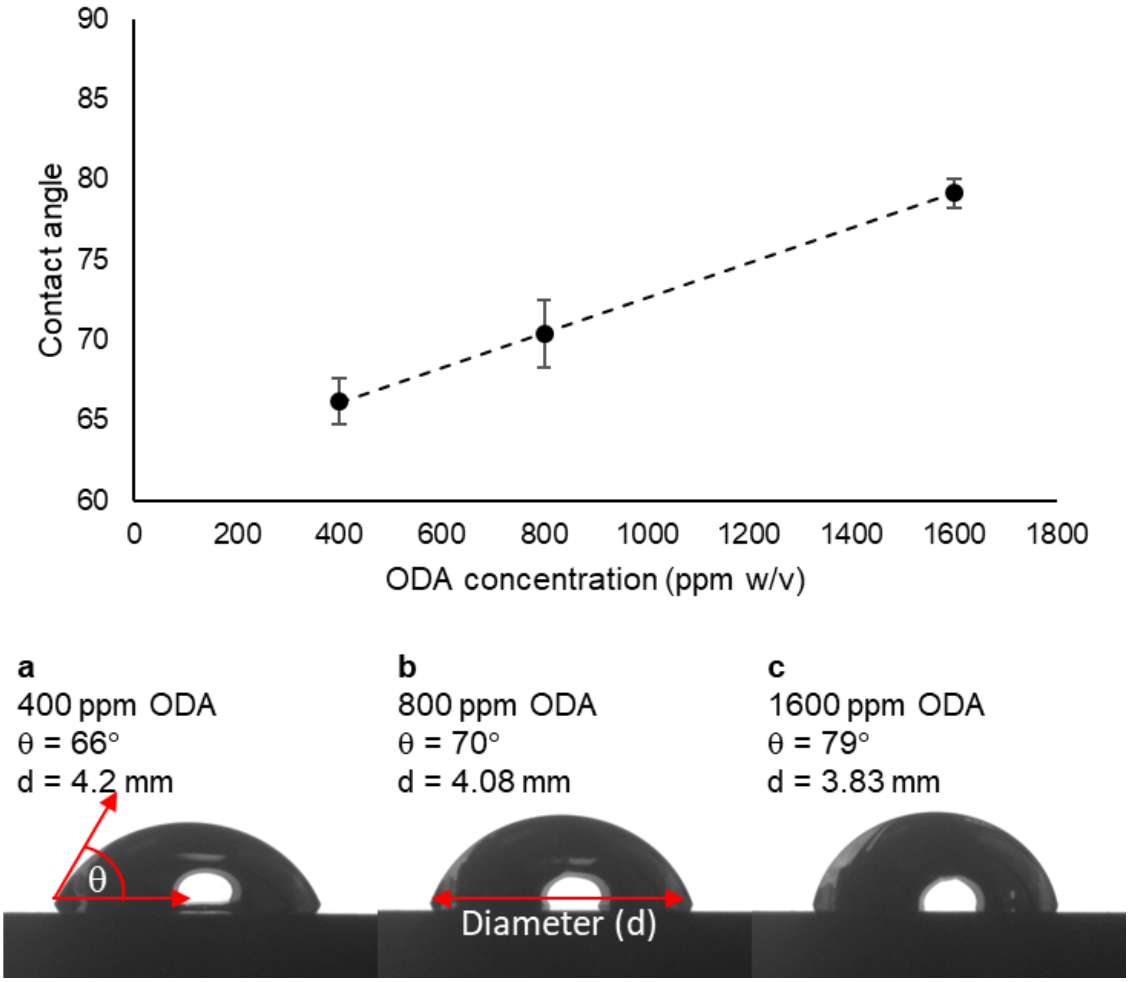

Figure 75 Contact angle of deionised water measured on 316 stainless steel substrates immersed in TRF solutions containing different ODA concentrations.

5.4.2 Gum adsorption on 316 SS with and without ODA: Gravimetry

The gum solution in TRF with varying ODA content (0, 50, 500, 1000, 2000 ppm) that had been characterised by UV-Vis (section 5.3) were used to study how they interacted with 316 stainless steel substrates. The 316 SS substrates were immersed in these solutions for 10 s at room temperature. After emersion from solution the weight gain was determined gravimetrically, using a half-micro balance. Repeatability of the results was found to be within 0.0004 g, which is well within the allowable error margin of 0.001 g in the ASTM D-6201 standard test method for the evaluation of intake valve deposit formation from unleaded spark-ignition engines fuels. (25)

The surface density (weight per unit area, Figure 76) of deposits in the absence of ODA was 0.11 mg/cm^2 and increased significantly to 0.19 mg/cm^2 at an ODA concentration of 50 ppm. For higher concentrations of ODA the additional deposition was much less, with surface densities of 0.21, 0.21, and 0.24 mg/cm^2 (11%, 0%, and 14% increases) for 500, 1000, and 2000 ppm samples, respectively. On their own, these data suggested that ODA enhanced adhesion of deposits from the solution, and that the surface was almost saturated with deposits at 50 ppm ODA content, to the extent that no further gum deposition took place at higher ODA concentrations. However, increasing the ODA concentration by approximately 40 times (50 to 2000 ppm) did not seem to have a correspondingly strong effect. To understand these observations better, SEM/EDX was applied to get a better understanding of the morphological changes at the surface.

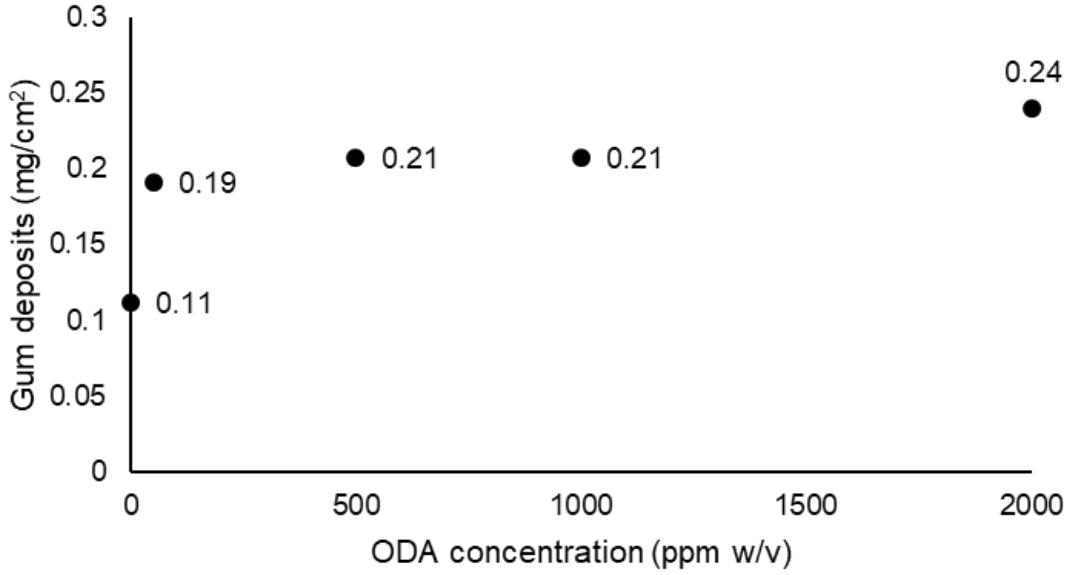

Figure 76 Surface density (weight per unit area) of deposits from oxidised TRF as a function of the concentration of added ODA.

5.4.3 Gum adsorption on 316 SS with and without ODA: Scanning electron microscopy with energy dispersive analysis of X-ray (SEM/EDX)

Stainless steel substrates were treated with oxidised TRF containing 0, 50, 500, 1000, and 2000 ppm ODA, left to dry, and then examined by SEM/EDX. Generally, the images indicated strong surface heterogeneity of the deposits, with the presence of large (~ 200 µm diameter) circular ring deposits, next to smaller irregular deposits, in the presence of ODA (50, 500, 1000, and 2000 ppm).

The SEM image of the sample treated without ODA (0 ppm) revealed islands of deposited gum scattered across the coupon substrate (Figure 77). The shape of these islands is circular, but often elongated or with other significant morphological irregularities. EDX elemental mapping detected C, O, N, Fe, and Ni. Using the element contrast for mapping revealed that the gum composition was mainly of carbon and oxygen, as expected. Nitrogen was observed uniformly distributed across the images, which indicates that some N is intrinsic to the SS 316 substrates. More advanced surface sensitive techniques such as XPS are required to provide deeper insight into the chemical composition of the surfaces and the deposits. However, it is worth mentioning that the EDX results are reminiscent of elemental analysis data for deposits at PFI tips in DISI engines, which likewise showed dominance of carbon and oxygen in the deposits. (192) Small concentration of sulphur and calcium were found at sites closer to PFI tips, which are not evident here because no compounds with these elements were used in the formulation of the model gum fuel.

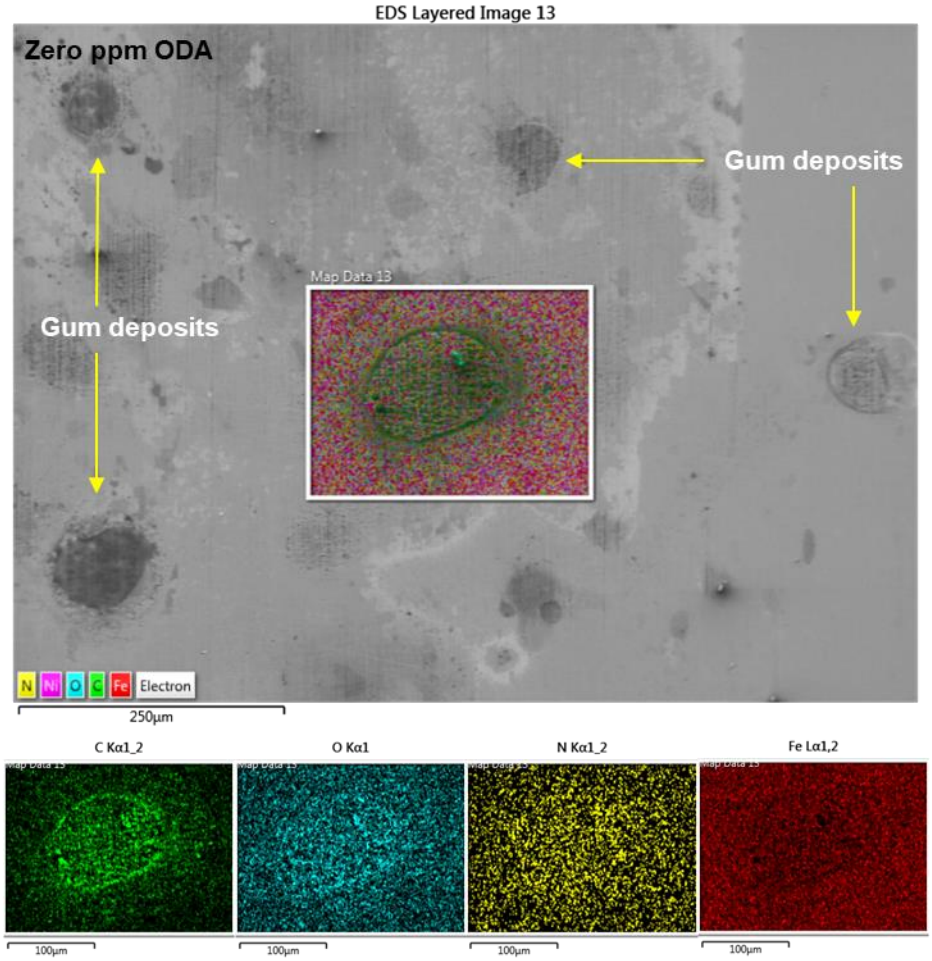

Figure 77 SEM/EDX image of gum deposits on a stainless substrate in the absence of ODA in the fuel (0 ppm ODA). The deposits are mainly C and O.

For 50 ppm ODA, a similar gum distribution was observed. EDX mapping revealed more regular oval and circular shapes, with ring-like edges of higher deposit concentrations. A slight indication of association between C and N was evident, with the latter likely coming from the ODA. It seems that ODA is particularly concentrated in those regions of the images where C from gum is highly concentrated as well, which indicates co-deposition with the gum. Note that 50 ppm is well below the CMC of ODA in TRF (~ 100 ppm, section 5.2.2), so deposition of ODA micelles, which may also explain circular and ring-like features is unlikely to take place. The co-location of N and C in the element maps in Figure 78 clearly shows that ODA and gum are associated in the deposits, suggesting that the chemical interaction of ODA and gum in solution, which was already indicated by UV-Vis (section 5.3.1), leads to formation of stable complexes that deposit together.

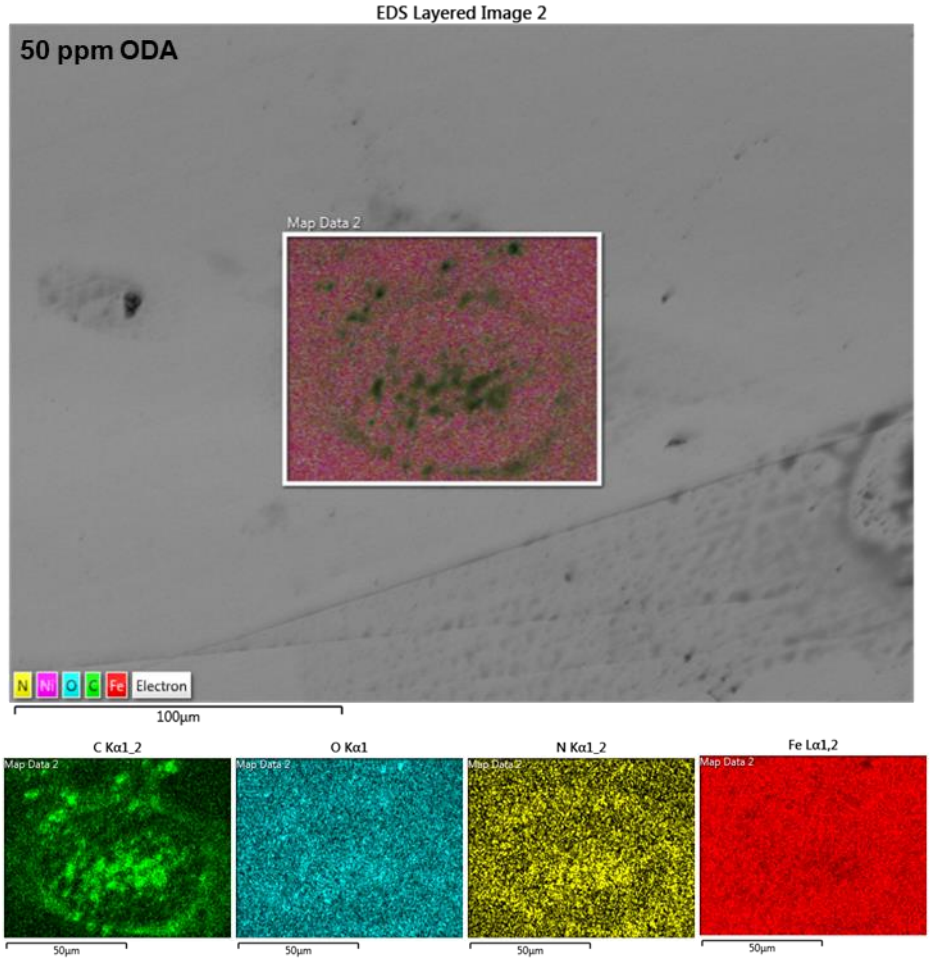

Figure 78 SEM/EDX image of deposits on 316 SS from an oxidised TRF blend containing 50 ppm ODA. Element maps indicate co-location of C, N and O.

At 500 ppm ODA, the sample exhibited similar deposit sizes (~ 100 µm) and morphologies as observed for 50 ppm. EDX mapping showed ring-shaped deposits composed of C, N, and O. N was evident around the edges of the analysed gum deposit, which again indicates association with gum components. In contrast to previous sample, 500 ppm of ODA would be sufficient to form micelles in the solution, but the results indicate that it remains associated with gum. Again, this is in line with the UV-Vis absorption of the solutions, which indicate strong interaction between gum and ODA.

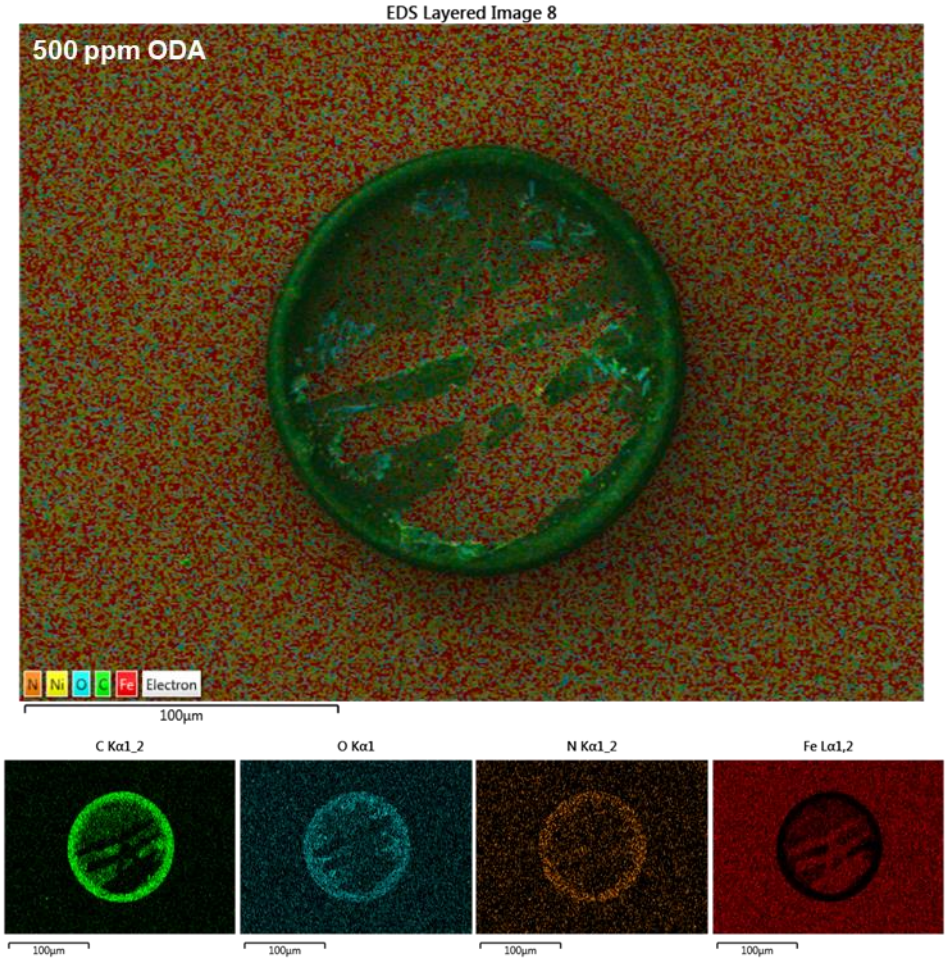

Figure 79 SEM/EDX image of gum deposits on 316 SS from oxidised TRF blend containing 500 ppm ODA. Element maps indicate co-location of C, N, and O.

The same conclusions can be drawn from the SEM/EDX visualisation of deposits in the presence of 1000 ppm ODA (Figure 80). In the presence of ODA there is a clear indication of oval (50 ppm) and circularly shaped deposits (500 and 1000 ppm), with an outer ring. Such deposits are reminiscent of features formed by droplet deposition, wetting, and drying on surfaces. The progression of the deposit shapes from homogeneous irregularly shaped in the absence of ODA, to oval and still slightly irregular shapes in the presence of 50 ppm ODA to almost perfectly circular shapes with 500 and 1000 ppm suggests that the association of ODA and gum in solution facilitates the formation of droplet-like structures, likely gum solubilised in ODA surfactant micelles. The clear association between C and N in the resulting deposits indicates strongly that interaction of ODA and gum in solution leads to colloidal structures that deposit on the surface.

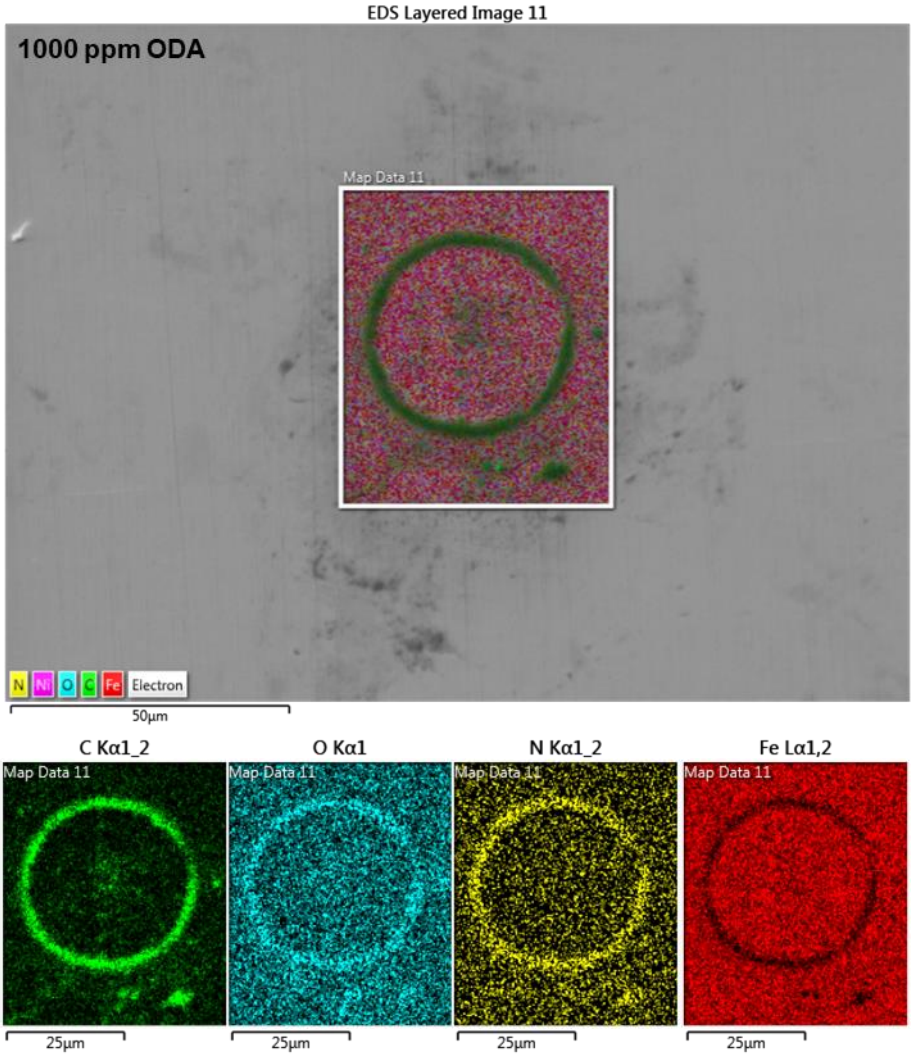

Figure 80 SEM/EDX image of gum deposits on 316 SS from an oxidised TRF blend containing 1000 ppm ODA. Element maps indicate co-location of C, N, and O, and at this concentration even for smaller size deposits (see bottom right quarter of the EDX maps for example).

At the highest concentration, 2000 ppm ODA, similar association behaviour was observed between C, N, and O. It was also evident that the morphology of the circular, ring-shaped deposits reverted to irregular, much larger deposits on the surface, compared to the previous sample (1000 ppm). However, by linking this observation to the only 14% increase, at 2000 ppm ODA (Gravimetry 5.4.2), one may perhaps presume that the increase in deposits size is potentially due the presence of excess ODA in the system, which was released onto the surface during drying of deposit droplets. Further surface sensitive analysis is required to test this hypothesis.

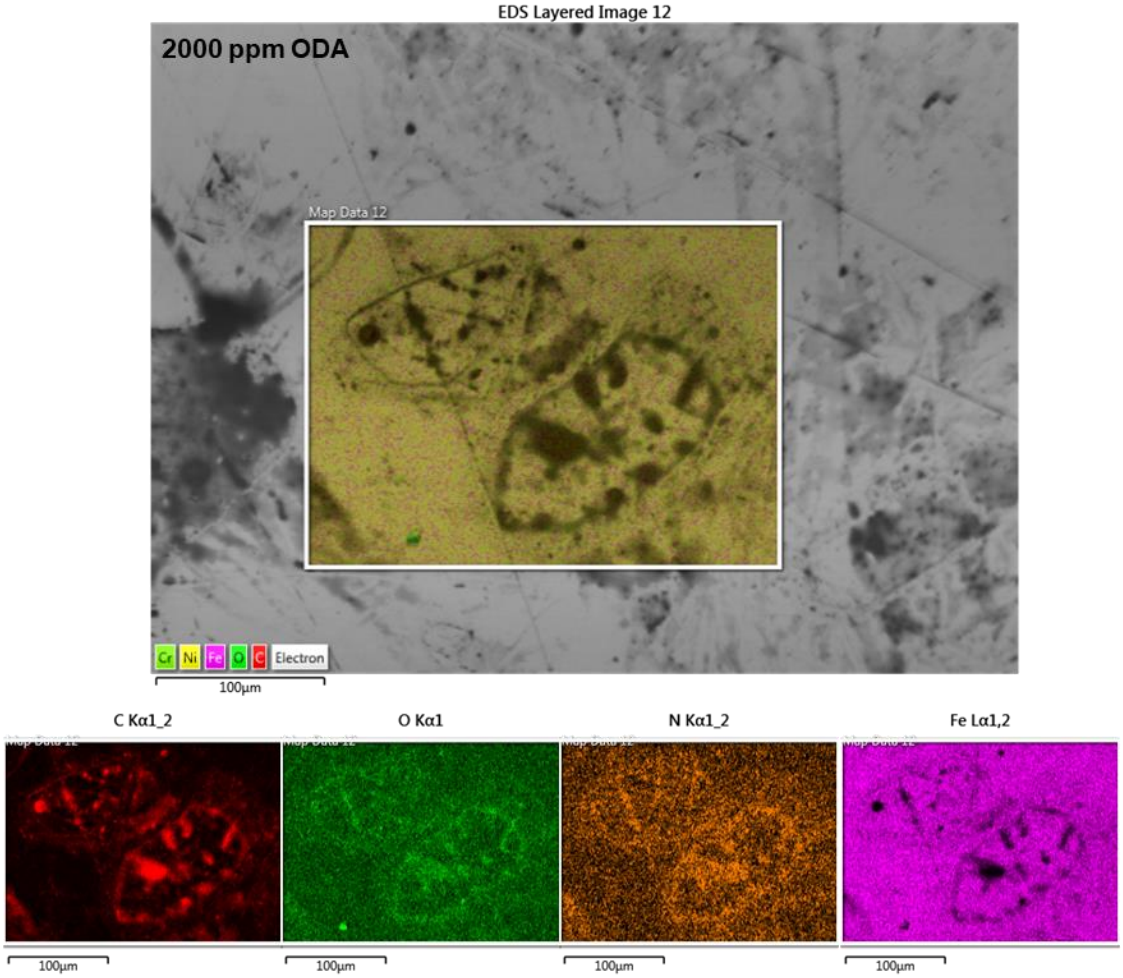

Figure 81 SEM/EDX image of gum deposits on 316 SS from an oxidised TRF blend containing 1000 ppm ODA. Element maps indicate co-location of C, N, and O. Even larger, irregular deposits are observed at excess ODA concentration.

Moreover, based on the SEM/EDX images, we can conclude that the surfaces were not homogeneously saturated with gum or ODA; as C, N, and O were only evident at the deposits sites and not on the whole surface. Separate adsorption of ODA on the 316 SS surfaces was not evident, but EDX may well not be surface sensitive enough to detect small quantities such as adsorbed monolayers. More advanced surface sensitive techniques are required to verify their presence.

5.4.4 Gum adsorption on 316 SS with and without ODA: X-ray photoelectron spectroscopy (XPS)

XPS elemental analysis of the immersed 316 SS coupons was therefore undertaken to characterise the surface properties in more detail and with higher surface sensitivity. As for the SEM/EDX studies, substrates were analysed without any post-emersion treatment (i.e. without, e.g. soaking in TRF or rinsing with n-heptane). However, an additional pristine reference coupon (not exposed to TRF, gum/TRF, or ODA solutions) was included in the analysis to distinguish surface features intrinsic to the 316 SS substrates from extrinsic features introduced by the TRF/gum/ODA treatments. The elemental composition of the surfaces was in all cases to 98% composed of C, N, O and Fe. Ca and Cr were found to make up the remaining 2%. Traces of silicon (0.59 %) and sodium (0.12 %) were found on the reference coupon (Figure 82).

The data in Figure 82 show that the Cr 2p photoemission is by far strongest for the untreated SS 316 coupon. Cr is intrinsic only to the SS 316 substrate and significantly attenuated for all other samples, suggesting that TRF/gum and ODA treatments lead to the creation of overlayer deposits. However, to say that these overlayers, whether present as islands (as SEM/EDX did suggest in the previous section) or adsorbed films, are thin enough to let a significant amount of Cr 2p photoelectrons pass, would suggest very thin overlayers on the order of 1 nm thickness or less. This model would be incompatible with the results of the gravimetric analysis, which suggested macroscopically measurable weight increases across all samples. Taken together, these results clearly demonstrate that deposition of these heavy deposits takes place mainly in the form of thick multilayer islands visible by SEM, while surface regions in between are at most covered by ultrathin adsorption layers.

The C 1s emission was used to quantify the C content of the surface, and was found to be between 54 – 66 at% (Figure 83). For 0 ppm ODA it is not much lower than for 50 ppm ODA, while the gravimetric analysis indicated a 76% increase in adsorption from 0 ppm to 50 ppm ODA. What this suggests is that the addition of 50 ppm ODA appears to lead to the deposition rather than more or spatially more extensive deposits. Note that the Cr 2p signal is still visible (Figure 83), so much of the surface must still be free from thick adsorbate overlayers, which is in line with the SEM/EDX observations. Further increasing the ODA concentration to 500 ppm and 1000 ppm does not seem to affect the C content at the surface (Figure 83), which is also in line with the gravimetric and SEM/EDX analysis (*vide supra*), suggesting that more ODA merely increases the thickness of the deposit islands. At 2000 ppm the C surface concentration rises significantly (by about

15%). This is in line with the SEM/EDX findings from Figure 81, which suggest that the ODA concentration carried over from solution exceeds the amount of ODA that can be stabilised alongside the dry gum, so phase separation may take place and migration of ODA, ultimately adsorbing in the regions of the surface between the thick deposits. As the ODA will adsorb with the C_{18} hydrophobic tail pointing away from the surface this may explain the additional C 1s signal intensity. This would also be compatible with the observation that the Fe 2p and Cr 2p signals are attenuated after 2000 ppm ODA treatment, compared to 500 ppm and 1000 ppm: the additional C_{18} hydrocarbon overlayer would absorb a significant amount of these electrons in the regions in between the gum/ODA deposits.

It is important to note here that any such adsorbed ODA does not stem from adsorption of free ODA from solution. For the ODA concentration range investigated here, the difference UV-Vis spectra indicated a linear relationship between the intensity of the additional light absorption and the ODA concentration, suggesting that even at 2000 ppm there was no free ODA in the solutions.

To summarise briefly, the XPS analysis based on the C 1s intensities suggests that two competing processes are taking place: (i) deposition of heavy gum and gum/ODA aggregate from solution and (ii) adsorption of released ODA in the otherwise nearly clean (apart perhaps from thin adsorbed hydrocarbon solvent molecules and adventitious contamination) substrates areas in between the thick carbonaceous gum/ODA islands. This mechanistic hypothesis shall now be examined further by looking at the photoemission intensities from the other elements.

First, the N content on the surface was determined from the N 1s emission line, and found to be relatively higher for the low ODA concentration (0, 50, and 500 ppm) and then strongly reduced for 1000 and 2000 ppm ODA. It should perhaps be noted also that the N 1s emission is quite weak for the untreated reference substrate (Figure 82). However, as discussed previously, the intrinsic N 1s emission intensity across the 316 SS surfaces was generally found to be extremely variable, with some areas of the substrates even exhibiting no N 1s emission at all, so this observation should not be overinterpreted. The high concentration for 0 ppm ODA must be intrinsic to the 316 SS substrate, as there are no other sources of N in the system. It appears that for 50 and 500 ppm ODA the N 1s signal intensity from the co-deposited ODA approximately cancels out the decrease in the N 1s substrate emission by the gum/ODA overlayer. Only 1000 and 2000 ppm ODA lead to further attenuation of the N concentration (Figure 83), with the system at 2000 ppm likely attenuating the substrate signal

completely due to the proposed adsorption of ODA in the areas between the islands of gum/ODA. The low N 1s emission intensity for 1000 ppm ODA appears to be an outlier, as neither the C 1s nor the O 1s (see below) intensities nor any of the other analytical results (SEM/EDX, gravimetry) indicated a major change for this sample. The anomaly of this result may be related to the abovementioned patchiness of the N distribution in the substrate, since the magnitude of the deviation from the trend is compatible with this. More studies would be needed to confirm this.

Turning to the O concentrations (Figure 83), which were determined from the O 1s emission intensities, they follow the same trend as the N concentrations, because O can stem from either adsorbed gum or the 316 SS substrate. For 0, 50, 500 and 1000 ppm there appears to be a fairly stable O concentration due to a balance of additional O from gum adsorption and attenuation of the substrate O signal by the adsorbed gum/ODA islands. At 2000 ppm ODA, significant attenuation of the O 1s signal is in line with the proposed adsorption of ODA in the surface areas intervening the gum/ODA islands, further supporting the proposed model.

Finally, the Fe concentration (determined from the Fe 2p emission) is most attenuated for gum deposition in the presence of 0 ppm and 50 ppm ODA. For 0 ppm this is in line with the observation of the larger number of irregularly shaped and thinner islands observed by SEM/EDX. It appears that 50 ppm ODA addition, while associated with a strong increase in adsorption (as shown by the gravimetry), is guiding the extra mass covering the surface into increasing the thickness of the gum/ODA islands, while limiting the surface area they are covering, perhaps by minimising the area through creating circular shapes, and beginning to build up thick deposit surface areas during drying as rings. This may explain why the Fe 2p substrate signal remains constant, even though gravimetry indicates a significant increase in adsorbed mass. For 500 and 1000 ppm ODA, it appears that this limiting effect due to morphology control by the ODA is maximised, leading to the exposure of more Fe emission intensity. Note in this context that the observed Fe concentrations are still small, a few % compared to those of C and O, so the observed variations are compatible with the variations in C, N and O contents. At 2000 ppm the Fe 2p signal seems to be attenuated for the same reason as the Cr 2p and the O 1s – ODA may adsorb in the surface regions between the gum/ODA islands and thereby attenuate the Fe 2p signal significantly. One should perhaps also keep in mind that this analysis assumes that no intermixing of Fe from the substrate and the overlayers can take place. It may well be the case that some Fe ions migrate into the overlayer to form compounds. Based on the available data this cannot be ruled out completely.

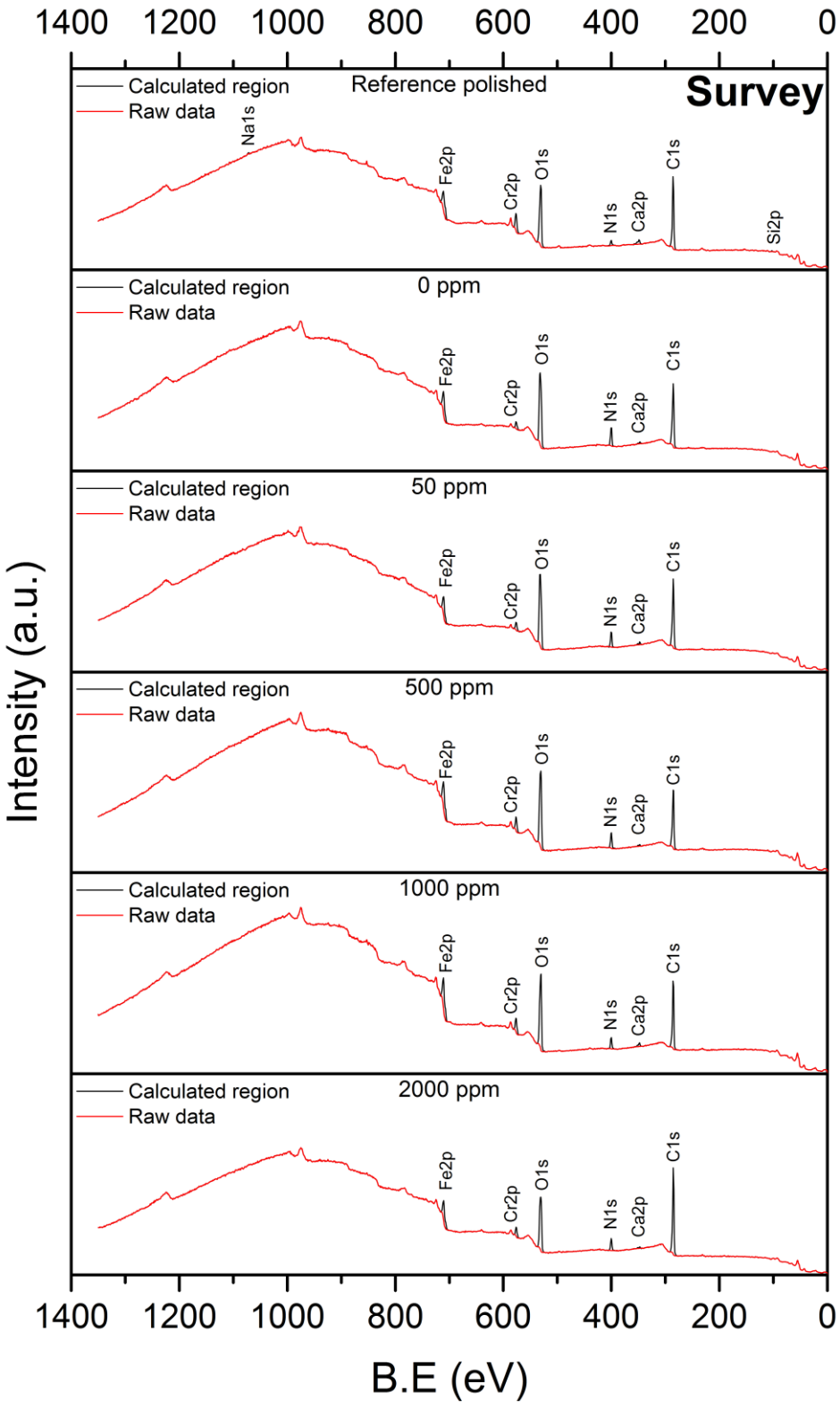

Figure 82 XPS survey spectra of immersed coupons compared to reference substrate. All spectra were scaled to the same arbitrary intensity of $1x10^6$ a.u.

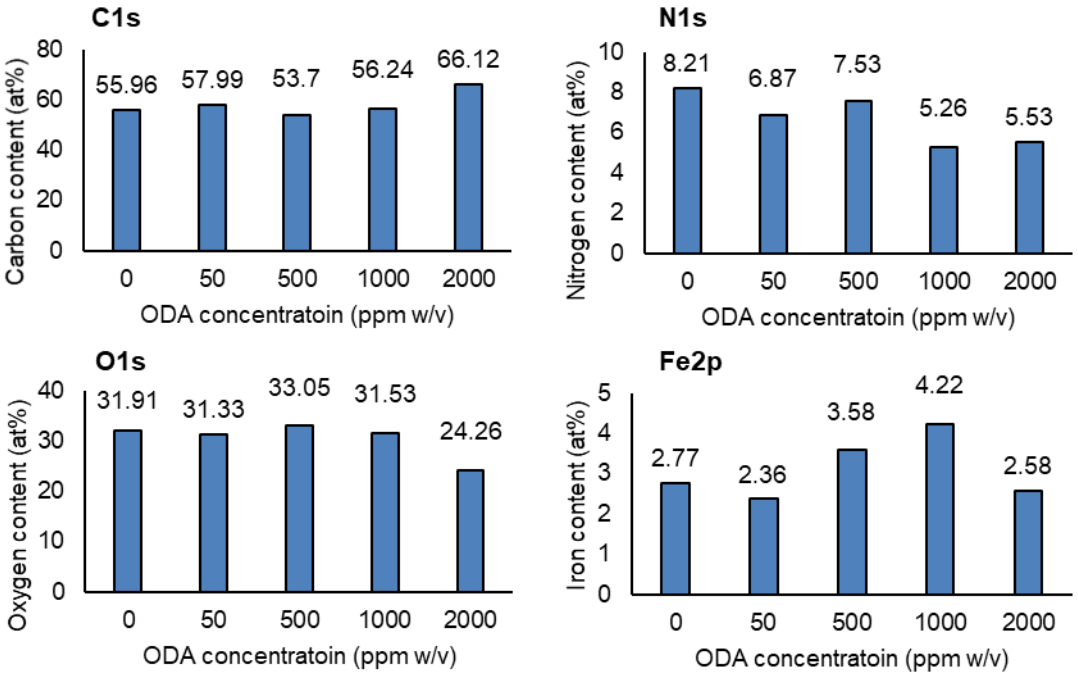

Figure 83 Elemental composition of major surface elements as a function of ODA concentration. Data retrieved from Figure 82.

5.5 Conclusion

ODA was blended with oxidised TRF surrogates and analysed with UV-Vis. The resulting solutions indicated strong interaction between gum and ODA. Even at 2000 ppm ODA, there was no free ODA in solution – all ODA appears to be bound to gum. The CMC point of ODA in gum-free solution was determined by DLS and found to be ~ 100 ppm (w/v). Likewise, contact angle measurements show that ODA adsorption from gum-free solutions can take place with the associated changes in the hydrophobicity of the metallic substrate surfaces. SEM images revealed gum deposits on the order of 100 µm radius across the surface. ODA appears to change the morphology of these deposits into spherical/circular shapes, forming ultimately rings during drying. The morphology change minimises the area of the surface covered in gum while allowing the build-up of thicker overlayers in the areas where gum is adhering. EDX elemental mapping of the gum deposits indicated dominant composition of C and O of these deposits. The N signal in EDX shows that ODA is strongly associated with the deposited gum. XPS analysis of the elemental composition of the surface are in line with the proposed morphology and composition model, but appears to indicate also that at the highest ODA concentration (2000 ppm) phase separation between gum and ODA takes place during drying, with a fraction of ODA migrating and adsorbing in the surface regions in between the gum/ODA deposits islands.

These results suggest that for the investigated system the ‘deposit elimination by surface passivation’ vs. ‘capture and wash’ scenario may be too simplistic to describe the actual interactions and structure formation taking place. The main action of ODA in solution seems to associate with gum and possibly stabilise it colloidally, as in the ‘capture and wash’ model. The effect of the solubilisation seems to be a minimisation of the surface area of the gum colloids by forming spherical micellar shapes. Not predicted by ‘capture and wash’ is that these can deposit on the surface forming circular and ring-shape deposits of considerable thickness, leaving the remaining steel surface almost entirely clean. At very high concentrations, some ODA appears to be released on drying and covers the remaining steel surface as in the ‘deposit elimination by surface passivation’ model. However, this may or may not passivate the remaining surface against further gum deposition. The evidence from this study suggests that the affinity between gum and ODA is very high, and it may well be that the adsorbed ODA layer attracts additional gum, associates with it, and minimises surface coverage by rolling it up into 3D rather than 2D deposits.

Based on the promising preliminary results in this chapter, further systematic approach was designed to better understand ODA effects on gum adsorption. In the next chapter, XPS will be applied much more systematically as a surface sensitive technique to extensively probe the surfaces and examine chemical speciation as a function of ODA.

5.6 Recap

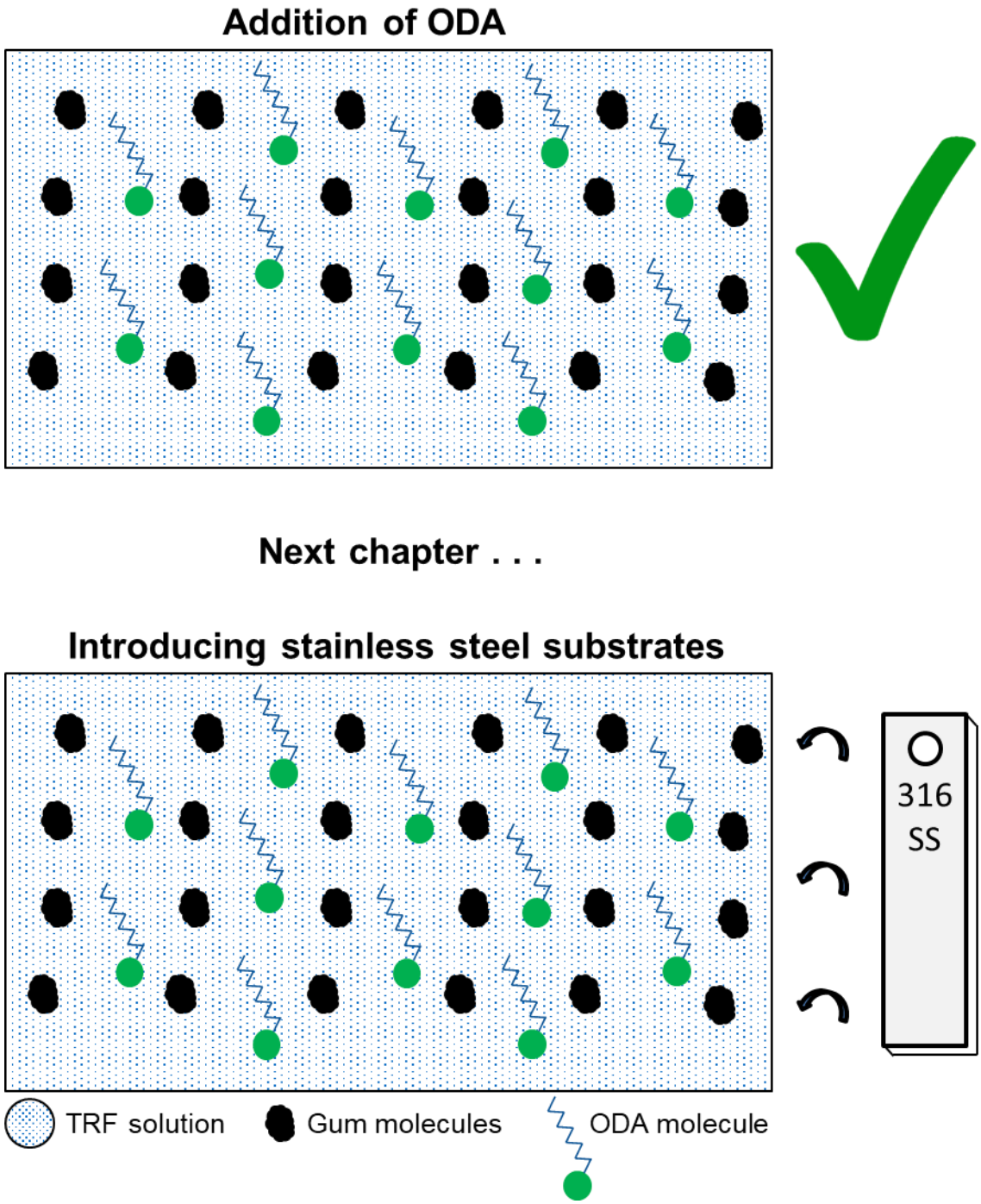
Addition of ODA
Next chapter . . .
Introducing stainless steel substrates
316
SS
TRF solution
Gum molecules
ODA molecule

Chapter 6 Systematic studies of interfacial behaviour by XPS

6.1 Introduction

In the previous chapters, the formulation, oxidation, characterisation of TRF surrogate fuel and gum, the impact of model detergent (ODA) on oxidised TRF, and an initial study of deposition on 316 SS surfaces have been examined. A mechanistic hypothesis for the detergency effect of ODA on gum was derived. To better understand the associated interfacial chemistry, the model system will now be investigated in more detail and more systematically. At the centre of this work will be the measurements of chemical shifts in XPS. Three series of experiments were carried out to gain a better understanding of the adsorption, detergency, and surface chemical interactions in the 316 SS-gum/TRF/ODA system. All experiments were performed by immersion of stainless steel coupons in TRF blends containing ODA, gum, ODA and gum, or none. The flow-chart scheme illustrated in Figure 84 summarises the performed experimental work.

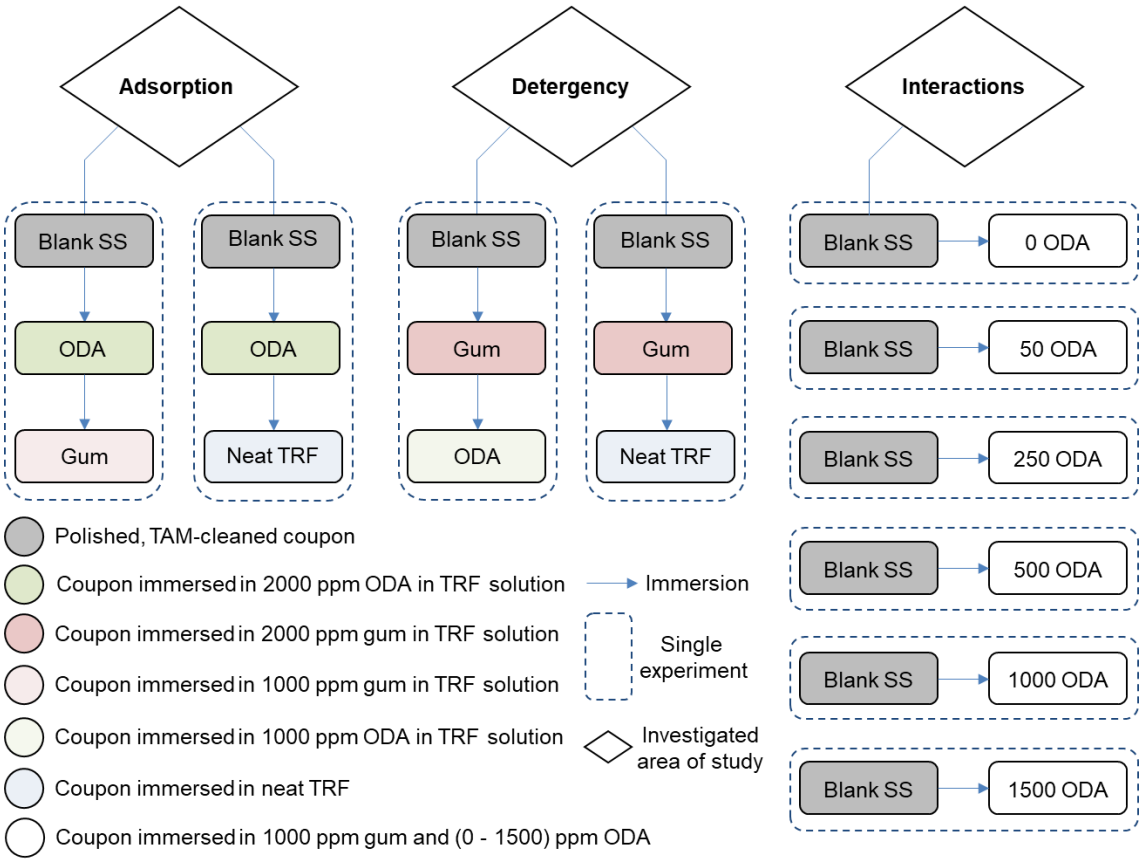

Figure 84 Colour-coded flow chart detailing the experimental design of the XPS work carried out in this chapter.

All coupons were characterised by XPS prior to immersion (i.e. Blank SS), after each stage of immersion in the case of ‘adsorption’ and ‘detergency’, and after immersion in ODA/gum/TRF solutions in the case of ‘interactions’. Each experiment in a sequence was carried out using the same coupon. All immersions were carried out at room temperature for 24 h in tightly closed vials. As illustrated in Figure 84, blank SS coupons, ODA, and gum were key components in the experimental design. Consequently, it was vital to obtain XPS data of these components as a reference for understanding their surface chemistry and chemical states prior to any immersion or interaction processes.

6.2 XPS of individual components

6.2.1 XPS of stainless steel coupons

As discussed in the literature review (section 2.3), grade 316 stainless steel (316 SS) was chosen to be the model substrate material. Since the main objective of the research was to understand adsorption behaviour, it was critical to ensure realistic bonding and adsorption capacity of the model substrate. Various studies have demonstrated that surface treatment processes such as grit blasting (mechanical), acid etching, or plasma treating (chemical) can contribute to surface free energy, by increasing surface area, and consequently result in more adsorption, especially on surfaces with μm scale roughness. (156, 193) As discussed and illustrated in chapter 3.5.2, the established polishing method significantly decreased surface roughness to less than 1% of the value for the untreated (as received) coupon, from 1.15 to 0.01 μm. The as received (denoted in this chapter as ‘unpolished’) stainless steel coupons had been grit blasted and glass bead finished by the manufacturer (RCSL corrosion monitoring). Wide range XPS survey scans were collected for two reference coupons before and after the in-house mirror-polishing, as per the parameters in Table 33. This allowed for better quantification of changes in surface elemental composition as a function of surface roughness. Both coupons were kept as references and were never used as part of any immersion study during this project.

Table 33 XPS scanning parameters used to analyse the surface of the reference coupons.

Scan range	Pass energy (eV)	Dwell time (s)	Step size (eV)	Number of scans
Survey	100	0.1	1	1

Figure 85 and Figure 86 show the survey spectra and elemental compositions of the unpolished and polished reference coupons.

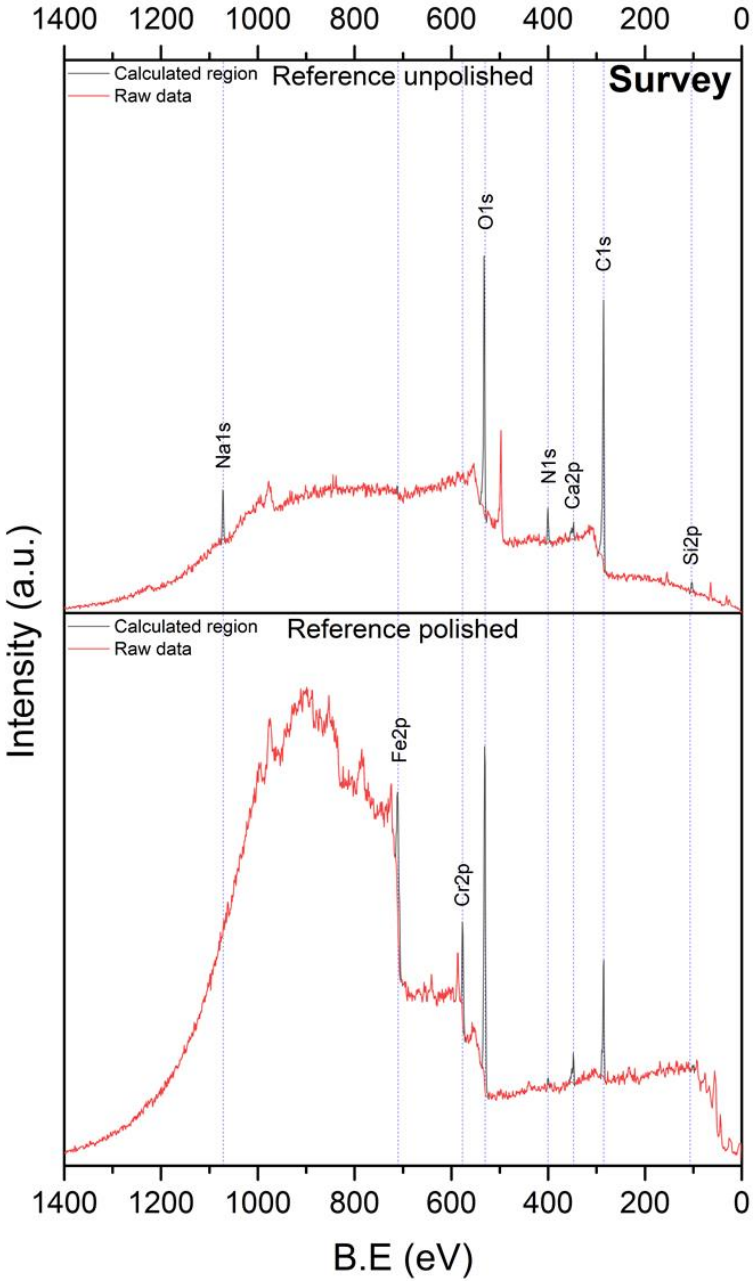

Figure 85 Survey spectra of reference stainless steel coupons (unpolished vs polished), showing significant differences in iron and chromium intensities. Spectra were scaled to the same arbitrary maximum intensity (37500 a.u.).

For easier comparison, a table showing changes in composition for each element was visualised as a bar chart in Figure 86. It can be easily seen that polishing the surface has increased the Cr (Cr $2p_{3/2}$) and iron (Fe $2p_{3/2}$) emission intensities; in contrast, the unpolished surface mainly consisted of adventitious C, N, O, and Si. Similar observations for untreated 316 SS have been reported previously. (156) As in the present case, Si (Si 2p) was present in a relatively high concentration

on both unpolished and polished coupons (3.07 at% and 1.35 at%, respectively). These Si deposits are likely the results of the glass bead finishing and the use of silicon carbide papers during polishing. Although more than 1 at% of sodium (Na 1s) was detected on the surface of the unpolished coupon, this was likely due to surface contamination. Besides the Na 1s peak at 1072 eV, Na was also evident through an intense Auger peak (Na KLL) at 497 eV. (146) In line with being a surface contaminant, polishing the coupons removed all Na contamination.

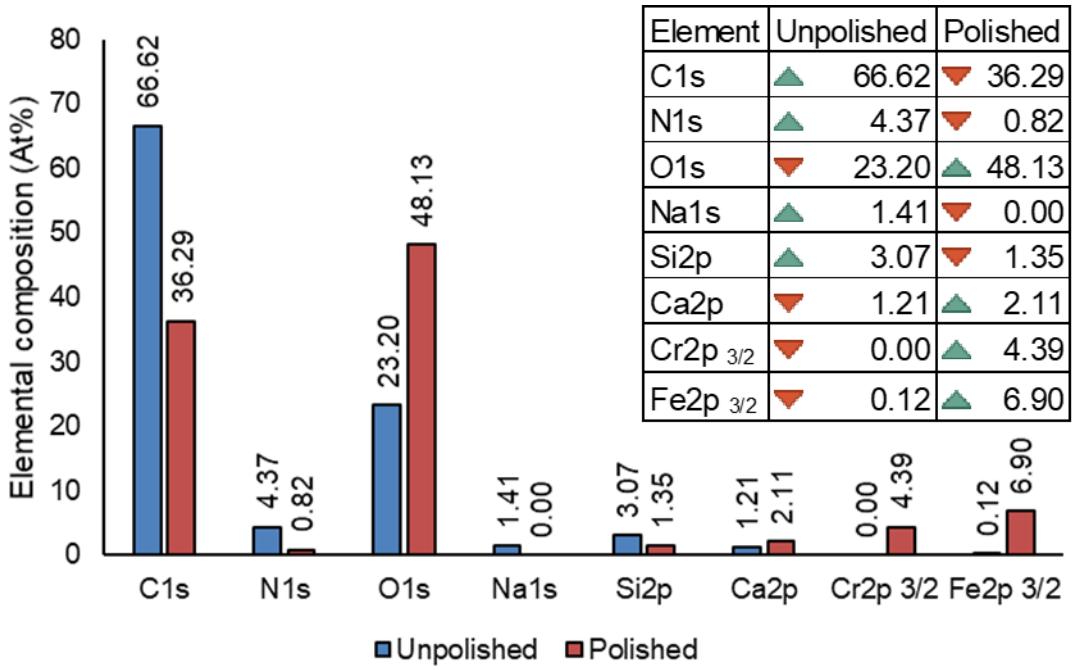

Element	Unpolished	Polished
C1s	▲ 66.62	▼ 36.29
N1s	▲ 4.37	▼ 0.82
O1s	▼ 23.20	▲ 48.13
Na1s	▲ 1.41	▼ 0.00
Si2p	▲ 3.07	▼ 1.35
Ca2p	▼ 1.21	▲ 2.11
Cr2p 3/2	▼ 0.00	▲ 4.39
Fe2p 3/2	▼ 0.12	▲ 6.90

Figure 86 Surface elemental composition of as received vs treated coupons, as calculated from survey spectra. The table at the top right corner compares compositional changes in at% using directional icons (green - higher vs red - lower) for each element across the two measured coupons.

Prior to embarking onto detailed analysis and discussion of the high-resolution spectra, it was sensible to estimate the probing depth (or signal escape depth) of the analysis. This allows for more meaningful interpretation of the acquired data and establishes an understanding of the binding energies and chemical interactions at the interface. As mentioned in chapter 3.4.2, emitted photoelectrons come from the upper 5 nm of the surface. (144) Consequently, probing the solid-liquid interactions at the interface by XPS requires adsorbed, or adventitious, layers of less than a few nm thickness. The carbon (C 1s) layer thickness was calculated as per the following estimation method proposed in (194):

Equation 14

$$d = -\lambda_{C1s,C} \cos\theta \ln(1 - \frac{x}{100})$$

Where d is layer thickness in nm, $\lambda_{C\,1s,C}$ is carbon effective attenuation length in the adventitious layer, approximately 3 nm (156), θ is electron take-off angle, which was 0° (bulk angle), and x is the elemental composition of carbon within the sample in at%.

Using the above equation and the data tabulated in Figure 86, the adventitious carbon layer thickness for the unpolished and polished coupons was estimated to be 3.3 and 1.4 nm, respectively. In comparison, superior treatment methods such as plasma cleaning was able to decrease adventitious carbon layer from 4.5 nm (as received) to 0.6 nm (treated for 5 min) on similar substrate's material. (156) On the other hand, the oxide (O 1s) adventitious layer on metal substrates was thoroughly reviewed in (195). It was concluded that in XPS applications, metal oxides can be easily distinguished from other oxygen species by the peak around ~ 530 eV. Moreover, aerobic oxidation of metallic surfaces at room temperature and atmospheric pressure, which is the case in the present work, typically results in a maximum layer thickness of approximately 2 nm. (196-198) By linking the above calculated thicknesses to the reproducibility studies discussed in chapter 3.5.3, it was estimated that the thickness of the combined adventitious carbon and oxide layers, on all clean substrates used for the present work, was approximately 3 – 4 nm.

High-resolution spectra were acquired for the main surface elements, namely carbon, nitrogen, oxygen, and iron (2p $_{3/2}$). This set of elements was covered throughout the subsequent sections as they regularly make up 90 - 95% of all examined surfaces. XPS measurements were performed as per the instrumental parameters described in Table 21 (chapter 3.5.2.3), with a change in pass energy and dwell time to 30 eV and 0.2 seconds, respectively. Moreover, due to the criticality and importance of obtaining reliable binding energy values and chemical states of nitrogen (N 1s) species on the surface, N 1s spectra were collected at a pass energy of 50 eV to improve the signal to noise ratio.

Carbon (C 1s) spectra were collected over the range from 270 – 300 eV and the binding energy scale was calibrated to the aliphatic C-C peak component at 285.0 eV. (109, 110) Adventitious carbon species were deconvoluted into three main peaks, namely C-C, C-O, and C=O for both polished and unpolished coupons. Such species are commonly found on metallic surfaces. (156, 199-201) Their relative abundance, however, may vary depending on the history and state of the sample. Adventitious hydrocarbon from the atmosphere reacts almost

instantaneously with oxygen and H_2O molecules, resulting in oxidised carbon species, C-O. (199) Concentration of C-O species were found to be more than doubled at the unpolished surface, which suggests that adventitious hydrocarbon species on rough surfaces are more susceptible to oxidation reactions. In smoother surfaces, however, metallic species are more exposed to the atmosphere and thus more metal oxides are typically found. (195) Correlation between C-O (C 1s) and hydroxides (OH, O 1s) levels in the unpolished sample was found to be in good agreement with the aforementioned statements. In the case of the polished coupon, significantly higher content of metal oxides was found on the surface. Table 34 lists the binding energies, intensities, and at% for each component deconvoluted from the carbon (C 1s) and oxygen (O 1s) spectra, followed by XPS spectra (Figure 87).

Table 34 C 1s and O 1s XPS core level binding energies, FWHM, intensities, and composition of the reference coupons.

	Unpolished coupon				**Polished coupon**			
				C 1s				
Species	**B.E (eV)**	**FWHM**	**Peak area**	**at%**	**B.E (eV)**	**FWHM**	**Peak area**	**at%**
C-C	285.0	1.4	301.33	50.12	285.0	1.1	201.85	70.03
C-O	286.0	1.8	237.29	39.47	286.5	1.3	50.83	17.64
C=O	288.8	1.7	62.62	10.41	288.6	2.0	35.57	12.34
				O 1s				
Metal oxides	529.9	1.3	3.47	1.82	530.1	1.2	125.22	38.26
OH	532.0	1.9	127.01	66.60	--	--	--	--
SiO_2	532.9	2.2	60.22	31.58	--	--	--	--
Na KLL	536.5	2.5	N/A*	N/A*	--	--	--	--
C-O	--	--	--	--	531.5	1.9	146.39	44.73
C=O	--	--	--	--	532.9	2.0	55.66	17.01

* Na KLL Auger peak overlapping with O 1s peaks was given RSF value of 0; as it does not contain any oxygen atoms and thus should not be calculated as part of the O 1s spectra. -- Species not found.

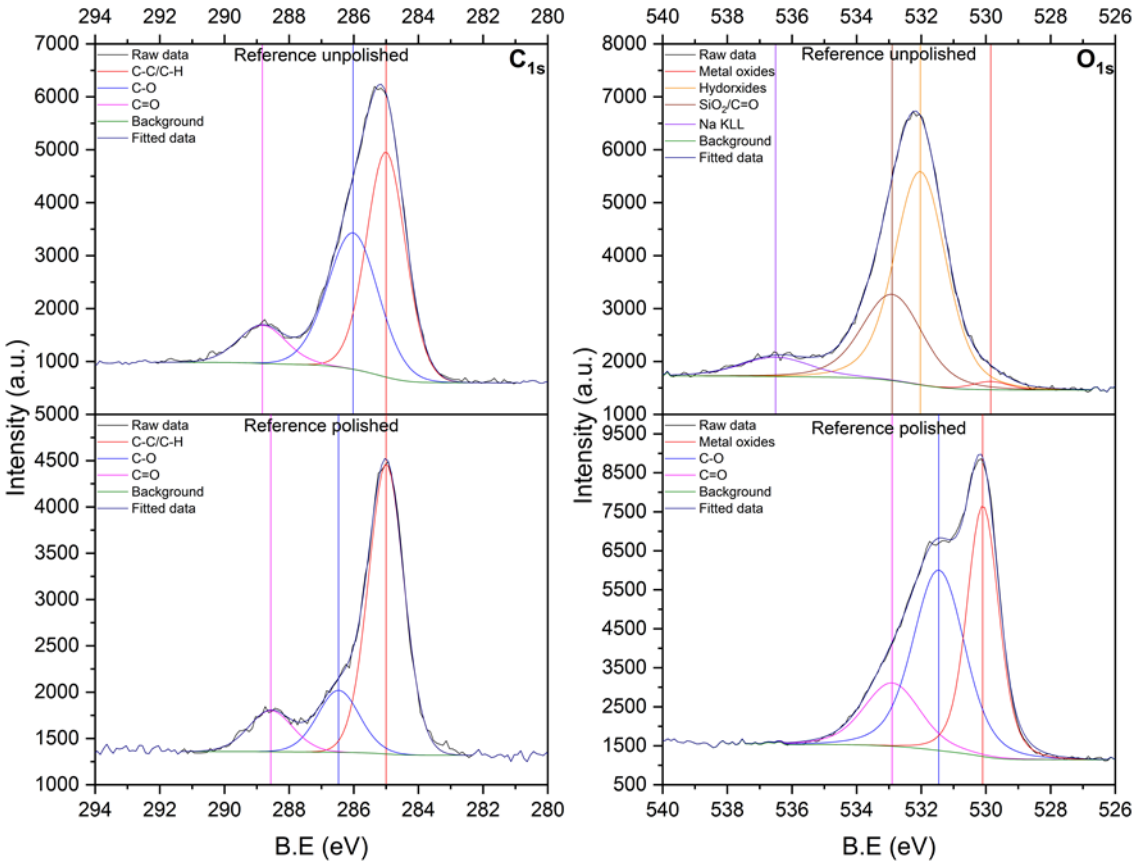

Figure 87 C 1s (left) and O 1s (right) XPS high-resolution spectra showing chemical species on the surfaces of the reference coupons (unpolished – top vs polished – bottom).

It can be seen that polishing the surface has resulted in a totally different surface composition, especially for oxygen species. Addressing the O 1s spectra (Figure 87, right), all peaks were fitted to Lorentzian function line shape, LF(1,1,25,280). The peak at the lower B.E value of ~ 530 eV is characteristic of metal oxides species (O^{2-}). (131, 202, 203) The massive increase in content (1.82 vs 38.26 at%) was attributed to mechanical polishing, which exposed core metal surface to atmosphere resulting in an instantaneous formation and adsorption of the oxide layer. (129, 195) The peak at B.E ~ 532 eV in the unpolished spectra was assigned to hydroxide species (OH) resulting from adventitious hydrocarbon on the surface. (199, 202, 204, 205) The polished sample showed no evidence of hydroxide species on the surface. The C-O and C=O (O 1s) on the polished surface are attributed to the adventitious hydrocarbon layer commonly found on metallic surfaces. (156, 199-201) Moving towards higher B.E, the peak at 532.9 eV was assigned to silicon oxide and C=O in the unpolished and polished spectra, respectively. (206) Although both species had the same centroid energies, considerable concentration of elemental silicon (Si 2p) was found on the unpolished surface which in turn contributed to the formation of silicon oxides

(SiO_2). The assignment of SiO_2 peak was verified by calculating the ratio of silicon to oxygen (i.e. Si 2p/SiO_2) which was found to be 0.50 (1:2), confirming the expected stoichiometry of SiO_2 species. However, it could very well be that the C=O and the SiO_2 peaks are overlapping at the same centroid energy, especially that C=O environments were clearly evident in the C 1s spectrum. Finally, the peak located at 536.5 eV in the unpolished sample was assigned to sodium Auger peak (Na KLL). (146) The sodium peak disappeared completely after polishing, indicating contamination removal (Figure 87, right).

Moving on to the assignments of the C 1s spectra (Figure 87, left), all peaks were fitted to Gaussian-Lorentzian line shape, GL(30). The peak at the lowest B.E (285.0 eV) is conventionally assigned to adventitious carbon in XPS applications of polymeric and hydrocarbon materials. This aliphatic C-C peak was used as a charging reference to calibrate the B.E scale. In both reference coupons, the peaks at ~ 286 and ~ 288.7 eV were assigned to oxidised hydrocarbon species, C-O and C=O, respectively. (156, 199-201) However, the concentration of C-O species was found to be significantly higher in the unpolished sample. One possible explanation is that it might be a combination of C-O and C-N peaks; which both were reported at B.E ~ 286 eV. (146, 207) Another explanation is that polar hydrocarbon, C-O in this case, may easily deposit in the valleys of rough surfaces. As shown in chapter 3.5.2.2, average of maximum valley depth values (R_v) and average maximum profile heights (R_t) for the unpolished reference were 3.52 and 9.78 µm, respectively. Whereas the average values of the three polished coupons were 0.04 and 0.12 µm for R_v and R_t respectively. Such significant reduction in surface valleys depth has resulted in more surface area for non-polar hydrocarbons to be better adsorbed. (156, 193) Concentration of aliphatic C-C has increased by 40% following sample treatment. When high concentration of such long chain molecules are adsorbed onto the uppermost layers of the surface, lesser content of smaller species (e.g. C-O) will be able to penetrate to deeper layers. Figure 88 illustrates the hierarchy of layers on metallic substrates based on surface free energy. (195)

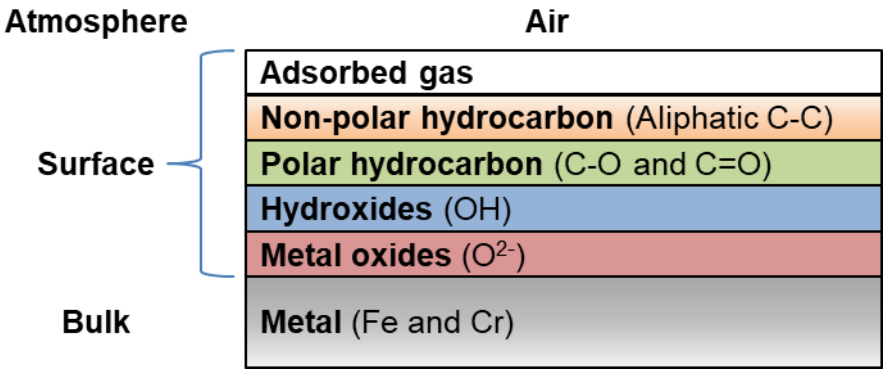

Figure 88 Schematic representation of surface layers on metallic substrates adapted from (156). Comments between brackets refer to the present system.

Iron (Fe 2p) was in the B.E window from 690 – 740 eV. Although metals are typically fitted into Doniach-Sunjic line shape, all Fe 2p peaks in this work were fitted to Gaussian-Lorentzian line shape, GL(30), for simplicity. The Fe $2p_{3/2}$ peak, typically 705 – 715 eV, was used for analysis and quantification. (146) Moreover, it is important to establish that the fitting method applied on all Fe $2p_{3/2}$ peaks throughout this PhD followed the technique of deconvoluting each oxidation state into a single peak (132, 204, 208, 209), in contrast to splitting the Fe^{2+} and Fe^{3+} peaks into multiplets (210). As shown in Figure 86, the concentration of Fe 2p on the surface of the unpolished reference was at minimal (0.1 at%) and therefore high-resolution spectra did not produce any quantifiable features (Figure 89, left). Iron content on the treated surface, however, was significantly higher as a result of mechanical polishing (6.9 at%). Fe $2p_{3/2}$ region was deconvoluted into two main peaks, namely metallic Fe (Fe^0) at B.E ~ 707.1 eV (FWHM 1.2, at% 16.47) and iron oxide Fe_2O_3 (Fe^{3+}) at B.E ~ 710.9 eV (FWHM 3.9, at% 83.53). The difference in oxidation state contributes to the shift towards higher binding energy, where more electrons are found. Although Fe 2p spectra are conventionally attributed to three oxidation states Fe^0, Fe^{3+}, and Fe^{2+}, it was believed that the Fe^{2+} peak arising from this sample was much weaker than the Fe^{3+} peak due to high concentration of iron oxide (Fe_2O_3) on the surface. Figure 89 shows the Fe $2p_{3/2}$ high-resolution spectra for reference coupons.

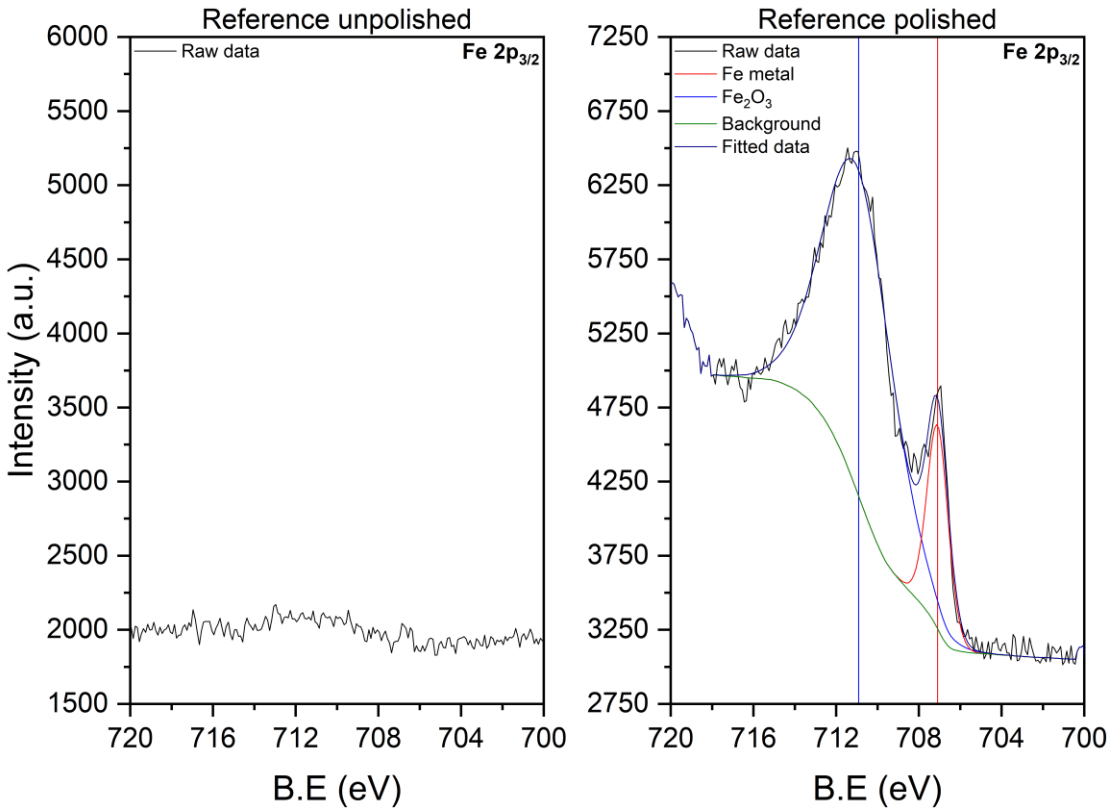

Figure 89 XPS high-resolution spectra of iron (Fe 2p) for the unpolished vs polished reference coupons, scaled to the same arbitrary intensity (4500 a.u.).

Addressing the nitrogen (N 1s) spectra, data were collected over the energy range from 395 – 415 eV for reference coupons and peaks were fitted with Gaussian-Lorentzian line shape, GL(30). For both references, the peak at B.E ~ 400 eV was assigned as 'adsorbed N_2' which corresponds to nitrogen species adsorbed onto stainless steel surfaces. The exact chemical state, however, was ambiguous and challenging to identify, especially in the unpolished sample. Since surface elemental composition of iron was at minimal, it seems possible that the detected nitrogen was associated with the adventitious carbon layer (i.e. C-N), not the metal bulk. (211) This correlates with the considerable concentration of C-O/C-N found on the unpolished reference (Figure 87, top left). Comparable studies have attributed the peak at 400 ± 0.5 eV to anionic nitrogen in nitro compounds such as NO^- and NO_2^-. (124, 208, 212) However, such species would typically result in another characteristic feature at slightly higher B.E ~ 404 – 406 eV, which was not the case in here (Figure 90, left). (36) Organic nitrogen compounds such as alkylamines ($C\text{-}NH_2$) were also reported to be found at B.E ~ 400 eV. (86, 111) Yet, no such species were believed to be on the surface of the unpolished substrate. The peak at the lower B.E (397.5 eV) in the polished reference, however, was arising from nitrogen species bonded to metallic iron, denoted as 'Fe-N' in this work. (123, 124, 157)

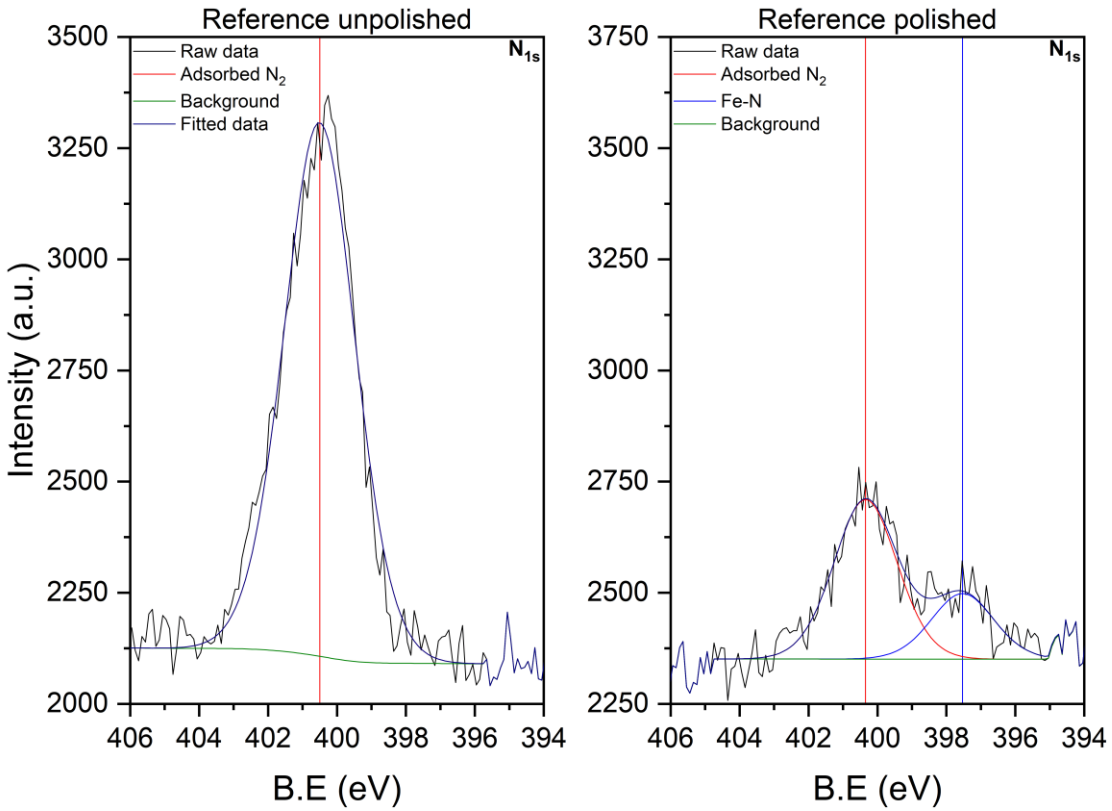

Figure 90 XPS high-resolution spectra of nitrogen (N 1s) for the unpolished vs polished reference coupons, scaled to the same arbitrary intensity (1500 a.u.).

The fact that the Fe-N peak was only found in the polished substrate correlates well with the composition and chemical species found on the surface, namely Fe $2p_{3/2}$, Cr $2p_{3/2}$, and Fe_2O_3 (Figure 86 and Figure 89). In other words, polishing the surface has indeed exposed more of the bulk metal (Figure 88), resulting in a totally different surface chemistry. Table 35 compares the centroid energies, FWHM, intensities, and at% of the assigned peaks.

Table 35 N 1s XPS core level binding energies, FWHM, intensities, and composition of the reference coupons

	Unpolished coupon				**Polished coupon**			
Species	**B.E (eV)**	**FWHM**	**Peak area**	**at%**	**B.E (eV)**	**FWHM**	**Peak area**	**at%**
Ads. N_2	400.5	2.4	40.84	100	400.4	2.2	10.88	71.12
Fe-N	--*	--	--	--	397.5	2.1	4.42	28.88

* -- Species not found.

The data shown in Figure 86 and Figure 90, as well as the cited literature, indicated that nitrogen is an integral component of the stainless steel bulk, not only the surface. Furthermore, by looking into stainless steel manufacturing processes, it was found that introducing inert gases such as argon and nitrogen is an essential stage of the process which aids to hinder undesirable aerobic oxidation. One conventional application of purging nitrogen gas into the melt is to enhance performance properties such as strength and corrosion resistance. (213, 214) Other motivations to purge nitrogen, or nitrogen containing gases, include cost effectiveness and producing nickel-free stainless steel, by substituting nickel with nitrogen to prevent contact dermatitis from nickel. (215) Nevertheless, as part of the reproducibility study conducted for this work (Figure 44 and Figure 47), it was well established that nitrogen content across the examined stainless steel substrates was non-uniformly distributed. Figure 91 depicts our understanding of how nitrogen is distributed on the SS surfaces.

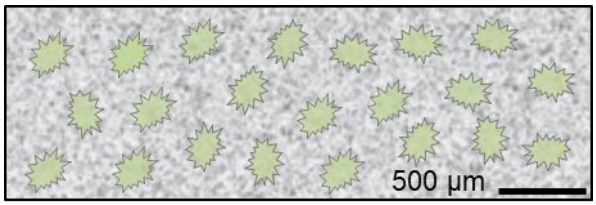

Figure 91 Visual representation of nitrogen island (green) on stainless steel substrates (grey), at micrometre scale.

6.2.2 XPS of pure ODA

XPS data of pure ODA were acquired with an EnviroESCA™ electron spectrometer (SPECS™ Surface Nano Analysis GmbH) under near ambient pressure (NAP-XPS). The sample was manually pressed into a pellet and measurements were conducted in an analysis chamber pressure of 9 mbar. High purity Argon (Ar 4.8, ≥ 99.998%) was used at a flow rate of 1 ml/min to compensate for sample charging. High-resolution XPS spectra of carbon (C 1s) and nitrogen (N 1s) were collected at analysis windows of 275 – 300 eV and 394 – 410 eV, respectively. C 1s peaks were fitted to Lorentzian function line shape, LF(1,1,25,280); as they were too narrow for the conventional GL(30). Pass energy, dwell time, and step size were kept at 50 eV, 0.1 s, and 0.1 eV respectively for both elements. Number of scans was increased from 4 (C 1s) to 25 (N 1s) to enhance signal to noise ratio. The following figure shows real images of the analysed ODA pellet inside the analysis chamber.

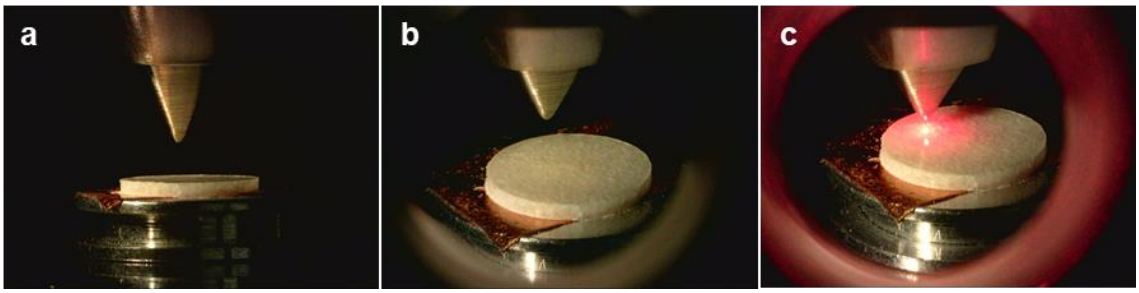

Figure 92 High-resolution images taken using the digital microscope cameras fitted within the EnviroESCA™ of **a)** side-view showing analyser nozzle, ODA pellet, and specimen stub (top-middle-bottom), **b)** top angle-view of the sample, and **c)** scanned site indicated by the red laser point.

Addressing the C 1s spectra, data were deconvoluted into four peaks namely aliphatic C-C, C-N, C-O, and COOH. (86) The area of the peak arising from the polar head ($C\text{-}NH_2$) was constrained to a ratio of 1/17 from the aliphatic C-C peak. FWHM of C-N, C-O, and COOH peaks was constrained to 0.8 – 1.2. Table 36 lists the B.E values, FWHM, peak areas, and at% of the assigned peaks.

Table 36 C 1s deconvolution parameters of pure ODA XPS spectra.

Species	B.E (eV)	FWHM	Peak area	Conc. (at%)
Aliphatic C-C	285.0	1.2	61.79	89.56
C-N	286.0	0.8	3.63	5.27
C-O	287.1	1.2	2.03	2.94
COOH	288.8	1.2	1.55	2.24

Although ODA is solely carbon and nitrogen (and undetectable H), it is well established that ODA and similar long chain alkylamines (C_{12} – C_{18}) undergo carbamation process once exposed to atmospheric CO_2, even at room temperature. (86, 89, 216) The chemical reaction is reversible, depending on the presence of CO_2, as per the equation proposed in (86). The reaction, however, is time-dependent and only prolonged exposure of CO_2 may permanently produce alkyl carbamates (R-NH-COOH). (86, 216)

$$\begin{matrix} R\text{-}NH_2 \\ R\text{-}NH_2 \end{matrix} + CO_2 \rightleftharpoons \begin{matrix} R\text{-}NH_3^+ \\ R\text{-}NH\text{-}COO^- \end{matrix}$$

In addition to purging the analysis chamber with inert gas, extra measures were taken to maintain minimal exposure time when analysing pure ODA for this work.

Thus, it was believed that the collected XPS spectra was of ODA although traces of C-O and COOH environments were detected on the surface.

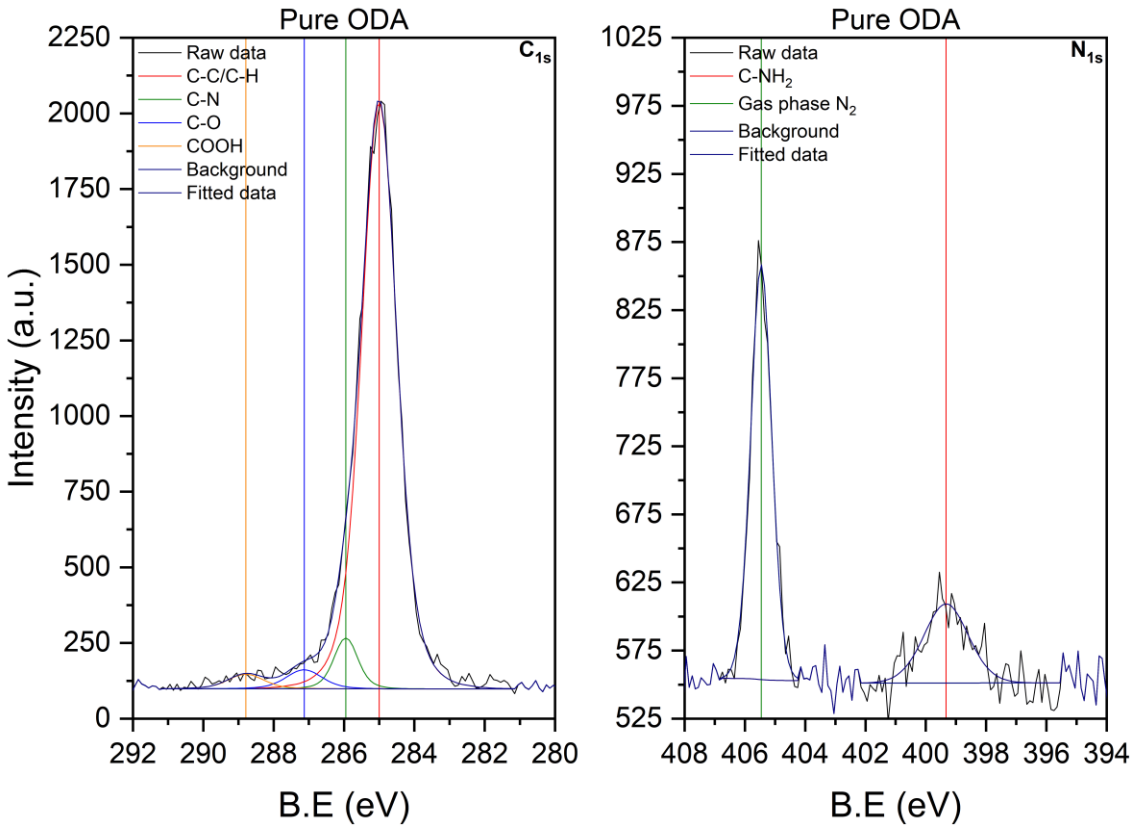

Figure 93 XPS high-resolution spectra of the carbon C 1s (left) and nitrogen N 1s (right) regions for pure ODA.

Nitrogen XPS spectra were deconvoluted into two main peaks, C-NH_2 arising from the amine head group at 399.3 eV and gas phase nitrogen at 405.5 eV. (86, 148, 217) The FWHM of these peaks was 1.7 and 0.8 eV, respectively. In previous XPS studies of alkylamine systems, the C-NH_2 peak was reported at the same B.E value of 399.3 eV for gold nanoparticles capped with dodecylamine (DA, C_{12}) and ODA (93), at 399.4 eV (FWHM 1.8) for pure ODA (86), 399.5 eV for solid DA (96), 399.0 eV for primary amines (128), and in the range of 399.1 – 399.6 eV for aminosiloxane and aminothiolates deposited on silicon and gold substrates, respectively (113). On the other hand, protonated amine species (-NH_3^+) were reported at B.Es of 401.1 eV (90), 401.2 eV (93), 401.3 eV (86), 401.9 eV (112), and in the range of 400.9 – 401.7 eV as reported in (113). Nevertheless, the N 1s spectra in the present study never featured multiple peaks within the reported range, indicating that positively charged amine groups were not formed on the surface. However, due to the carbamate species found on the surface, nitrogen to carbon ratio, C-NH_2 (N 1s) to C-C (C 1s), was found to be approximately 2%.

An attempt was made to better quantify carbamate species on the surface by collecting oxygen (O 1s) high-resolution XPS spectra of pure ODA. However, no quantifiable features were attained and thus data was not included in this section.

6.2.3 XPS of gum (TRF oxidation product)

The surface chemistry of the synthesised gum was probed with NAP-XPS on the EnviroESCA™, as per the instrumental parameters detailed in 6.2.2. Samples were smeared onto a TAM-cleaned, polished stainless steel coupon (Figure 94) and measured for survey, carbon (C 1s), and oxygen (O 1s). Table 37 lists the XPS scanning parameters applied. The elemental composition from the survey scan (Figure A 7) showed that the surface of the synthesised gum was made up of carbon and oxygen in the ratio of ~ 16:1 (94.0 and 6.0 at% respectively). Purging gas (Ar) as well as traces of gas phase nitrogen and oxygen were also evident in the spectra, but did not significantly affect sample's composition or quantification. More importantly, no indications of the substrate's bulk (i.e. Fe, Cr, or metal oxides) were detected in the spectra, which confirms that the measured sample was purely gum.

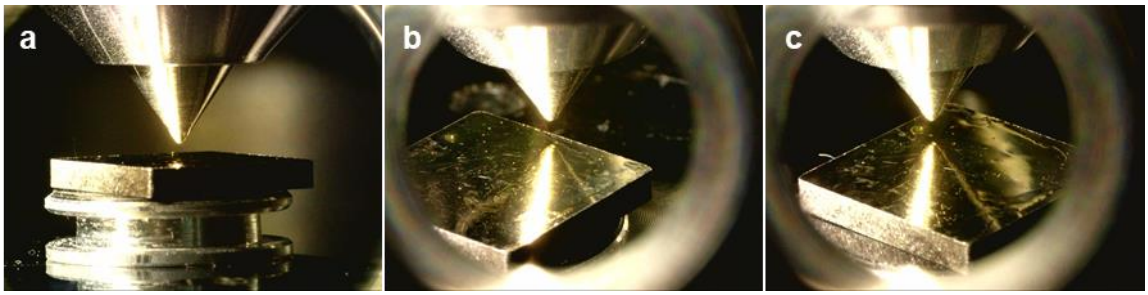

Figure 94 Digital microscope images of the analysed sample inside the analysis chamber showing **a)** side-view of analyser nozzle, SS coupon, and specimen stub (top-middle-bottom), **b and c)** top angle-views of the analysed sample showing thick, polymeric gum and nozzle reflection on the polished substrate.

Table 37 XPS scanning parameters used to investigate the surface of synthesised gum.

Scan range	Pass energy (eV)	Dwell time (s)	Step size (eV)	Number of scans
Survey	100	0.1	1	1
C 1s	30	0.1	0.1	4
O 1s	30	0.1	0.1	4

C 1s spectra were deconvoluted into three main peaks, aliphatic C-C at 285.0 eV, C-O at 286.4 eV, and C=O at 287.8 eV. (36, 146, 201, 211) By comparing aliphatic C-C peak area of ODA to that of gum (Table 36 and Table 38), it was estimated that gum molecules on the surface had a chain length of C_{16}, which correlates with the ratio of carbon to oxygen calculated from survey scan. O 1s spectra, on the other hand, were fitted by Lorentzian line shapes, LF(1,1,25,280) and deconvoluted into C=O at 532.5 eV and OH at 533.4 eV. (36, 112, 128, 129) The two chemical groups assigned in the O 1s spectra correlate with the ATR-FTIR assignments of carbonyl (C=O) and hydroxyl (OH) vibration stretch observed at 1707 cm^{-1} and 3446 cm^{-1}, respectively (Figure 62 and Figure 63).

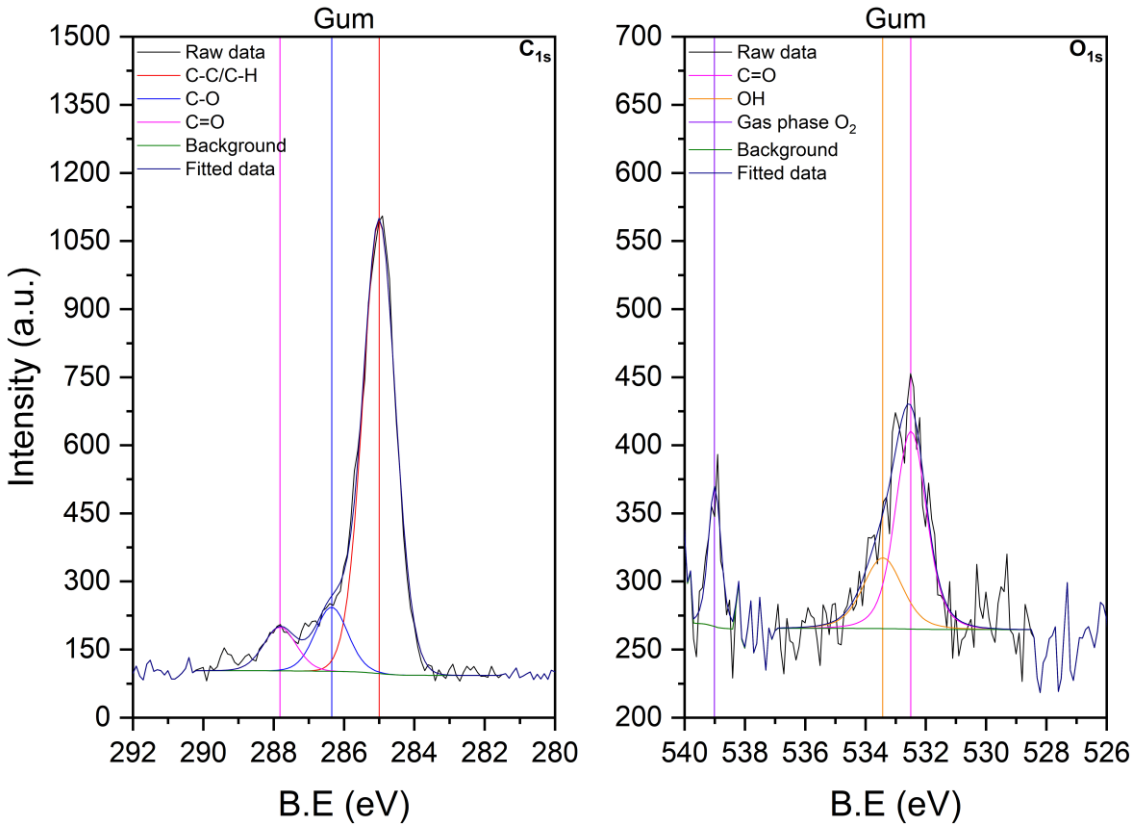

Figure 95 XPS high-resolution spectra of the carbon C 1s (left) and oxygen O 1s (right) regions for the synthesised gum.

Table 38 Carbon (C 1s) and oxygen (O 1s) core level XPS binding energies, FWHM, peak areas, and concentration of species found on tshe surface on the surface of the analysed gum sample.

	C 1s				O 1s			
Species	**B.E (eV)**	**FWHM**	**Peak area**	**at%**	**B.E (eV)**	**FWHM**	**Peak area**	**at%**
C-C	285.0	1.1	54.46	80.80	--*	--	--	--
C-O	286.4	1.1	7.70	11.42	--	--	--	--
C=O	287.8	1.1	5.24	7.78	532.5	1.2	8.73	65.05
OH	--	--	--	--	533.4	1.5	3.91	29.11

* -- Species not found.

6.3 XPS of gum/ODA adsorption from solution

This section is devoted to analysing the immersion experiments as per the experimental design summarised in Figure 84. XPS measurements of stage one (i.e. blank SS) and two (i.e. immersion in 2000 ppm ODA or gum) were conducted on the EnviroESCA™, whereas stage three (i.e. immersion in 1000 ppm ODA, gum, or in neat TRF) were measured on a conventional ultrahigh vacuum (UHV) XPS (due to an unforeseen malfunction in the EnviroESCA). Full explanation of experimental conditions and data analysis procedures for accurate quantification can be found in Appendix 3. Since different XPS instruments were utilised, scanning parameters were optimised for each instrument as per Table 39. Nitrogen (N 1s) high-resolution scans were further optimised to reduce signal to noise ratio and consequently improve the collected data.

Table 39 XPS scanning parameters used throughout all measurements conducted as part of the adsorption and detergency studies for this chapter.

Scan range	Pass energy (eV)	Dwell time (s)	Step size (eV)	Number of scans	Analysis window (eV)
		EnviroESCA			
Survey	100	0.1	1	1	-3 – 1387
C 1s	30	0.1	0.1	4	275 – 300
N 1s	50	0.1	0.1	25	394 – 410
O 1s	30	0.1	0.1	4	520 – 540
Fe 2p	30	0.1	0.1	4	695 – 735
		UHV-XPS*			
Survey	50	0.2	0.5	1	-3 – 1387
C 1s	50	0.2	0.1	4	275 – 300
N 1s	50	0.2	0.1	16 or 32	385 – 420
O 1s	50	0.2	0.1	4	520 – 540
Fe 2p	50	0.2	0.1	4	695 – 735

* Charging correction was performed using ions flood gun at a moderate 2 eV energy, 25 μA electron emission, and a filament current of 2.1 A.

It is also important to mention that since ODA and gum molecules are predominantly carbon-containing species, data from C 1s high-resolution spectra were extensively analysed in the following sections. Trends and observations from other elements complementing the C 1s data were also discussed.

6.3.1 Adsorption study (keep clean mechanism)

In these experiments, the ‘stick and eliminate’ hypothesis was investigated by deliberately adsorbing ODA molecules onto a stainless steel substrate via immersion in a TRF solution containing high concentration of ODA (2000 ppm w/v) for 24 h. The same substrate was then immersed in a TRF solution containing 1000 ppm of gum (w/v) to examine the elimination process proposed in literature. This experiment was titled as ‘ODA in gum’ throughout this chapter. To further validate the findings, a complementary experiment was conducted addressing the behaviour of adsorbed ODA in neat TRF solutions. Thus, another

stainless steel coupon was immersed in ODA/TRF solution of the same high concentration and then immersed in a neat TRF solution. This experiment was titled as ‘ODA in neat TRF’ throughout this chapter. Such work should set the scene to answer the fundamental dilemma of whether detergents remain adsorbed onto metal surfaces in fuel systems, as the hypothesis proposes, or they would dissolve and migrate from the surface.

6.3.1.1 XPS of ODA in gum experiment

Analysis of survey scans revealed consistent surface elemental composition, namely C, N, O, Cr, Fe, F, Ca, and Na across all immersion stages. Calcium (Ca 2p) species were found to be present in minimal concentrations of 0.5 at% of the surface. Sodium (Na 1s) species, however, were found at a concentration of approximately 3 at% on the gum-covered sample, which was measured in the UHV XPS. Consequent experiments showed similar concentration of sodium on the surfaces of all samples stored during the transition between the EnviroESCA and UHV. Therefore, it was considered an extrinsic contamination and only C, N, O, Cr, and Fe were considered to be major surface elements.

Addressing elemental composition from survey spectra (Figure 96), immersing the substrate in 2000 ppm ODA resulted in a 16.8 at% increase in carbon (C 1s) contents on the surface as well as a 1.7 at% increase in nitrogen (N 1s) contents. On the other hand, oxygen (O 1s) and iron (Fe $2p_{3/2}$) species were reduced by 12.5 and 3.07 at% respectively. The formation of carbon and nitrogen in conjunction with the reduction in oxygen and iron levels, which are mainly bulk components, were all a positive indication of a newly-formed ODA layer on the surface. However, C:N ratio, oxidation states, and other chemical information were yet to be verified by the high-resolution spectra. By linking this experiment to the hypothesis in question, one would expect the surface to withhold the same compositional ratios once exposed to a gum-containing environment to eliminate deposition, or at least a significant reduction in iron levels which signifies gum deposition on top of the ODA layer. Yet, data from post-immersion experiment (1000 ppm gum) revealed that iron (Fe 2p) content has increased by 1.6 at% and nitrogen (N 1s) levels decreased to levels below that of the blank, which suggests no ODA layer on the surface.

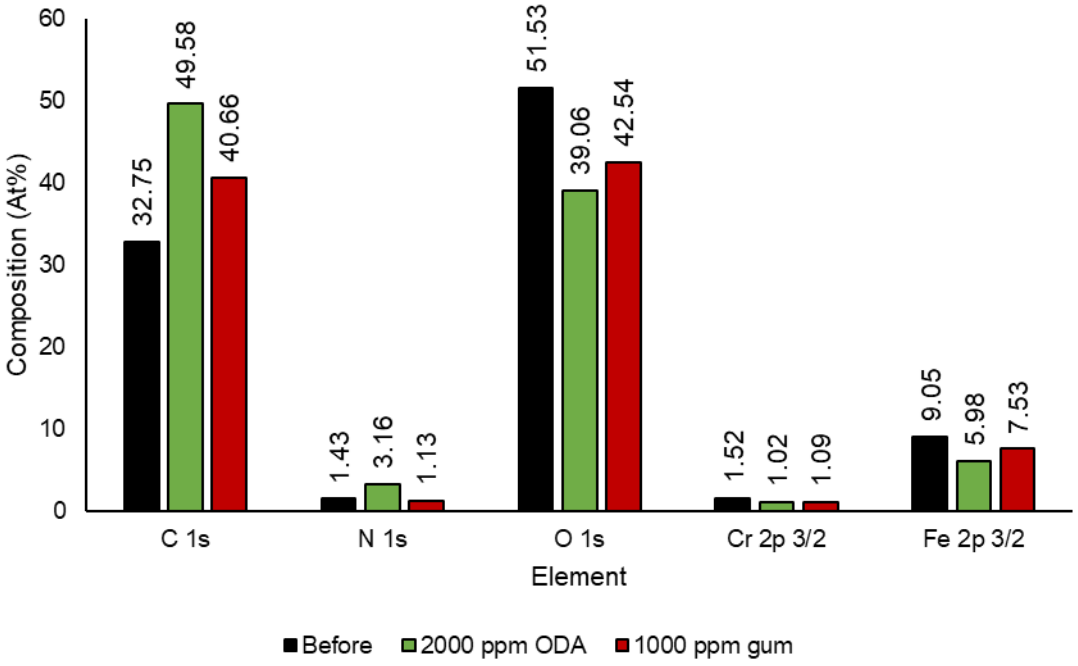

Figure 96 Composition of major surface elements from survey spectra of 'ODA in gum' experiment. Legend is displayed in order of immersion.

Peaks from high-resolution spectra were deconvoluted and assigned as per Table 40. Sodium contamination was evident in the N 1s and O 1s spectra of the gum-immersed sample. Upon deconvoluting all peaks, it was believed the contaminant was in the form of sodium nitrate ($NaNO_3$) based on the characteristic peak at B.E ~ 407.0 eV. Therefore, some peaks were challenging to identify and could not be assigned. Yet, we can confirm that the integrity of this work was not compromised as a result of this contamination.

Since at% does not account for intensity changes across different samples, chemical changes as a function of immersion were quantified as a percentage of change ($\%_{change}$) using peak areas, as per the following equation.

Equation 15

$$\%_{change} = \left[\frac{A - A_0}{A_0}\right] * 100$$

Where: A_0 = Peak area before immersion and A = Peak area after immersion.

The proposed equation allowed for a meaningful comparison between reoccurring chemical species in different samples. By examining the C 1s high-resolution spectra (Figure 97), it was found that aliphatic C-C composition has increased by 16.5% (Table 41) following immersion in ODA. Moreover, The peak at B.E 285.6 eV (FWHM 0.9, at% 3.46) was assigned to C-N environment arising from the ODA amine head group ($C\text{-}NH_2$), which was comparable in

characteristics to the C-NH_2 observed at B.E 286.0 eV in pure ODA (Table 36). Findings correlate with the literature cited in 6.2.2 for alkylamines and ODA adsorption. Moreover, nitrogen to carbon ratio, C-NH_2 (N 1s) / C-C (C 1s), was found to be 5.54%, which is close to the ratio of N:C in ODA molecules (5.56%).

Table 40 XPS core level B.E for all species assigned in the high-resolution spectra, showing actual shifts in reoccurring peaks across all stages of the adsorption and detergency studies. Error margin in B.E was estimated to be ± 0.3 eV.

Element	Species	Position (eV)	Shift (eV)	References
C 1s	C-C/C-H	285.0	N/A*	(109, 110)
	C-N	285.85	(± 0.25)	(146, 207)
	C-O	286.4	(± 0.3)	(156, 199-201)
	C=O	288.55	(± 0.15)	
N 1s	Adsorbed N_2	399.95	(± 0.15)	(211)
	C-NH_2	399.5	(± 0.4)	(86, 111)
	FeN	397.65	(± 0.95)	(123, 124, 157)
	NO^-	402.2	--$^+$	(124, 208, 212)
	NO_3^-	407.0	--$^+$	
O 1s	Metal oxides	529.75	(± 0.25)	(131, 202, 203)
	C-O	531.2	(± 0.6)	(156, 199-201)
	NO_3^-	532.2	--$^+$	(124, 208, 212)
	C=O/C-OH	532.75	(± 0.55)	(156, 199-201)
	Na KLL	536.05	(± 0.55)	(146)
Fe 2p	Fe metal	706.8	(± 0.3)	(132, 204, 208-210)
	FeO	710.25	(± 0.15)	
	Fe_2O_3	711.4	(± 0.4)	

* Position used for B.E scale calibration. $^+$ -- Contamination.

Furthermore, a clear shift in B.E was observed in the O 1s spectra following ODA immersion, especially for the C-O and C=O species (-0.4 and -0.8 eV, respectively). Typically, negative shifts in B.E indicate electrons gain within the studied system. Number of studies have been conducted to explore adsorption behaviour of organic molecules onto metallic substrates. (130, 195, 218) It was suggested that 'back bonding' via electron donation from the metal may contribute to the extent of adsorption stability. However, no comparable shift was observed in the Fe 2p spectra (Figure 97). Thus, it was believed that ODA was adsorbed onto the substrate via bonding to the oxide layers sitting on top of the bulk material (Figure 88). The central peak at ~ 400 eV (N 1s) exhibited an increase in intensity of ca. 14% due to ODA adsorption. This increase was accompanied by an attenuation in total iron (Fe 2p) and metal oxide (O 1s) contents by approximately 25% and 27% respectively, which agrees with the trends observed in C 1s and N 1s spectra. Analyses followed from gum-immersion stage (i.e. +1000 ppm gum), revealed disappearance of the C-N (C 1s) peak as well as a clear attenuation in nitrogen (N 1s) contents. Moreover, by overlaying the C 1s spectral profiles, it can be clearly seen that the intensity of the C-O and C=O species were still higher than that of the two previous stages (Figure 98). Nevertheless, when comparing intensities of the aliphatic C-C species, a slight increase was found. Observations suggest that gum molecules have displaced ODA on the surface to a certain extent, which explains the hazy layer seen on the substrate (Figure 98, c). Overall increase in carbon content was found to be approximately 22% (blank to +1000 ppm gum), indicating a residual layer on the surface. Experiments to follow where designed to address whether ODA has dissolved in the TRF or migrated from the surface to capture the dissolved gum species.

Table 41 C 1s core level binding energy, corrected peak area, and concentration (at%) as a function of immersion. ▲ and ▼ indicate change in chemical species compared to previous stage.

Sample	Species	Position (eV)	Area	at%
SS coupon (Blank)	C-C/C-H	285.0	3345.67	64.20
	C-O	286.6	830.83	15.94
	C=O	288.7	1035.83	19.86
2000 ppm ODA	C-C/C-H	285.0	▲3899.10	58.84
	C-N	285.6	229.27	3.46
	C-O	286.1	▲1641.70	24.77
	C=O	288.7	▼857.99	12.94
1000 ppm gum	C-C/C-H	285.0	▲3974.14	63.26
	C-O	286.5	▼1114.07	17.73
	C=O	288.5	▲1193.82	19.00

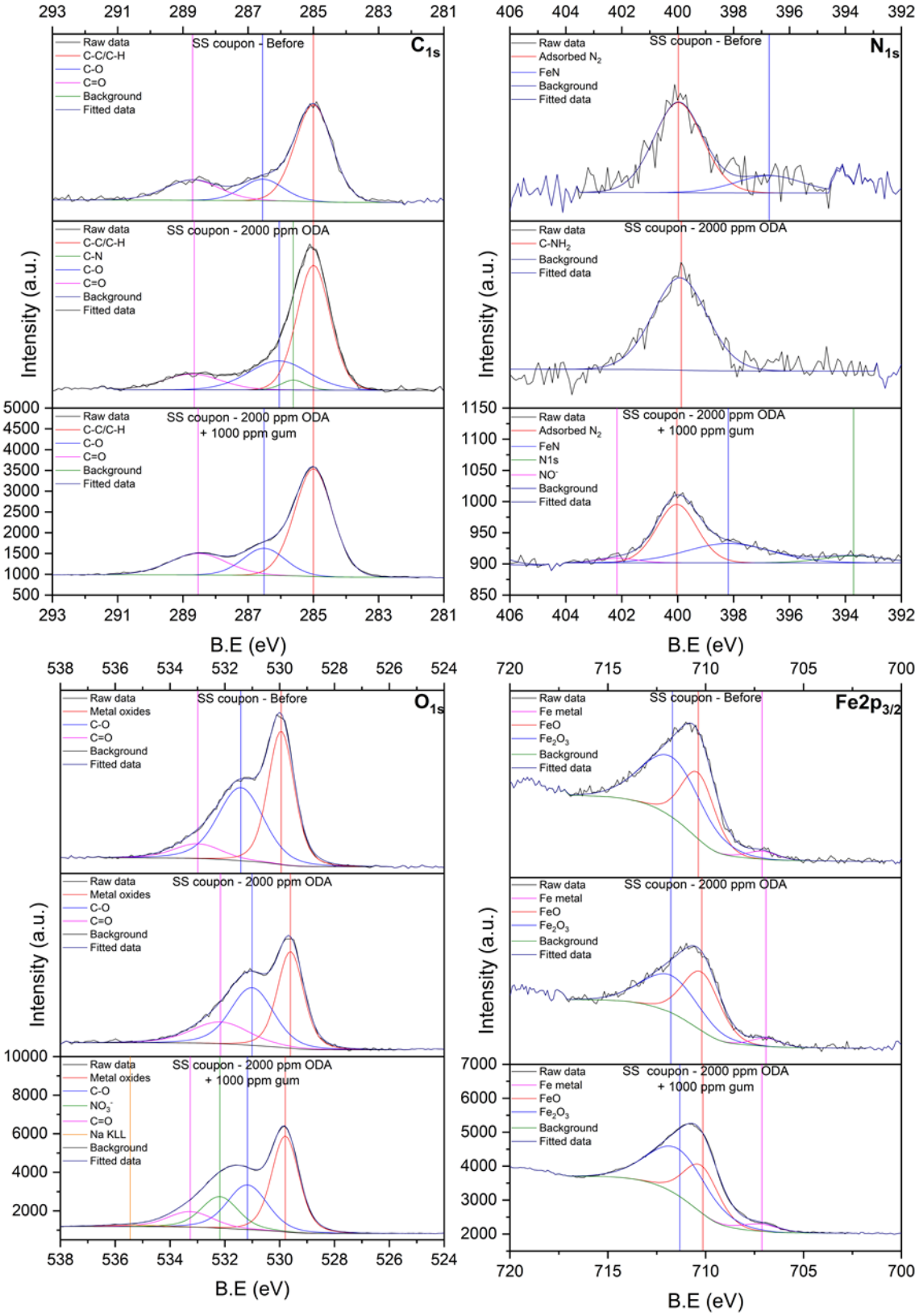

Figure 97 C 1s, N 1s, O 1s, and Fe 2p XPS high-resolution spectra of the 'ODA in gum' experiment, as a function of immersion. Each elemental spectrum was scaled to the arbitrary intensity shown on their relevant figure.

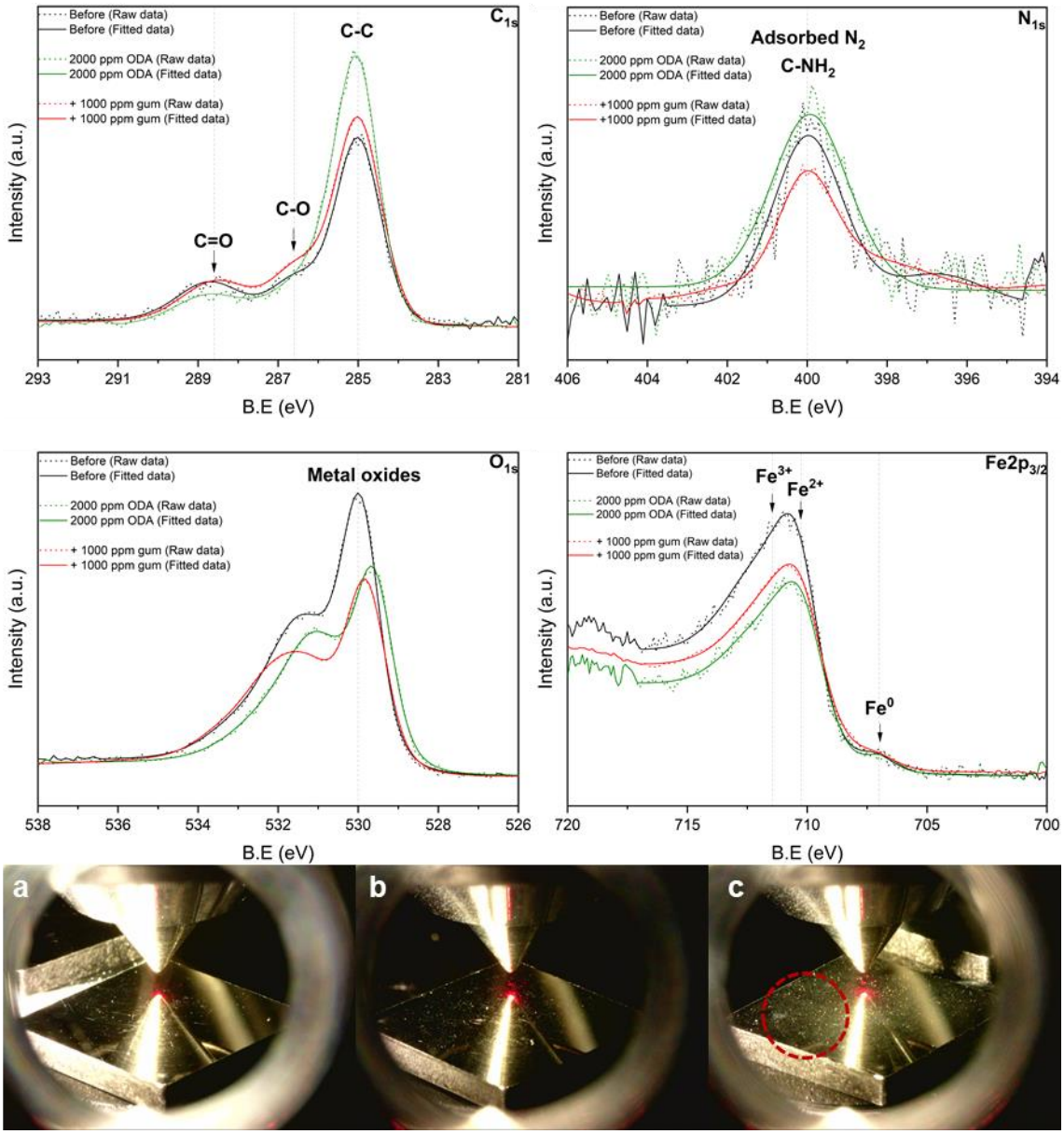

Figure 98 Overall attenuation profile of the C 1s, N 1s, O 1s, and Fe 2p spectra as a function of immersion (data retrieved from Figure 97). Legend is displayed in order of immersion. Microscope images represent **a)** blank substrate, **b)** substrate after immersion in 2000 ppm ODA, and **c)** substrate after immersion in 1000 ppm gum, where a thin, hazy layer of adsorbed gum was observed on the surface (circled in red).

6.3.1.2 XPS of ODA in neat TRF experiment

Analysis of survey scans (Figure 99) showed comparable elemental composition of the blank (before) substrate to that of the previous sample (6.3.1.1). Following immersion in ODA/TRF solution, significant concentration of carbon (C 1s) was found on the surface. Nitrogen (N 1s) content also had increased, which indicates a thick layer of ODA. In line with this, oxygen, chromium, and iron have attenuated by 58%, 77%, and 64% respectively. The adsorbed ODA was visually observed as a white, cloudy layer on the surface (Figure 101, a). Interestingly, elemental composition on the surface was almost restored following neat TRF immersion. The substrate appeared visually cleaner as well (Figure 101, b). The XPS data indicate some residual ODA layer on the surface, but not much. Comparison between the 'neat TRF' sample (in blue) against the '2000 ppm ODA' from the previous experiment (in green) showed good correlations in carbon, oxygen, and iron contents (46 vs 50 at%, 40 vs 39 at%, and 7.4 vs 7.5 at% respectively). These observations along with the relatively high concentration of nitrogen (1.8 at%) suggest similar adsorbed ODA layers in both cases. Further analysis of the high-resolution spectra could give deeper insight into the surface chemistry.

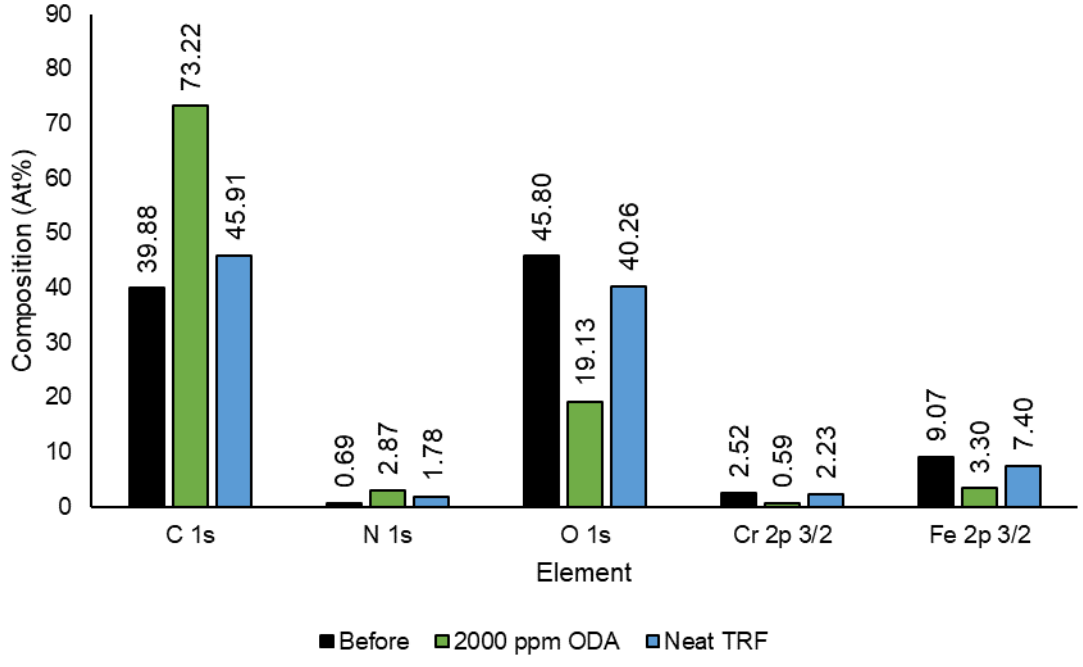

Figure 99 Composition of major surface elements from survey spectra of 'ODA in neat TRF' experiment. Legend is displayed in order of immersion.

High-resolution spectra were therefore analysed as per Table 40. Following immersing the substrate in a 2000 ppm ODA/TRF solution, the C 1s spectra revealed C-N and COOH peaks at B.Es of 285.9 and 288.2 eV, respectively. These values are comparable to those of pure ODA (286.0 and 288.8 eV). N 1s spectra showed three distinctive peaks which were assigned to unreacted C-NH_2 at 396.5, C-NH_2 at 399.1 eV, and NH_3^+ at 400.9 eV. (86, 90, 111, 113) The distinct increase in aliphatic C-C concentration (Table 42), along with the observation of unreacted amine groups on the surface suggest that the surface contained some ODA in a second layer on top of the chemisorbed first layer. Furthermore, the carbon to nitrogen ratio was found to be very similar to what was observed for pure ODA, 2.2%. Similar B.E shifts as in the previous experiment were observed in the O 1s spectra. Metal oxides, C-O, and C=O signals all appeared chemically shifted by -0.9, -0.8, and -0.4 eV, respectively. In the Fe 2p spectra, a chemical shift of -0.9 eV was evident.

After immersion in neat TRF in the absence of gum, C 1s spectra revealed a composition similar to that of the blank substrate, with an exception for the C-N peak at 286.1 eV. C 1s and N 1s data presented in Figure 101 showed comparable profiles to that of the blank sample, yet with a higher intensity. The overall increase in carbon content relative to the blank sample was found to be approximately 16%, confirming the residual ODA layer on the surface that was suggested based on the survey spectra. The O 1s and Fe 2p profiles were accordingly attenuated.

Several studies have discussed the adsorption behavior of long-chain alkylamines onto various substrates. The proposed adsorption mechanisms have included ‘back bonding’ to metal oxide species on the surface (90, 113, 130, 195), or ‘protonation’, where the -NH_2 head group interacts with oxygenated species (e.g. C=O and OH) to form hydrogen bonds. (86, 96) The former mechanism was experimentally observed on metal surfaces, unlike the latter where surfaces such as mica and silicates were considered. Although no experimental evidence for adsorption via protonation was found in (86), both mechanisms seem viable and their confirmation will require thorough, more systemic research. In the literature, there seems to have been an inclination to support ‘back bonding’ mechanism, especially on metallic substrates. For the systems investigated here, no experimental evidence of adsorption via protonation was found. The B.E shifts observed for O 1s and Fe $2p_{3/2}$ as a function of ODA immersion, along with the increase in aliphatic C-C and nitrogen contents, were all indicative of adsorption via ‘back bonding’ to metal oxides.

Table 42 C 1s core level binding energy, corrected peak area, and concentration (at%) as a function of immersion. ▲ and ▼ indicate change in chemical species compared to previous stage.

Sample	Species	Position (eV)	Area	at%
SS coupon (Blank)	C-C/C-H	285.0	15903.50	73.60
	C-O	286.4	3058.86	14.16
	C=O	288.6	2645.04	12.24
2000 ppm ODA	Adventitious carbon	284.15	7221.30	8.10
	C-C/C-H	285.0	▲74064.90	83.10
	C-N	285.9	4118.01	4.62
	COOH	288.2	3720.92	4.17
Neat TRF	C-C/C-H	285.0	▼19122.62	76.26
	C-N	286.1	▼1124.41	4.48
	C-O	286.7	1872.07	7.47
	C=O	288.6	2956.51	11.79

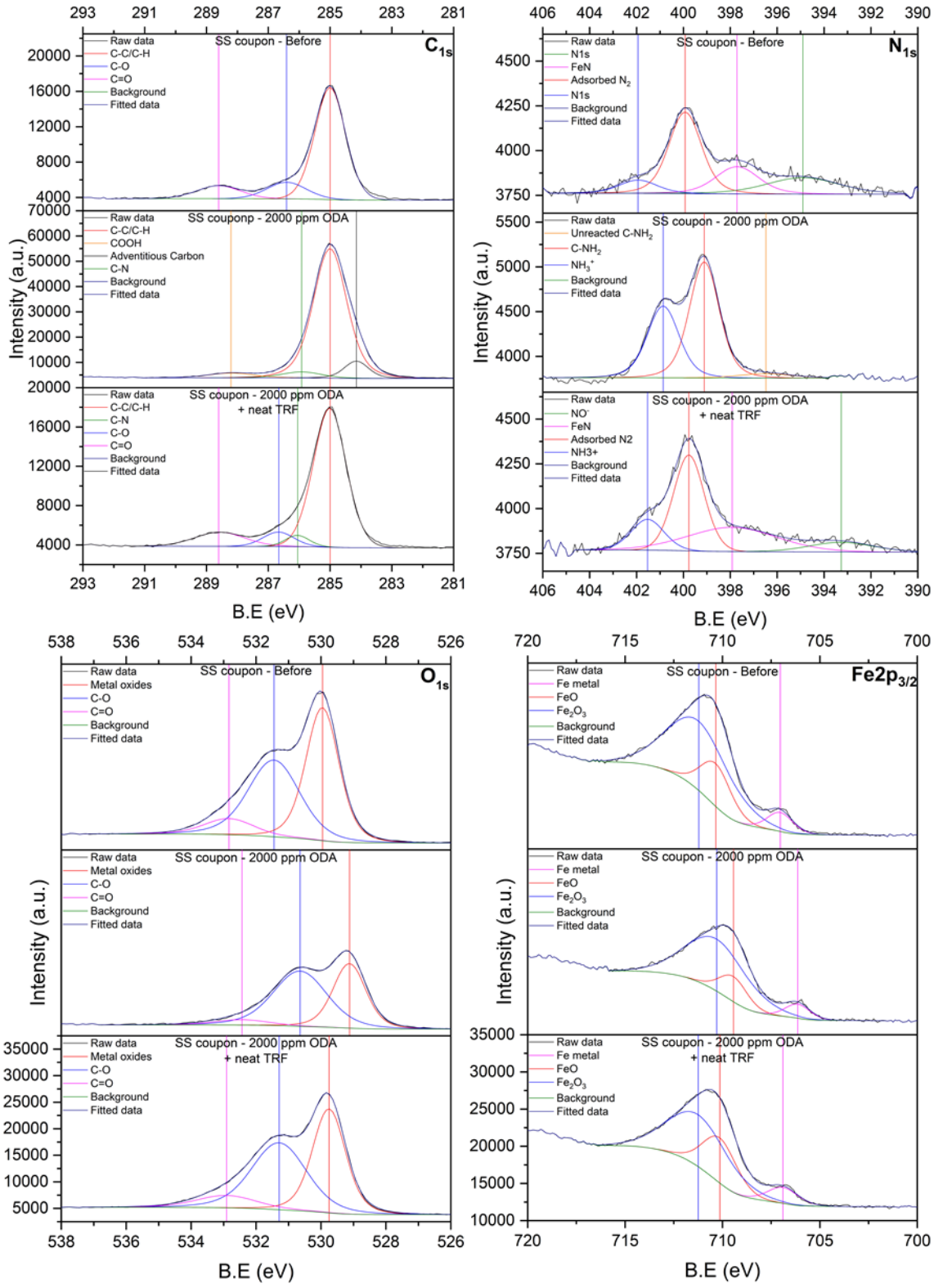

Figure 100 C 1s, N 1s, O 1s, and Fe 2p XPS high-resolution spectra of the 'ODA in neat TRF' experiment, as a function of immersion. Each elemental spectra was scaled to the arbitrary intensity shown on their relevant figure.

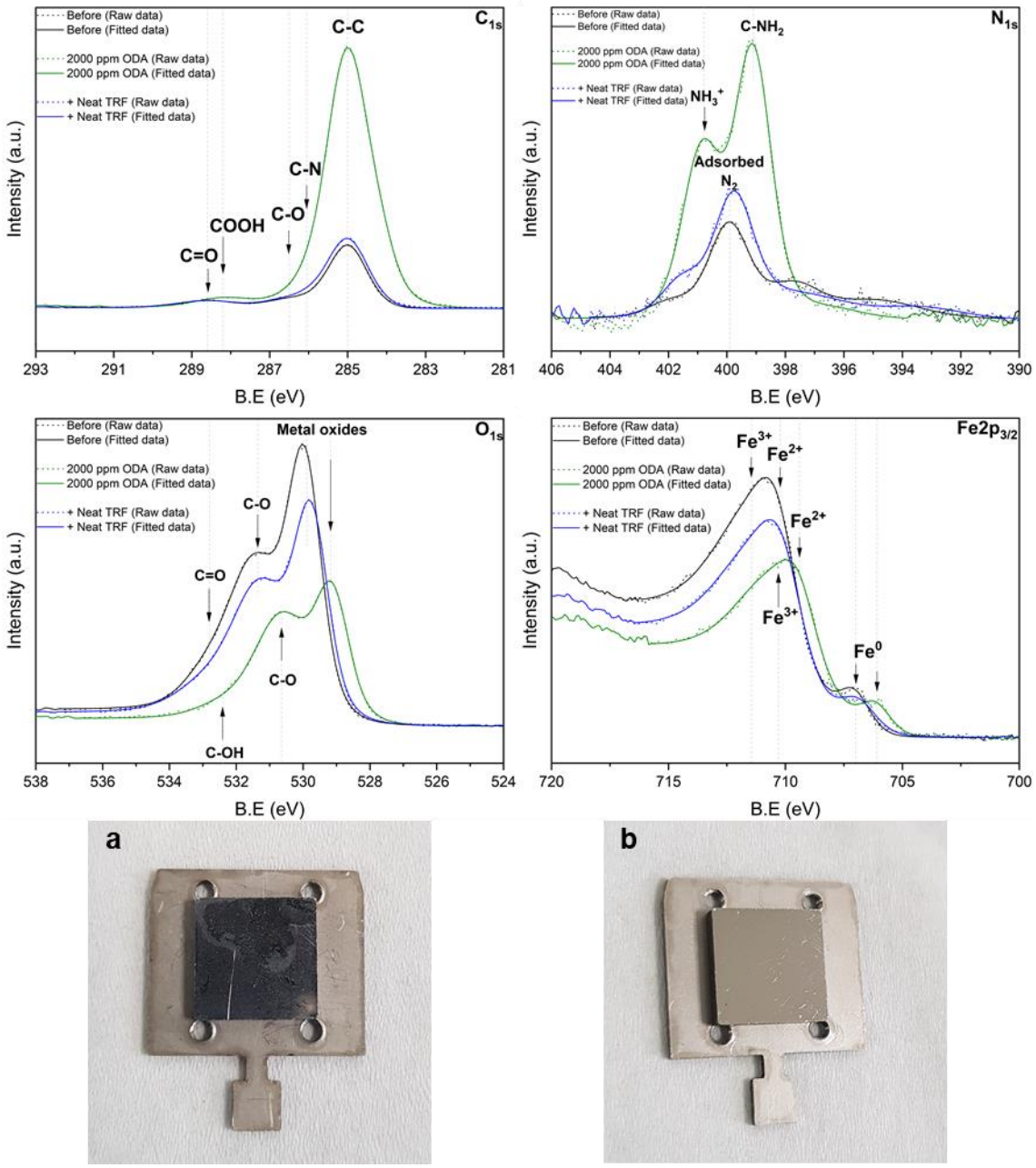

Figure 101 Overall attenuation profile of the C 1s, N 1s, O 1s, and Fe 2p spectra as a function of immersion (data retrieved from Figure 100). Legend is displayed in order of immersion. Microscope images represent **a)** substrate immersed in 2000 ppm ODA, **b)** substrate after immersion in neat TRF, showing significantly cleaner surface.

6.3.2 Detergency study (clean-up mechanism)

In these experiments, two stainless steel substrates were immersed in separate TRF solutions containing 2000 ppm gum each. One coupon was then immersed in a TRF solution containing 1000 ppm of ODA, whereas the other was immersed in neat TRF. The former experiment, titled as ‘gum in ODA’, was designed to understand gum adsorption behaviour on metallic surfaces and consequently ODA detergency mechanism. The latter, termed ‘gum in neat TRF’, was performed to gauge gum dissolution in surrogate fuel systems, without the aid of nitrogen-based compounds. Combining the results from both experiments will provide insight into the ODA detergency effects in oxidised surrogate fuels.

6.3.2.1 XPS of gum in ODA experiment

Analysis of survey scans (Figure 102) showed similar surface chemical composition to previous experiments (6.3.1.1). The concentration of adsorbed gum found on the surface was, however, significantly higher than that of adsorbed ODA. Following gum immersion, the carbon content had increased by 67%, compared to 51% for ODA. Nitrogen, oxygen and iron contents all showed noticeable changes of -100%, -25%, and -51% respectively, due to the adsorbed gum layer, which can be clearly seen in Figure 104, b. It was expected that oxygen will show the least reduction; as the change was mainly attributed to attenuation in metal oxide species only (Figure 103, O 1s).

Immersing the coupon in ODA/TRF solution reduced the carbon content by 23%. Visually, the coupon’s surface appeared significantly cleaner (Figure 104, c). However, the concentration was still higher than that of the blank sample (45 vs 35 at%, respectively) indicating residual carbonaceous deposits on the surface. Analysis of the high-resolution spectra should reveal more information about the chemical nature (see below). The substrate was more exposed as indicated by the high chromium and iron emission signals, but still less than that of the blank sample due to the residual overlayer. The nitrogen content provides insight into the amount of ODA in the residual layer. The nitrogen concentration on the surface was found to be only slightly less than the values for the blank (1.0 vs 1.1 at%), suggesting that not much ODA is present and indicating that the ‘elimination via passivation’ hypothesis for amine-based detergents is unlikely to be the cause for detergency. This conclusion will also be borne out by the following analysis of the corresponding high-resolution spectra.

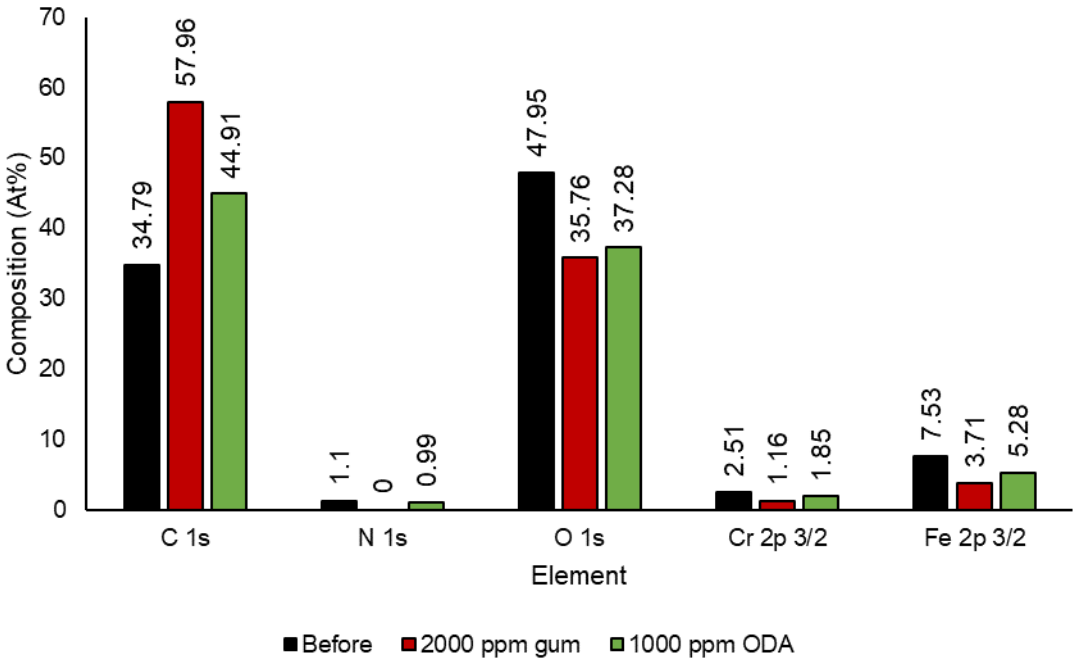

Figure 102 Composition of major surface elements from survey spectra of 'gum in ODA' experiment. Legend is displayed in order of immersion.

In the high-resolution spectra, all peaks have been fitted and assigned as per the literature cited in Table 40. Upon deconvoluting the C 1s spectra, significant increase was observed in the concentration of C-O species as a result of gum adsorption (Table 43). A similar increase was also observed in the C-OH peak from O 1s spectra, with noticeable attenuation in metal oxide and iron (Fe $2p_{3/2}$) levels indicating thick layers of gum on the surface (Figure 103). Moreover, the intensity of the aliphatic C-C and C=O (C 1s) peaks increased by 31% and 36%, respectively. Comparable shift of -0.5 eV was observed in the binding energies of O 1s and Fe $2p_{3/2}$ species, which may be indicative of electron donation to the metal core due to gum adsorption.

Following the second stage immersion, oxygenated gum species in C 1s spectra (C-O and C=O) attenuated by 73% and 43% respectively, indicating very effective detergency by ODA (Figure 104). The aliphatic C-C composition, however, did not exhibit similar attenuation and no C-N peak was observed. To further investigate the passivation hypothesis, the total nitrogen content (as peak areas) was quantified and found to be 12% less than that of the blank sample. Moreover, nitrogen to carbon ratio was lower than what would be expected for ODA (1.1% vs 5.6% respectively) suggesting the nitrogen signal was intrinsic to the substrate, as previously found for the reference coupons (section 6.2.1). Consequently, all indications suggest that the residual carbon layer was not ODA and no passivation has occurred. With that being said, the data also suggest that ODA

interacts with the adsorbed gum molecules at their C=O sites, in a similar way discussed in the ‘ODA in gum’ experiment (6.3.1.1), which strengthen the aforementioned migration scenario.

Table 43 C 1s core level binding energy, corrected peak area, and concentration (at%) as a function of immersion. ▲ and ▼ indicate change in chemical species compared to previous stage.

Sample	Species	Position (eV)	Area	at%
SS coupon (Blank)	C-C/C-H	285.0	3275.41	59.77
	C-O	286.2	780.41	14.24
	C=O	288.5	1425.68	25.99
2000 ppm gum	C-C/C-H	285.0	▲4282.56	40.96
	C-O	286.1	▲4233.00	40.47
	C=O	288.6	▲1943.20	18.57
1000 ppm ODA	C-C/C-H	285.0	▲4876.01	68.16
	C-O	286.4	▼1163.33	16.26
	C=O	288.5	▼1114.83	15.58

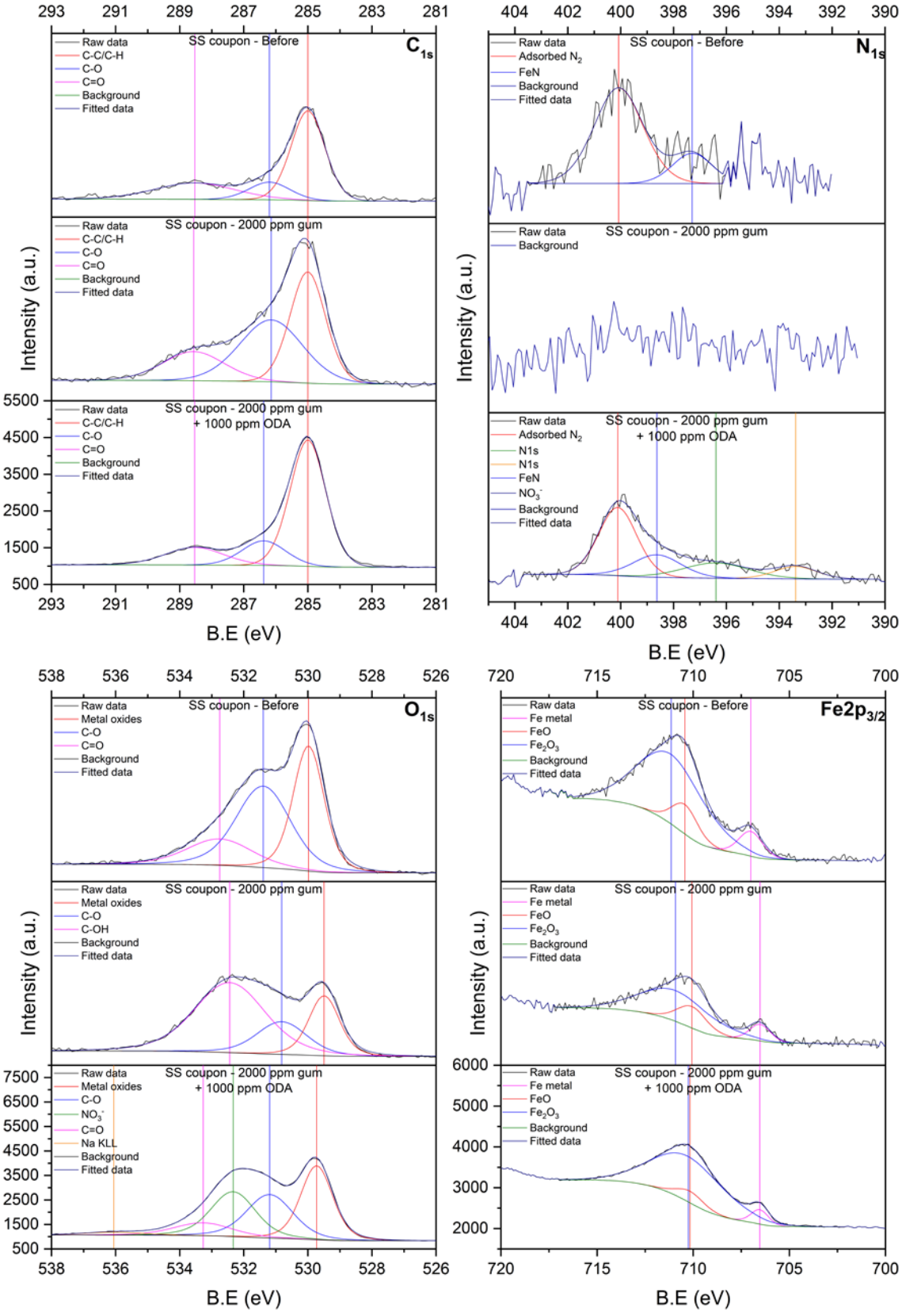

Figure 103 C 1s, N 1s, O 1s, and Fe 2p XPS high-resolution spectra of the 'gum in ODA' experiment, as a function of immersion. Each elemental spectra was scaled to the arbitrary intensity shown on their relevant figure.

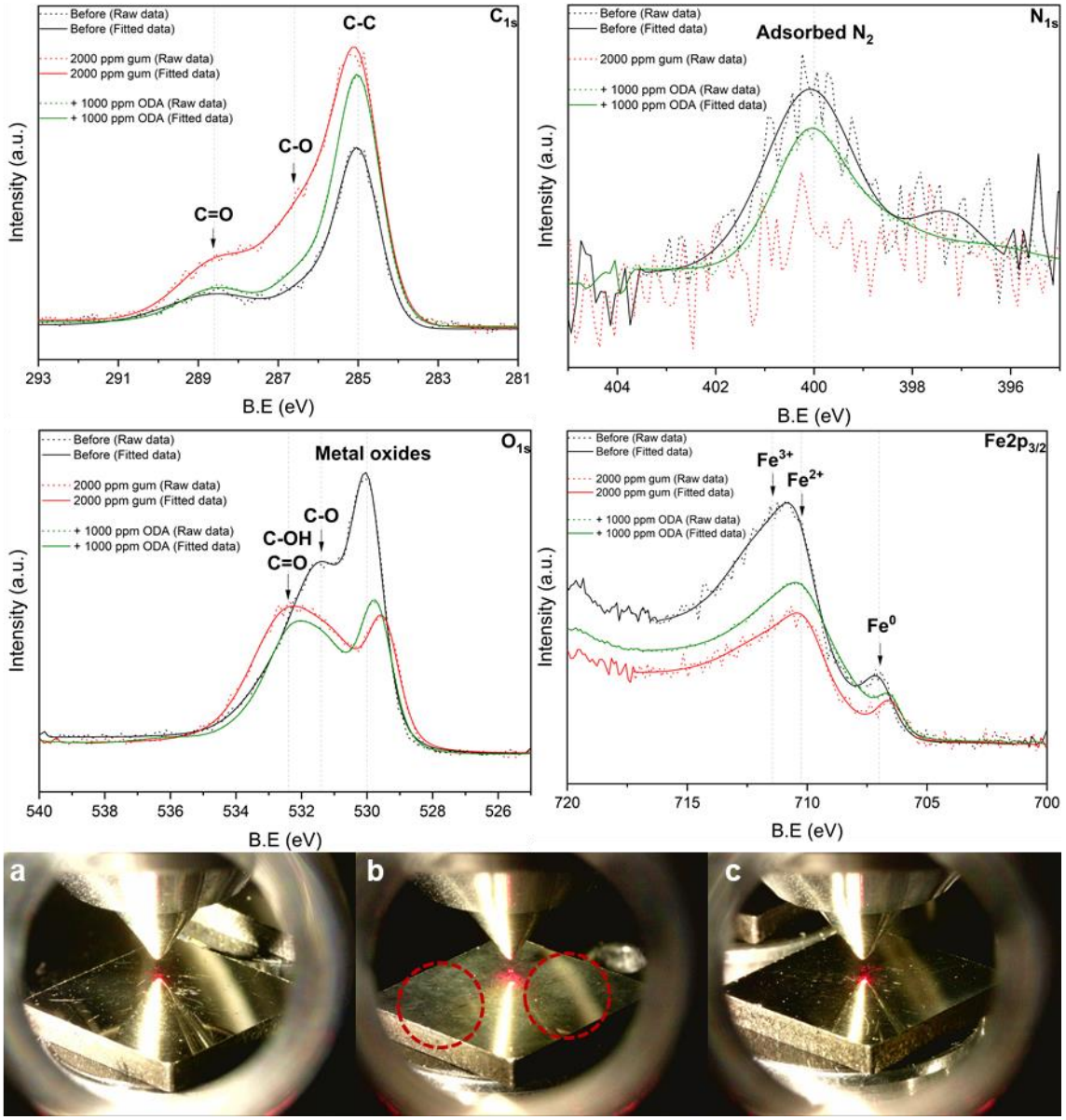

Figure 104 Overall attenuation profile of the C 1s, N 1s, O 1s, and Fe 2p spectra as a function of immersion (data retrieved from Figure 103). Legend is displayed in order of immersion. Microscope images represent **a)** blank substrate, **b)** substrate after immersion in 2000 ppm gum (circled in red), and **c)** substrate after immersion in 1000 ppm ODA, showing significantly cleaner surface.

6.3.2.2 XPS of gum in neat TRF experiment

Having established the ODA detergency effects, it was crucial to understand whether gum has been removed solely by ODA, or if the TRF solution has also contributed. Analysis from the survey spectra (Figure 105) showed very similar and comparable trends to the gum-immersion stage in the previous sample (6.3.2.1). Thus, this section will mainly focus on the TRF immersion stage. Data showed that carbon content was attenuated by 17% (compared to 23% with ODA). The residual carbon concentration was also higher than that of the blank substrate (44 vs 33 at% respectively). The bulk elements signals increased when some of the gum was removed. However, both chromium and iron levels were found to be lower than the values before treatments. The extent in which ODA or TRF has contributed to the exposure of bulk elements is a crude measure of detergency effectiveness. The percentage of change comparing the increase in iron contents, as a function of ODA vs. neat TRF, was calculated and found to be 42% and 34% respectively, suggesting higher effectiveness for ODA. Although the iron concentration has increased, oxygen levels (mainly arising from metal oxides) have slightly attenuated indicating residual gum on top of the oxides layer. All results taken together suggest that ODA was more effective than neat TRF in cleaning the surface. Very thin layers of gum was observed visually on the surface (Figure 107, c).

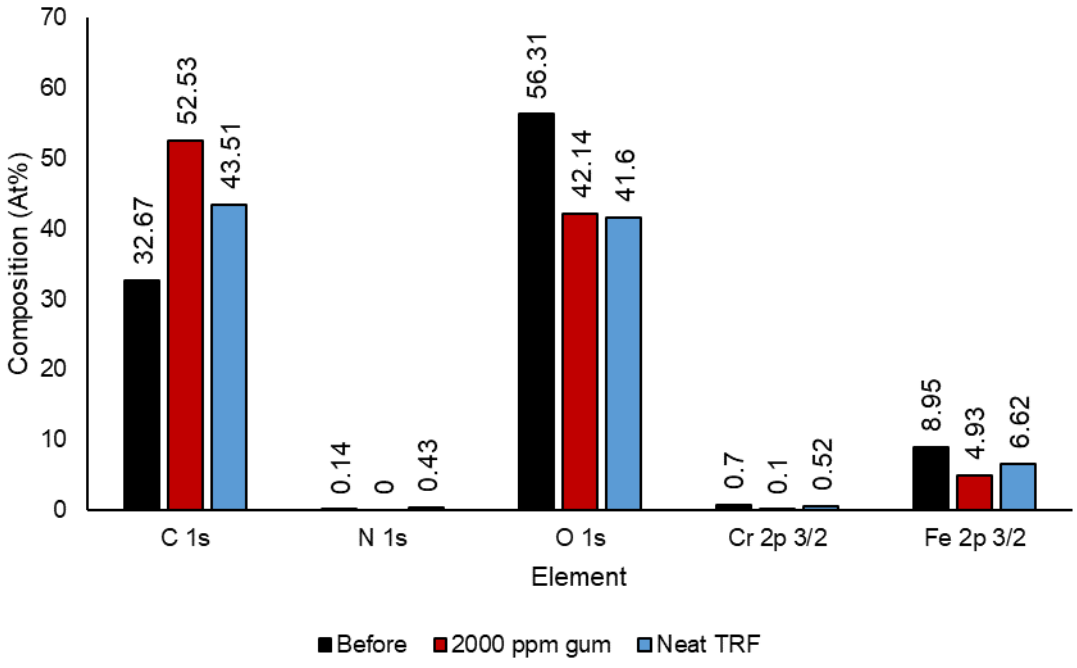

Figure 105 Composition of major surface elements from survey spectra of 'gum in neat TRF' experiment. Legend is displayed in order of immersion.

C 1s high-resolution spectra (Figure 106) showed noticeable attenuation in the C-O and C=O peaks by 75% and 38% respectively (Table 44). Since ODA interacts with gum molecules at the C=O sites, it was expected to find lower C=O $\%_{change}$ in the absence of ODA. Moreover, total carbon content (as peak areas) was quantified and found to be 19% higher in the case of TRF immersion, indicating weaker cleaning effectiveness compared to ODA.

Turning to a discussion of these results, several studies have discussed and established the positive effects of nitrogen-based detergents on SI engine deposits. (2, 6, 8, 61) As discussed previously, the mechanistic basis for deposit formation and cleaning mechanisms are yet to be fully understood. (5, 17) The work discussed in chapter 4.3 already addressed gum formation mechanisms in fuel systems. It appears that the carbonyl (C=O) groups within the gum (Figure 62) are of central importance to achieving detergency, by acting as a receptor to the solubilising detergent molecules. (18, 19) Findings from this work correlate with literature in this regard and verify the cleaning efficacy of ODA in the presence of gum. By comparing the C 1s overall profiles illustrated in Figure 104 and Figure 107, we can clearly see the effects of ODA in attenuating the oxygenated species levels, especially C=O. Overall gum contents $\%_{change}$ calculated from C 1s values in Table 43 and Table 44 were found to be -32% and -18% respectively, clearly underlying the efficacy of ODA vs neat TRF. In other words, the presence of ODA has helped in 'lifting' 44% more gum off the surface, yet with no concomitant build-up of carbon or nitrogen species.

Table 44 C 1s core level binding energy, corrected peak area, and concentration (at%) as a function of immersion. ▲ and ▼ indicate change in chemical species compared to previous stage.

Sample	Species	Position (eV)	Area	at%
SS coupon (Blank)	C-C/C-H	285.0	4173.62	69.81
	C-O	286.6	606.69	10.14
	C=O	288.6	1199.02	20.04
2000 ppm gum	C-C/C-H	285.0	▼4026.20	38.9
	C-O	286.2	▲3613.72	34.9
	C=O	288.4	▲2713.75	26.2
Neat TRF	C-C/C-H	285.0	▲5934.24	69.65
	C-O	286.6	▼907.38	10.65
	C=O	288.4	▼1679.00	19.71

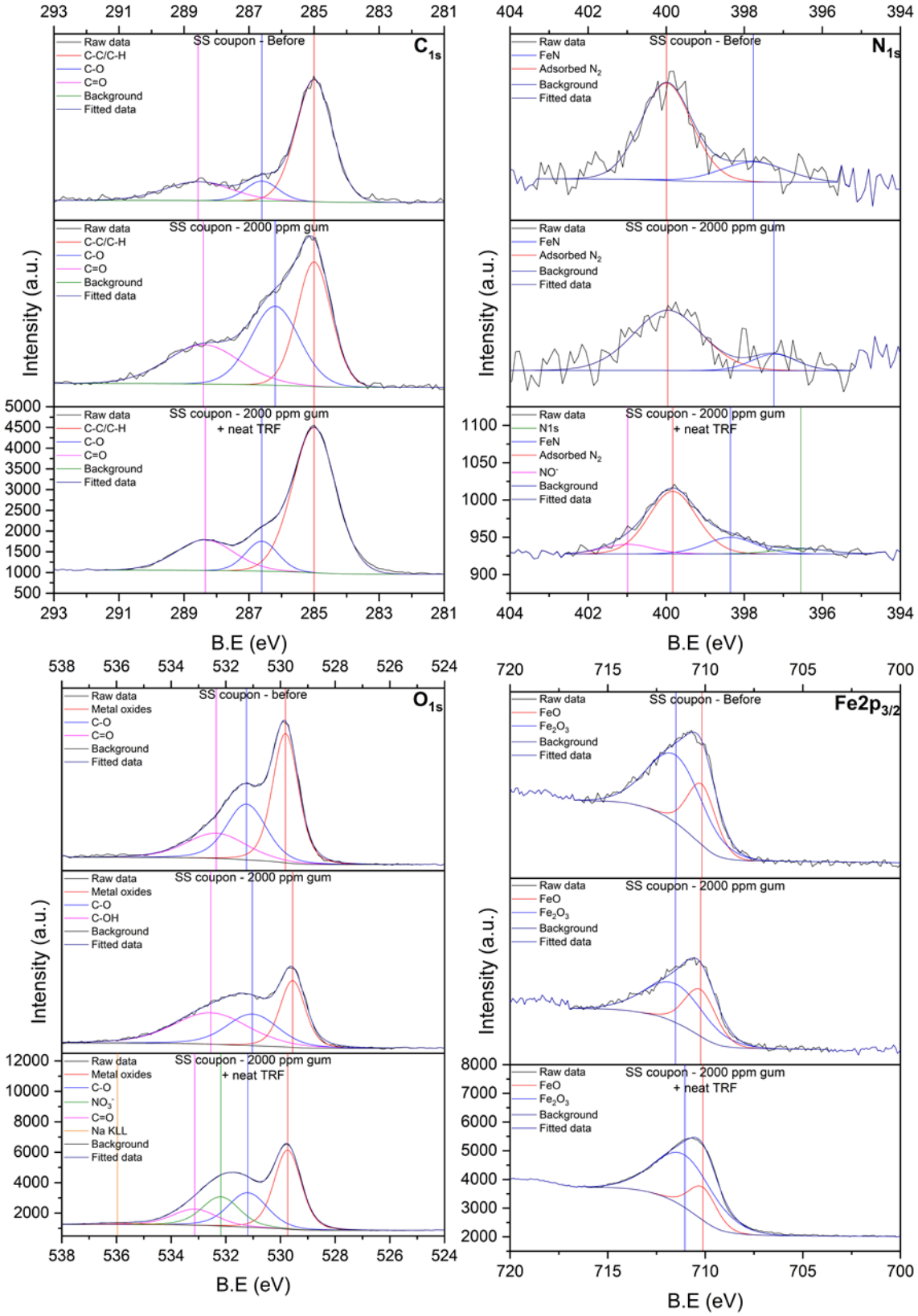

Figure 106 C 1s, N 1s, O 1s, and Fe 2p XPS high-resolution spectra of the 'gum in neat TRF' experiment, as a function of immersion. Each elemental spectra was scaled to the arbitrary intensity shown on their relevant figure.

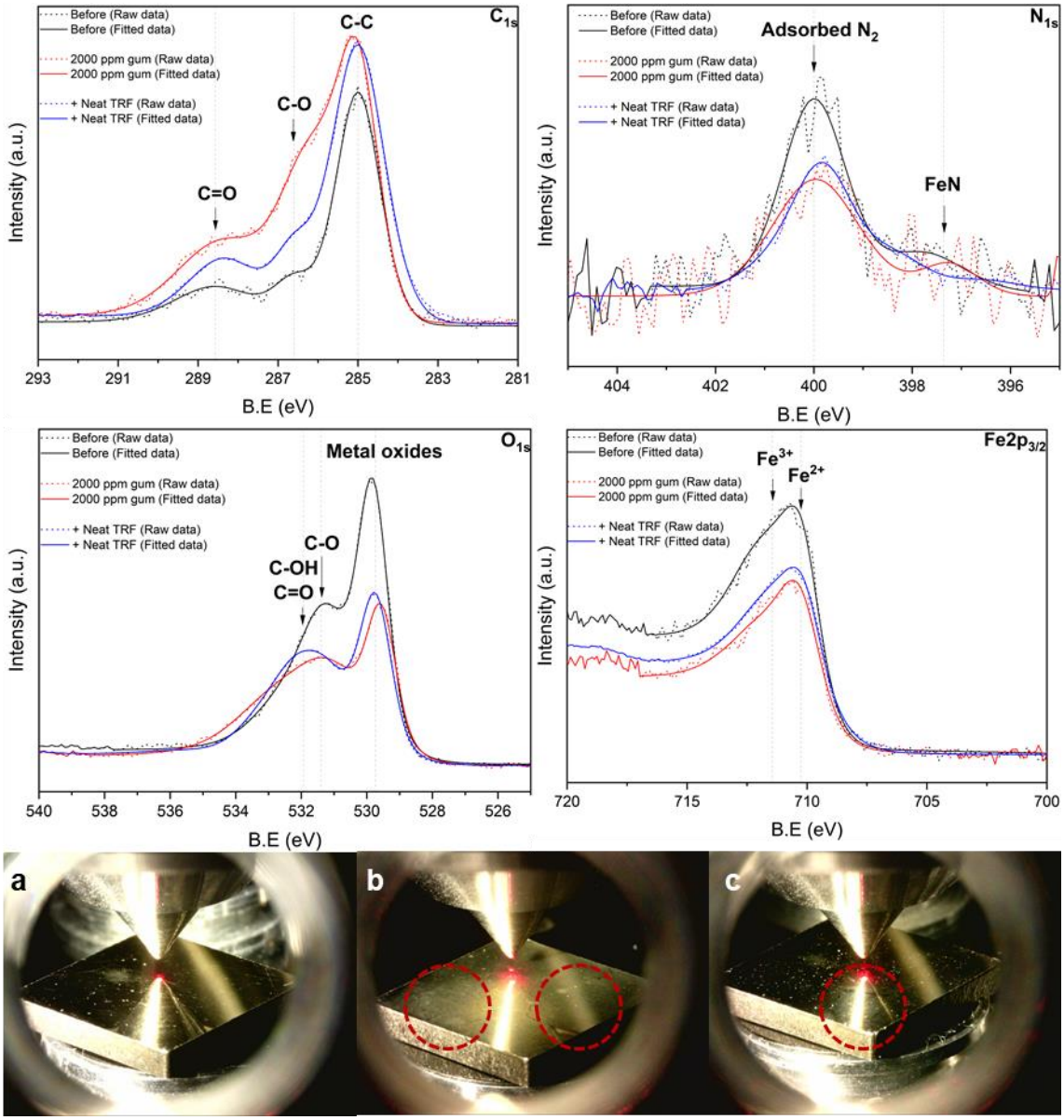

Figure 107 Overall attenuation profile of the C 1s, N 1s, O 1s, and Fe 2p spectra as a function of immersion (data retrieved from Figure 106). Legend is displayed in order of immersion. Microscope images represent **a)** blank substrate, **b)** substrate after immersion in 2000 ppm gum (circled in red), and **c)** substrate after immersion in neat TRF, showing residual gum on the surface.

6.3.3 Interactions study

In these experiments, six different TRF solutions were prepared by adding various ODA concentrations, ranging from 0 to 1500 ppm, to 1000 ppm of gum to understand the interactions between the two components within the formulated surrogate fuel system. Unlike the previous studies in 6.3.1 and 6.3.2, only one immersion stage was performed in this part; as both ODA and gum were added at the same time. XPS measurements of all 'before' spectra were performed on the EnviroESCA, whereas immersed coupons were measured on the UHV-XPS. Correction factors were applied as per the normalisation method explained in Appendix 3. XPS parameters for the survey and high-resolution scans were identical to the parameters listed in Table 39.

Interactions between ODA and gum were evaluated by calculating the change in elemental composition as a function of immersion (Figure 108). Overall change in carbon (C 1s) content exhibited the expected hump-effect pattern in such systems, where low dosage of detergent results in higher depositions. (22) Moreover, noticeable reduction from 12.9 to 2.1 at% was observed despite multiplying ODA concentration by approximately 30 folds (i.e. 50 – 1500 ppm). The apparent increase, however, from 0 – 50 ppm was believed to be due to unreacted ODA and gum species on the surface. It was also indicative that adsorption of gum species was obstructed by ODA molecules even at 1:4 and 1:2 ODA to gum ratios. Only at ratios of 1:1 and above, ODA molecules were capable of reducing the change in carbon content to values below that of the 100% gum sample. The reduction trend in composition change signifies the ability of ODA molecules to capture gum species in the bulk and consequently minimise their susceptibility towards adsorption. Moreover, the change of C 1s and O 1s signals on the surface mirrored each other as a function of ODA concentration, which in turn suggests strong association between ODA and gum species on the surface. Changes in Fe 2p content on the surface were also of significant importance to this argument. Data revealed that beyond 250 ppm of ODA, change in iron contents decreased incrementally to the point where a positive value was achieved, indicating a cleaner post-immersion substrate.

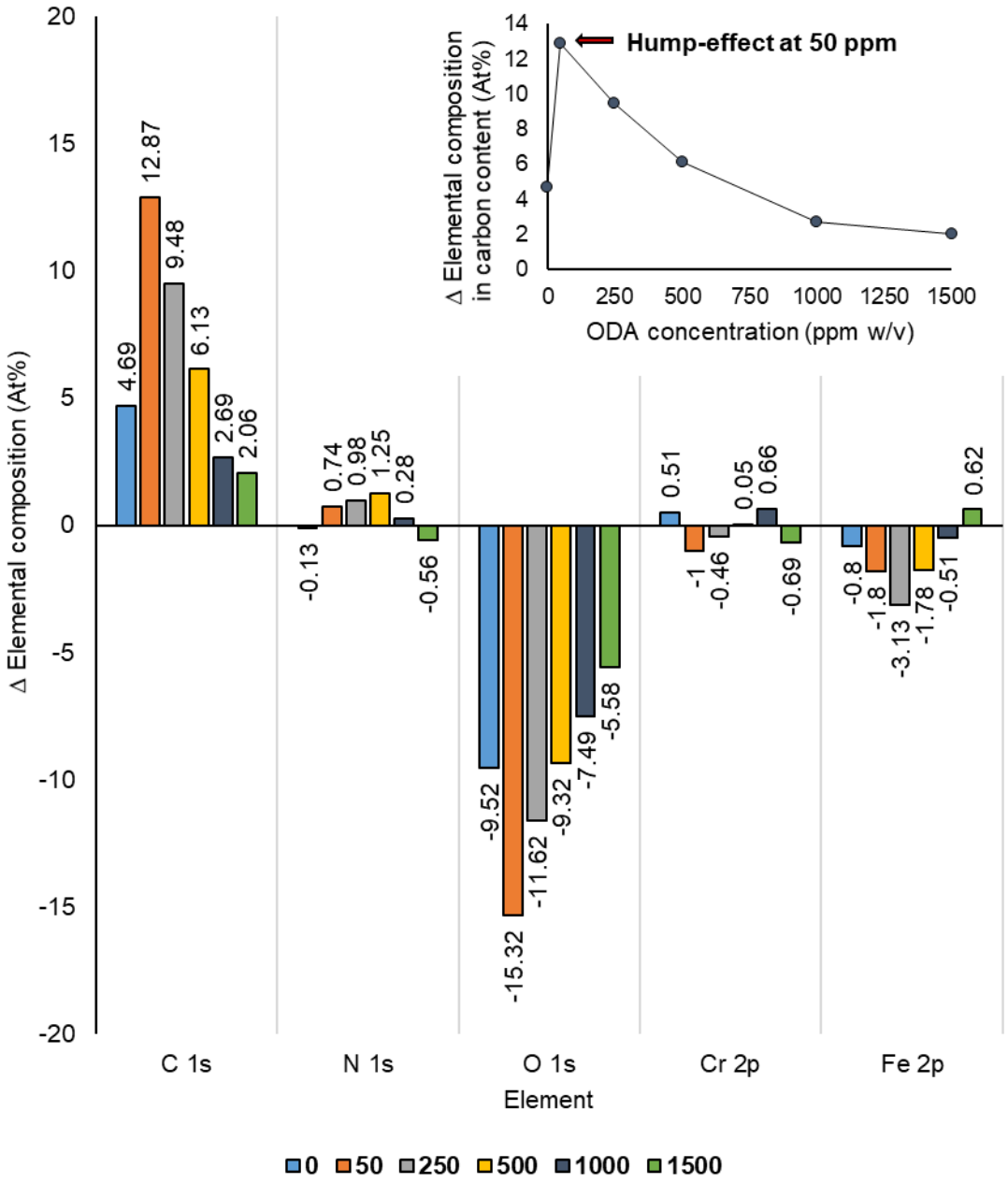

Figure 108 Change in composition of the major elements on the surface as a function of ODA concentration (0 – 1500 ppm w/v). Top right corner: Illustration of the hump-effect observed in carbon (C 1s) content on the surface.

However, it is important to mention that these hypotheses are not conclusive without fully understanding the behaviour of C 1s and Fe 2p individual species such as oxygenated environments (C-O and C=O) and iron oxides (Fe^{3+}). A deeper discussion of these issues will follow below in this section, linking to observations from high-resolution spectra. For the experiments described in this section, nitrogen content could not be quantified in three out of six blank coupons (Table 45), and thus any change in N 1s species was not attributed to ODA

adsorption unless other complementary data such as C:N ratio or aliphatic C-C increase were found to be indicative.

Table 45 Concentration of major surface elements in at% before (B) and after (A) immersion as a function of ODA concentration (0 – 1500 ppm w/v). Higher vs lower values are distinguished by ▲ and ▼ respectively.

Element	0	50	250	500	1000	1500
	Composition (at%)					
C 1s	**B:** ▼35.09 **A:** ▲39.78	▼31.31 ▲44.18	▼29.58 ▲39.06	▼34.26 ▲40.39	▼33.70 ▲36.39	▼35.43 ▲37.49
N 1s	▲1.05 ▼0.92	▼0.00* ▲0.74	▼0.00 ▲0.98	▼0.00 ▲1.25	▼0.60 ▲0.88	▲1.18 ▼0.62
O 1s	▲51.91 ▼42.39	▲54.83 ▼39.51	▲55.62 ▼44.00	▲51.08 ▼41.76	▲53.98 ▼46.49	▲48.56 ▼42.98
Cr 2p	▼0.00 ▲0.51	▲2.84 ▼1.84	▲1.01 ▼0.55	▼2.29 ▲2.34	▼0.00 ▲0.66	▲3.16 ▼2.47
Fe 2p	▲7.79 ▼6.99	▲7.91 ▼6.11	▲10.54 ▼7.41	▲8.29 ▼6.51	▲8.73 ▼8.22	▼7.20 ▲7.82

* Values shaded in red were not found in survey scans due to non-uniform distribution of surface elements.

In the high-resolution spectra, raw and envelope (fitted) data of pre- and post-immersion measurements were normalised to the same baseline and plotted against each other for comparison. Peak areas $\%_{change}$ was then calculated for all chemical species to quantify changes on the surface as a function of immersion. In all C 1s data, 'before' and 'after' spectra were deconvoluted into three main peaks namely aliphatic C-C at 285.0 eV, C-O at ~ 286.5 (± 0.1 eV), and C=O at ~ 288.6 (± 0.3 eV). The overall profile of carbon regions showed clear attenuation to the features arising from gum species (C-O and C=O), as a function of ODA concentration (Figure 109, left). The attenuation pattern was further complemented by the iron (Fe 2p) overall profile, which indicated restoration of iron content on the surface at higher ODA concentrations (Figure 109, right). Moreover, visual evidence of reduced gum adsorption was observed on substrates immersed in ODA-containing solutions, when compared to the substrate immersed in 1000 ppm gum only. The substrate immersed in 1500 ppm ODA is shown in Figure 110 as an example.

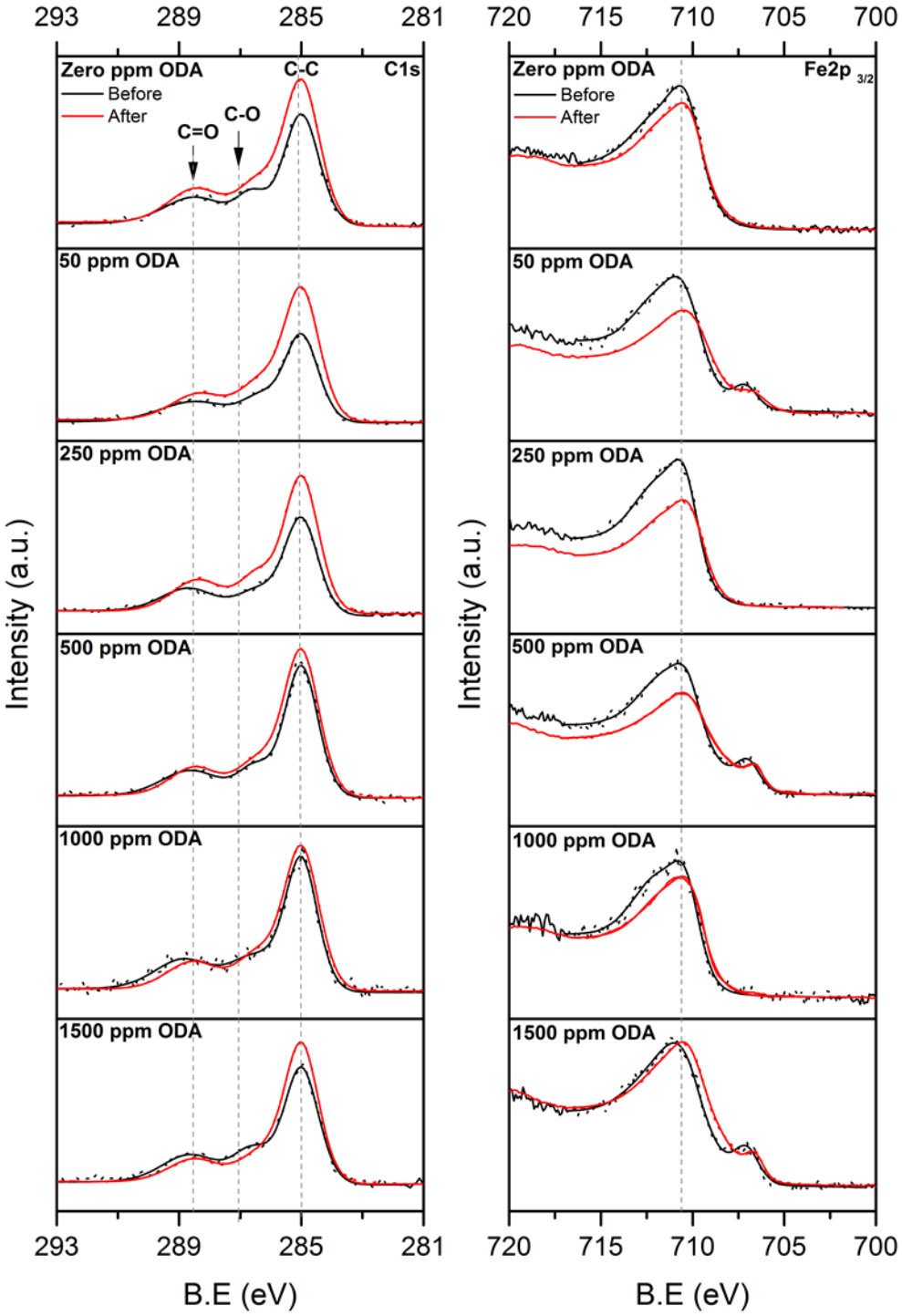

Figure 109 Left: Carbon C 1s raw and envelope data (dotted vs solid line) showing post-immersion (after) reduction of gum species (C-O and C=O), as a function of ODA concentration. Spectra scaled to arbitrary intensity of 4000 a.u. Right: Iron (Fe $2p_{3/2}$) data showing positive effects of ODA in restoring iron species on the surface to blank's levels (before). Spectra scaled to 4750 a.u.

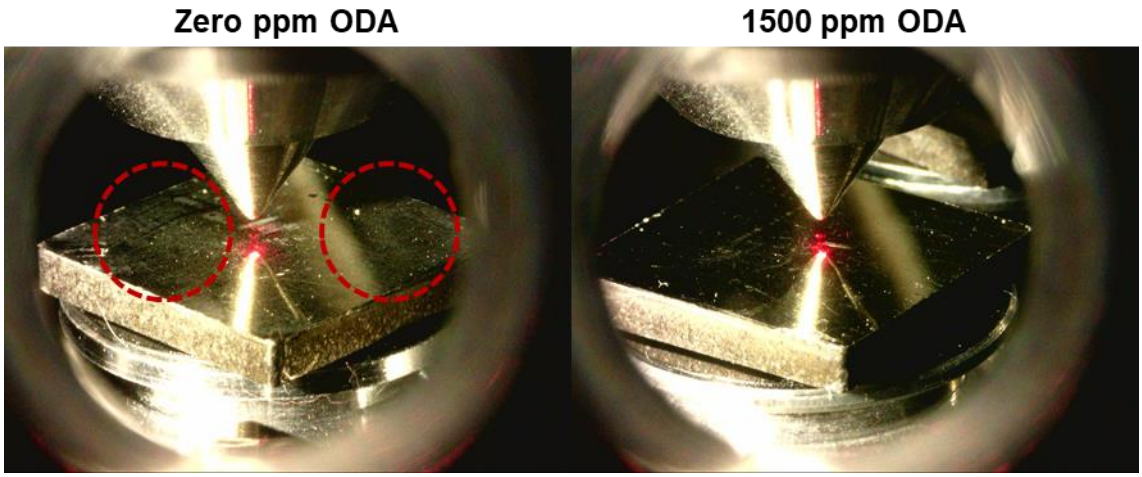

Figure 110 Digital microscope images showing the effect of 1500 ppm ODA in cleaning surface-adsorbed gum observed as a thin, hazy layer (circled in red).

The $\%_{change}$ in aliphatic C-C species exhibited typical hump-effect phenomena at 50 ppm followed by a steady state at higher ODA concentrations (500, 1000, and 1500 ppm). Beyond 50 ppm, summation of gum species (C-O and C=O) showed significant reduction on the surface as a function of ODA. Remarkably, this reduction was not associated with any build-up in aliphatic C-C species, indicating no ODA on the surface. In addition, more iron species from the substrate's bulk (Fe_2O_3) were exposed to the surface as a function of ODA concentration (Figure 111). Such observations correlate well with the trends observed in Figure 108 and strongly suggest that ODA molecules have hindered gum adsorption via 'capture and wash' mechanism while in solution, not by surface passivation. Data in Figure 111 were derived from Table A 7 (Appendices).

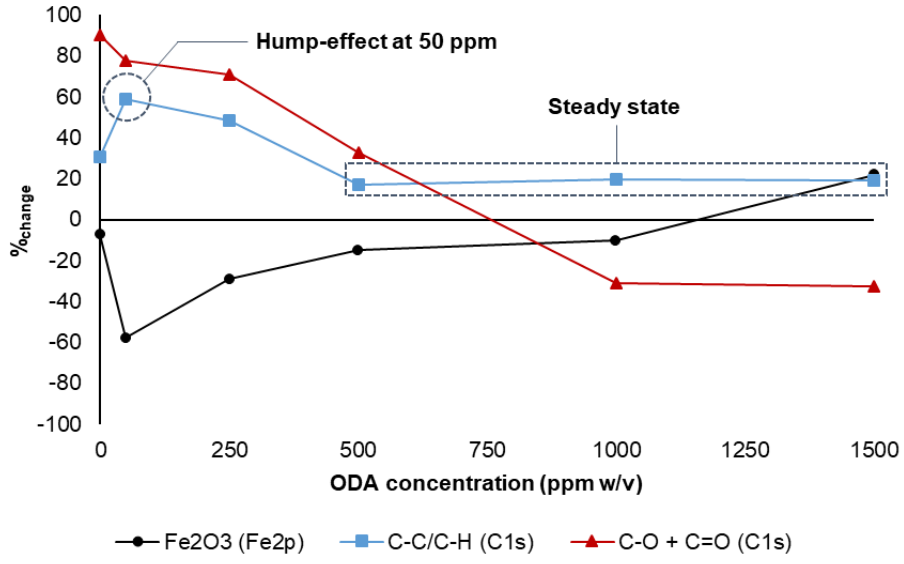

Figure 111 Percentage of change in iron oxide (Fe^{3+}), aliphatic C-C, and total gum (C-O and C=O) species as a function of ODA concentration.

The hump-effect observed at 50 ppm for aliphatic C-C species correlate well with the UV-Vis absorption spectra shown in Figure 73 (chapter 5.3.1). In both cases, it was believed that ODA molecules remained inactive at low concentrations, causing lower UV absorption in solution and higher adsorption on the surface. At sufficient concentration, however, strong association between gum and ODA was observed, as suggested by the SEM/EDX data in chapter 5.4.3. Although adsorption of long-chain alkylamines and saturated fatty acids on iron oxides have been well demonstrated in literature (91, 92, 219), the presence of oxygenated molecules has been notorious for adding to the complexity. (220) In a comparable study using iso-octane as a fuel model, the adsorption isotherm profile of a Mannich base surfactant with a C_{12} tail on hematite (α-Fe_2O_3) was examined with and without the presence of ethanol (C_2H_5OH). Results revealed logarithmic rise of adsorption isotherm as a function of surfactant's concentration. However, the adsorption rate has significantly changed following ethanol addition. (92)

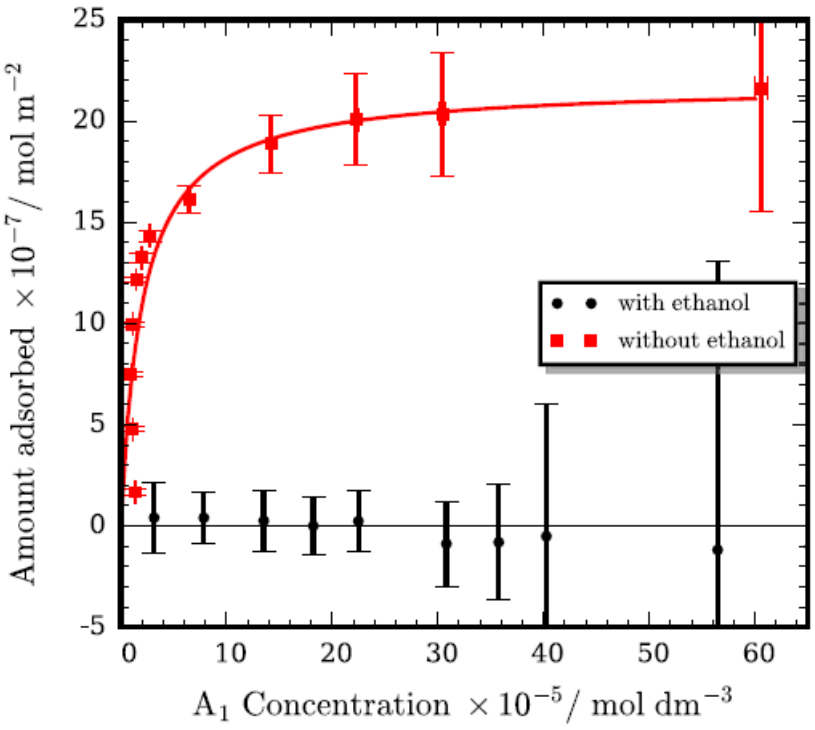

Figure 112 Adsorption isotherm profile of the Mannich base surfactant (denoted as A_1) with and without the presence of ethanol. (92)

The aforementioned study agree with the findings that ODA would prefer to migrate from the surface in the presence of gum. Once in solution and at sufficient concentration, polar head groups ($-NH_2$) start to interact with the gum molecules at the carbonyl site (C=O) in order to capture the gum via reverse micellisation.

6.4 Conclusion

In this chapter, we have employed a systematic approach to investigate the adsorption, detergency, and interaction behaviours of ODA as a model detergent. The adsorption and detergency studies summarised in Figure 84 were able to replicate the double-mode of action reported for gasoline detergents (i.e. keep clean and clean-up mechanisms), but revealed finer mechanistic details not captured by these simple models. XPS analysis from the adsorption study revealed a high tendency for ODA to adsorb onto stainless steel substrates. The newly formed C-N peak at B.E 285.85 (±0.25) eV along with the B.E shift observed in the O 1s spectra for metal oxides, C-O, and C=O indicated adsorption of ODA ($-NH_2$) to metal oxides via 'back bonding' as previously suggested (90, 113, 130, 195). The overall increase in carbon contents for the gum and neat TRF immersion experiments was found to be 22% and 16%, respectively. Analysis from high-resolution spectra confirmed that the 22% was mainly due to residual gum layer on the surface, eradicating the 'stick and eliminate' hypothesis.

Results from the detergency study, on the other hand, confirmed high adsorption affinity of gum for stainless steel surfaces. Clear and distinct detergency effects of ODA were illustrated in Figure 104 when compared to Figure 107 (neat TRF). Overall gum contents (C 1s, as $\%_{change}$) were attenuated following immersion in ODA and neat TRF, by 32% and 18% respectively. It is hypothesised that polar head groups within the model detergent ($-NH_2$) lift off the adsorbed gum molecules by binding to the carbonyl (C=O) sites. Although no evidence of hydrogen bonding ($-NH_2\ \delta+/C{=}O\ \delta-$) was found in this study, it was still believed to be the case for ODA detergency mechanism. (18, 19)

The interactions studies revealed an interesting pattern for ODA and gum molecules as a function of concentration. At a low concentration of 50 ppm, a hump-effect was clearly observed in both the survey and high-resolution spectra of C 1s intensities from the adsorbed layers, indicating deposition of ODA and gum molecules on the surface. It was remarkable to see the steady state of aliphatic C-C species (Figure 111) in conjunction with the reduction in gum species (C-O and C=O). Such observations strongly confirm the effects of ODA in hindering gum adsorption while in the liquid phase via 'capture and wash' mechanism. Once ODA was attached to the gum, it was believed that ODA formed reverse micelles to trap gum molecules and remain in solution. Further work is needed to thoroughly investigate the liquid-liquid interactions to complement the postulated hydrogen bonding and micellisation hypotheses.

Brief concluding remarks along with schematic illustrations of the aforementioned mechanisms are summarised in Table 46 and Figure 113.

Table 46 Concluding comments on all studies conducted to examine ODA and gum behaviour in surrogate fuel systems as depicted in Figure 113.

Figure	Experiment title (Area of study)	Remarks
a	ODA immersion	ODA adsorbed onto the stainless steel substrate via ‘back bonding’ to the metal oxide layer (Figure 97). (90, 113, 130, 195)
b	ODA in gum (Adsorption)	ODA migrated from the surface to capture the gum molecules dissolved in TRF solution (Figure 97). (92)
c	ODA in neat TRF (Adsorption)	ODA dissolved in TRF solution, yet residual ODA also found on the surface (Figure 100). (86, 90, 91)
d	Gum immersion	Significant amount of gum adsorbed onto the substrate. (Figure 103)
e	Gum in ODA (Detergency)	ODA molecules interacted with gum on the surface via ‘lifting mechanism’, resulting in a cleaner surface (Figure 104). (18, 19)
f	Gum in neat TRF (Detergency)	Gum dissolved in TRF solution in a lesser extent, compared to ODA ‘lifting mechanism’. (Figure 107)
g	No ODA (Interactions)	Significant amount of gum adsorbed onto the substrate (Figure 109).
h	Low ODA (Interactions)	Unreacted ODA species were found on the surface along with gum molecules, causing the observed hump-effect (Figure 111). (22)
i	Medium ODA (Interactions)	ODA molecules start to interact with gum species potentially via hydrogen bonding (Figure 111). (18, 19)
j	High ODA (Interactions)	Most gum content was ‘captured’ once sufficient ODA concentration was present, resulting in a cleaner surface (Figure 109 and Figure 111). (18, 19, 92)

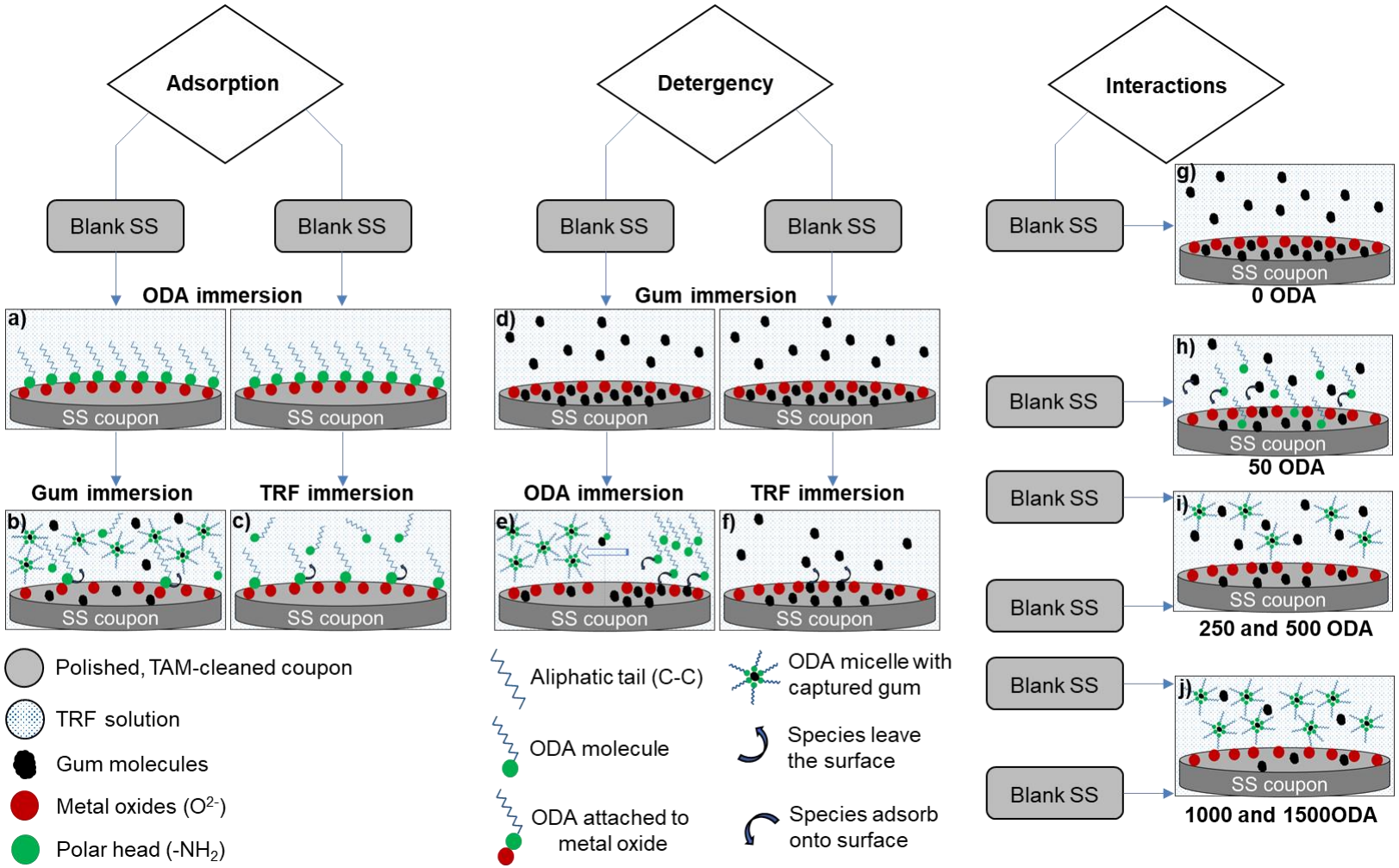

Figure 113 Schematic flow chart depicting ODA and gum behaviour under each stage of the investigated areas of study. Description of figures a – j can be found in Table 46. Substrates g – j were immersed in solutions containing 1000 ppm gum.

Chapter 7 Conclusion and future work

Some conclusions and graphical summaries of the research outcomes were already presented at the end of Chapter 4, Chapter 5, and Chapter 6. This chapter brings these previous conclusions once more together and provides an overall summary of the research outcomes.

Broadly, the research reported in this thesis can be divided into work on **(i)** the selection and synthesis of the TRF/gum model system, **(ii)** its interaction with ODA, and **(iii)** the interaction of the ODA/gum/TRF systems with stainless steel surfaces.

7.1 Oxidative formation of gum in model surrogate fuel

Chapter 4 described a reproducible method for the formulation of a gasoline surrogate with significant gum content. Olefin and aromatic contents of the formulated TRF were optimised in accordance with the British and European standards of unleaded petrol (EN-228). ATR-FTIR spectroscopy was employed to validate the TRF formulation and aerobic oxidation methods. The use of a radical initiator, tert-butylhydroperoxide (tBHP), to oxidise the mono- and diolefin components in the surrogate fuel showed positive results. The presence of oxidation products with carbonyl (C=O) and hydroxyl (OH) functional groups in the oxidised TRF blends was confirmed by FTIR. GC-MS and TGA were employed to further characterise the synthesised model gum. The molecular weight and decomposition profiles correlated well with gum formed in practical gasoline fuels. This synthesis method therefore provides a reproducible surrogate fuel for gum deposition studies, extending traditional applications of formulated TRFs in engine combustion modelling and simulation studies. (39, 42) The novelty of this method is the ability to produce synthetic gum from low boiling point surrogate fuels (i.e. < 110°C). In previous adsorption studies, gum was produced from the higher fraction of the fuel (boiling point 100 – 220°C), where the lower fraction is typically stripped via evaporation in pre-treatment steps. (36)

7.2 Addition of ODA into oxidised surrogate fuel

In chapter 5, it was shown that the interaction of a model amine detergent (ODA) with the oxidised components in TRF surrogate fuel depends on its concentration. UV-Vis spectroscopy revealed characteristic interactions between ODA and the

carbonyl components of gum in the surrogate fuel. DLS showed that ODA forms colloidal structures in gum-free fuels at concentrations above the CMC point, at approximately 100 ppm, which was in agreement with theoretical values. (186) Contact angle measurements and XPS indicated that ODA adsorbs strongly on steel surfaces in the absence of gum. Combined SEM, EDX, and XPS studies of mirror-polished 316 stainless steel substrates exposed to mixtures of ODA and TRF/gum systems revealed that the morphology and composition of the carbonaceous deposits depend strongly on the ODA concentration. Without ODA, there is a strong gum adsorption leading to deposits in irregularly-shaped, thick patches. The combined SEM/EDX/XPS data showed clearly that addition, or increasing concentrations, of ODA to 500 and 1000 ppm leads to circular deposits in the form of distinct multilayer rings on the substrate surface, while keeping much of the surface clear from multilayer deposits. Gum and ODA are strongly associated with each other in these deposits, likely reflecting the affinity already observed in solutions. These phenomena were already partially apparent, but not fully developed, at ODA concentrations as low as 50 ppm ODA. EDX and XPS indicate that the affinity between gum and ODA is strong to the extent that direct ODA adsorption on the steel substrate only begins to compete when ODA is present in excess (likely when the number of binding sites available in the gum is exceeded), as observed for systems with 2000 ppm ODA. These data indicated for the first time that the structure evolution at the ODA/gum/TRF interface was more complex than the ‘capture and wash’ or ‘stick and eliminate’ models employed in previous research. (5, 21, 27)

7.3 Systematic studies of interfacial behaviour by XPS

XPS was extensively employed as a main surface sensitive technique in order to investigate the solid-liquid interactions at the model system interfaces (i.e. SS – TRF/gum/ODA). The experimental design summarised in Figure 84 allowed for a structured, systematic approach to challenge the ‘stick and eliminate’ and ‘capture and wash’ hypotheses (Figure 2), as a function of ODA concentration, from three main angles: adsorption, detergency, and liquid-liquid interactions.

Adsorption studies have tested the ‘stick and eliminate’ hypothesis, where a TAM-cleaned, mirror-polished SS coupon was immersed in a TRF solution containing high concentration of ODA (2000 ppm w/v) to ‘stick’ thin ODA films on the surface and subsequently test their ‘elimination’ ability by immersion in a TRF solution containing 1000 ppm of gum (w/v). Analysis of XPS high-resolution spectra revealed that ODA molecules adsorbed onto the surface via back bonding to the

metal oxide layer (Fe_2O_3). Once oxygenated species (gum) was present in the system, aliphatic C-C levels (C 1s) attenuated to approximately original levels and C-N species from adsorbed ODA have almost disappeared from the surface. These observations have confirmed that ODA molecules were no longer adsorbed onto the surface. C-O and C=O compositions have suggested minimal gum deposition. However, by comparing the C 1s levels of gum introduced following ODA adsorption against levels of gum adsorbed directly onto the surface, the detergency effect of ODA on minimising gum adsorption was evident. However, no evidence of inhibition via passivation (i.e. ‘stick and eliminate’) was found. In other words, interactions between gum and ODA in solution appear to dominate over the additional surface effects

Under the detergency studies, the mechanism of ‘cleaning up’ gum layers adsorbed on SS substrates from TRF solutions, with and without ODA, was explored. Two prepared SS substrates were immersed in TRF solutions containing 2000 ppm of gum (w/v), and then immersion in ODA/TRF solution (1000 ppm w/v) was compared to immersion in neat TRF. XPS data revealed high affinity for gum to adsorb on SS substrates. Following the immersion in the ODA/TRF solution, carbon content had attenuated by ~ 13.1 at%, indicating ODA detergency. Chemical speciation showed significant reduction in C-O and C=O content (73% and 43%, respectively). Most importantly, no evidence of ODA adsorption was found. On the other hand, the neat TRF solution showed much lesser efficacy in removing adsorbed gum layers form the surface.

In the interactions study, various concentrations of ODA were dissolved in TRF solutions containing 1000 ppm of gum to explore ODA effects over gum adsorption. Analysis revealed clear trends of reduction in gum species with ODA concentration. A distinctive hump-effect in aliphatic C-C content was evident at low concentrations (50 ppm). Remarkably, it was followed by a steady state accompanied by an attenuation in gum species and an increase in iron contents on the surface, which strongly contradicts the ‘stick and eliminate’ hypothesis.

7.4 Concluding remarks and direction for future research

The results presented in this thesis have provided a new insight into the molecular basis of aliphatic amine detergents in preventing gum deposition on steel surfaces. They challenge the dichotomic 'inhibition via passivation' hypothesis for gasoline detergents, suggesting that surfactant behaviour is a lot more complex than just colloid vs interfacial passivation film formation. Amine surface passivation did not seem to occur in the presence of oxygenated model gum species. Solubilisation of gum as a colloid appears to take place in solution, in part shifting the adsorption equilibrium towards retaining gum in the liquid state, but not preventing adsorption altogether. Rather, colloid formation appears to result in the minimisation of the substrate surface areas affected by gum deposition. The mechanistic picture is summarised in Figure 114.

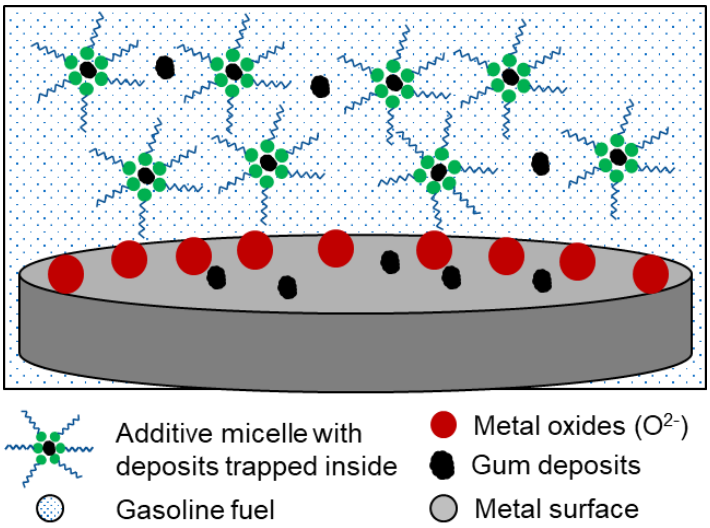

Figure 114 Schematic representation of the solubilisation hypothesis proposed for the detergency mechanism of DCAs in gasoline fuels.

Based on these research findings, deeper and more systematic research into the liquid-liquid interactions is strongly recommended to better understand the complex detergency mechanism of DCAs in gasoline fuels. More advanced characterisation techniques, e.g. *in situ* X-ray absorption spectroscopy of liquids and interfaces may be employed to investigate such systems in greater detail. (221, 222) Molecular dynamic simulations could be used to generate a more dynamic molecular-level view of the underpinning physical processes, and to integrate with findings from the experimental solid-liquid and liquid-liquid interface studies. Validation studies using real-world components (i.e. gasoline fuel and commercial detergents) are of great importance to verify the findings from the proposed fundamental studies. Using this methodology, we can now realistically hope to achieve a molecular-level understanding of DCA action in gasoline fuels.

Appendices

List of Figures

List of tables

List of appendices

Chapter 3 Experimental materials and methods

Appendix 1 TRF blend composition calculation at RON = 95 and P = 0.5 using Maple 18. Where X, X_{io}, and X_{nh} are the volume compositions of toluene, iso-octane, and n-heptane respectively. chi = X

$> 0 = 100\,P + a1 \cdot \mathrm{chi} \cdot P + a2 \cdot \mathrm{chi} + a3 \cdot \mathrm{chi}^2 - R$

$0 = -22.651\,\chi^2 + 86.815\,\chi - 45.0$

$\xrightarrow{\text{solve}}$

$\{\chi = 3.214734679\}, \{\chi = 0.6179879379\}$

$P := 0.5$

0.5

$a1 := -111.95\,\#atolp$

-111.95

$a2 := 142.79\,\#atol$

142.79

$a3 := -22.651\,\#atol2$

-22.651

$R := 95$

95

$P = \dfrac{Xio}{(Xio + Xnh)}$

$0.5 = 0.5000000000$

$Xio := 100 \cdot P - (100 \cdot \mathrm{X} \cdot P)$

19.10000

$X := .6180$

0.6180

$Xnh := 100 - Xio - (100 \cdot \mathrm{X})$

19.10000

$$S = a4 \cdot X + a5 \cdot X^2 + \frac{a6 \cdot X \cdot \left(R - (a2 \cdot X) - \left(a3 \cdot X^2\right)\right)}{100 + \left(a1 \cdot X^2\right)}$$

$S = 9.037424066$

$a4 := 14.79 \#astol$

14.79

$a5 := -3.444 \#astol2$

-3.444

$a6 := 7.29 \#astolp$

7.29

$Vol = (100 \cdot X) + Xio + Xnh$

$Vol = 100.0000000$

Appendix 2 Maple calculation of RON value at any TRF blend composition. Sensitivity equation can also be applied for validation. Example shown is for 60%, 20%, 20% v/v of toluene, n-heptane, and iso-octane respectively.

$> R := 100 \cdot P + a1 \cdot X \cdot P + a2 \cdot X + a3 \cdot X^2$

solve for R →

93.93464000

$a1 := -111.95 \#atolp$

-111.95

$a2 := 142.79 \#atol$

142.79

$a3 := -22.651 \#atol2$

-22.651

$X := 0.60 \#xtol$

0.60

$Xnh := 0.2$

0.2

$Xio := 0.2$

0.2

$$P := \frac{Xio}{(Xio + Xnh)}$$

0.5000000000

$Vol = 100 \cdot (X + Xnh + Xio)$

$Vol = 100.00$

$$S = a4 \cdot X + a5 \cdot X^2 + \frac{a6 \cdot X \cdot \left(R - (a2 \cdot X) - \left(a3 \cdot X^2\right)\right)}{100 + \left(a1 \cdot X^2\right)}$$

$S = 8.836867126$

$a4 := 14.79 \#astol$

14.79

$a5 := -3.444 \#astol2$

-3.444

$a6 := 7.29 \#astolp$

7.29

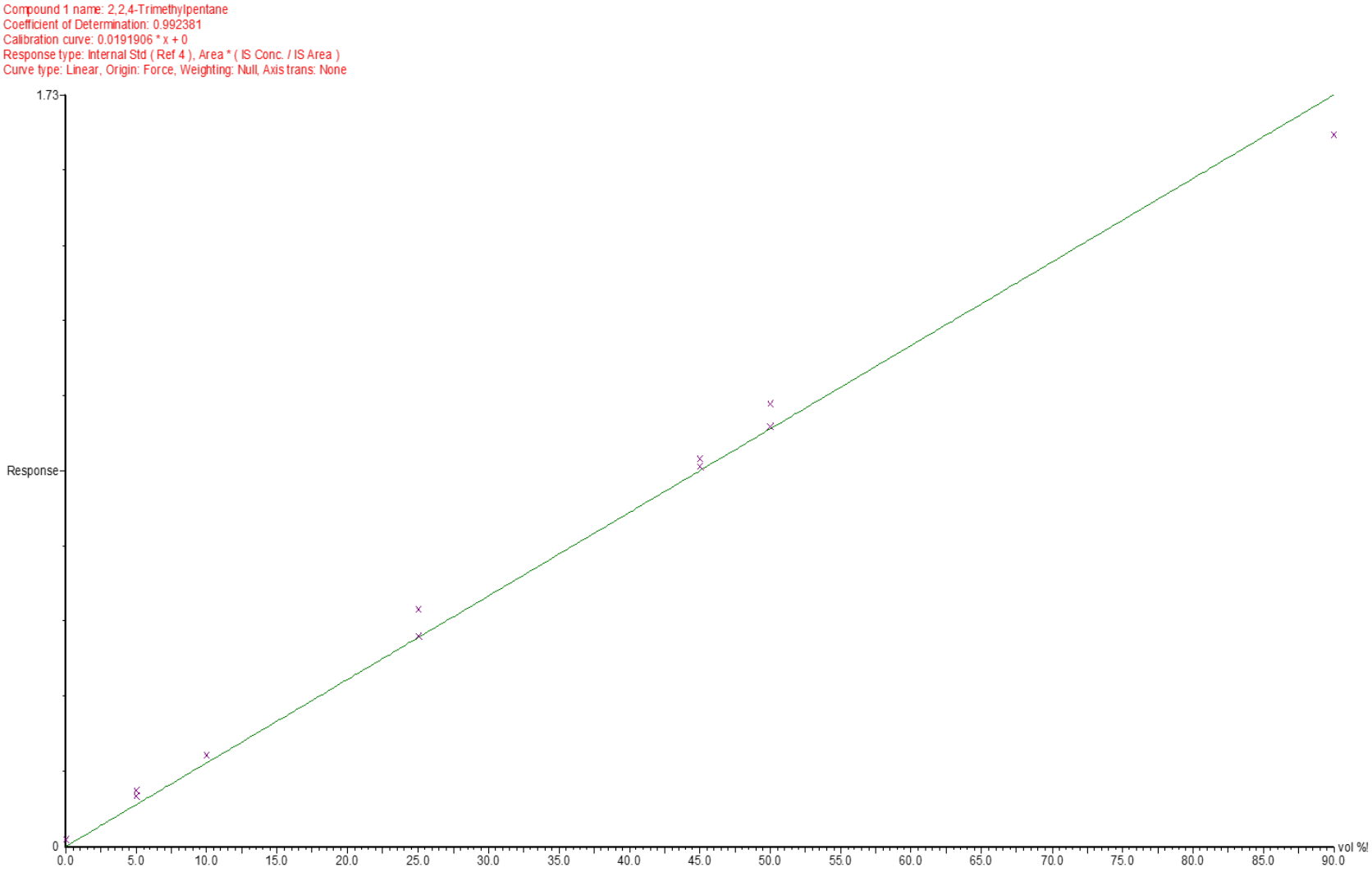

Figure A 1 GC-MS calibration curve of iso-octane (2,2,4-Trimethylpentane) concentration in the calibration standards.

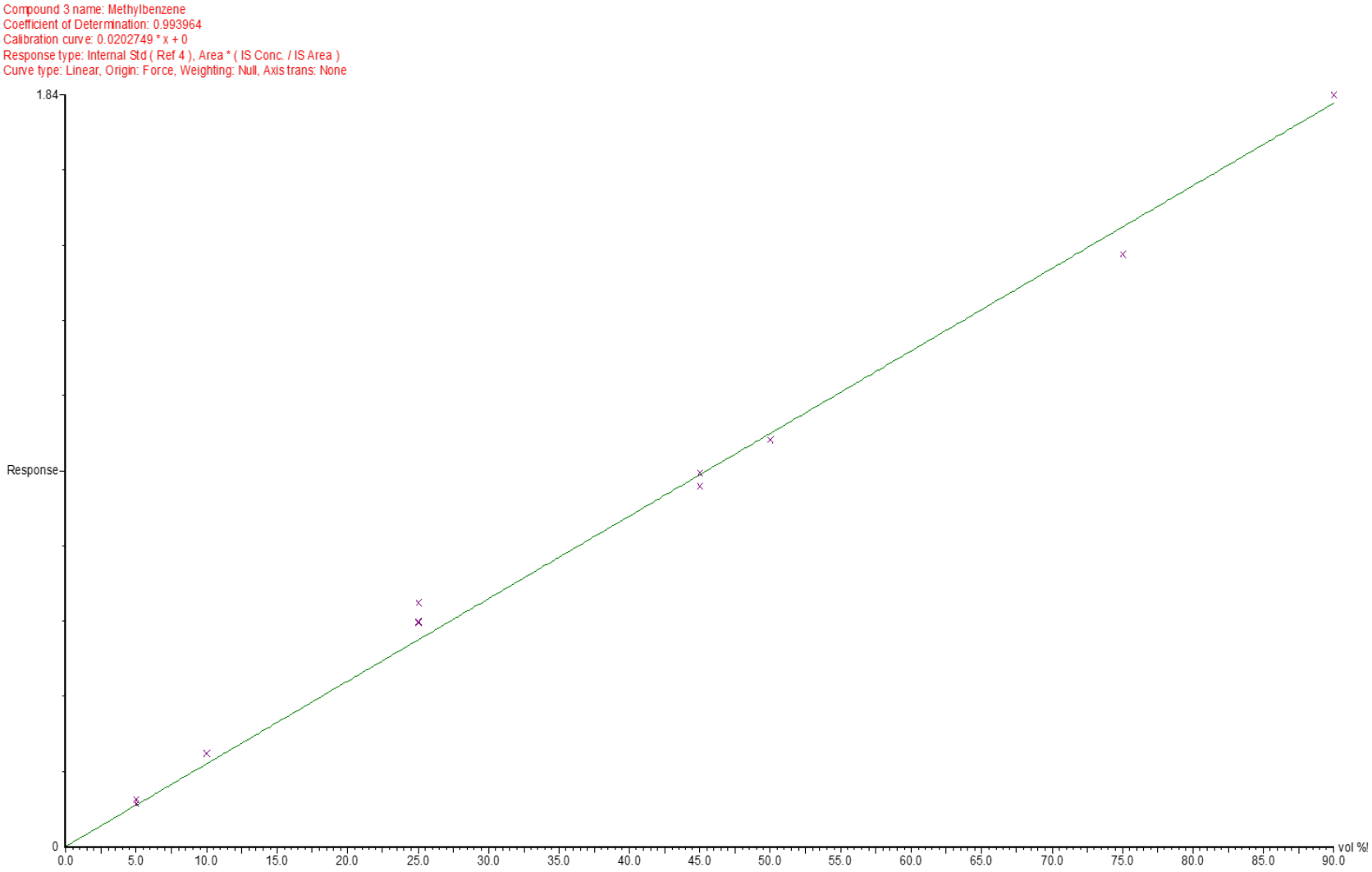

Figure A 2 GC-MS calibration curve of toluene (methylbenzene) concentration in the calibration standards.

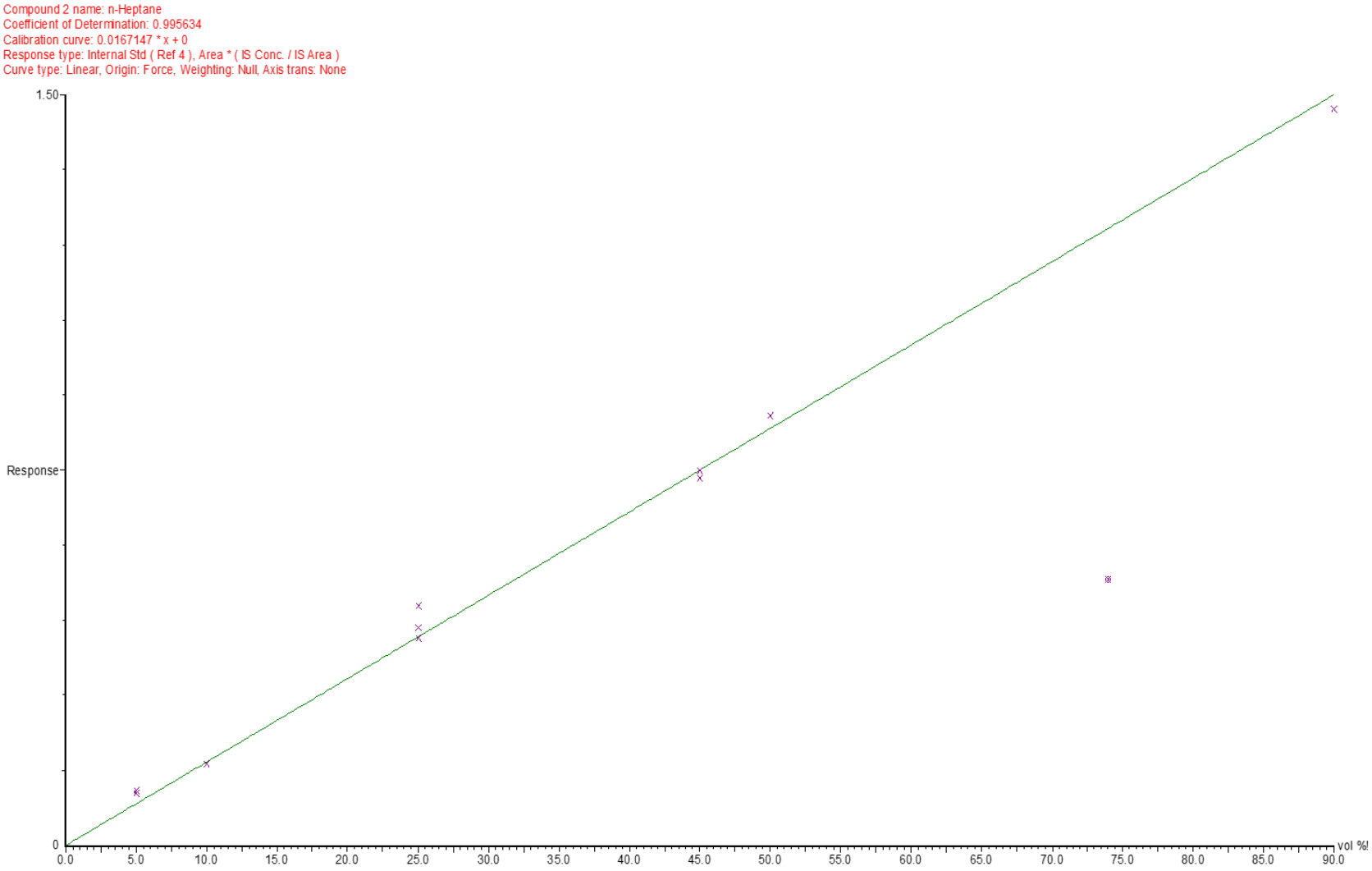

Figure A 3 GC-MS calibration curve of n-heptane concentration in the calibration standards.

Table A 1 Composition of surface elements in atomic percentage (at%) calculated from survey scans (Figure A 4 and Figure A 5). Averages shaded in green fall within an error margin of ± 1 σ (St. Dev.) from total average (blue).

Coupon	C 1s	N 1s	O 1s	F1s	Ca 2p	Cr 2p $_{3/2}$	Fe 2p$_{3/2}$
Blank 1 - Site 1	35.09	1.05	51.91	2.93	1.23	0.00	7.79
Blank 1 - Site 2	30.23	0.84	55.59	2.67	1.08	0.98	8.61
Avg. Blank 1	**32.66**	**0.95**	**53.75**	**2.80**	**1.16**	**0.49**	**8.20**
Blank 2 - Site 1	31.31	0.00	54.83	2.59	0.52	2.84	7.91
Blank 2 - Site 2	38.21	0.00	47.46	3.90	0.00	2.78	7.65
Avg. Blank 2	**34.76**	**0.00**	**51.15**	**3.25**	**0.26**	**2.81**	**7.78**
Blank 3 - Site 1	29.58	0.00	55.62	3.26	0.00	1.01	10.54
Blank 3 - Site 2	28.64	0.00	56.92	3.27	0.00	0.83	10.34
Avg. Blank 3	**29.11**	**0.00**	**56.27**	**3.27**	**0.00**	**0.92**	**10.44**
Blank 4 - Site 1	34.26	0.00	51.08	3.05	1.04	2.29	8.29
Blank 4 - Site 2	37.05	0.00	49.06	3.17	0.65	2.74	7.32
Avg. Blank 4	**35.66**	**0.00**	**50.07**	**3.11**	**0.85**	**2.52**	**7.81**
Blank 5 - Site 1	33.17	1.33	52.69	3.42	0.67	0.00	8.72
Blank 5 - Site 2	33.70	0.60	53.98	2.80	0.18	0.00	8.73
Avg. Blank 5	**33.44**	**0.97**	**53.34**	**3.11**	**0.43**	**0.00**	**8.73**
Blank 6 - Site 1	35.43	1.18	48.56	3.81	0.67	3.16	7.20
Blank 6 - Site 2	35.58	1.09	49.05	3.13	0.98	2.76	7.40
Avg. Blank 6	**35.51**	**1.14**	**48.81**	**3.47**	**0.83**	**2.96**	**7.30**
Average	**33.52**	**0.51**	**52.23**	**3.17**	**0.59**	**1.62**	**8.38**
St. Dev.	**2.24**	**0.51**	**2.50**	**0.20**	**0.39**	**1.18**	**1.02**

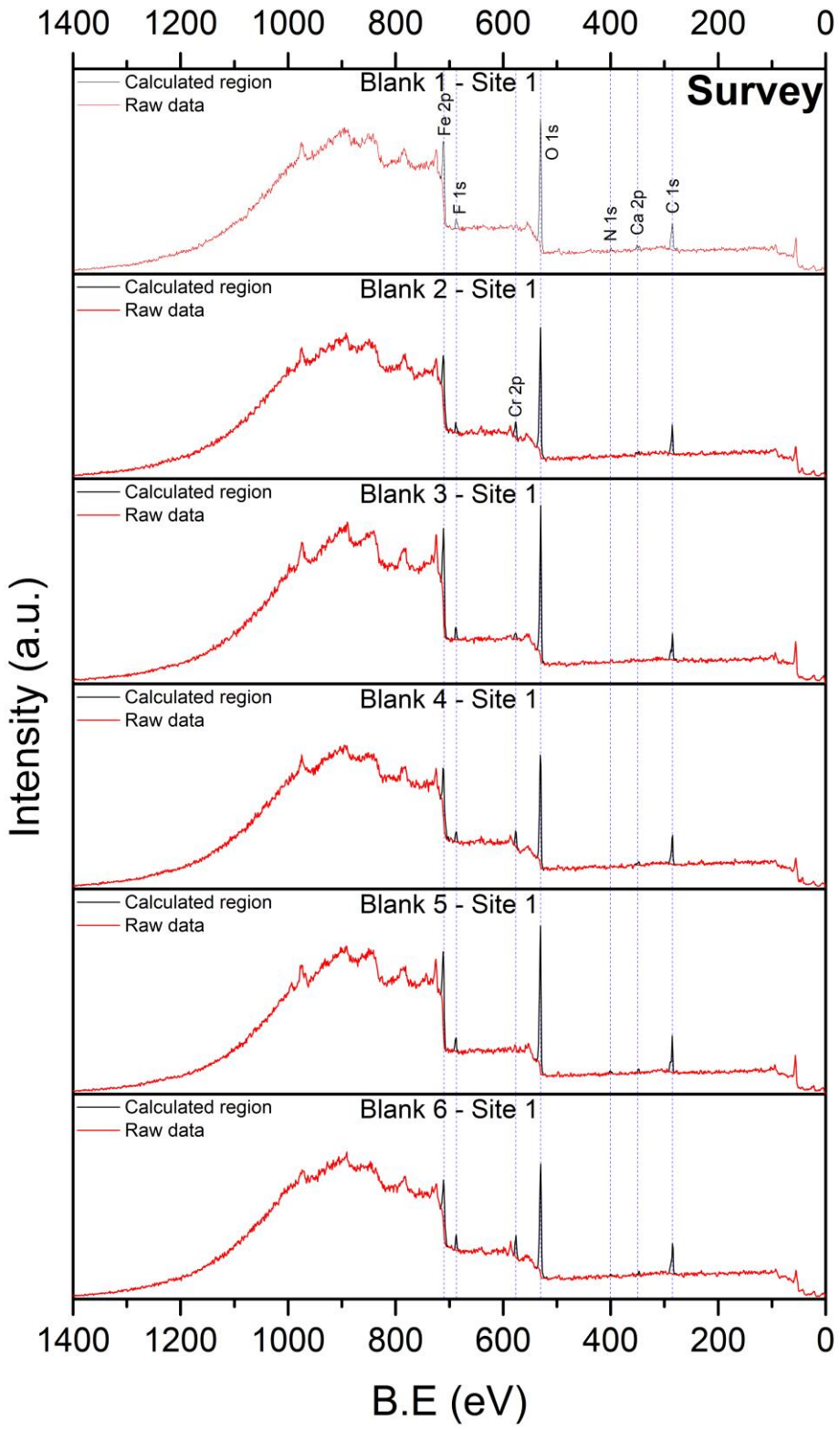

Figure A 4 Survey spectra measured for six TAM-cleaned, polished coupons at site 1.

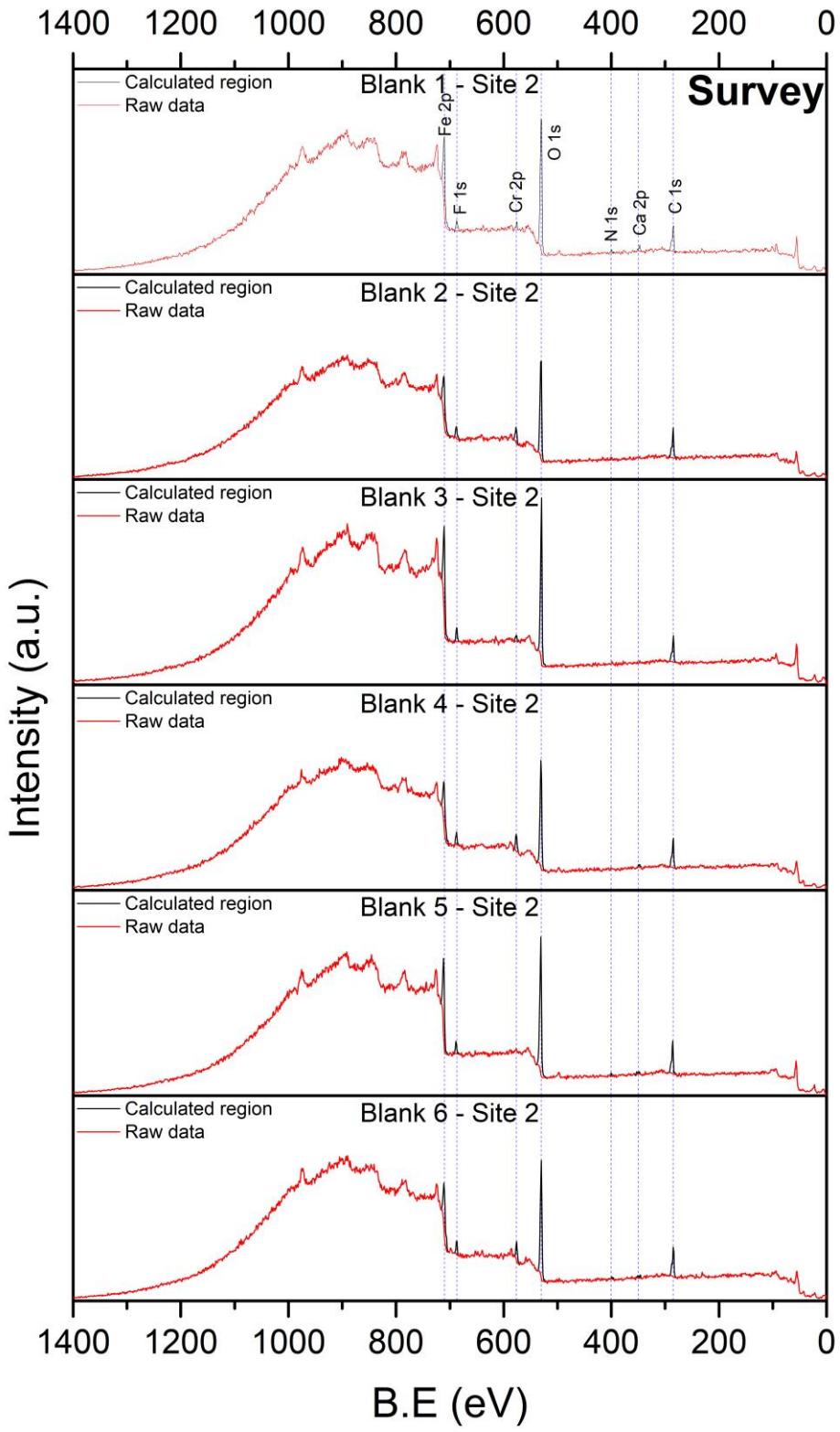

Figure A 5 Survey spectra measured for six TAM-cleaned, polished coupons at site 2

Chapter 4 Oxidative formation of gum in model surrogate fuel

Table A 2 Table of characteristic IR absorption bands of 2,2,4 tri-methyl pentane (iso-octane). Reference IR regions retrieved from (160).

Material	Region (cm^{-1})	Frequency (cm^{-1})	Assignment
Iso-octane	~ 970	979	CH_3 rock in $-C(CH_3)_3$
	1165-1175	1168	C-C stretch in $C(CH_3)_2$
	1165-1225	1206	C-C rock in $-C(CH_3)_3$
	1245-1255	1247	C-C rock in $-C(CH_3)_3$
	1350-1395	1365	2,2, CH_3 symmetric bend
	1350-1395	1393	2,2, CH_3 symmetric bend
	1435-1475	1468	CH_3 vibration in $-C(CH_3)_3$
	2865-2875	2870	CH_3 symmetric stretch
	2840-2940	2900	CH stretch $CH(CH_3)_2$
	2950-2975	2954	CH_3 asymmetric stretch

Table A 3 Table of characteristic IR absorption bands of n-heptane. Reference IR regions retrieved from (160).

Material	Region (cm^{-1})	Frequency (cm^{-1})	Assignment
n-heptane	720-725	723	Rock vibration in $-(CH_2)_n$
	1370-1390	1378	Symmetric $-CH_3$ rock
	1440-1465	1467	Asymmetric $-CH_3$ bend
	2840-2870	2858	Symmetric $-CH_2$ stretch
	2865-2885	2873	Symmetric $-CH_3$ stretch
	2915-2940	2924	Asymmetric $-CH_2$ stretch
	2950-2975	2958	Asymmetric $-CH_3$ stretch

Table A 4 Details of characteristic IR absorption bands of methyl benzene (toluene). Reference IR regions retrieved from (160).

Material	Region (cm^{-1})	Frequency (cm^{-1})	Assignment
Toluene	670-710	693	=CH out of plane vibration
	720-820	727	=CH out of plane vibration
	1000-1040	1030	=CH in plane vibration
	1050-1085	1080	=CH in plane vibration
	1430-1470	1457	–C=C– (mono benzene)
	1470-1525	1495	–C=C– (mono benzene)
	1590-1625	1604	–C=C– stretch (in ring)
	2865-2875	2879	CH3 stretch
	2840-2940	2939	CH stretch
	3000-3105	3030	=CH stretch

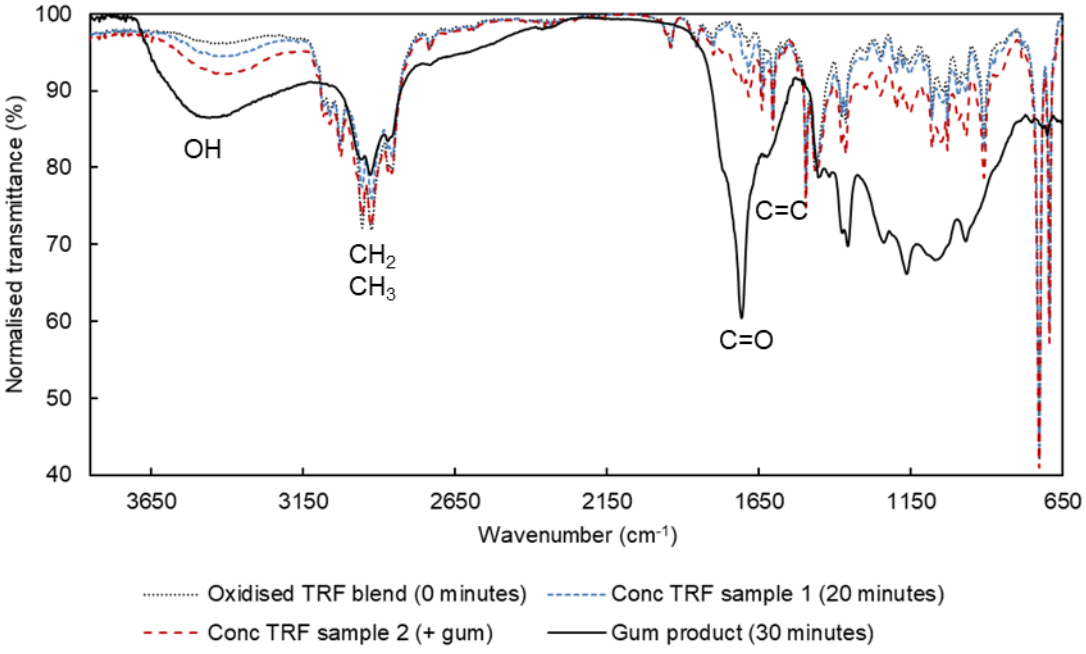

Figure A 6 ATR-FTIR spectra of the oxidised TRF blends and oxidation products.

Chapter 6 Systematic studies of interfacial behaviour by XPS

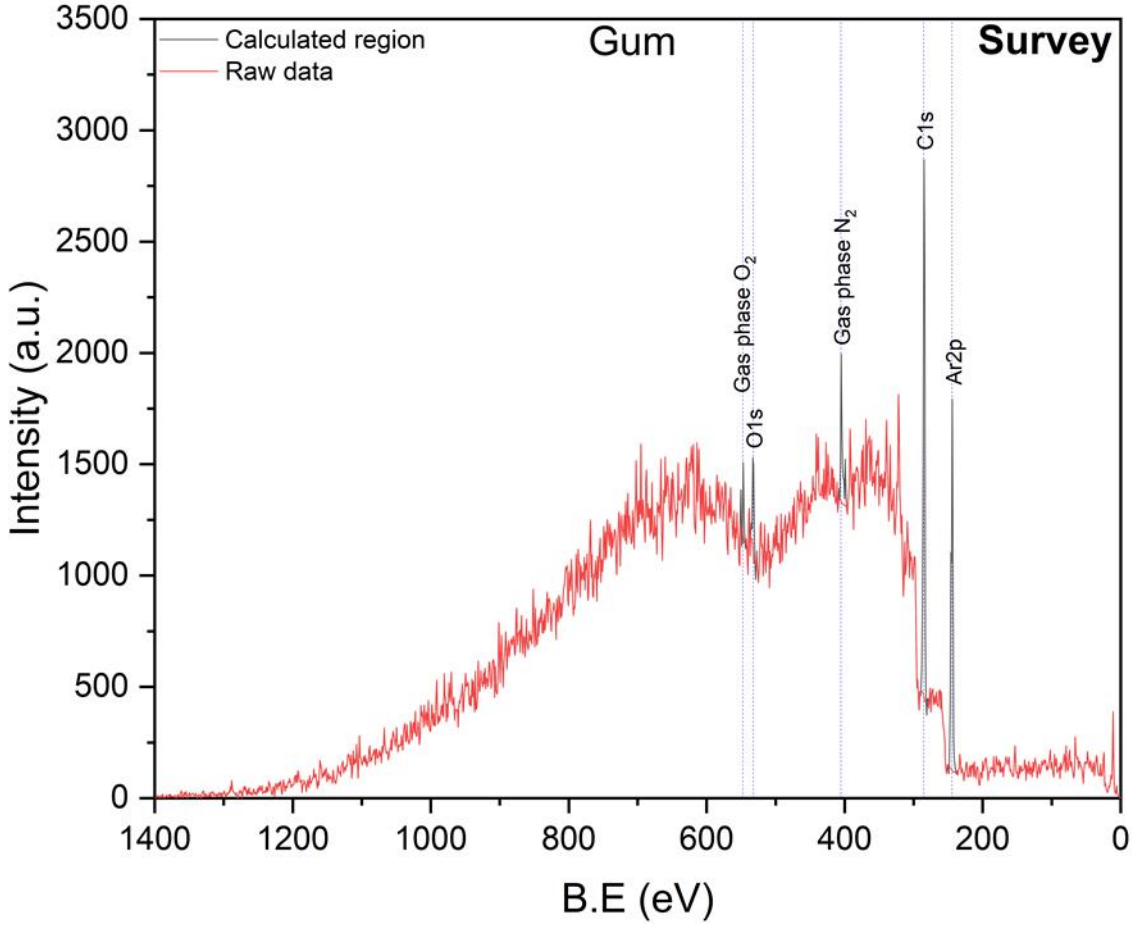

Figure A 7 XPS survey scan of the synthesised gum showing composition solely consisted of carbon and oxygen. Regions of purging gas (Ar2p) as well as gas phase N_2 and O_2 are also shown.

Appendix 3 XPS data correction method (chapter 6.3).

Until scanning time was available on the UHV-XPS, samples remained intact on their stubs by placing them in a paper pin-mount storage box which was stored inside a desiccator at room temperature to avoid humidity and contamination. Due to the variations in vacuuming capabilities as well as other instrumental parameters between the UHV and the EnviroESCA, intensity of the collected photoelectrons was approximately an order of magnitude higher in the UHV. Thus, a normalisation method had to be factored in for each single experiment to achieve a meaningful comparison across the three immersion stages (e.g. before, ODA, gum). The normalisation factor was calculated based on average intensity of 5 eV, where possible, at the lower binding energy of the 'before' spectra (i.e. blank SS). Average intensities of 5 eV from the other two stages were then normalised to the 'before' average to have the same baseline at the lower binding energy for all three spectra. Correction of the 'gum in ODA' experiment from the detergency study is illustrated in below as an example.

Table A 5 Correction factors used to normalise the intensities and baselines of stage two and stage three spectra.

Sample (immersion stage)	**Average 5 eV intensity (a.u.)**	**Correction factor (Avg. sample/Avg. before)**
Before (Blank SS)	960.57	1.00
2000 ppm gum	740.39	0.77
1000 ppm ODA	645.25	0.67

Similarly, individual peaks were normalised using the same correction factor to have comparable peak areas and consequently meaningful quantification.

Table A 6 Raw area vs. corrected area of all identified species. Corrected areas were used throughout all derived quantifications.

Sample	Species	Raw area	Corrected area (Raw area/correction factor)
Before	C-C/C-H	3275.41	3275.41
	C-O	780.41	780.41
	C=O	1425.68	1425.68
2000 ppm gum	C-C/C-H	3300.90	4282.56
	C-O	3262.70	4233.00
	C=O	1497.77	1943.20
1000 ppm ODA	C-C/C-H	48244.00	4876.01
	C-O	11510.20	1163.33
	C=O	11030.30	1114.83

By obtaining corrected intensities, baselines, and peak areas, it was possible to quantify the changes as a function of immersion stage for all spectra. Figure A 8 shows the obtained XP spectra before and after correction.

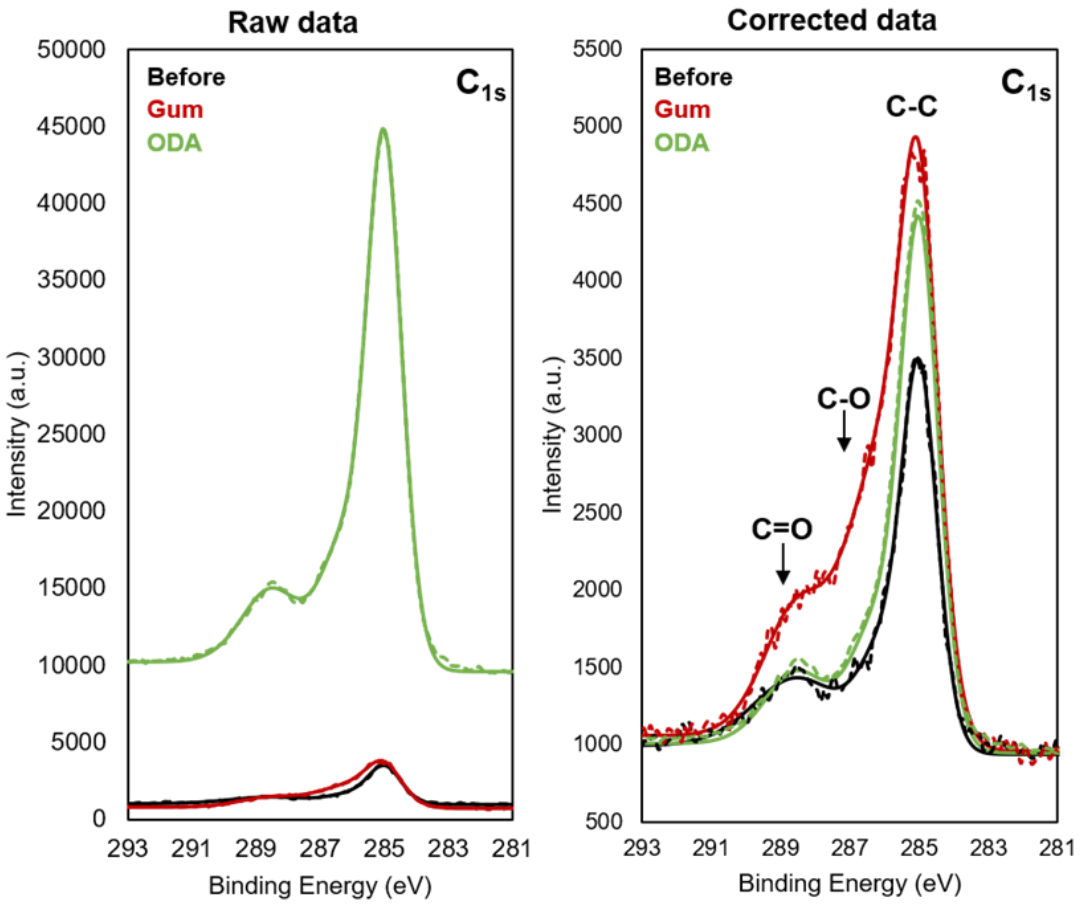

Figure A 8 Raw (dotted line) and envelope (solid line) data of the C 1s spectra pre- and post-correction (left vs. right) using the normalisation factors calculated in Table A 5.

Once all spectra were normalised to a comparable baseline, it was much easier to observe and quantify changes as a function of immersion. For instance, it can be clearly seen from the corrected spectra in Figure A 8 that gum immersion has significantly contributed to the intensities of C-O and C=O species. Moreover, ODA immersion was able to attenuate the C-O and C=O peaks and reduce their levels to approximately ‘before’ levels.

Table A 7 Peak areas of the C-C, C-O, C=O, and Fe_2O_3 species described in Figure 111 before (B) and after (A) immersion, as a function of ODA concentration (0 – 1500 ppm w/v). Higher vs lower values are distinguished by ▲ and ▼ respectively.

Species	0	50	250	500	1000	1500
	Peak area					
C-C/C-H (C 1s)	**B:** ▼3426	▼2551	▼2741	▼3766	▼724	▼3442
	A: ▲4468	▲4058	▲4062	▲4403	▲865	▲4105
C-O (C 1s)	▼679	▼638	▼726	▼796	▲256	▲1013
	▲1209	▲1119	▲1017	▲1117	▼223	▼918
C=O (C 1s)	▼1422	▼1233	▼1075	▲1302	▲298	▲1343
	▲1594	▲1258	▲1409	▼1204	▼247	▼1033
Fe_2O_3 (Fe 2p)	▲8011	▲5036	▲9531	▲8582	▲2090	▼7237
	▼7427	▼2120	▼6749	▼7305	▼1876	▲8815

References

1. ACEA, Alliance, EMA and JAMA. *Worldwide Fuel Charter.* 5th ed. Belgium, USA, and Japan, 2013.
2. da Silva, M.P.F., Brito, L.R.e., Honorato, F.A., Paim, A.P.S., Pasquini, C. and Pimentel, M.F. Classification of gasoline as with or without dispersant and detergent additives using infrared spectroscopy and multivariate classification. *Fuel.* 2014, **116**, pp.151-157.
3. Rizwanul Fattah, I.M., Masjuki, H.H., Kalam, M.A., Hazrat, M.A., Masum, B.M., Imtenan, S. and Ashraful, A.M. Effect of antioxidants on oxidation stability of biodiesel derived from vegetable and animal based feedstocks. *Renewable and Sustainable Energy Reviews.* 2014, **30**, pp.356-370.
4. Del Rio, D., Bastos, R. and Sedran, U. Commercial additives for sulfur control in FCC gasoline: Overall analysis of their impact on LCO and gasoline. *Catalysis Today.* 2013, **213**, pp.206-210.
5. Kalghatgi, G.T. Deposits in Gasoline Engines - A Literature Review. *SAE Technical Paper Series.* 1990.
6. Tupa, R.C. and Koehler, D.E. Gasoline Port Fuel Injectors - Keep Clean/Clean Up With Additives. In.: SAE International, 1986.
7. Rogers, T.H., Bussies, J.L. and Ward, P.T. Gum Formation in Gasoline. *Industrial & Engineering Chemistry.* 1933, **25**(4), pp.397-402.
8. Taniguchi, B.Y., Peyla, R.J., Parsons, G.M., Hoekman, S.K. and Voss, D.A. Injector Deposits — The Tip of Intake System Deposit Problems. In: *International Fuels and Lubricants Meeting and Exposition*, *Pennsylvania, USA*. SAE International, 1986.
9. Zand, A.D., Nabi bidhendi, G., Mikaeili T, A. and Pezeshk, H. The influence of deposit control additives on exhaust CO and HC emissions from gasoline engines (case study: Tehran). *Transportation Research Part D: Transport and Environment.* 2007, **12**(3), pp.189-194.
10. Gumout. *Engine Problems.* [Online]. 2014. [Accessed 2016]. Available from: https://gumout.com/gumout-science/performance/combustion-chamber
11. Zerda, T.W., Yuan, X. and Moore, S.M. Effects of fuel additives on the microstructure of combustion engine deposits. *Carbon.* 2001, **39**(10), pp.1589-1597.
12. Adam Beck, M.B., and Jeno Hancsok. *Development of Multifunctional Detergent-Dispersant Additives Based on Fatty Acid Methyl Ester for Diesel and Biodiesel Fuel.* InTech, 2011.

13. *Shell Nitrogen Enriched Gasolines.* [Online]. 2012. [Accessed May 2015]. Available from: http://www.shell.us/products-services/shell-for-motorists/fuels/nitrogen-enriched-gasolines.html
14. Bucher, B.A. and Weatherford, T.M. *Fuel additive and fuel composition*. WO2013028453 A1. 2013.
15. Alemán-Vázquez, L.O. and Villagómez-Ibarra, J.R. Polyisobutenylsuccinimides as detergents and dispersants in fuel: infrared spectroscopy application. *Fuel.* 2001, **80**(7), pp.965-968.
16. Kumar, R., De, P., Zheng, B., Huang, K.-W., Emert, J. and Faust, R. Synthesis of highly reactive polyisobutylene with $FeCl_3$/ether complexes in hexane; kinetic and mechanistic studies. *Polym. Chem.* 2015, **6**(2), pp.322-329.
17. Pradelle, F., Braga, S.L., Martins, A.R.F.A., Turkovics, F. and Pradelle, R.N.C. Gum Formation in Gasoline and Its Blends: A Review. *Energy & Fuels.* 2015, **29**(12), pp.7753-7770.
18. Ahmed, N.S., Nasser, A.M. and Kamal, R.S. Influence of Some Compounds as Antioxidants and Detergents/Dispersants for Lube Oil. *Journal of Dispersion Science and Technology.* 2011, **32**(7), pp.1067-1074.
19. Pirouz, S., Wang, Y., Chong, J.M. and Duhamel, J. Characterization of the Chemical Composition of Polyisobutylene-Based Oil-Soluble Dispersants by Fluorescence. *Journal of Physical Chemistry B.* 2014, **118**(14), pp.3899-3911.
20. Balabin, R.M. and Safieva, R.Z. Gasoline classification by source and type based on near infrared (NIR) spectroscopy data. *Fuel.* 2008, **87**(7), pp.1096-1101.
21. Marbach, H.W., Johnston, A.A., Bowden, J.N. and LePera, M.E. A Novel Laboratory Method for Evaluating Induction System Deposits in Gasoline Engines. 1979.
22. Schwahn, H., Lutz, U. and Kramer, U. Deposit Formation of Flex Fuel Engines Operated on Ethanol and Gasoline Blends. *SAE Int. J. Fuels Lubr.* 2010, **3**(2), pp.22-37.
23. Voelkel, L. Gasoline Performance Additives -The Key to Higher Quality Fuels. In: *Hart World Refining and Fuels Conference*, *Beijing, China*. 2006.
24. De La Cruz, J.L. and Estafan, R.M. *Test Apparatus and Method for Determining Deposit Formation Characteristics of Fuels*. US5693874A. 1997.
25. ASTM D6201-04(2014). *Standard Test Method for Dynamometer Evaluation of Unleaded Spark-Ignition Engine Fuel for Intake Valve Deposit Formation,.* ASTM International, West Conshohocken, PA, 2014.
26. McLeary, D., Longstaff, D. and Ajina, A. *Gasoline Fuel Detergency Program [Internal report].* Dhahran, Saudi Arabia: R&DC, Saudi Aramco, 2013.

27. Udelhofen, J.H. and Zahalka, T.L. Gasoline Additive Requirements for Today's Smaller Engines. In: *1988 SAE International Fall Fuels and Lubricants Meeting and Exhibition USA*. SAE International, 1988.
28. Yasar, A., Haider, R., Tabinda, A.B., Kausar, F. and Khan, M. A Comparison of Engine Emissions from Heavy, Medium, and Light Vehicles for CNG, Diesel, and Gasoline Fuels. *Pol. J. Environ. Stud.* 2013, **22**(4), pp.1277-1281.
29. Streva, E.R., Pasa, V.M.D. and Sodré, J.R. Aging effects on gasoline–ethanol blend properties and composition. *Fuel.* 2011, **90**(1), pp.215-219.
30. Teixeira, L.S.G., Souza, J.C., dos Santos, H.C., Pontes, L.A.M., Guimarães, P.R.B., Sobrinho, E.V. and Vianna, R.F. The influence of Cu, Fe, Ni, Pb and Zn on gum formation in the Brazilian automotive gasoline. *Fuel Processing Technology.* 2007, **88**(1), pp.73-76.
31. Pereira, C.C. and Pasa, V.M.D. Effect of Alcohol and Copper Content on the Stability of Automotive Gasoline. *Energy & Fuels.* 2005, **19**(2), pp.426-432.
32. Zanier, A. Thermal-oxidative stability of motor gasolines by pressure d.s.c. *Fuel.* 1998, **77**(8), pp.865-870.
33. Ye, Z., Meng, Q., Mohamadian, H.P., Wang, J.T., Chen, L. and Zhu, L. Investigation of deposit formation mechanisms for engine in-cylinder combustion and exhaust systems using quantitative analysis and sustainability study. *International Journal of Thermophysics.* 2007, **28**(3), pp.1056-1066.
34. Nagpal, J.M., Joshi, G.C., Singh, J. and Rastogi, S.N. Gum forming olefinic precursors in motor gasoline, a model compound study. *Fuel Science and Technology International.* 1994, **12**(6), pp.873-894.
35. Kim, C., Tseregounis, S.I. and Scruggs, B.E. Deposit Formation on a Metal Surface in Oxidized Gasolines. *SAE Technical Paper Series.* 1987.
36. Tseregounis, S.I. Thin Deposit Films from Oxidized Gasoline on Steel Surfaces as Determined by ESCA. *SAE Technical Paper Series.* 1988.
37. Gibbs, L.M. Gasoline Additives - When and Why. In.: SAE International, 1990.
38. Nikitina, E.A., Emel'yanov, V.E., Krylov, I.F. and Fedorova, A.V. Detergent additives to automotive gasolines. *Chemistry and Technology of Fuels and Oils.* 2006, **42**(1), pp.30-34.
39. Knop, V., Pera, C. and Duffour, F. Validation of a ternary gasoline surrogate in a CAI engine. *Combustion and Flame.* 2013, **160**(10), pp.2067-2082.
40. Pitz, W.J., Cernansky, N.P., Dryer, F.L., Egolfopoulos, F.N., Farrell, J.T., Friend, D.G. and Pitsch, H. *Development of an Experimental Database and Chemical Kinetic Models for Surrogate Gasoline Fuels.* 2007.
41. Kalghatgi, G. *Fuel/Engine Interactions.* Warrendale, PA: SAE International, 2014.

42. Morgan, N., Smallbone, A., Bhave, A., Kraft, M., Cracknell, R. and Kalghatgi, G. Mapping surrogate gasoline compositions into RON/MON space. *Combustion and Flame.* 2010, **157**(6), pp.1122-1131.

43. Vanhove, G., Petit, G. and Minetti, R. Experimental study of the kinetic interactions in the low-temperature autoignition of hydrocarbon binary mixtures and a surrogate fuel. *Combustion and Flame.* 2006, **145**(3), pp.521-532.

44. Pera, C. and Knop, V. Methodology to define gasoline surrogates dedicated to auto-ignition in engines. *Fuel.* 2012, **96**, pp.59-69.

45. Cancino, L.R., Fikri, M., Oliveira, A.A.M. and Schulz, C. Ignition delay times of ethanol-containing multi-component gasoline surrogates: Shock-tube experiments and detailed modeling. *Fuel.* 2011, **90**(3), pp.1238-1244.

46. Naik, C.V., Pitz, W.J., Westbrook, C.K., Sjöberg, M., Dec, J.E., Orme, J., Curran, H.J. and Simmie, J.M. Detailed Chemical Kinetic Modeling of Surrogate Fuels for Gasoline and Application to an HCCI Engine. *SAE Technical Paper Series.* 2005.

47. Yahyaoui, M., Djebaïli-Chaumeix, N., Dagaut, P., Paillard, C.E. and Gail, S. Experimental and modelling study of gasoline surrogate mixtures oxidation in jet stirred reactor and shock tube. *Proceedings of the Combustion Institute.* 2007, **31**(1), pp.385-391.

48. Fikri, M., Herzler, J., Starke, R., Schulz, C., Roth, P. and Kalghatgi, G.T. Autoignition of gasoline surrogates mixtures at intermediate temperatures and high pressures. *Combustion and Flame.* 2008, **152**(1–2), pp.276-281.

49. Lenhert, D.B., Miller, D.L., Cernansky, N.P. and Owens, K.G. The oxidation of a gasoline surrogate in the negative temperature coefficient region. *Combustion and Flame.* 2009, **156**(3), pp.549-564.

50. Mehl, M., Chen, J.Y., Pitz, W.J., Sarathy, S.M. and Westbrook, C.K. An Approach for Formulating Surrogates for Gasoline with Application toward a Reduced Surrogate Mechanism for CFD Engine Modeling. *Energy & Fuels.* 2011, **25**(11), pp.5215-5223.

51. Andrae, J.C.G., Brinck, T. and Kalghatgi, G.T. HCCI experiments with toluene reference fuels modeled by a semidetailed chemical kinetic model. *Combustion and Flame.* 2008, **155**(4), pp.696-712.

52. Heywood, J.B. *Internal combustion engine fundamentals.* New York;London;: McGraw-Hill, 1988.

53. Kalghatgi, G., Risberg, P. and Ångstrom, H.-E. A Method of Defining Ignition Quality of Fuels in HCCI Engines. In: *SAE International Spring Fuels & Lubricants Meeting*, *Yokohama, Japan*. SAE International, 2003.

54. Kalghatgi, G.T. and Head, R.A. The Available and Required Autoignition Quality of Gasoline - Like Fuels in HCCI Engines at High Temperatures. *SAE Technical Paper Series.* 2004.

55. European Committee for Standardization (CEN). *Automotive fuels - Unleaded petrol - Requirements and test methods.* Brussels, Belgium IEEE GlobalSpec, 2012.

56. ASTM D873 - 12(2018). *Standard Test Method for Oxidation Stability of Aviation Fuels (Potential Residue Method).* West Conshohocken, PA: ASTM International, 2012.

57. ASTM Standard D381-12(2017). *Standard Test Method for Gum Content in Fuels by Jet Evaporation.* West Conshohocken, PA: ASTM International, 2017.

58. Stavinoha, L.L., Bowden, J.N. and LePera, M.E. *Evaluation of Motor Gasoline Stability.* Fort Belvoir, VA, 1990.

59. Mayo, F.R. and Lan, B.Y. Gum and deposit formation from jet turbine and diesel fuels at 130.degree.C. *Industrial & Engineering Chemistry Product Research and Development.* 1986, **25**(2), pp.333-348.

60. Kolobielski, M. and McCaleb, F. *Gasolines and Engine Oils: Literature Review, New Laboratory Oxidation Method, and Significance of Olefins in Fuel.* Fort Belvoir, VA, 1980.

61. Benson, J.D. and Yaccarino, P.A. The Effects of Fuel Composition and Additives on Multiport Fuel Injector Deposits. In: *International Fuels and Lubricants Meeting & Exposition*, *Pennsylvania, USA*. SAE International, 1986.

62. Rogers, D.T. and Jon Ac H, F.L. Mechanism of Intake Valve Underside Deposit Formation. In: *SAE National Fuels and Lubricants Meeting*, *Oklahoma, USA*. SAE International, 1958.

63. Schwartz, F.G., Whisman, M.L., Allbright, C.S. and Ward, C.C. *Storage Stability of Gasoline: Fundamentals of Gum Formation Including a Discussion of Radiotracer Techniques.* Washington, D. C., 1964; Bulletin 626.

64. Kawahara, F.K. Composition of Gum in Cracked Naphtha. *I&EC Product Research and Development.* 1965, **4**(1), pp.7-9.

65. European Union. *Directive 2003/17/EC of the European Parliament and of the Council of 3 March 2003 amending Directive 98/70/EC relating to the quality of petrol and diesel fuels.* EUROPA.EU, 2003.

66. Zuidema, H.H. *The performance of lubricating oils.* 2nd ed. USA: Reinhold Pub. Corp., 1959.

67. Heneghan, S.P. and Zabarnick, S. Oxidation of jet fuels and the formation of deposit. *Fuel.* 1994, **73**(1), pp.35-43.

68. de la Puente, G. and Sedran, U. Formation of Gum Precursors in FCC Naphthas. *Energy & Fuels.* 2004, **18**(2), pp.460-464.

69. A'reff, H.A. Effect of the Copper and Iron Concentration on Gum Formation in Gas Oil of Baiji Refinery *J. Chem. Chem. Eng.* 2011, **5**, pp.652-656.

70. Pereira, R.C.C. and Pasa, V.M.D. Effect of mono-olefins and diolefins on the stability of automotive gasoline. *Fuel.* 2006, **85**(12–13), pp.1860-1865.

71. Tupa, R.C. Port Fuel Injectors-Causes/Consequences/Cures. *SAE Technical Paper Series.* 1987.

72. Lindgren, R., Skogsberg, M., Sandquist, H. and Denbratt, I. The Influence of Injector Deposits on Mixture Formation in a DISC SI Engine. In: *SAE International Spring Fuels & Lubricants Meeting*, *Yokohama, Japan*. SAE International, 2003.

73. Arters, D.C. and Macduff, M.J. The Effect on Vehicle Performance of Injector Deposits in a Direct Injection Gasoline Engine. *SAE Technical Paper Series.* 2000.

74. Gething, J.A. Performance-Robbing Aspects of Intake Valve and Port Deposits. *SAE Technical Paper Series.* 1987.

75. Studzinski, W.M., Liiva, P.M., Choate, P.J., Acker, W.P., Litzinger, T., Bower, S., Smooke, M. and Brezinsky, K. A Computational and Experimental Study of Combustion Chamber Deposit Effects on NOx Emissions. *SAE Technical Paper Series.* 1993.

76. Interlloy. *440C Martenistic Stainless Steel Bar.* [Online]. 2011. [Accessed 2016]. Available from: http://www.interlloy.com.au/our-products/stainless-steel/440c-martensitic-stainless-steel-bar/

77. Kang, J.H., Park, I.W., Jae, J.S. and Kang, S.S. A study on a die wear model considering thermal softening: (I) Construction of the wear model. *Journal of Materials Processing Technology.* 1999, **96**(1–3), pp.53-58.

78. AKSteel. *316/316L Stainless Steel.* [Online]. 2007. [Accessed 2106]. Available from: http://www.aksteel.com/pdf/markets_products/stainless/austenitic/316_316l_data_sheet.pdf

79. Imdadul, H.K., Masjuki, H.H., Kalam, M.A., Zulkifli, N.W.M., Rashed, M.M., Rashedul, H.K., Monirul, I.M. and Mosarof, M.H. A comprehensive review on the assessment of fuel additive effects on combustion behavior in CI engine fuelled with diesel biodiesel blends. *RSC Advances.* 2015, **5**(83), pp.67541-67567.

80. Charles, A.P. and Tze-Chi, J. Application of Surfactants in Lubricants and Fuels. In: *Handbook of Detergents, Part E*. CRC Press, 2008, pp.331-344.

81. Reck, R.A. In: Johnson, R.W. and Frtiz, E. eds. *Fatty acids in industry*. New York, USA: Marcel Dekker, Inc., 1989.

82. Visek, K. Amines, Fatty. In: *Kirk-Othmer Encyclopedia of Chemical Technology*. Michigan, USA: John Wiley & Sons, 2003.

83. D'Alencon, L., Lallemand, M., Harle, V., Moreton, D.J., MacDuff, M.G.J. and Pudlarz, M. *Fuel additive composition containing a dispersion of iron particles and a detergent*. 9914892. 2011.

84. Li, H., Lea-Langton, A., Biller, P., Andrews, G.E., Hadavi, S., Charlton, A. and Richards, P. Effect of Multifunctional Fuel Additive Package on Fuel Injector Deposit, Combustion and Emissions using Pure Rape Seed Oil for a DI Diesel. *SAE Int. J. Fuels Lubr.* 2009, **2**(2), pp.54-65.

85. Czarnocka, J., Matuszewska, A. and Odziemkowska, M. Autoxidation of Fuels During Storage. In: Biernat, K. ed. *Storage Stability of Fuels*. London, UK: InTech, 2015, pp.157-188.

86. Benítez, J.J., San-Miguel, M.A., Domínguez-Meister, S., Heredia-Guerrero, J.A. and Salmeron, M. Structure and Chemical State of Octadecylamine Self-Assembled Monolayers on Mica. *The Journal of Physical Chemistry C.* 2011, **115**(40), pp.19716-19723.

87. Georgiadou, V. and Dendrinou-Samara, C. Impact of the Presence of Octadecylamine on the Properties of Hydrothermally Prepared $CoFe_2O_4$ Nanoparticles. *European Journal of Inorganic Chemistry.* 2014, **2014**(23), pp.3645-3656.

88. Ge, H.H., Zhou, G.D., Liao, Q.Q., Lee, Y.G. and Loo, B.H. A study of anti-corrosion behavior of octadecylamine-treated iron samples. *Applied Surface Science.* 2000, **156**(1), pp.39-46.

89. Oviedo, J., San-Miguel, M.A., Heredia-Guerrero, J.A. and Benítez, J.J. Electrostatic Induced Molecular Tilting in Self-Assembled Monolayers of n-Octadecylamine on Mica. *The Journal of Physical Chemistry C.* 2012, **116**(12), pp.7099-7105.

90. Wood, M.H., Welbourn, R.J.L., Charlton, T., Zarbakhsh, A., Casford, M.T. and Clarke, S.M. Hexadecylamine Adsorption at the Iron Oxide–Oil Interface. *Langmuir.* 2013, **29**(45), pp.13735-13742.

91. Doig, M. and Camp, P.J. The structures of hexadecylamine films adsorbed on iron-oxide surfaces in dodecane and hexadecane. *Physical Chemistry Chemical Physics.* 2015, **17**(7), pp.5248-5255.

92. Chia, C.L., Alloway, R.M., Jephson, I., Clarke, S.M., Filip, S.V., Siperstein, F.R. and Avendaño, C. Competitive Adsorption of a Multifunctional Amine and Phenol Surfactant with Ethanol on Hematite from Nonaqueous Solution. *The Journal of Physical Chemistry B.* 2019, **123**(6), pp.1375-1383.

93. Kumar, A., Mandal, S., Selvakannan, P.R., Pasricha, R., Mandale, A.B. and Sastry, M. Investigation into the Interaction between Surface-Bound Alkylamines and Gold Nanoparticles. *Langmuir.* 2003, **19**(15), pp.6277-6282.

94. Lin, Z., Liu, Y. and Wong, C.-p. Facile Fabrication of Superhydrophobic Octadecylamine-Functionalized Graphite Oxide Film. *Langmuir.* 2010, **26**(20), pp.16110-16114.

95. Zahirifar, J., Karimi-Sabet, J., Moosavian, S.M.A., Hadi, A. and Khadiv-Parsi, P. Fabrication of a novel octadecylamine functionalized graphene oxide/PVDF dual-layer flat sheet membrane for desalination via air gap membrane distillation. *Desalination.* 2018, **428**, pp.227-239.

96. Chernyshova, I.V., Rao, K.H., Vidyadhar, A. and Shchukarev, A.V. Mechanism of Adsorption of Long-Chain Alkylamines on Silicates. A Spectroscopic Study. 1. Quartz. *Langmuir.* 2000, **16**(21), pp.8071-8084.

97. Leja, J. *Surface chemistry of froth flotation.* New York, USA: Plenum Press, 1982.

98. Smith, R.W. and L Scott, J. Mechanisms of Dodecylamine Flotation of Quartz. *Mineral Processing and Extractive Metallurgy Review.* 1990, **7**(2), pp.81-94.

99. Smith, R.W. and Akhtar, S. Gaudin memorial volume. In: Fuerstenau, M.C. ed. *Flotation*. New York, USA: American Institute of Mining Engineers, 1976, pp.87-116.

100. Smith, R.W. In: Somasundaran, P. and Moudgil, B.M. eds. *Reagents in mineral technology*. New York, USA: Marcel Dekker, 1988, pp.219-256.

101. Rutland, M., Waltermo, A. and Claesson, P. pH-dependent interactions of mica surfaces in aqueous dodecylammonium/dodecylamine solutions. *Langmuir.* 1992, **8**(1), pp.176-183.

102. Novich, B.E. and Ring, T.A. A predictive model for the alkylamine-quartz flotation system. *Langmuir.* 1985, **1**(6), pp.701-708.

103. Gaudin, A. and Fuerstenau, D. Quartz flotation with cationic collectors. *Transactions of the Society of Mining Engineers of AIME.* 1955, **202**, pp.958-962.

104. Somasundaran, P. and Fuerstenau, D.W. Mechanisms of Alkyl Sulfonate Adsorption at the Alumina-Water Interface1. *The Journal of Physical Chemistry.* 1966, **70**(1), pp.90-96.

105. Fuerstenau, D.W. and Jang, H.M. On the nature of alkylsulfonate adsorption at the rutile/water interface. *Langmuir.* 1991, **7**(12), pp.3138-3143.

106. Hunter, R.J. *Zeta potential in colloid science.* London, UK: Academic Press, 1981.

107. Chandar, P., Somasundaran, P. and Turro, N.J. Fluorescence probe studies on the structure of the adsorbed layer of dodecyl sulfate at the alumina—water interface. *Journal of Colloid and Interface Science.* 1987, **117**(1), pp.31-46.

108. Somasundaran, P., Healy, T.W. and Fuerstenau, D.W. Surfactant Adsorption at the Solid—Liquid Interface—Dependence of Mechanism on Chain Length. *The Journal of Physical Chemistry.* 1964, **68**(12), pp.3562-3566.

109. Beamson, G. and Briggs, D. High Resolution XPS of Organic Polymers: The Scienta ESCA300 Database (Beamson, G.; Briggs, D.). *Journal of Chemical Education.* 1993, **70**(1), p.A25.

110. Briggs, D. *Surface Analysis of Polymers by XPS and Static SIMS* Cambridge: Cambridge University Press, 1998.

111. Meylheuc, T., Methivier, C., Renault, M., Herry, J.-M., Pradier, C.-M. and Bellon-Fontaine, M.N. Adsorption on stainless steel surfaces of biosurfactants produced by gram-negative and gram-positive bacteria: Consequence on the bioadhesive behavior of Listeria monocytogenes. *Colloids and Surfaces B: Biointerfaces.* 2006, **52**(2), pp.128-137.

112. Clark, D.T., Peeling, J. and Colling, L. An experimental and theoretical investigation of the core level spectra of a series of amino acids, dipeptides and polypeptides. *Biochimica et Biophysica Acta (BBA) - Protein Structure.* 1976, **453**(2), pp.533-545.

113. Graf, N., Yegen, E., Gross, T., Lippitz, A., Weigel, W., Krakert, S., Terfort, A. and Unger, W.E.S. XPS and NEXAFS studies of aliphatic and aromatic amine species on functionalized surfaces. *Surface Science.* 2009, **603**(18), pp.2849-2860.

114. Cases, J.M. and Villieras, F. Thermodynamic model of ionic and nonionic surfactants adsorption-abstraction on heterogeneous surfaces. *Langmuir.* 1992, **8**(5), pp.1251-1264.

115. Harwell, J., Schechter, R., Wade, W. and Cases, J. Solid-Liquid Interactions in Porous Media. *Cases, J. M., Ed.* 1984, p.371.

116. Benítez, J.J., Heredia-Guerrero, J.A. and Salmeron, M. Steering the Self-Assembly of Octadecylamine Monolayers on Mica by Controlled Mechanical Energy Transfer from the AFM Tip. *The Journal of Physical Chemistry C.* 2010, **114**(29), pp.12630-12634.

117. Betova, I., Bojinov, M. and Saario, T. Film-Forming Amines in Steam/Water Cycles–structure, properties, and influence on corrosion and deposition processes. *VTT, Espoo, Finland.* 2014.

118. Pensini, E., van Lier, R., Cuoq, F., Hater, W. and Halthur, T. Enhanced corrosion resistance of metal surfaces by film forming amines: A comparative study between cyclohexanamine and 2-(diethylamino)ethanolbased formulations. *Water Resources and Industry.* 2017.

119. Ruan, C.-M., Bayer, T., Meth, S. and Sukenik, C.N. Creation and characterization of n-alkylthiol and n-alkylamine self-assembled monolayers on 316L stainless steel. *Thin Solid Films.* 2002, **419**(1), pp.95-104.

120. Feng, Y., Chen, S., You, J. and Guo, W. Investigation of alkylamine self-assembled films on iron electrodes by SEM, FT-IR, EIS and molecular simulations. *Electrochimica Acta.* 2007, **53**(4), pp.1743-1753.

121. Olajire, A.A. Corrosion inhibition of offshore oil and gas production facilities using organic compound inhibitors - A review. *Journal of Molecular Liquids.* 2017, **248**, pp.775-808.

122. Bertrand, N., Drévillon, B., Gheorghiu, A., Sénémaud, C., Martinu, L. and Klemberg-Sapieha, J.E. Adhesion improvement of plasma-deposited silica thin films on stainless steel substrate studied by x-ray photoemission spectroscopy and in situ infrared ellipsometry. *Journal of Vacuum Science & Technology A.* 1998, **16**(1), pp.6-12.

123. Kothari, D.C., Nair, M.R., Rangwala, A.A., Lal, K.B., Prabhawalkar, P.D. and Raole, P.M. XPS studies at various temperatures of nitrogen implanted 304 stainless steel. *Nuclear Instruments and Methods in Physics Research Section B: Beam Interactions with Materials and Atoms.* 1985, **7-8**, pp.235-241.

124. Overbury, S.H., Mullins, D.R., Huntley, D.R. and Kundakovic, L. Chemisorption and Reaction of NO and N_2O on Oxidized and Reduced Ceria Surfaces Studied by Soft X-Ray Photoemission Spectroscopy and Desorption Spectroscopy. *Journal of Catalysis.* 1999, **186**(2), pp.296-309.

125. Kam, D.H., Bhattacharya, S. and Mazumder, J. Control of the wetting properties of an AISI 316L stainless steel surface by femtosecond laser-induced surface modification. *Journal of Micromechanics and Microengineering.* 2012, **22**(10), p.105019.

126. Zhang, F. and Srinivasan, M.P. Self-Assembled Molecular Films of Aminosilanes and Their Immobilization Capacities. *Langmuir.* 2004, **20**(6), pp.2309-2314.

127. Kim, J., Park, H., Jung, D. and Kim, S. Protein immobilization on plasma-polymerized ethylenediamine-coated glass slides. *Analytical Biochemistry.* 2003, **313**(1), pp.41-45.

128. Truica-Marasescu, F. and Wertheimer, M.R. Nitrogen-Rich Plasma-Polymer Films for Biomedical Applications. *Plasma Processes and Polymers.* 2008, **5**(1), pp.44-57.

129. Walczak, M.S., Morales-Gil, P., Belashehr, T., Kousar, K., Arellanes Lozada, P. and Lindsay, R. Determining the Chemical Composition of Corrosion Inhibitor/Metal Interfaces with XPS: Minimizing Post Immersion Oxidation. *JoVE.* 2017, (121), p.e55163.

130. Bailey, R. and Castle, J.E. XPS study of the adsorption of ethoxysilanes on iron. *Journal of Materials Science.* 1977, **12**(10), pp.2049-2055.

131. Al-Refaie, A.A., Walton, J., Cottis, R.A. and Lindsay, R. Photoelectron spectroscopy study of the inhibition of mild steel corrosion by molybdate and nitrite anions. *Corrosion Science.* 2010, **52**(2), pp.422-428.

132. Jung, R.-H., Tsuchiya, H. and Fujimoto, S. XPS characterization of passive films formed on Type 304 stainless steel in humid atmosphere. *Corrosion Science.* 2012, **58**, pp.62-68.

133. Smith, B.C. *Fundamentals of fourier transform infrared spectroscopy.* Second ed. Boca Raton, USA: CRC Press, 2011.

134. Halliday, D., Resnick, R. and Krane, K.S. *Physics.* 4th ed. New York, USA: Wiley, 1992.

135. De Caro, C. and Haller, C. *UV/VIS Spectrophotometry - Fundamentals and Applications.* Schwerzenbach, Switzerland: Mettler-Toledo AG, Analytical, 2015.

136. Thomas, M. *Ultraviolet and visible spectroscopy. .* Second ed. West Sussex, England: John Wiley & Sons., 1996.

137. Bottom, R. Thermogravimetric Analysis. In: Gabbott, P. ed. *Principles and Applications of Thermal Analysis*. Oxford, UK: Blackwell Publishing, 2008, pp.87-118.

138. Sakho, E.H.M., Allahyari, E., Oluwafemi, O., Thomas, S. and Kalarikkal, N. Dynamic Light Scattering (DLS). In: Thomas, S. et al. eds. *Thermal and Rheological Measurement Techniques for Nanomaterials Characterization*. Amesterdam, Netherlands: Elsevier, 2017, pp.37-49.

139. Girão, A., Caputo, G. and Ferro, M.C. Application of Scanning Electron Microscopy-Energy Dispersive X-ray Spectroscopy (SEM-EDS). In: Rocha-Santos, T. and Duarte, A. eds. *Characterization and Analysis of Microplastics*. Elsevier, 2017.

140. Goodhew, P., Humphreys, J. and Beanland, R. *Electron Microscopy and Analysis.* 3rd ed. London, UK: CRC Press, 2001.

141. Kazmiruk, V. ed. *Scanning Electron Microscopy.* Rijeka, Croatia: InTech, 2012.

142. Garratt-Reed, A.J., Bell, D.C. and Nicholson, P. *Energy-dispersive X-ray analysis in the electron microscope.* Oxford, UK: Bios Scientific, 2003.

143. MEE. *X-Ray Photoelectron Spectroscopy (XPS).* [Online]. 2019. [Accessed 2019]. Available from: https://www.mee-inc.com/hamm/x-ray-photoelectron-spectroscopy-xps/

144. Watts, J.F. and Wolstenholme, J. *An Introduction to Surface Analysis by XPS and AES.* West Sussex, England: John Wiley & Sons Ltd, 2005.

145. ThirmoFisher. *Analysis Features.* [Online]. 2013-2019. [Accessed 2019]. Available from: https://xpssimplified.com/UPS.php

146. Moulder, J.F., Stickle, W.F., Sobol, P.E. and Bomben, K.D. *Handbook of X-ray Photoelectron Spectroscopy.* Minnesota, USA: Perkin Elmer Corp, 1992.

147. Dietrich, P.M., Bahr, S., Yamamoto, T., Meyer, M. and Thissen, A. Chemical surface analysis on materials and devices under functional conditions – Environmental photoelectron spectroscopy as non-destructive tool for routine characterization. *Journal of Electron Spectroscopy and Related Phenomena.* 2019, **231**, pp.118-126.

148. Linford, M., Roychowdhury, T. and Shah, D. Near Ambient Pressure XPS (NAP-XPS). A New Paradigm for the Technique. *Vacuum Technology & Coating.* 2018, (August), pp.26-28.

149. *Maple (18). [Software].* Maplesoft, a division of Waterloo Maple Inc.: Waterloo, Ontario.

150. BUEHLER. *BUEHLER® Alpha, Beta & Vector™ GRINDER-POLISHERS AND POWER HEAD.* [Online]. 2005. [Accessed 2017]. Available from: http://www.labequip.com/stock/pictures/24711.pdf

151. Gadelmawla, E.S., Koura, M.M., Maksoud, T.M.A., Elewa, I.M. and Soliman, H.H. Roughness parameters. *Journal of Materials Processing Technology.* 2002, **123**(1), pp.133-145.

152. Gardin, E., Zanna, S., Seyeux, A., Allion-Maurer, A. and Marcus, P. Comparative study of the surface oxide films on lean duplex and corresponding single phase stainless steels by XPS and ToF-SIMS. *Corrosion Science.* 2018, **143**, pp.403-413.

153. Becker, S., Merz, R., Hasse, H. and Kopnarski, M. Solvent cleaning and wettability of technical steel and titanium surfaces. *Adsorption Science & Technology.* 2016, **34**(4-5), pp.261-274.

154. Taborelli, M. Cleaning and surface properties In: *CAS-CERN Accellerator School and ALBA Synchrotron Light Facility. Course on Vacuum in Accelerators*: CERN, 2006.

155. Somorjai, G.A. and Li, Y. Impact of surface chemistry. *Proceedings of the National Academy of Sciences.* 2011, **108**(3), p.917.

156. Williams, D.F., Kellar, E.J.C., Jesson, D.A. and Watts, J.F. Surface analysis of 316 stainless steel treated with cold atmospheric plasma. *Applied Surface Science.* 2017, **403**, pp.240-247.

157. Honda, F. and Hirokawa, K. A photoelectron spectroscopic observation of iron surfaces exposed to N_2, N_2O, NO, NO_2 and air at 200 torr or 1 atm. *Journal of Electron Spectroscopy and Related Phenomena.* 1976, **8**(3), pp.199-211.

158. Thirouard, B. and Cherel, J. Nature of CAI Combustion and Air/Fuel Ratio Stratification Effects. *Oil & Gas Science and Technology - Rev. IFP.* 2006, **61**(1), pp.95-119.

159. E. Dec, J. and Sjöberg, M. *Isolating the Effects of Fuel Chemistry on Combustion Phasing in an HCCI Engine and the Potential of Fuel Stratification for Ignition Control.* 2004.

160. Socrates, G. *Infrared and Raman characteristic group frequencies: tables and charts.* Chichester, UK: Wiley & Sons Ltd, 2001.

161. Johnston, R.W.B., Appleby, W.G. and Baker, M.O. Determination of Olefins in Gasoline. *Analytical Chemistry.* 1948, **20**(9), pp.805-812.

162. NIST. *1-Pentene.* [Online]. [Accessed 2016]. Available from: http://webbook.nist.gov/cgi/cbook.cgi?ID=C109671&Mask=4

163. NIST. *1-Octene.* [Online]. [Accessed 2016]. Available from: http://webbook.nist.gov/cgi/cbook.cgi?ID=C111660&Units=SI&Mask=7FF

164. Lin-Vien, D. *The handbook of infrared and Raman characteristic frequencies of organic molecules.* San Diego;London;: Academic Press, 1991.

165. Patai, S. *The chemistry of peroxides.* Chichester;New York;: Wiley, 1983.

166. Makota, O. and Bulgakova, L. The Influence of Metal Carbides on the Oxidation Processes of 1-Octene by Molecular Oxygen and tert-Butyl Hydroperoxide. *ISRN Physical Chemistry.* 2012, **2012**, p.4.

167. Alfa-Aeser. *tert-Butyl hydroperoxide, 70% aqueous solution (MSDS).* Ward Hill, MA, USA: Johnson Matthey Catalog Company, Inc., 2013.

168. Clayden, J., Greeves, N. and Warren, S.G. *Organic chemistry.* Oxford: Oxford University Press, 2012.

169. Kharasch, M.S., Pauson, P. and Nudenberg, W. The Chemistry of Hydroperoxides. Xii. The Generation and Properties of Free RO_2. Radicals. *The Journal of Organic Chemistry.* 1953, **18**(3), pp.322-327.

170. Story, L.G., Provine, R.W. and Bennett, H.T. Chemistry of Gum Formation by Cracked Gasoline. *Industrial & Engineering Chemistry.* 1929, **21**(11), pp.1079-1084.

171. Anton Paar. *How to measure the gum content of fuels.* [Online]. 2018. [Accessed 2018]. Available from: https://wiki.anton-paar.com/en/how-to-measure-the-gum-content-of-fuels/

172. Pretsch, E., Bühlmann, P. and Affolter, C. *Structure Determination of Organic Compounds: Tables of Spectral Data.* Springer, 2000.

173. Wenig, P. and Odermatt, J. OpenChrom: a cross-platform open source software for the mass spectrometric analysis of chromatographic data. *BMC Bioinformatics.* 2010, **11**(1), p.405.

174. Hanwell, M.D., Curtis, D.E., Lonie, D.C., Vandermeersch, T., Zurek, E. and Hutchison, G.R. Avogadro: an advanced semantic chemical editor, visualization, and analysis platform. *Journal of Cheminformatics.* 2012, **4**(1), p.17.

175. Avogadro. *Molecular Mechanics & Force Fields.* [Online]. 2018. [Accessed 2018]. Available from: https://avogadro.cc/docs/optimizing-geometry/molecular-mechanics/

176. Neese, F. The ORCA program system. *Wiley interdisciplinary Reviews - Computational Molecular Science.* 2012, **2**(1), pp.73-78.

177. Weigend, F. and Ahlrichs, R. Balanced basis sets of split valence, triple zeta valence and quadruple zeta valence quality for H to Rn: Design and assessment of accuracy. *Physical Chemistry Chemical Physics.* 2005, **7**(18), pp.3297-3305.

178. Neese, F., Wennmohs, F., Hansen, A. and Becker, U. Efficient, approximate and parallel Hartree–Fock and hybrid DFT calculations. A 'chain-of-spheres' algorithm for the Hartree–Fock exchange. *Chemical Physics.* 2009, **356**(1), pp.98-109.

179. Barnes, L., Schindler, B., Allouche, A.-R., Simon, D., Chambert, S., Oomens, J. and Compagnon, I. Anharmonic simulations of the vibrational spectrum of sulfated compounds: application to the glycosaminoglycan fragment glucosamine 6-sulfate. *Physical Chemistry Chemical Physics.* 2015, **17**(39), pp.25705-25713.

180. Snyder, R.G., Liang, G.L., Strauss, H.L. and Mendelsohn, R. IR spectroscopic study of the structure and phase behavior of long-chain diacylphosphatidylcholines in the gel state. *Biophysical journal.* 1996, **71**(6), pp.3186-3198.

181. Koji, N., Toshio, G. and Mamoru, O. Infrared Spectra of Organic Ammonium Compounds. *Bulletin of the Chemical Society of Japan.* 1957, **30**(4), pp.403-408.

182. Carretti, E., Dei, L., Baglioni, P. and Weiss, R.G. Synthesis and Characterization of Gels from Polyallylamine and Carbon Dioxide as Gellant. *Journal of the American Chemical Society.* 2003, **125**(17), pp.5121-5129.

183. Chunhachaichana, C. and Srichana, T. Efficiency of sildenafil encapsulation in poloxamer micelles. *Journal of Dispersion Science and Technology.* 2018, pp.1-8.

184. Wallace, S.J., Li, J., Nation, R.L., Prankerd, R.J., Velkov, T. and Boyd, B.J. Self-assembly behavior of colistin and its prodrug colistin methanesulfonate: implications for solution stability and solubilization. *The journal of physical chemistry. B.* 2010, **114**(14), pp.4836-4840.

185. Jeraal, M.I., Roberts, K.J., McRobbie, I. and Harbottle, D. Process-Focused Synthesis, Crystallization, and Physicochemical Characterization of Sodium

Lauroyl Isethionate. *ACS Sustainable Chemistry & Engineering.* 2018, **6**(2), pp.2667-2675.

186. Wang, D. *Flotation Reagents: Applied Surface Chemistry on Minerals Flotation and Energy Resources Beneficiation.* Springer Singapore, 2016.
187. Malvern. *Surfactant micelle characterization usingdynamic light scattering.* Worcestershire, UK: Malvern Instruments Limited, 2015.
188. Steers, D., Gerrard, C., Hirst, B., Sibbett, W. and Padgett, M.J. Gasoline analysis and brand identification using a static Fourier-transform ultraviolet spectrometer. *Journal of Optics A: Pure and Applied Optics.* 1999, **1**(6), pp.680-684.
189. Hameed, B.S., Bhatt, C.S., Nagaraj, B. and Suresh, A.K. Chapter 19 - Chromatography as an Efficient Technique for the Separation of Diversified Nanoparticles. In: Hussain, C.M. ed. *Nanomaterials in Chromatography*. Elsevier, 2018, pp.503-518.
190. First-Ten-Angstroms. *Contact Angle and Surface Energy Measurements on Steel.* Portsmouth, Virginia, USA., 2003.
191. Law, K.-Y. Definitions for Hydrophilicity, Hydrophobicity, and Superhydrophobicity: Getting the Basics Right. *The Journal of Physical Chemistry Letters.* 2014, **5**(4), pp.686-688.
192. Dearn, K., Xu, J., Ding, H., Xu, H., Weall, A., Kirkby, P., Cooper, B., Edington, I. and Krueger-Venus, J. An Investigation into the Characteristics of DISI Injector Deposits Using Advanced Analytical Methods. *SAE International Journal of Fuels and Lubricants.* 2014, **7**(3), pp.771-782.
193. Molitor, P., Barron, V. and Young, T. Surface treatment of titanium for adhesive bonding to polymer composites: a review. *International Journal of Adhesion and Adhesives.* 2001, **21**(2), pp.129-136.
194. Smith, G.C. Evaluation of a simple correction for the hydrocarbon contamination layer in quantitative surface analysis by XPS. *Journal of Electron Spectroscopy and Related Phenomena.* 2005, **148**(1), pp.21-28.
195. Castle, J.E. The Composition of Metal Surfaces After Atmospheric Exposure: An Historical Perspective. *The Journal of Adhesion.* 2008, **84**(4), pp.368-388.
196. Cabrera, N. and Mott, N.F. Theory of the oxidation of metals. *Reports on Progress in Physics.* 1949, **12**(1), pp.163-184.
197. Fromm, E. and Mayer, O. Interaction of oxygen and nitrogen with clean transition metal surfaces. *Surface Science.* 1978, **74**(1), pp.259-275.
198. Jeurgens, L.P.H., Reichel, F., Frank, S., Richter, G. and Mittemeijer, E.J. On the development of long-range order in ultra-thin amorphous Al_2O_3 films upon their transformation into crystalline γ-Al_2O_3. *Surface and Interface Analysis.* 2008, **40**(3-4), pp.259-263.

199. Piao, H. and McIntyre, N.S. Adventitious carbon growth on aluminium and gold–aluminium alloy surfaces. *Surface and Interface Analysis.* 2002, **33**(7), pp.591-594.

200. Crist, B.V. *Handbooks of Monochromatic XPS Spectra.* USA: XPS International, LLC, 1999.

201. Venkataraman, R. and Eser, S. Characterization of deposits formed on diesel injectors in field test and from thermal oxidative degradation of n-hexadecane in a laboratory reactor. *Chem Cent J.* 2008, **2**, p.25.

202. Cutting, R.S., Muryn, C.A., Vaughan, D.J. and Thornton, G. Substrate-termination and H_2O-coverage dependent dissociation of H_2O on Fe_3O_4(111). *Surface Science.* 2008, **602**(6), pp.1155-1165.

203. Fujii, T., de Groot, F.M.F., Sawatzky, G.A., Voogt, F.C., Hibma, T. and Okada, K. In situ XPS analysis of various iron oxide films grown by NO_2-assisted molecular-beam epitaxy. *Physical Review B.* 1999, **59**(4), pp.3195-3202.

204. Yamashita, T. and Hayes, P. Analysis of XPS spectra of Fe^{2+} and Fe^{3+} ions in oxide materials. *Applied Surface Science.* 2008, **254**(8), pp.2441-2449.

205. Flori, M., Gruzza, B., Bideux, L., Monier, G. and Robert-Goumet, C. A study of the 42CrMo4 steel surface by quantitative XPS electron spectroscopy. *Applied Surface Science.* 2008, **254**(15), pp.4738-4743.

206. Mullet, M., Khare, V. and Ruby, C. XPS study of Fe(II)-Fe(III) (oxy)hydroxycarbonate green rust compounds. *Surface and Interface Analysis.* 2008, **40**(3-4), pp.323-328.

207. Stevens, J.S., Byard, S.J., Muryn, C.A. and Schroeder, S.L.M. Identification of Protonation State by XPS, Solid-State NMR, and DFT: Characterization of the Nature of a New Theophylline Complex by Experimental and Computational Methods. *The Journal of Physical Chemistry B.* 2010, **114**(44), pp.13961-13969.

208. Nanayakkara, C.E., Jayaweera, P.M., Rubasinghege, G., Baltrusaitis, J. and Grassian, V.H. Surface Photochemistry of Adsorbed Nitrate: The Role of Adsorbed Water in the Formation of Reduced Nitrogen Species on α-Fe_2O_3 Particle Surfaces. *The Journal of Physical Chemistry A.* 2014, **118**(1), pp.158-166.

209. Baltrusaitis, J., Cwiertny, D.M. and Grassian, V.H. Adsorption of sulfur dioxide on hematite and goethite particle surfaces. *Physical Chemistry Chemical Physics.* 2007, **9**(41), pp.5542-5554.

210. Grosvenor, A.P., Kobe, B.A., Biesinger, M.C. and McIntyre, N.S. Investigation of multiplet splitting of Fe 2p XPS spectra and bonding in iron compounds. *Surface and Interface Analysis.* 2004, **36**(12), pp.1564-1574.

211. Tseregounis, S.I. Analysis by x-ray photoelectron spectroscopy/depth profiling of thin, gasoline-derived deposit films. *Industrial & Engineering Chemistry Research.* 1990, **29**(9), pp.1954-1962.

212. Baltrusaitis, J., Jayaweera, P.M. and Grassian, V.H. XPS study of nitrogen dioxide adsorption on metal oxide particle surfaces under different environmental conditions. *Physical Chemistry Chemical Physics.* 2009, **11**(37), pp.8295-8305.

213. Ma, S., Chu, S., Zhang, Z. and Qiu, Y. Principle and Practice of High Nitrogen Steel Melting by Blowing Ammonia Gas. *Journal of Iron and Steel Research, International.* 2010, **17**(2), pp.6-9.

214. Patra, S., Nayak, J., Singhal, L.K. and Pal, S. Prediction of Nitrogen Content of Steel Melt during Stainless Steel Making Using AOD Converter. *steel research international.* 2017, **88**(5), p.1600271.

215. Uggowitzer, P.J., Magdowski, R. and Speidel, M.O. Nickel Free High Nitrogen Austenitic Steels. *ISIJ International.* 1996, **36**(7), pp.901-908.

216. Belman, N., Israelachvili, J.N., Li, Y., Safinya, C.R., Bernstein, J. and Golan, Y. The Temperature-Dependent Structure of Alkylamines and Their Corresponding Alkylammonium-Alkylcarbamates. *Journal of the American Chemical Society.* 2009, **131**(25), pp.9107-9113.

217. Kjærvik, M., Schwibbert, K., Dietrich, P., Thissen, A. and Unger, W.E.S. Surface characterisation of Escherichia coli under various conditions by near-ambient pressure XPS. *Surface and Interface Analysis.* 2018, **50**(11), pp.996-1000.

218. Annand, R.R., Hurd, R.M. and Hackerman, N. Adsorption of Monomeric and Polymeric Amino Corrosion Inhibitors on Steel. *Journal of The Electrochemical Society.* 1965, **112**(2), pp.138-144.

219. Wood, M.H., Casford, M.T., Steitz, R., Zarbakhsh, A., Welbourn, R.J.L. and Clarke, S.M. Comparative Adsorption of Saturated and Unsaturated Fatty Acids at the Iron Oxide/Oil Interface. *Langmuir.* 2016, **32**(2), pp.534-540.

220. Chia, C.L. *Classical and ReaxFF Molecular Dynamics Simulations of Fuel Additives at the Solid-fluid Interface*. Ph.D. thesis, University of Manchester, 2018.

221. Smith, J.W. and Saykally, R.J. Soft X-ray Absorption Spectroscopy of Liquids and Solutions. *Chemical Reviews.* 2017, **117**(23), pp.13909-13934.

222. Chang, S.Y., Kathyola, T., A. Willneff, E., John Willis, C., Wilson, P., J. Dowding, P., Cibin, G., Kroner, A., Shotton, E. and Schroeder, S. *A Versatile Liquid-Jet/Sessile Droplet System for Operando Studies of Reactions in Liquid Dispersions and Solutions by X-ray Absorption Spectroscopy.* 2019.